The University Of Sheffield.

Improved Durability and Sustainability of Alkali-Activated Slag Cements

By

Xinyuan Ke

Supervisors:

Professor John L. Provis

Dr. Susan A. Bernal

A thesis submitted in total fulfilment of the requirements for the degree of

Doctor of Philosophy

Department of Materials Science and Engineering

The University of Sheffield

June 2017

“…every discovery contains an invitation to make further discoveries, and that a failed experiment means only that the wrong question is being asked, not that there are no answers.”–Theodore Zeldin

Abstract

Alkali-activated binders, produced through the chemical reaction between an aluminosilicate precursor and an alkali activator, are gaining interest as a sustainable and technically sound alternative to traditional Portland cement for production of concretes. This study aimed to determine factors controlling microstructural features of these materials, so alkali-activated slag cements with improved durability and sustainability can be tailored for specific performance requirements.

Prediction of the performance of alkali-activated slag (AAS) is challenging due to the lack of detailed understanding of the existing relationship between the curing conditions adopted and the physico-chemical properties of the anhydrous slag, and the type and concentration of the alkali activator used. Among these, the nature of the alkaline activator strongly influences the environmental impact associated with its production, and the most widely used alkaline activators (e.g. sodium metasilicates and/or hydroxides) contribute the majority of the environmental footprint assigned to alkali-activated cements. The fact that these activators can be corrosive is of concern, and their handling and utilisation require skilled personnel for the safe production of alkali-activated cements, which is not always available in construction sites.

In search for more cost-effective and user-friendly alkali sources for production of AAS cements, the use of the near-neutral activator sodium carbonate was investigated. The use of sodium carbonate as an activator has been limited by the prolonged setting and delayed strength development identified in some binders produced with this salt, compared with those produced with sodium silicate or hydroxide activators. In this study, the correlation between slag chemistry, reaction kinetics and phase assemblage of sodium carbonate-activated slag cements was determined.

The reaction mechanism of sodium carbonate activated slag cements was elucidated, where the consumption process of free carbonate ions and formation of carbonate bearing

phases in these binders are controlled by the formation of layered double hydroxides (LDHs). It was demonstrated that sodium carbonate activated slag cements do not always present delayed setting times, and this is strongly dependent on the slag chemistry. Considering this, the effectiveness in controlling reaction kinetics and phase assemblage evolution of adding a smart mineral addition (a calcined layered double hydroxide (CLDH)), resembling LDHs forming in high MgO content slags, was assessed. The prolonged setting time of sodium carbonate activated slag cements was significantly shortened with the addition of CLDH, along with an increase in the compressive strength and reduction in the permeability of the specimens.

Chloride-induced pit corrosion is one of the main causes leading to degradation of steel reinforced concrete structures. The resistance of structural concrete to external chloride attack is largely depending on the penetration rate of the external chloride. This closely relates to the water transport and chloride ionic interaction taking place in the cementitious matrix. The ionic binding capacity of chlorides in alkali-activated cements, therefore is crucial for predicting the long term performance of AAS as a structural construction material.

For a better understanding of the chloride binding behaviour of AAS cements, synthetic sodium substituted calcium aluminosilicate hydrate (C-(N)-A-S-H) type gels, a hydrotalcite-like phase, and strätlingite were produced, and their interaction with chloride were studied individually. Chemical substitution (ion-exchange) and surface adsorption are the two major mechanisms of chloride ions binding onto hydrated phases forming in AAS binders. This interaction significantly reduces the free chloride concentration in AAS pore solution. It was elucidated in this study that C-(N)-A-S-H gel and hydrotalcite-like phase mainly bind chlorides in the diffuse layer through a surface adsorption mechanism, while strätlingite binds chloride through substitution of interlayer species via ion-exchange.

Therefore, the chloride binding capacity of AAS cements is strongly dependent on the mix design of these materials, which governs the formation of specific hydrated phases. When using sodium carbonate as alkali activator a reduced chloride binding capacity was observed, compared with pastes produced with a commercial sodium silicate, associated with the

differences in phase assemblage between these two cementitious systems. However, the inclusion of 5 wt.% of the CLDH mineral addition modified the chloride binding capacity of these materials, so that AAS produced with sodium carbonate showed higher chloride binding capacity than that of sodium silicate activated samples. This is consistent with the higher compressive strength, reduced permeability and lower chloride migration coefficients identified in CLDH modified specimens.

This study established the fundamental relationships between slag chemistry and reaction kinetics of sodium carbonate-activated slag. The application of the smart chemical addition CLDH for sodium carbonate-activated slag based on the understanding of slag chemistry, has not only made the sodium carbonate activator a plausible option for implementation, but more of a better option with performance advantages. The knowledge developed in this study about the ionic interaction between chlorides and individual reaction product filled in gaps in literature, and becomes a useful tool whose usage is not limited to tailing of sodium carbonate-activated slag, but also for optimising mix design of all types of AAS for achieving better performance.

Acknowledgements

First and foremost, I would like to express my sincere gratitude to my supervisors, Professor John L. Provis and Dr. Susan A. Bernal for involving me in this very interesting project, and providing me with great support throughout my PhD. The guidance they have provided me is invaluable and inspiring, which goes beyond the state of the art knowledge, but also vision of the research field.

I wish to devote my greatest gratitude to my parents, Mr. Hanyang Ke and Mrs. Huilan Cai, who are always encouraging me to try new things, and always have great faith in me. I also want to thank my husband, Dr. Yu Duan, my life partner and also my closest friend, without whose understanding, care and support I would not be able to accomplish so far.

Thanks to Dr. Oday H. Hussein, who has trained me to all the equipment in the cement lab, and has been given me great help in the lab. And also thanks to Dr. Nik Reeves-McLaren, who has helped me greatly with his knowledge on X-ray diffractometry. I would like to express my gratitude to all my colleagues from the Immobilisation Science Laboratory and Sheffield Cement group, they have created a pleasant working environment, and I am proud to be part of it.

Thanks all my friends in Sheffield. You were great company and offered unmeasurable support for technical and non-technical issues.

I would like to acknowledge the European Research Council and the China Scholarship Council (CSC) for sponsoring my PhD studies. I would also like to thank the MIDAS Facility at the University of Sheffield, established with support from the UK Department of Energy and Climate Change, for providing equipment used in this study.

Contents

List of Figures

List of Tables

Chapter 1.

INTRODUCTION

Alkali-activated materials are derived from the chemical reaction of an aluminosilicate powder referred to as the '*precursor*', and a highly alkaline solution referred to as the '*activator*', and have become the object of much study in the past decades. These materials have gained interest as an alternative to traditional Portland cement for production of concrete, and are now produced on an industrial scale and commercialised in several countries. Among all the aluminosilicate sources used in alkali-activation, blast furnace slag derived from the iron making process is one of the most widely used precursors, and can yield high performance materials. Sodium hydroxide and sodium silicate are two activators commonly used for producing alkali-activated slag (AAS) cements. However, the high alkalinity and environmental impact associated with the use of those two activators poses technical and sustainability challenges in the industrial scale production of these materials.

Despite the technical and environmental advantages associated with AAS as an alternative cementitious material for structural and non-structural applications, these materials do not yet have a long in-service track record, and the understanding of factors controlling their potential long-term performance is quite limited. In the particular case of chloride-induced pit corrosion of embedded steel, which is one of the main causes of degradation of steel reinforced concrete, it remains unknown how chloride ions interact with the hydrated phases comprising AAS, and whether the mobility of chloride within these cements can be hindered via binding mechanisms.

The aim of this study was to evaluate the effectiveness of a near-neutral salt, sodium carbonate, as an activator for blast furnace slags, as a function of the chemistry of the slag used. Specifically, this study investigates the effect of adding to these cements mineral additions resembling the hydrated phases formed upon activation in AAS. A calcined layered double hydroxide (CLDH) mineral additive was used in designing Na_2CO_3-activated AAS

cements which are intended to be more cost-effective and more durable than AAS produced with commercial sodium silicate activators. The interactions between free chlorides and synthetic phases resembling those forming in AAS cement were assessed in high alkalinity simulated pore solutions, underpinning a new conceptual mechanistic description of the factors controlling durability of these materials in service.

Chapter 2 presents a literature review about phase assemblage formation in alkali-activated slag cements, and the possible interactions between chloride and AAS cement paste. The pore solution chemistry and the phase assemblage of AAS cement, mainly consisting of C-(N)-A-S-H gel, layered double hydroxides (LDHs), and amorphous N-(A)-S-H gel, are governed jointly by the slag chemistry and the type of activators used. The possible interaction between chlorides and individual reaction products under similar aqueous conditions to pore solutions are discussed. Correlations between microstructure, pore network, and durability performance are also discussed.

Chapter 3 provides information regarding the materials used in this study, including the physical and chemical properties of the anhydrous slags, and the grades and sources of the chemical reagents used. Methods for preparing samples in this study have been described. Technical details of the characterisation methods applied are also given in this chapter.

In the work described in Chapter 4, Na_2CO_3-activated slag cements were produced from four different blast furnace slags, each blended with a calcined layered double hydroxide (CLDH) derived from thermally treated hydrotalcite. The aim of this mix design was to expedite the reaction kinetics of these cements, which would otherwise react and harden very slowly. The inclusion of CLDH in these Na_2CO_3-activated cements accelerates their reaction, and promotes hardening within 24 h. The MgO content of the slag also defines the reaction kinetics, associated with the formation of hydrotalcite-type LDH as a reaction product. The effectiveness of the CLDH is associated with removal of dissolved CO_3^{2-} from the fresh cement, yielding a significant rise in the pH, and also potential seeding effects. The key factor controlling the reaction kinetics of Na_2CO_3-activated slag cements is the activator functional

group, and therefore these cements can be designed to react more rapidly by controlling the slag chemistry and/or including reactive additives.

In Chapter 5, three types of synthetic phases (Mg-Al hydrotalcite-like phase, AFm structure (strätlingite), and C-(N)-A-S-H gel) were produced and investigated to better understand the ionic interactions taking place between chlorides, carbonates, and the individual solid phases in AAS, using simulated pore solution environments. Surface adsorption and interlayer ion-exchange of chlorides occurred in both the Mg-Al and AFm type LDH phases; however, chloride uptake in hydrotalcite-group structures is governed by surface adsorption, while strätlingite shows the formation of a hydrocalumite-like phase and ion exchange. Only surface adsorption was identified for C-(N)-A-S-H gels with different compositions, but changes in lattice parameters were also observed. For both Ca-Al and Mg-Al LDHs, decreased chloride uptake levels were observed from solutions with increased $[CO_3^{2-}]/[OH^-]$ ratios, due to the formation of carbonate-containing hydrotalcite and decomposition of AFm phases, respectively.

The work described in Chapter 6 evaluates the chloride binding capacity of AAS cement pastes, and the chloride transport in AAS mortars, prepared using two different types of activators: sodium silicate and sodium carbonate. Sodium carbonate activated paste with 5% CLDH modification was also prepared for evaluation of the effect of CLDH on chloride binding capacities of the AAS paste, and on chloride transport in AAS mortar. The benefit of using chloride-rich simulated pore solutions for evaluating the chloride binding capacity of AAS has been investigated by comparing with the results from using neutral sodium chloride solutions. The mineralogy of the studied AAS paste after exposure to chloride-rich simulated pore solutions is analysed using the knowledge built up from the preceding chapters. The chloride transport within the three studied formulations is evaluated, correlating their chloride binding capacity and microstructures. The improved performance of CLDH modified sodium carbonate activated slag mortars is credited to the higher degree of reaction, higher chloride binding capacity, as well as the refined pore structures achieved in these materials.

Finally, Chapter 7 contains conclusions and some recommendations for future work on developing near-neutral salt activation, and predicting the life-time performance of AAS concrete when exposed to chlorides.

Chapter 2.

LITERATURE REVIEW

Note: Some sections in this chapter are derived from the paper "*Controlling the reaction kinetics of sodium carbonate-activated slag cements using calcined layered double hydroxides*", by X. Ke, S. A. Bernal, J. L. Provis, published in *Cement and Concrete Research*, **2016**, *81*, pp. 24-37, and from "*Uptake of chloride and carbonate by Mg-Al and Ca-Al layered double hydroxides in simulated alkali-activated slag cement pore solutions*", by X. Ke, S. A. Bernal, J. L. Provis, 100, 1-13.

2.1. Introduction

2.1.1. Alkali-activation of blast furnace slags

An alkali-activated material is a cementitious material formed by the reaction between an aluminosilicate precursor and an alkaline activator H. Blast furnace slag is an industrial by-product derived from the iron making industry, that mainly consists of CaO, SiO, Al_2O_3, and MgO in a glassy or poorly crystalline structure (Demoulian et al., 1980, Lothenbach et al., 2011, Osborn et al., 1969, Scott et al., 1986). The earliest record of using alkali-activated slag for synthesising cementitious material has been traced back to a patent awarded to Whiting in 1895 (Whiting, 1895); however, it was not until recent decades that the use of alkali-activated slag has become the object of much study, gaining interest as an alternative to traditional Portland cement to produce concretes, which are now produced on an industrial scale and commercialised in several countries (Provis, 2014a, Provis et al., 2014, van Deventer et al., 2010). Alkali-activated cement has demonstrated, in many aspects, comparable performance to blended Portland cement (Bernal et al., 2011a, Bernal et al., 2014a, Shi, 1996). Some of the standing concrete buildings made using alkali-activated slag cement have proven to have high durability after 30-60 years of service life (Buchwald et al., 2015, Provis et al., 2014).

The performance of alkali-activated slag materials cannot easily be predicted simply from the chemistry of the slag, as there are many additional factors that can modify their microstructure and transport properties, such as the fineness, composition, mineralogy and thermal history of the slag used, the type and concentration of the alkali activator, the mixing time, and the curing conditions (Fernández-Jiménez and Puertas, 2003a, Song et al., 2000, Wang et al., 1994, Winnefeld et al., 2015).

The chemical compositions and physical properties (including particle size distribution, fineness *etc.*) of blast furnace slag are most closely related to the type of iron ores used, the steel making process, as well as their cooling process, all of which might vary from different source of supplier and different locations (Demoulian et al., 1980, Lothenbach et al., 2011, Osborn et al., 1969, Scott et al., 1986, Shi et al., 2006). The chemistry and physical properties of the slag used in preparing alkali-activated slag cement influence the rheology and workability of the paste (Kashani et al., 2014, Wu et al., 1990), the kinetics of reaction at early age (Ben Haha et al., 2011, 2012, Bernal et al., 2014c, Shi and Day, 1996), as well as the nature and amount of reaction products formed (also known as the 'phase assemblage') (Ben Haha et al., 2012, Bernal et al., 2014c, Hong and Glasser, 2002, L'Hôpital et al., 2015, Lothenbach and Gruskovnjak, 2007).

A variety of alkaline solutions are used as activators for producing AAS, the most commonly used alkali-activators are highly alkaline solutions, such as sodium hydroxide and/or sodium silicates (Bernal et al., 2015a, Duran Atiş et al., 2009, Escalante-García et al., 2003, Shi and Day, 1996). Potassium hydroxide or potassium silicates have also been studied, but less often used for large scale production due to the higher cost of potassium than sodium (Kashani et al., 2014). The dose and composition of the activator used upon activation of blast furnace slags will influence the initial dissolution mechanism and rate, the kinetics of reaction, and the phase evolution (Krizan and Zivanovic, 2002). Consequently, it will influence the physical and mechanical properties of the hardened alkali-activated materials.

The selection of the type of activator strongly influences the microstructural features and consequently the physico-mechanical properties of AAS (Bernal et al., 2015a, Duran Atiş et al., 2009, Fernández-Jiménez and Puertas, 2001), as well as the environmental impacts associated with the production of these materials (Habert et al., 2011, Habert and Ouellet-Plamondon, 2016, Provis, 2014b). Although AAS binders have much lower global warming potentials than Portland cement (Habert and Ouellet-Plamondon, 2016), the use of strong alkalis (solution pH higher than 12) such as sodium hydroxide and sodium silicate as activators brings higher environmental impact than PC in aspects including human toxicity, fresh water and marine ecotoxicity. In the search for more cost-effective, user-friendly and environmentally friendly alternatives, the use of near-neutral salts (solution pH lower than 12) such as sodium carbonate (solution pH around 11) and/or sodium sulphate (solution pH around 7) as activators for blast furnace slag has attracted the attention of academia and industry (Bernal et al., 2014b, Bernal et al., 2015a, Glukhovsky et al., 1983, Jin and Al-Tabbaa, 2015, Kovtun et al., 2015, Provis, 2014b, Shi and Day, 1996, Xu et al., 2008). The industrial production of sodium silicate is also an energy intensive process, and the commonly used furnace process requires reacting soda ash (Na_2CO_3) and sand (SiO_2) at a melting temperature of around 1100 °C-1200 °C (Fawer et al., 1999). As for production of sodium carbonate chemicals, thought the industrial synthesis process could also be energy consuming, around a quarter of the world soda ash are produced from natural deposits (Kostick, 2012), the process of which leads to significantly lower greenhouse gases emission (Office of Air and Radiation, 2009). To replace sodium silicate with sodium carbonate, refined soda ash, as alternative alkali-activator would bring down the environmental impact of alkali-activated slag, especially in regions where there are abundant geological storage of soda ashes (or Trona) mining (Sharma, 1991). However, as a non-conventional type of activator, the utilisation of sodium carbonate as activator is still facing challenges before being carried out for industrial production. The challenges and possible solutions for implementation of sodium carbonate as activator will be discussed in detail in section 2.3.

2.1.2. Phase assemblage of alkali-activated slag binders

The cementitious properties of alkali-activated binders depend on the bulk chemical composition and mineralogy of the raw material used, the fineness of the particles, and the type and amount of the activator used (Lothenbach and Gruskovnjak, 2007, Provis, 2014a, Provis and Bernal, 2014). Nevertheless, (Al,Na)-substituted calcium silicate hydrate (C-(N)-A-S-H[1]) type gels and layered double hydroxides (LDHs), are two main groups of phases that commonly identified in alkali-activated blast furnace slag systems, as illustrated in Figure 2-1 (Provis and Bernal, 2014).

The main hydration product forming in alkali-activated slag cements, independent of the type of slag or activator used, is C-(N)-A-S-H type gel, which has a disordered tobermorite-like structure (Fernández-Jiménez et al., 2003, Myers et al., 2013, Puertas et al., 2011). The commonly identified secondary phases include LDHs such as hydrotalcite-like and monocarboaluminate (AFm)-like phases, which may also be significantly disordered. A hydrotalcite-like phase, an Mg-Al layered double hydroxide), has been identified when the MgO content in the alkali-activated slag system is higher than 5-7% (Bernal et al., 2014c, Provis and Bernal, 2014, Song and Jennings, 1999). The AFm phase is not always identifiable by X-ray diffraction analysis; however, it has been suggested that its formation is taking place in these binders, and AFm-like layers are closely intermixed into the C-(A)-S-H structure on a nano-scale (Bernal et al., 2013, Wang and Scrivener, 1995). When high calcium (CaO > 30 wt.%), low magnesium (MgO < 5 wt.%) blast furnace slags are activated, instead of observable hydrotalcite, crystalline zeolites such as gismondine, heulandite and garronite have been identified (Bernal et al., 2011b, Bernal et al., 2014c).

[1] Cement chemistry notation is used throughout this study, with A=Al_2O_3, C=CaO, F=Fe_2O_3, H=H_2O, M=MgO, N=Na_2O, S=SiO_2.

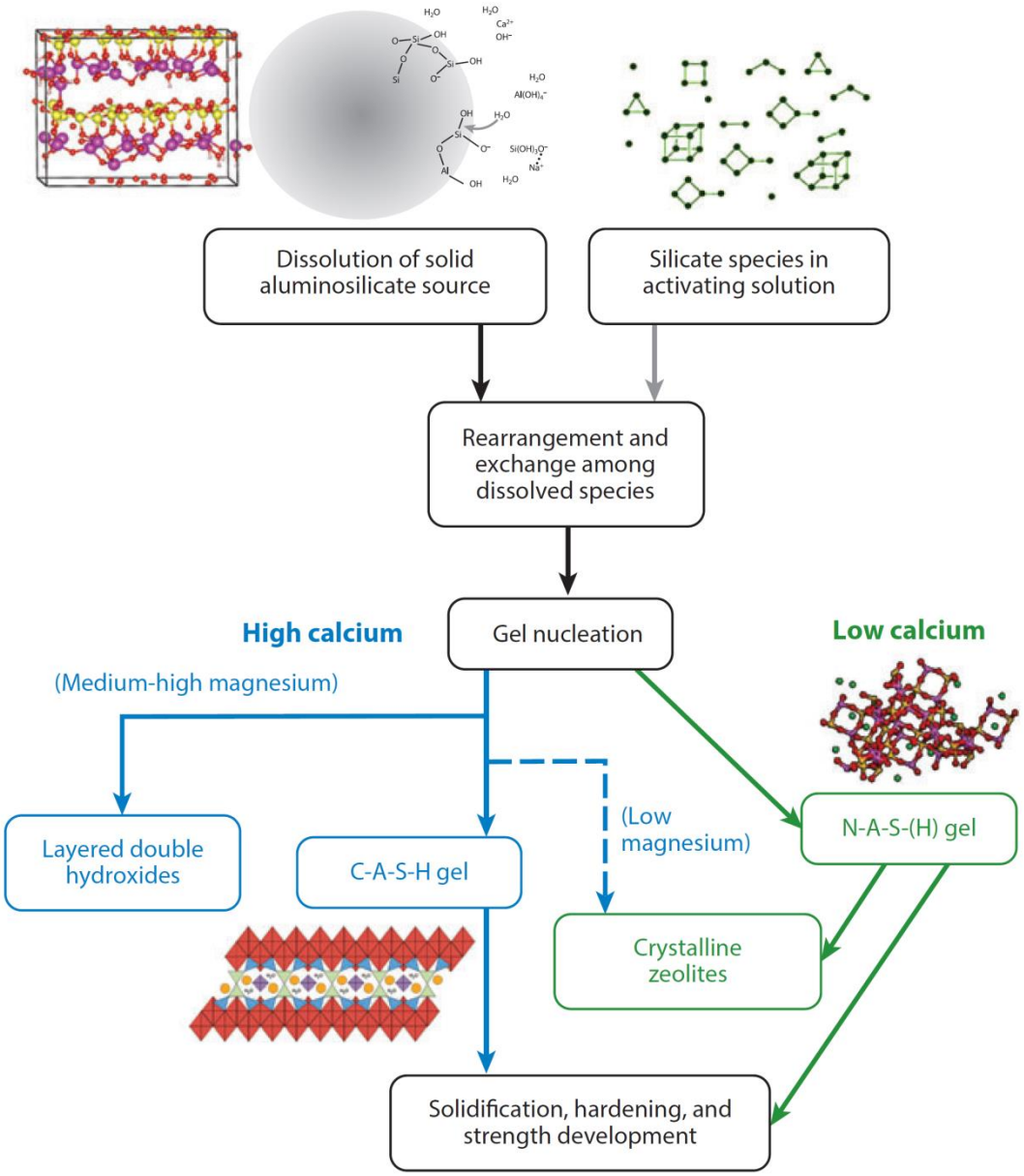

Figure 2-1 Process and reaction products of alkaline activation of a solid aluminosilicate precursor. High-calcium systems react according to the left-hand (blue) pathway, with the nature of secondary products determined by Mg content, whereas low-calcium systems react according to the right-hand (green) pathway. Adapted from (Provis and Bernal, 2014)

2.1.2.1. *C-(N)-A-S-H type gels*

The C-(N)-A-S-H type gels typically identified in hardened alkali-activated slag cement, have a disordered tobermorite-like structure, with a bulk Ca/(Al+Si) ratio ranging from 0.7-1.3 (Faucon et al., 1999, Fernández-Jiménez et al., 2003, L'Hôpital et al., 2015, Myers et al., 2013, Puertas et al., 2011, Richardson et al., 1994, Schneider et al., 2001). The chemistry and local structure of these type of gels is strongly influenced by the slag chemistry, nature of the activator used, as well as the curing temperature (Ben Haha et al., 2012, Fernández-Jiménez et al., 2003, L'Hôpital et al., 2015, Myers et al., 2013, Myers et al., 2015a, Puertas et al., 2011, Schneider et al., 2001). These C-(N)-A-S-H type gels have a higher amount of Na^+ balancing the charges of end of chain Q^1(I) silica sites (-Si-O-Na^+) compared to those formed in Portland cement (PC), or PC/slag blends, as a result of the sodium rich environment (Hong and Glasser, 2002, Myers et al., 2014). The use of sodium metasilicate as activator favours the formation of highly cross-linked structures, with a higher percentage of Q^2 and Q^3 silica sites in the silica chains, while using sodium hydroxide as activator would result in lower cross-linking density in the silica sites (Fernández-Jiménez et al., 2003).

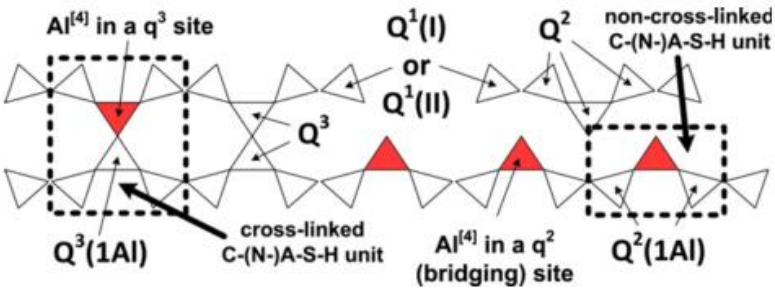

Figure 2-2 Schematic representation of cross-linked and non-cross-linked chain structures of C-(N)-A-S-H gels. The red tetrahedra represent the aluminate species, and the white tetrahedra represent the silicate species. Adapted from (Myers et al., 2014).

The Al/Si ratio in C-(N)-A-S-H type gel generally increases as the availability of Al_2O_3 in the slag used increases (Ben Haha et al., 2012, L'Hôpital et al., 2015, Schneider et al., 2001),

or when the availability of MgO in the slag used decreases (Ben Haha et al., 2011, Bernal et al., 2014c). When using non-silicate activators, such as sodium hydroxide, a higher alkalinity of the solution would often result in a higher Al/Si ratio as it promotes the dissolution of aluminium in the aqueous phase (L'Hôpital et al., 2015). While when using silica-based activators, such as sodium silicate, with the same alkali content (e.g. equivalent Na_2O content), a lower overall Al/Si ratio in the C-(N)-A-S-H type gel could be achieved, as the addition of silica controls the pH of the solution and provides an additional silica source as well (Ben Haha et al., 2012, Fernández-Jiménez and Puertas, 2003b). However, since only Al[IV] exists in the C-(N)-A-S-H chain structure (Richardson et al., 1993, Schneider et al., 2001, Wang and Scrivener, 2003), the Al-O-Al structure is ruled out from the chain structure based on Loewenstein's law (Loewenstein, 1954). Therefore, the highest possible Al-substitution in the C-(N)-S-H gel is limited to between 0.1 to 0.167 by its cross-linked structure, as shown in Figure 2-2 (L'Hôpital et al., 2015, Myers et al., 2013). However, the bulk Al/Si ratio could be higher as interlayer charge balancing Al[V] species might also exist (Andersen et al., 2006, Sun et al., 2006). The excess Al provided by the slag will promote formation of secondary reaction products such as layered double hydroxides, as a function of the type of activator used.

2.1.2.2. *Layered double hydroxides (LDHs)*

The family of layered double hydroxides (LDHs) is a group of minerals derived from the basic brucite-like, $Mg(OH)_2$, lattice structure (hexagonal close-packed lattice structure) (Catti et al., 1995, Gastuche et al., 1967). The partial substitution of divalent cations in the brucite-like structure by trivalent cations leads to a positively charged layered structure (Duan and Evans, 2006, Miyata, 1975, Sato et al., 1988). And since both the divalent cations and substitute trivalent cations can involve different elements, the general formula of LDHs can be concluded as $[M^{II}_{1-x}M^{III}_x(OH)_2]^{x+}[A^{m-}]_{x/m}\cdot nH_2O$ (Duan and Evans, 2006, Marchi and Apesteguía, 1998, Miyata, 1975).

LDHs and their thermally treated forms (calcined LDH, or CLDH) have the capacity of removing anions from aqueous solution, which is influenced by the chemical composition of the brucite-like layer, including the element types of both M^{II} (e.g. Cu, Zn, Ca, Mg) and M^{III} (e.g. Fe, Al), the M^{II}/M^{III} ratios, as well as the anions initially occupying the interlayer (Miyata, 1983, Morimoto et al., 2012, Theiss et al., 2014, Wan et al., 2015).

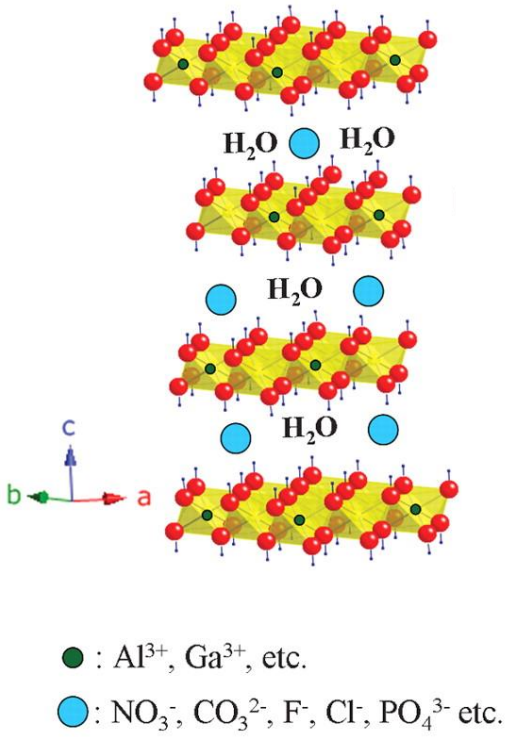

Figure 2-3 A polyhedral representation of the LDH structure showing the metal hydroxide octahedra stacked along the crystallographic c axis. Water and anions are present in the interlayer region. Each hydroxyl group (small dark blue dot connected with large red sphere representing H and O respectively) is oriented toward the interlayer region and may be hydrogen-bonded to the interlayer anions and water (Sideris et al., 2008).

There are two types of layered double hydroxides (LDHs) commonly identified as reaction products in AAS cements: Mg-Al-LDHs (hydrotalcite-like phases) and Ca-Al-LDHs (calcium aluminate monosulfate, named AFm) with a hydrocalumite-like structure (e.g.

hemicarboaluminate, monocarboaluminate or monosulfoaluminate)), the physico-chemical properties of which are influenced by the slag chemistry and the type of activator used (Ben Haha et al., 2011, 2012, Bernal et al., 2014b, Bernal et al., 2014c, Provis and Bernal, 2014, Richardson et al., 1994).

Mg-Al hydrotalcite-like phase

Hydrotalcite-like phases share the general formula $[Mg_{1-x}Al_x(OH)_2]^{x+}[A^{m-}]_{x/m}\cdot nH_2O$, where A^{m-} is often Cl^-, CO_3^{2-} or NO_3^-, and $(1-x)/x$ is generally between 2 and 3. (Mills et al., 2012, Miyata, 1975). Hydrotalcite-like phases are commonly identified in AAS systems, as secondary reaction products, when the MgO content in the raw material is higher than 5 wt.%, in conjunction with the C-(A)-S-H gel which dominates the binder structure (Provis and Bernal, 2014)

Hydrotalcite-like phases are often identified when slags with moderate to high MgO content (> 5 wt.%) are used to produce AAS, particularly when sodium silicate, hydroxide or carbonate are used as alkali activators (Ben Haha et al., 2011, Bernal et al., 2014c). An Mg/Al molar ratio between 2 to 3 generally characterises hydrotalcite-group minerals (Mills et al., 2012, Miyata, 1975); Mg/Al~2.1 has been observed in long-term cured AAS samples (Ben Haha et al., 2011a, 2011b, Bernal et al., 2015a, Richardson, 2013a), and also predicted through thermodynamic modelling (Myers et al., 2015b). More ordered hydrotalcite-likes phase are identified in sodium hydroxide and sodium carbonate-activated slag cement, while less structural ordering was identified in sodium silicate-activated slag paste (Ben Haha et al., 2011, Puertas et al., 2004). A carbonate-containing hydrotalcite-like phase is commonly inferred from experimental data (Ben Haha et al., 2011, Bernal et al., 2014c, Bernal et al., 2015a), although formation of fully hydroxylated meixnerite-like phases (with only hydroxyl groups as interlayer species, seen Table 2-1) is predicted from thermodynamic modelling (Myers et al., 2015b).

Table 2-1 Chemical formulae and mineral names of hydrotalcite-like phase with Mg/Al ratios 2 and 3 (Miyata, 1975, Theiss et al., 2015, Tongamp et al., 2007).

Interlayer species	**Mg/Al=2**		**Mg/Al=3**	
	Chemical formula	Mineral name	Chemical formula	Mineral name
OH^- only	"M_4AH_{13}"	no assigned mineral name	$Mg_6Al_2(OH)_{18}•4H_2O$	Meixnerite
CO_3^{2-} and OH^-	$Mg_4Al_2(OH)_{12}(OH, CO_3)·3H_2O$	Quintinite	$Mg_6Al_2(OH)_{16}$ (OH,CO_3) $•4(H_2O)$	Hydrotalcite

Ca-Al AFm phase

Several different types of AFm-like Ca-Al LDH phases have been identified in AAS cements, generally with a Ca/Al ratio of around 2 and the same basic positively charged layered structure of $Ca_2Al(OH)_6^+$, but with different interlayer species including anions like OH^-, CO_3^{2-}, SO_4^{2-}, and aluminosilicate groups, and some neutral water molecules. (Ben Haha et al., 2012, Bernal et al., 2014b, Matschei et al., 2007a, Schneider et al., 2001). Table 2-2 summarises the chemical formulae and mineral names (as well as common names) of the AFm phases commonly identified in different AAS cements.

The type of activator chosen for preparing AAS cement has a decisive influence on the mineralogy of AFm-type phase formed (Bernal et al., 2013, Myers et al., 2015b, Wang and Scrivener, 1995, 2003); and the chemical composition of the slag used, especially the Al_2O_3 content has a strong influence on the content of AFm formed in AAS cement (Ben Haha et al., 2012, Myers et al., 2015b, Winnefeld et al., 2015). In sodium hydroxide and sodium silicate-activated slag cements, the AFm type phase strätlingite, with an aluminosilicate interlayer anion, has been identified (Wang and Scrivener, 2003). This mostly appears to be present in AAS in disordered forms that are difficult to detect by X-ray diffraction. However, this phase has been identified with combined chemical element analysis (SEM-EDX plots) and ^{27}Al magic-angle spinning nuclear magnetic resonance (MAS NMR) spectroscopy (Bernal et al., 2013, Wang and Scrivener, 1995) and been predicted from thermodynamic modelling (Myers et al., 2015b). Conversely, in sodium carbonate-activated slag cement, the

crystalline AFm phase calcium hemicarboaluminate was identified in some early age samples, which converted to calcium monocarboaluminate ("monocarbonate") gradually over the time of curing (Bernal et al., 2014b), consistent with the thermodynamic modelling predictions reported by Myers et al. (Myers et al., 2015b).

Table 2-2 Chemical formulae and mineral names/common names of AFm phases that are often identified in AAS cement (Damidot et al., 1994, Matschei et al., 2007a, Rinaldi et al., 1990, Wang and Scrivener, 2003).

Interlayer species	**Ca/Al=2**	
	Chemical formula	Mineral name/ Common name
OH^- only	$Ca_2Al(OH)_7 \cdot nH_2O$	Hydroxy-AFm
CO_3^{2-} and OH^-	$Ca_2Al(OH)_6(OH)_x(CO_3)_{(1-x)/2} \cdot nH_2O$	Hemicarboaluminate (x=0.5) Monocarboaluminate (x=0)
SO_4^{2-}	$Ca_2Al(OH)_6(SO_4)_{0.5} \cdot nH_2O$	Kuzelite/Monosulfoaluminate
Aluminosilicate groups $[AlSi(O_8H_8)0.25H_2O]^-$	$Ca_2Al(AlSi)O_2(OH)_{10} \cdot 2.25H_2O$	Strätlingite

2.2. Chloride induced damage in concrete

The durability of a concrete is related to the longevity of both the cement matrix and the steel reinforcement in the concrete structure (Tuutti, 1982). Chloride induced pit corrosion is one of the major cause of structural failure in steel reinforced concretes, which is often induced by an increase in free chloride concentration in the pore solution at the interface between the steel surface and the cement matrix (Ann and Song, 2007, Tuutti, 1982, Yuan et al., 2009).

In general, there are two types of chloride source which are important in concrete durability: the internal chloride supplied from the mix components or contaminated water for mixing, and external chloride, which is commonly supplied by de-icing salts or sea water

(Thunqvist, 2004). The internal chloride content should be controlled by the manufacture of the raw material; which in the case of PC the chloride content is restrained to less than 0.2 to 0.4% by the mass of the cement for producing concrete with reinforcements, according to EN 206:2013 (British Standards Institute, 2013). Also the mixing water should meet the standard by (British Standards Institute, 2002). Therefore, the durability of a structural concrete produced using binder material that meets this standard is more likely to be subject to the attack from the external chlorides.

The resistance of structural concretes to external chloride attack is largely dependent on the penetration rate of the external chloride (Andrade et al., 2000, Glasser et al., 2008, Samson et al., 2003), which reflects the reduction of chloride concentrations in pore solutions as a function of time and distance towards the surface. There are many factors that influence the penetration rate of chlorides, including the concentration of the external chlorides, the porosity and tortuosity of the binder materials, the chemical composition in its pore solution, the interaction between chlorides and the binder phases, and the weathering conditions under which the surface of the structural concretes are exposed (Andrade et al., 2000, Glasser et al., 2008, Martín-Pérez et al., 2000, Samson et al., 2003, Song et al., 2008a).

Alkali-activated slag (AAS) cements are often reported to exhibit low chloride permeability compared with Portland cement[2] (Ismail et al., 2013, Ma et al., 2015, Shi, 1996). This has been partially attributed to the low capillarity identified in these materials (Bernal et al., 2011a, Shi, 2004). The potentially high[3] chloride binding capacity of the AAS cement binder postulated in some studies might also contribute to the higher resistance to chloride ingress (Ismail et al., 2013, Ma et al., 2015), and this will be tested in detail in this thesis.

[2] The chloride migration coefficient of cement mortars prepared using CEM I (according to BS EN 197-1:2011), with w/c ratio around 0.4 and sand fraction around 33%, are normally around 8 ± 1 x10^{-12} m^2/s (Elfmarkova et al., 2015, Halamickova et al., 1995, Yang et al., 2015)

[3] The chloride binding capacity of PC cement paste is normally below 20 mg/g (Delagrave et al., 1997, Luping and Nilsson, 1993).

The diffusivity of chlorides in cementitious materials is normally determined by standardized testing methods built from Fick's 2nd law (Tang and Nilsson, 1992), which do not always take account the binding of free chloride in the cement matrix (Samson et al., 2003). The retention of chlorides in alkali-activated slag binders by chemical binding is expected to delay the ionic transport of chlorides through the concrete, thus reducing the chloride migration rate (Martín-Pérez et al., 2000). For a more accurate prediction of the long–term performance of alkali-activated slag cement, understanding the ionic binding behavior (rates and capacities) of chlorides within a cementitious matrix is crucial in determining the rate of chloride transport through a cement or concrete sample (Angst et al., 2009, Martín-Pérez et al., 2000).

2.2.1. Chloride binding in AAS cements

The interactions between chloride ions and binder materials take place mainly through surface adsorption and/or chemical reaction (including ion-exchange and lattice substitution). Previous studies have demonstrated that the chemistry of the pore solution and the phase assemblage of the binder materials are the main factors that control the chloride binding behaviour in cementitious materials (Arya et al., 1990, Delagrave et al., 1997, Dhir et al., 1996, Ramachandran, 1971, Tritthart, 1989, Yuan et al., 2009).

It is expected that the chloride binding capacity of AAS cements will be largely dependent on the chloride binding capacities of the individual phases forming in these systems, as the total binding capacity of the cement overall will be the sum of the capacities of the constituent phases.

To understand the ionic interactions between chlorides and AAS binder, and to be able to appropriately estimate the binding capacities of these binder materials in service, it is

therefore important that the chloride binding behaviour of individual reaction products can be studied under chemical environment that resembles the pore solution in AAS. However, this knowledge is not available currently from the literature. It will be valuable to generate these data as a starting point for understanding the chloride induced-damage in AAS concrete.

2.2.1.1. Pore solution chemistry of AAS

Previous studies on blended Portland cement showed that the physico-chemical properties of the chloride-rich aqueous solution, including pH, temperature, and the existence of other cations and competitive ions, dominate the chloride up-take capacity of the cement binder (Arya et al., 1990, Saillio et al., 2014, Song et al., 2008b, Tritthart, 1989). Similarly, the chemistry of pore solution of AAS cement will influence the chloride binding behaviour of the binding gels forming in alkali-activated materials (Zhu et al., 2012).

The water in a cement can be classified into four categories based on where it is present and its difficulty to be removed from the matrix: capillary water (including free water in large pores connected to the capillary pores), adsorbed water, interlayer water, and chemically bonded water (Feldman and Sereda, 1970, Jennings, 2008, Muller et al., 2013). The capillary water, existing in the capillary pores and connected large pores, with a diameter of around (or larger than) 50 nm, accounts for the major part of water content in cement after the setting of the cement. It is also generally referred to as pore solution (Barneyback and Diamond, 1981, Mehta and Monteiro, 2006, Page and Vennesland, 1983).

Currently, most of the pore solution composition data available in the literature are for PC or PC-blended cement (Andersson et al., 1989, Vollpracht et al., 2016). Studies evaluating the pore solution chemistry of AAS system are, by comparison, limited. There are many factors that might influence the chemical composition and pH of the pore solution. Apart from the

properties of the raw material, the type of activator and the water/binder ratio used during the activation reaction, and the curing conditions, would all be expected to influence the chemistry of the pore solution (Lloyd et al., 2010, Puertas et al., 2004, Shi, 1996, Song and Jennings, 1999).

Song & Jennings (Song and Jennings, 1999) studied the chemistry of the pore solution of AAS binders, and the influence of slag grind fineness and the concentration of the alkali activator on the pH and concentration of different cations (Si, Al, Ca, Mg), as a function of hydration time. This study showed that the slag fineness does not have a significant influence on the pH of the pore solution or the concentrations of the cations, except for Ca^{2+}. A higher concentration of the alkali activator resulted in a higher pH and higher concentration of soluble Si and Al, but it does not increase the dissolved concentration of Ca^{2+}. The main conclusion of that study was that the solubility of these cations is pH-dependent, which can also be explained by the solubility of the different species dissolving from the slag (Song and Jennings, 1999).

Puertas *et al.* (Puertas et al., 2004) studied the influence of different activators on the pH and concentration of cations including Si, Al, Ca, Mg and Na, in the pore solution of alkali-activated slag binders. For slag activated with sodium hydroxide, the availability of Si and Al is significantly higher than that activated by sodium silicate, which is attributed to the higher pH reached when using NaOH as the activator. Regardless of the type of activator, the free Na concentration observed in that study was always around 2000 mmol/L and the pH between 13.5-14.

Myers *et al.* (Myers et al., 2015b) predicted the pore solution chemical compositions of sodium silicate-activated slag cement using thermodynamic modelling, which matches with experimental observations, shown in Figure 2-4. As slag reacts over time, the concentrations

of Na^+ and OH^- each approach 1000 mmol/L, and other ions co-exist in the pore solutions at concentrations at least one or two orders of magnitude lower than Na^+ and OH^-. The modelling data correlate well with previous studies using slags with similar chemical compositions (Gruskovnjak et al., 2006).

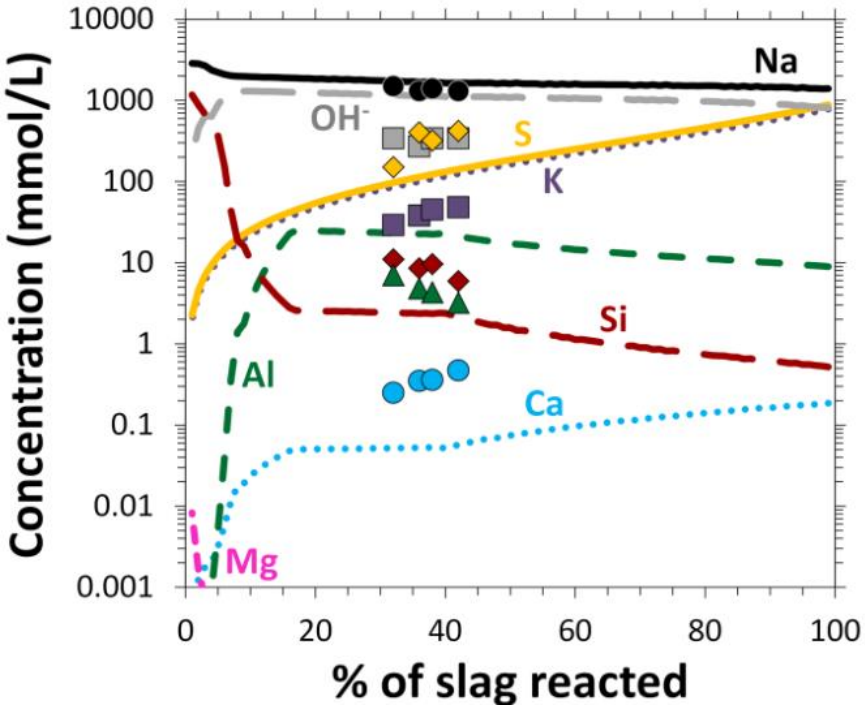

Figure 2-4 Simulated pore solution chemical compositions of sodium silicate-activated slag cement (in lines). Symbols in the figure above represent the sodium silicate-activated slag pore solution data reported by (Gruskovnjak et al., 2006). Adapted from (Myers et al., 2015b)

In summary, the pore solution of alkali-activated cement mostly consists of around 500 to 3000 mmol/L Na with traces of Mg, Ca and Al (Gruskovnjak et al., 2006, Lloyd et al., 2010, Myers et al., 2015b, Puertas et al., 2004, Song and Jennings, 1999, Vollpracht et al., 2016). The concentration of Si is variable, depending on the type of activator used during the alkali-activation reaction. The pH of the pore solution after 28 days of curing was about 13 to 14. Based on this, it is reasonable to synthesise simulated pore solution for the purpose of chloride binding experiments using 0.1-1.0 M NaOH solutions (Myers et al., 2015b, Yang et

al., 2014). The high OH^- concentration in the pore solutions is expected to change the surface charging density (Trefalt et al., 2016), and therefore influence the interaction of chloride with binder gels through surface adsorption. The excess OH^- anions might also act as competitors to Cl^- for available ion-exchange sites (Birnin-Yauri and Glasser, 1998).

Co-ions and counter-ions (effect of Na^+, Ca^{2+}, and OH^-)

Atmospheric carbonation of AAS leads to a reduction in alkalinity and an increase in the concentration of dissolved carbonates in the pore solution (Bernal et al., 2012, Fernández Bertos et al., 2004). Carbonate ions may also play important roles in altering chloride uptake by the solid phases present in in AAS cement; CO_3^{2-} can be taken by LDH interlayers to form stable mineral phases (Morimoto et al., 2012). However, there has not been previous investigation of the stability of the chloride-bearing LDHs in the presence of carbonate ions, in simulated pore solutions relevant to AAS cements.

The presence of divalent anions (e.g. Ca^{2+} and Mg^{2+}) in the pore solution will favour chloride binding compared with monovalent anions (e.g. Na^+ and K^+) (Zhu et al., 2012). Goñi and Andrade (Goñi and Andrade, 1990) used synthetic pore solutions to investigate the chloride resistance of PC in presence of different cations (Na, K and Ca) and pH values. Kirkpatrick et al (Kirkpatrick et al., 2001) observed that the presence of Ca^{2+} in the pore solution/aqueous system promoted the uptake of chloride, as the Ca^{2+} forms ion couples with Cl^-, also described as the ion couple mechanism (Eq.2-1 and Eq.2-2),

$$\text{-Si-OH} \leftrightarrow \text{-Si-O}^- + H^+ \qquad \text{Eq.2-1}$$
$$\text{-Si-O}^- + Ca^{2+} + Cl^- \leftrightarrow \text{-Si-OCaCl} \qquad \text{Eq.2-2}$$

Consistent with this, Kameda et al. (Kameda et al., 2003) studied the influence of different

cations on the adsorption behaviour of hydrotalcite, demonstrating that the same amount of hydrotalcite-like phase could take up more chloride from $CaCl_2$ solution than from a NaCl solution. The same trend was further highlighted by the same researcher in a later study (Kameda et al., 2005).

2.2.1.2. Interaction between C-(N)-A-S-H and Cl^-

Beaudoin *et al.* (Beaudoin et al., 1990) studied the interaction between chloride and synthetic C-S-H gel, and found that the chloride interacting with C-S-H gel could be classified into two catalogues: "alcohol-insoluble chloride" (water leachable) and "tightly held chloride" which is not even leachable by water. These two chloride binding states are distinguished by their different binding energies, and could also be interpreted as chemisorption and lattice-substitution respectively. The binding capacity of C-S-H through chemisorption is dependent on the H_2O/Si and Ca/Si ratios of the C-S-H paste; however, the total amount of lattice substituted chloride appeared to be independent to the properties of the C-S-H gel (Beaudoin et al., 1990). However, the definitions given for the states of chloride in this early research are too vague for use in detailed interpretation of binding environments, and no further characterisation results were provided for more accurate chemical explanations.

Molecular dynamics modeling of chloride binding to the surfaces of calcium silicate phases (tobermorite) showed no surface bound Cl^- ions, which proved the low chloride binding capacity of this type of phase (Kalinichev and Kirkpatrick, 2002). Solid-state ^{35}Cl NMR showed that in general, Cl^- is coordinated primarily by network-modifying alkali or alkaline earth cations. No evidence for Al-Cl bonding was identified (Stebbins and Du, 2002). It is widely accepted that the interactions between Cl^- ions and C-(A)-S-H gel in portlandite saturated PC/blend cementitious binders are mainly governed by surface adsorption due to an

ionic pairing effect (≡Si-O-Ca-Cl), as expressed in Eq.2-1 and Eq.2-2. (Elakneswaran et al., 2009). The binding capacity of the C-S-H phase through electrochemical processes depends on the availability of Ca^{2+} and pH. In Portland cement $[CaOH]^+$ dissociated from portlandite has also been reported to have adsorption capacity (Eq.2-3), which could also be interpreted as an ion-exchange process (Eq.2-4).

$$[CaOH]^+ + Cl^- \leftrightarrow CaOHCl \qquad \text{Eq.2-3}$$

$$Ca(OH)_2 + Cl^- \leftrightarrow CaOHCl + OH^- \qquad \text{Eq.2-4}$$

In the case of AAS systems, C-(N)-A-S-H gel will precipitate before forming portlandite, consuming the free Ca^{2+} in the pore solution (Chen et al., 2004, Lothenbach and Gruskovnjak, 2007). Therefore, the above reactions (Eq.2-3 and Eq.2-4,) are less likely to take place in AAS cement. The overcharging[4] properties of C-S-H were observed by Labbez et al. (Labbez et al., 2007), and therefore the adsorption of Cl^- onto the diffuse layer of the positively charged C-(A)-S-H gel surface is more plausible. For C-(N)-A-S-H type gels, it was observed that the alkali binding is higher when the Ca/Si ratio is reduced (Hong and Glasser, 1999), and Al/Si ratio is increased (Hong and Glasser, 2002). However, with Al-substitution of the Si sites, the surface charge of C-(A)-S-H is reduced, and this might lead to lower capacity to physically bind chloride.

2.2.1.3. Interaction between Mg-Al hydrotalcite-like phase and Cl^-

The chloride binding/ion-exchange behaviour of Mg-Al hydrotalcite-like phase has been studied in the past decades as these phases are effective adsorbents for purifying water (Lv et al., 2006a, Lv et al., 2006b). Earlier studies showed that Mg-Al hydrotalcite-like phase could be intercalated by Cl^- ions (Boclair and Braterman, 1999, Constantino and Pinnavaia, 1995,

[4]An inversion of the effective surface charge of colloidal particles during electrokinetic measurements such as electrophoresis.

Miyata, 1975), although hydrotalcite-like phase with difference basal spacings were observed. Latter studies of surface complexation reactions of inorganic anions on hydrotalcite-like compounds (Constantino and Pinnavaia, 1995, Morimoto et al., 2012) showed that chloride ions would only be adsorbed/bound in the outer sphere of the hydrotalcite-like phase. The molecular dynamics model of chloride-bearing hydrotalcite based on experimental far infrared spectroscopy results predicted that, the interlayer Cl^- ions are partially bonded to the positively charged interlayer through hydrogen bonds, as shown in Figure 2-5 (Wang et al., 2003).

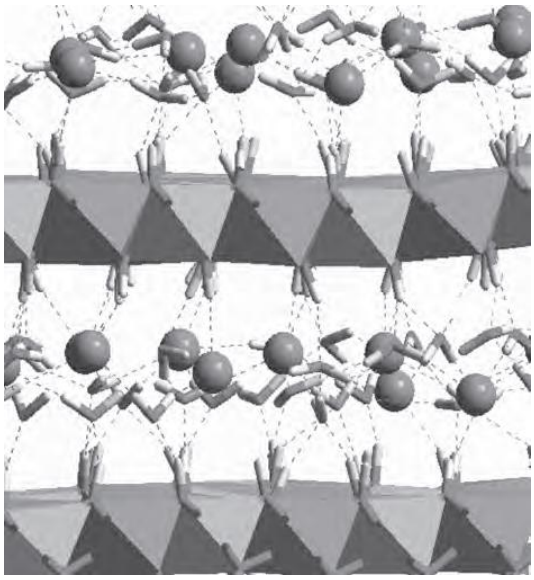

Figure 2-5 A fragment of the model Cl-bearing hydrotalcite crystal illustrating the instantaneous structure of the hydrogen-bonding network in the interlayer. The balls are Cl^- ions and V-shaped moieties are water molecules. The dashed lines represent hydrogen bonds. The main hydroxide layer is represented by Mg/Al octahedra and OH sticks (Wang et al., 2003).

Although hydrotalcite has the exhibited the potential capability to bind free Cl present in the pore solution of cementitious systems, the binding capacity and stability of the chloride-bearing hydrotalcite-like phase, especially in high alkali solutions (pH>13) is still yet to be

discovered. Also, the concentration of CO_3^{2-} ions in pore solutions would increase as a result of natural carbonation process of the sample (Anstice et al., 2005, Bernal et al., 2012, Puertas et al., 2006). Carbonate ions could also be taken by hydrotalcite-like phase as interlayer species (Allada et al., 2005, Brindley and Kikkawa, 1979, 1980). For hydrotalcite-like phase, divalent ions like CO_3^{2-} would be able to be bound in the inner sphere of the phase (Constantino and Pinnavaia, 1995, Morimoto et al., 2012). The thermodynamic properties of hydrotalcite-like phases with various interlayer species showed that the carbonated hydrotalcite-like phase showed the lowest the solubility comparing with those with halides (Cl^- and I^-) as interlayer species (Allada et al., 2005). This suggested that the chloride-bearing hydrotalcite-like phases in AAS cement can be unstable when carbonation occurred, and the bonded chlorides might readily be replaced by carbonate ions.

2.2.1.4. Interaction between AFm phases and Cl^-

Similar to the Mg-Al hydrotalcite-like phase, the interaction between chloride and AFm phase, which also belongs to the LDHs group, would depend on the type of pre-existing interlayer ions in the AFm phase, and the chemistry of the aqueous solutions (Balonis et al., 2010, Goñi et al., 2013, Mesbah et al., 2011a, Mesbah et al., 2012). Figure 2-6 summarises the different chloride-bearing AFm phases.

Friedel's salt ($Ca_4Al_2(OH)_6Cl_2{\cdot}2H_2O$) is commonly identified as the chloride ion-exchanged product of calcium monosulfoaluminate hydrate (AFm). With limited Cl^- in the system, Kuzel's salt $Ca_4Al_2(SO_4)_{0.5}(Cl)(OH)_{12}{\cdot}6H_2O$ would also form as a chloride–bearing AFm phase (Balonis et al., 2010). For calcium monocarboaluminate, when immersed at different Cl^- concentrations, a Friedel's salt type AFm(CO_3,Cl) solid solution could be formed (Goñi et al., 2013, Mesbah et al., 2011a). Similar solid solutions were identified in hydrocalumite, AFm(OH,Cl) (Birnin-Yauri and Glasser, 1998). However, the interaction of

chloride ions with strätlingite has not yet been characterised in detail.

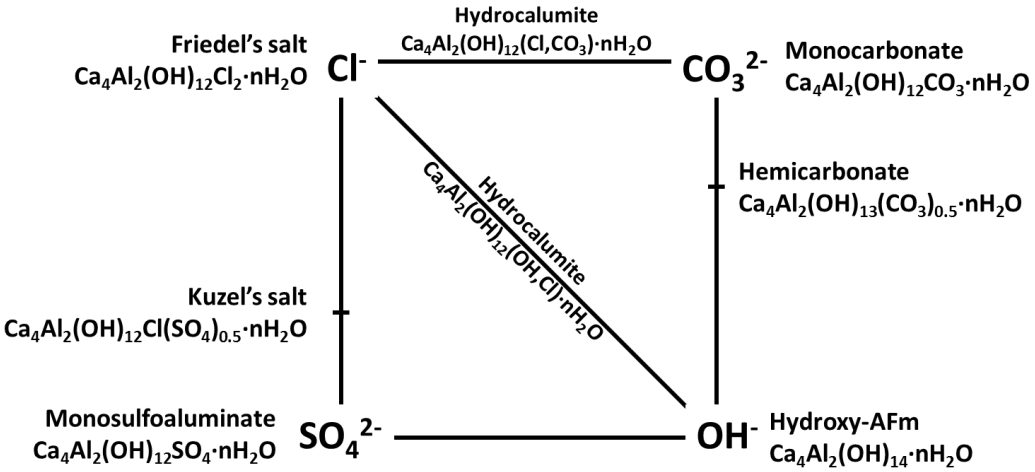

Figure 2-6 Diagram of AFm phases with interlayer species, CO_3^{2-} and OH^- (Fischer and Kuzel, 1982, François et al., 1998, Kuzel and Pöllmann, 1991), Cl^- and CO_3^{2-} (Goñi et al., 2013, Mesbah et al., 2011a), Cl^- and OH^- (Birnin-Yauri and Glasser, 1998, Renaudin et al., 1999), Cl- and SO_4^{2-} (Balonis et al., 2010, Mesbah et al., 2011b).

2.2.2. Chloride diffusion in AAS cements

There are commonly three means by which ion penetration occurs in concrete: capillary absorption, permeation, and diffusion (Goto and Roy, 1981, Page et al., 1981). Absorption is driven by moisture gradients, which usually happens on the surface of the material where the wetting and drying cycles take place (Tong and Gjørv, 2001, Zhang and Gjørv, 1996). Permeation requires a pressure gradient, an applied hydraulic head, so that the solution would be forced to penetrate through the matrix. Diffusion requires a concentration gradient of the chloride ion, which normally occurs when exposed to outer environments of chloride-bearing conditions. Of all these three processes, the main driving force to push chloride ions through saturated concrete is diffusion. The other two methods mainly influence the transportation of

water, and so may carry chloride along with the moving water (Goto and Roy, 1981, Yu and Page, 1991, Zhang and Gjørv, 1996).

The chloride diffusion under steady-state follows Fick's First Law, the one-dimensional situation of which is normally described as Eq.2-5 (Tang and Nilsson, 1992). For non-steady conditions Fick's Second Law is applied, Eq.2-6 (Tang and Nilsson, 1992). In theory, D_{eff} and D_{nss} should be the same, but in reality the values measured are often different (Tang and Sørensen, 2001). The diffusion coefficient is related to the microstructure of the concrete matrix, mostly the tortuosity in the pore network of the binders (Samson et al., 2003).

$$\boldsymbol{J = - D_{\text{eff}} \frac{dC}{dx}} \qquad \text{Eq.2-5}$$

$$\boldsymbol{\frac{\partial C}{\partial t} = D_{\text{nss}} \frac{\partial^2 C}{\partial^2 x}} \qquad \text{Eq.2-6}$$

J - flux of chloride ions,

$\boldsymbol{D_{eff}}$ – effective diffusion coefficient under steady-state conditions,

C - concentration of chloride

x - distance from the surface.

$\boldsymbol{D_{nss}}$ - diffusion coefficient under non-steady-state conditions,

The chloride diffusion coefficients are considered as critical parameters that reflect the mass transport of chloride ions in concrete (Tang and Nilsson, 1992). The chloride diffusion coefficients of cementitious materials are often determined by diffusion cells (Page et al., 1981) under steady state diffusion tests, or/and by immersing samples in solutions for non-steady state diffusion test (ASTM International, 2016, McGrath and Hooton, 1999, Nordtest Method, 1995). However, these test methods often require long test durations and might not always be suitable for engineering testing, for example the NordTest method NT BUILD 443 would take at least 35 days (Nordtest Method, 1995). For being able to evaluate the concrete structure within a much shorter time, rapid test methods were developed based on electrically driven migration tests (ASTM International, 2012a, NordTest Method, 1999, Tang and Nilsson, 1992).

Between the existing test methods, the chloride ponding tests (NordTest method NT BUILD 443 and/or ASTM C-1543-10a) are proven to be the most precise method, however the NT BUILD 492 test is often preferred as a rapid but relatively precise method (NordTest Method, 1999, Tang, 1996, Tang and Sørensen, 2001). Figure 2-7 explains the test setup and the function of each part of the apparatus. An initial current of the tested sample at 30 V is taken for determining the appropriate testing voltage (between 30 V to 60 V) and duration (from 6 h to 96 h), according to the recommendations given by the standard.

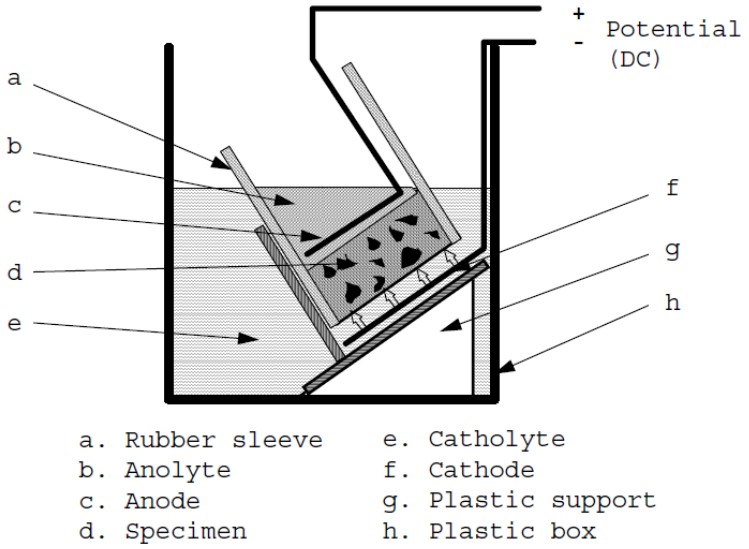

Figure 2-7 NT BUILD 492 setup (NordTest Method, 1999).

2.3. Tailoring sodium carbonate-activated slag

2.3.1. Challenges in using sodium carbonate as activator

As discussed in section 2.1.1., the use of near neutral salt as activator has the potential benefits of lower environmental impact. However, it also faces challenges in aspects like prolonged setting and delayed strength development.

It is well known that alkali-activation of slags is achievable using mild alkaline solutions based on sodium carbonate (Bai et al., 2011, Escalante-García et al., 2003, Fernández-Jiménez and Puertas, 2001, Glukhovsky et al., 1983, Provis and Bernal, 2014, Shi et al., 2006). However, the alkali-activation of slags using near neutral salts has received relatively little attention in the past decades, as the binders produced usually takes longer time to harden than is commercially required for concrete production, and then present a delayed compressive strength development (Bernal et al., 2014a, Fernández-Jiménez and Puertas, 2003b, Wang et al., 1994). Sodium carbonate-activated slag pastes often require up to 5 days to harden in some cases (Bernal et al., 2014b, Fernández-Jiménez and Puertas, 2001, 2003b, Shi and Day, 1996). The prolonged hardening process is related to the slow development of the alkalinity required to initiate the dissolution of the slag. In the alkali-activation process, Ca^{2+} released from the dissolved slag must react with CO_3^{2-} from the activator to form carbonate salts such as calcite and gaylussite, to increase the pH through the release of hydroxide ions (Bernal et al., 2014b). This takes place prior to the precipitation of C-(A)-S-H gel, consuming the Ca^{2+} released by the slag, and as the initial pH of the sodium carbonate activator is below 12, the dissolution of silicate species is slow. With surplus CO_3^{2-} ions present in the system, the pH of the liquid phase increases only slowly due to the unfavourable protonation process of the anhydrous slag (Bernal et al., 2014b, Fernández-Jiménez and Puertas, 2001). After the CO_3^{2-} ions have been exhausted, the later stage reaction mechanism is comparable to that of an NaOH-activated slag (Bernal et al., 2014b).

The formation of these carbonate salts and carbonated LDHs, which appear to have close connection with the reaction kinetics of sodium carbonate-activated slag, is closely related to the chemistry of slag used. Slag chemistry particularly influences the formation of secondary reaction phases such as layered double hydroxides and/or zeolites (Ben Haha et al., 2011, 2012, Bernal et al., 2014c, Provis and Bernal, 2014, Sakulich et al., 2010, Winnefeld et al., 2015), consequently affecting the performance and durability of alkali-activated slag cements. Systematic studies of the influence of slag chemistry on sodium carbonate-activated slag have not previously been published, but the work which is available for silicate and

hydroxide activators shows that the different oxides present in the slag, such as MgO and Al_2O_3, control the kinetics of reaction and the phase assemblage (Ben Haha et al., 2011, 2012, Bernal et al., 2014c, Ehrenberg, 2015, Sakulich et al., 2010, Winnefeld et al., 2015). In most studies, where slags with moderate MgO content (5.3 wt.% to 11.8 wt.%) were used, the Na_2CO_3-activated slag paste required a longer time to set than when using equivalent doses of Na_2SiO_3 or NaOH activator (Bernal et al., 2014b, Fernández-Jiménez and Puertas, 2001, Fernández-Jiménez and Puertas, 2003b, Sakulich et al., 2009). Conversely, Shi and Day (Shi and Day, 1995) used a basic slag with high MgO content (14.6 wt.%), and identified that upon activation with sodium carbonate the samples set within 24 hours, which was faster than when using an equivalent dose of sodium silicate activator. This shows that the slag chemistry plays a significant role in defining the kinetics of reaction when using sodium carbonate as alkali activator, and higher MgO content favours a shorter setting time.

2.3.2. The possibility of using CLDH as a smart addition

The MgO content of slag influences the reaction kinetics, microstructure and strength development of sodium silicate- or hydroxide-activated slag cements, constrained by the availability of Al. This has been mainly related to the formation of layered double hydroxides with a hydrotalcite-like structure, and potential changes in the composition of C-(N)-A-S-H type gels forming in these binders as a function of MgO content (Ben Haha et al., 2011, Bernal et al., 2014c, Winnefeld et al., 2015). Hydrotalcite-like phases have also been seen to increase the resistance to carbonation of alkali silicate-activated slag (Bernal et al., 2014c); the high CO_2 uptake capacity and selectivity of these Mg-Al layered double hydroxides make them effective as in-situ carbonate binding agents.

Thermally treated LDHs, also described as calcined layered double hydroxides (CLDH), can re-crystallise to produce LDHs in an aqueous environment, and the chemical composition and structure of CLDH derived from hydrotalcite are related to the nature of the untreated

LDHs and the thermal activation conditions (Hibino et al., 1995, Mourad et al., 2011). CLDH has been widely used over the past decades as adsorbents for water purification (Lv et al., 2006a, Lv et al., 2006b) and as a catalyst for organic synthesis (León et al., 2011, Tichit et al., 1998). Recently, hydrotalcite and its modified forms have attracted the attention of the cement industry as additions to increase the amount of LDH phases forming in cements to improve the ionic binding of chlorides, and therefore the durability of steel-reinforced concretes (Yang et al., 2014, Yoon et al., 2014b).

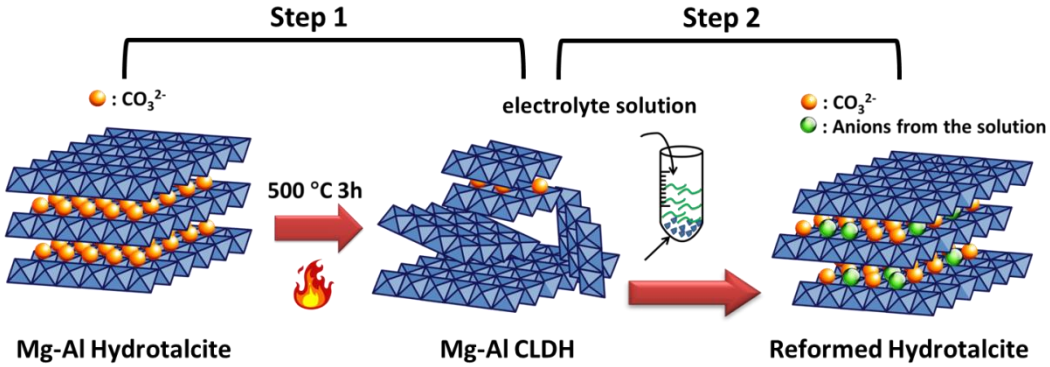

Figure 2-8 Schematic diagram of the decomposition of Mg-Al hydrotalcite into Mg-Al CLDH after calcination at 500 °C for 3 h (step 1), and recrystallisation of reformed hydrotalcite in electrolyte solution (step 2).

Modified LDHs have emerged as a new type of 'smart' addition that is intended to improve the durability of concretes (Kayali et al., 2012, Yang et al., 2012, Yang et al., 2013b, Yoon et al., 2014b). Modified Ca-Al-LDH (Yang et al., 2012, Yang et al., 2013b, 2014) as well as modified Mg-Al-LDH (Yang et al., 2012, 2013a) in their pure form have showed significant chloride binding capacities in chloride-rich solutions. Similar to hydrotalcite-like phases, Ca-Al AFm phases could potentially also be used as chemical additions in cementitious materials. The modified Ca-Al AFm phases (intercalated with nitrate and amino benzonate anions) in alkaline aqueous environment (simulated pore solution, 0.1 M NaOH, that could resemble that of AAS system) forms a Ca-Al-Cl type phase that has a crystal

structure very close to that of Friedel's salt (Birnin-Yauri and Glasser, 1998), which proved their chloride binding/ion-exchange capacity (Yang et al., 2012, Yang et al., 2013b, 2014). The use of CLDH in PC as a chemical addition to improve chloride binding capacity has been studied (Yoon et al., 2014b), and an improved chloride binding capacity has been observed in CLDH modified samples using chloride binding isotherms and X-ray fluorescence mapping. However, the binding of chloride onto recrystallised CLDH in the PC paste seemed to be restricted to physisorption (i.e. the chloride stayed in diffuse layers). The modified hydrotalcite-like phases (intercalated with nitrate and amino benzonate anions) were added to Portland cement based mortars and concretes to improve their performance against chloride penetration (Yang et al., 2015). Lower chloride migration coefficients (measured by NT BUILD 492) were measured from hydrotalcite-like phase modified sample, possibly associated with the lower porosity exhibited by those specimens. The addition of modified hydrotalcite for improving the performance of PC mortars is an innovative approach to improve durability of these materials. However, the influence of adding modified hydrotalcite at a microstructural level has not been discussed yet.

The addition of CLDH, or modified hydrotalcite-like phase into alkali-activated slag cement has not been studied so far. Based on its behaviour in aqueous solutions and in PC cement, it is possible that it will continue performing as effective ion binding phase, taking Cl^- and/or CO_3^{2-} as interlayer species. Although the production of CLDH will also have its own environmental impact, only a small fraction of CLDH incorporation might be needed to achieve potentially significantly higher performance and durability. However, as a promising candidate for tailoring the sodium carbonate-activated slag cement, systematic study of its role on sodium carbonate-activated slag cement is necessary.

2.4. Conclusions

In summary, there has been emerging interest from both academic and industry in optimising the production of alkali-activated slag cement, to achieve AAS cement products not only with low global warming potential but also with minimised environmental impacts in other categories, without having to sacrifice significantly its cost, mechanical performance and longevity. Replacing the highly alkaline activators, including sodium hydroxide and sodium silicate, completely with near-neutral salts such as study sodium carbonate, could significantly reduce the overall environmental impact for countries/regions with significant geological reserves of soda ash minerals. However, based on the current state of art, efforts will be needed to improve the setting behaviour, the strength and the durability performance of sodium carbonate-activated slag cement. The limited information available in the literature discussing chloride interactions with alkali-activated binder materials has also added difficulties for understanding the chloride-induced damage to steel in this type of novel cement.

This study is devoted to fill those knowledge gaps in the literature, and to provide a feasible solution to guarantee the performance of the sodium carbonate-activated slag cement while keeping its sustainability, by incorporating into the mix design a small amount of CLDH minerals as smart additions. In the following chapters, the role of CLDH in controlling the kinetics of reaction and development of desirable microstructures in sodium carbonate-activated slag cement will be discussed. The ionic interactions between potentially corrosive ions and individual reaction products in AAS cement in highly alkaline solutions have been studied in detail, to provide significant advances in understanding the durability of CLDH modified sodium carbonate-activated slag cement.

Chapter 3.

MATERIALS AND METHODS

3.1. Materials

3.1.1. Blast furnace slags

Four commercial slags were used in this study, whose chemical composition is listed in Table 3-1. The slag M01 was a granulated blast furnace slag from the factory Acerías Paz del Ríow in Columbia, the slag M05 was supplied by Zeobond Pty Ltd., Australia, the slag M06 was donated by Ecocem France, and the slag M14 was donated by Prof. Joseé Duchesne from Université Laval, Canada. The Blaine fineness, and the average particle size d_{50} determined using laser diffraction, of each slag are reported in Table 3-2. Slag IDs are assigned according to the MgO content of each of the materials. All four slags were used in Chapter 4, and only slag M06 was used in Chapter 6 and Chapter 7.

Table 3-1 Chemical composition of anhydrous slags, determined by X-ray fluorescence (XRF). LOI corresponds to the loss on ignition at 1000°C. All elements are represented on an oxide basis regardless of their oxidation state in the slag

Slag	CaO	SiO_2	Al_2O_3	MgO	SO_3	Fe_2O_3	TiO_2	MnO	K_2O	Others	LOI
M01	42.9	31.6	14.6	1.2	2.0	1.1	0.4	0.3	0.3	0.2	2.0
M05	42.3	32.3	13.3	5.2	2.9	0.6	0.5	0.2	0.3	0.0	-0.5
M06	41.3	36.0	11.3	6.5	0.7	0.3	0.5	0.3	0.4	0.3	2.0
M14	33.9	37.4	9.0	14.3	0.7	0.4	0.4	1.0	0.5	0.4	1.9

Table 3-2 Physical properties of the anhydrous blast furnace slags

Slag	Blaine Fineness (cm^2/g)$^+$	d_{50} (µm) $^{++}$
M01	4012 ± 49	14.8
M05	4435 ± 109	13.8
M06	5056 ± 22	11.2
M14	4794 ± 44	14.3

[+] Conducted according to ASTM C204-11; quoted uncertainties are the standard deviation of four replicate determinations

[++]Determined by laser diffraction using a dry dispersion unit, at least 4 measurements were taken for each slag, with standard deviation ±0.1 μm.

3.1.2. Alkali activators

Two types of activators, a commercial sodium silicate and sodium carbonate were used in this research. The activators were prepared by pre-dissolving analytical grade sodium metasilicate powder (Sigma Aldrich, $Na_2SiO_3 \geq 99.5\%$) and sodium carbonate powder (Sigma Aldrich, $Na_2CO_3 \geq 99.5\%$) into distilled water.

3.1.3. Calcined layered double hydroxides (CLDHs)

CLDH was produced by thermally treating a synthetic hydrotalcite (Sigma Aldrich) at 500°C at a heating rate of 5°C/min, and with a hold time of 3 h, then allowing the material to cool naturally inside the furnace to 105°C before it was moved to a sealed centrifuge tube and kept in a desiccator under vacuum. This is aiming for preventing the contamination of CLDH by water and/or CO_2 from the atmosphere. The MgO and Al_2O_3 contents of the hydrotalcite prior to thermal treatment were determined by XRF. CO_2 and H_2O contents (approximately add up to 45.5 wt.% according to Figure 3-1) were not detectable using XRF, and therefore determined using a CHNS Analyser (Perkin Elmer 2400).

Table 3-3 Chemical compositions of commercial hydrotalcite, determined by X-ray fluorescence (XRF), the mass percent is balanced by the release of H_2O and CO_2 during heating up

Compound (%)	MgO	Al_2O_3	SiO_2	P_2O_5	SO_3	CaO	Mn_3O_4	ZnO	SrO	ZrO_2	Sum
Hydrotalcite	34.97	18.98	0.01	0.06	0.18	0.30	0.01	0.01	0.01	0.01	54.53

Figure 3-1 shows simultaneous thermogravimetry-mass spectrometry (TG-MS) data for the commercial synthetic hydrotalcite used in this study. The chemical compositions yielded a charge-balanced chemical composition of $Mg_{0.7}Al_{0.3}(OH)_2(CO_3)_{0.15}{\cdot}0.63H_2O$. The thermal treatment conditions adopted in this study were selected based on the experimental results

discussed previously by Hibino et al. (Hibino et al., 1995). The thermal behaviour of synthetic hydrotalcite can be divided into three major steps:

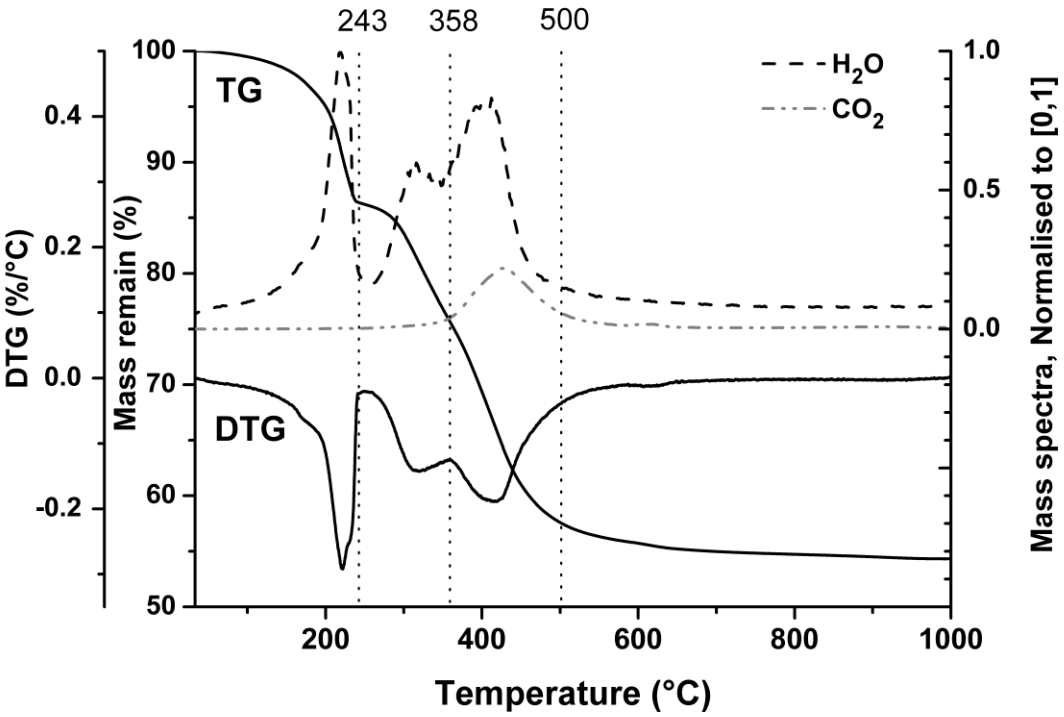

Figure 3-1 TG-MS curve of commercial hydrotalcite, obtained using a Perkin Elmer TGA 4000 instrument coupled with a Hiden mass spectrometer, heating from room temperature to 1000°C at 5°/min.

22°C - 243°C: removal of free water and combined water

$Mg_{0.7}Al_{0.3}(OH)_2(CO_3)_{0.15}{\cdot}0.63H_2O \rightarrow Mg_{0.7}Al_{0.3}(OH)_2(CO_3)_{0.15} + 0.63H_2O$ Eq.3-1

243°C - 358°C: partial dehydroxylation

$Mg_{0.7}Al_{0.3}(OH)_2(CO_3)_{0.15} \rightarrow Mg_{0.7}Al_{0.3}(O_{2-n/2}H_{2-n})\ (CO_3)_{0.15} + {}^{n}/_{2}H_2O$ Eq.3-2

358°C - 500°C: full dehydroxylation and decarbonation

$Mg_{0.7}Al_{0.3}(O_{2-n/2}H_{2-n})\ (CO_3)_{0.15} \rightarrow Mg_{0.7}Al_{0.3}O_{1.15}$ (CLDH) + $(2\text{-}n)H_2O + 0.15CO_2$ Eq.3-3

The CLDH used in this study (calcined at 500°C for 3h) was the product of dehydration, dehydroxylation and decarbonation of synthetic hydrotalcite. The CLDH produced in this study has a chemical composition of $Mg_{0.7}Al_{0.3}O_{1.15}$, as determined by XRF given the fact that during calcination only CO_2 and H_2O are released from solids, and after calcination Mg is in oxidation status Mg^{2+} and Al in Al^{3+} (Hibino et al., 1995).

3.2. Sample preparation

3.2.1. Synthetic gels

Three types of synthetic cementitious phases were prepared in this study: C-(N)-A-S-H type gel, a Mg-Al hydrotalcite-like phase, and the Ca-Al AFm phase strätlingite, for studying the interactions with chloride rich pore solutions. The methods for preparing these synthetic cementitious phases are described in detail in Chapter 5.

3.2.2. Alkali activated slag pastes

Sodium carbonate-activated slag pastes with the addition of different amounts of CLDH were produced using each of the slags studied. Sodium metasilicate-activated slag paste was prepared using only slag M06. The formulations of the pastes produced are shown in Table 3-4. For mix design purposes, the CLDH added to these cements was considered as an additive, and the amount of activator and water added to each unit mass of slag were kept constant (the effect of CLDH on consuming free water was also evaluated with additional samples, see Chapter 4, section 4.2. for more details). All the pastes were cast in centrifuge tubes, then sealed and stored at room temperature (20 ± 3 °C) until testing.

Table 3-4 Formulations of the pastes produced using different slags. The pH values of the activator solutions were determined using a digital pH meter (Oakton Acorn Series).

[+] **Sample ID**	**Slag (g)**	**Na_2CO_3 (g)**	**H_2O (g)**	**Chemical additive CLDH(g)**	**%CLDH (wt.%)**	**%Na_2CO_3 (wt.%)**	**pH of activator**	[++]**w/b**
P-NC-0	10	0.8	4.32	none	**0**	8.00	11.70	0.40
-	10	0.8	4.32	0.2	**2**	8.00	11.70	0.40
P-NC-1	10	0.8	4.32	0.5	**5**	8.00	11.70	0.4
-	10	0.8	4.32	1.0	**10**	8.00	11.70	0.40
	Slag (g)	**Na_2SiO_3 (g)**	**H_2O (g)**	**Chemical additive (g)**	**%CLDH (wt.%)**	**%Na_2SiO_3 (wt.%)**	[+++]**pH of activator**	**w/b***
P-NS-0	10	0.7	4.28	none	**0**	7.00	>13	0.40

[+] Sample ID used in Chapter 6 and Chapter 7.

[++]w/b = water/binder mass ratio (where binder is defined as slag + mass of solid sodium carbonate)

[+++] When measured using the pH meter the reading was always above 13, however since the sodium silicate solution under measurement was a gel-type viscous solution, a fully stabilised reading was not able to be achieved.

In Chapter 4, four different slags were used and only sodium carbonate-activated slag pastes were studied. The samples prepared without CLDH addition are referred to as 0 wt.%, while samples prepared with 2 wt.% and 10 wt.% of CLDH (by mass of anhydrous slag) are described as modified samples.

In Chapter 6, only slag M06 was studied, and both sodium carbonate-activated slag paste, with 0 wt.% and 5 wt.% CLDH and sodium metasilicate-activated slag paste, were prepared. The sample IDs are assigned as shown in Table 3-4. The activator dose (mass percent of either alkali activator solid with respect the to the mass of the slag used) of 7 wt.% for sodium silicate-activated slag paste was chosen as it was the maximum activator dose to achieve setting of the paste within 24 hours, a suitable workable time for implementation. The sodium silicate-activated slag paste with an activator dose of 8 wt.% was observed to require a longer time to set.

3.2.3. Alkali activated slag mortars

The three mix designs of alkali-activated slag mortars studied in Chapter 6 are shown in Table 3-5. Only slag M06 was used for preparing alkali activated slag mortars. Both sodium carbonate activator and sodium metasilicate activator were studied. A sand to slag ratio of 3:1 was applied to all samples. Standard sand (following BS EN 196-1:2005) was used for preparing the mortar specimens.

Table 3-5 Mix design of the mortar samples assessed in this study

Sample I.D.	**Activator type**	**Mass of the activator (g)**	**CLDH (g)**	**Anhydrous slag (g)**	**Water (g)**	**Sand (g)**	**$^{+}$w/b**
M-NC-0	Na_2CO_3	8	0	100	43.2	300	0.4
M-NC-1		8	5	100	43.2	300	0.4
M-NS-0	Na_2SiO_3	7	0	100	42.8	300	0.4

$^{+}$w/b = water/binder mass ratio (where binder is defined as slag + mass of activator)

Sodium silicate activated slag mortar specimens were prepared as a reference for evaluation of sodium carbonate activated slag mortar, with and without CLDH modification. Mortars were moulded in two types of moulds, 50 mm cubic moulds and Ø100 mm×200 mm cylinder moulds. All specimens were demoulded after 2 days of casting, kept in firmly sealed plastic bags and stored at 20 ± 3 °C. Both monoliths (50 mm×50 mm×50 mm), and thick discs (Ø 100mm×50 mm) were prepared for different tests.

3.3. Test methods

Kinetics of reaction of fresh slag pastes/ mortars were evaluated by isothermal calorimetry. In Chapter 4, alkali-activated slag paste samples cured for 28, 90 and 180 days were crushed and immediately treated with acetone to arrest reaction. The powdered specimens were then

dried in a desiccator for 24 h to remove the solvent, and then analysed by X-ray diffraction (XRD), thermogravimetric analysis, and ^{27}Al and ^{29}Si MAS NMR.

For solid samples analysed in Chapter 5 and Chapter 6, the separated solids were dried in a vacuum desiccator at a controlled relative humidity at 30 ± 3% (reached using saturated $CaCl_2$ salt) for 4 days before further analysis.

3.3.1. Isothermal calorimetry

Isothermal calorimetry can directly measure the heat flow released from the freshly mixed cement paste, and have been used widely for studying the kinetics of reaction of cementitious materials, including alkali-activated slag cement (Alonso and Palomo, 2001, Shi and Day, 1995).

For this study, all isothermal calorimetry experiments were conducted using a TAM Air isothermal calorimeter at a base temperature of 25 ± 0.02°C. The fresh slag cement mix was prepared by external hand-mixing for 3 minutes, weighed into an ampoule, and immediately placed in the calorimeter to record heat flow. For fresh pastes, approximately 20 g of freshly mixed samples were used, and heat flow during the first 300 h of reaction was recorded. For fresh mortars, about 30 g of samples were used, and the heat flows were recorded for the first 100 h. All results were normalised by the total mass of sample put in, either paste or mortar.

3.3.2. X-ray diffraction (XRD)

Alkali-activated binders are known to be X-ray amorphous, consistent with the formation of poorly ordered reaction products. The diffractograms of these materials usually show a hump associated with the glassy component of the raw materials, which varies in position

depending on the chemistry of the precursor used. Taking slag and fly ash as examples for high-Ca and low-Ca binders, the anhydrous slag usually shows a hump between 2θ=25°-30°, while fly ash shows a wider hump at 2θ=15°-35° (Ismail et al., 2014).

The main hydration products forming upon alkali-activation of high-Ca or low-Ca precursor, C-(A)-S-H and N-A-S-(H) type gels, are difficult to identify by XRD analysis as these type of gels present a poorly crystalline structure. The crystalline phases that are usually identified from the XRD results are secondary products forming in these binders (e.g. hydrotalcite-like phase, AFm phases, zeolites, carbonates among others), and the non-reactive phases present in the raw materials (Bernal et al., 2013, Burciaga-Díaz and Escalante-García, 2013, Ismail et al., 2014).

In this study, a Bruker D2 Phaser instrument with Cu-Kα radiation and a nickel filter was used to carry out XRD analysis. A step size of 0.02° and a counting time of 3 s/step was used for all measurements. For samples studied in Chapter 4, diffraction patterns from 5° to 55° (2θ) were recorded. In Chapter 6, diffraction patterns from 5° to 25° (2θ) were recorded.

For the synthetic cementitious phases produced and evaluated in Chapter 5, the same diffractometer and step size was used, but a counting time of 0.5 s/ step was applied. This is because the synthetic gels prepared in Chapter 5 were crystallised and/or semi-crystallised, therefore a counting time of 0.5 s/step was sufficient for obtaining high quality XRD results. And for C-(N)-A-S-H gel and strätlingite, diffraction patterns from 5° to 50° (2θ) were recorded, and for hydrotalcite-like phase, from 5° to 70° (2θ) was recorded.

3.3.3. Thermogravimetry analysis

Thermogravimetric analysis (TGA) of all samples studied in this research was carried out in a Perkin Elmer TGA 4000 instrument coupled with a Hiden mass spectrometer. 20 mg of

sample was tested from 30°C to 1000°C at a heating rate of 3°C/min. Commercial-grade nitrogen was used as protective gas at a flow rate of 20 mL/min.

3.3.4. Scanning electron microscopy

Environmental scanning electron microscopy and energy dispersive X-ray spectroscopy (SEM-EDX) were conducted, using a Hitachi benchtop ESEM TM3030 coupled with a Bruker Quantax 70 X-ray microanalysis detector. An acceleration voltage of 15 kV and a working distance of 1 mm were applied, and the acceleration voltage used in this study implies a hemispherical interaction volume with maximum penetration depth of around 1.5 μm - 2.5 μm (Wong and Buenfeld, 2006)Polished but uncoated samples were used for both backscattered electron imaging and EDX analysis under charge-up reduction mode. For per sample at each age and formulation, over 60 points (EDX spots) were randomly taken from 5 to 6 SEM images with a magnification factor of 4000. Between each data point taken from each image there was a minimum distance of 6 μm.

3.3.5. ^{27}Al and ^{29}Si MAS NMR

Magic angle spinning (MAS) nuclear magnetic resonance (NMR) spectroscopy is a powerful technique that can provide structural information for amorphous and poorly crystalline materials. In alkali-activated binder systems, ^{29}Si MAS NMR has been used to determine the extent of the reaction, the polymerisation degree of the aluminium-silicate chains and the extent of incorporation of Al into the C-S-H (Schneider et al., 2001, Wang and Scrivener, 2003). ^{27}Al MAS NMR is used to identify the Al environments, either tetrahedral or octahedral coordinated, present in C-(A)-S-H type gels and in other secondary hydration phases (Fig. 3) forming in alkali-activated cements (Bernal et al., 2014c, Sun et al., 2006).

For this study, solid-state ^{27}Al MAS NMR spectra were acquired at 104.20 MHz, on a Varian VNMRS 400 (9.4 T) spectrometer and a probe for 4 mm o.d. zirconia rotors, a

spinning speed of 12-14 kHz with a pulse duration of 1 µs (approximately 25°), a relaxation delay of 0.2 s, and a minimum of 7000 repetitions. ^{29}Si MAS NMR spectra were collected at 79.4 MHz on the same spectrometer using a probe for 6.0 mm o.d. zirconia rotors, and a spinning speed of 6 kHz. The ^{29}Si MAS NMR were collected with a 90° pulse duration of 4.5 or 6.4 µs, a relaxation delay of 5 s, and between 6000 and 17000 repetitions. ^{29}Si and ^{27}Al chemical shifts are referenced to external samples of tetramethylsilane (TMS) and a 1.0 M aqueous solution of $Al(NO_3)_3$, respectively.

3.3.6. Ion selective electrode (ISE)

The chloride concentration in the supernatant separated from various samples, discussed in Chapter 5 and Chapter 6, was obtained using an ion selective electrode (Cole-Parmer Epoxy solid-state chloride electrode, accuracy ± 2%) according to the standard test method for chloride ions in water (ASTM D512 – 12 (ASTM International, 2012b)).

Chapter 4.

CONTROLLING THE REACTION KINETICS OF SODIUM CARBONATE-ACTIVATED SLAG CEMENTS USING CALCINED LAYERED DOUBLE HYDROXIDES

Note: This chapter is based primarily on the paper "*Controlling the reaction kinetics of sodium carbonate-activated slag cements using calcined layered double hydroxides*", by X. Ke, S. A. Bernal, J. L. Provis, published in *Cement and Concrete Research*, **2016**, *81*, pp. 24-37.

4.1. Introduction

In sodium carbonate activated slags, a prolonged induction period of up to 5 days has been observed (Bernal et al., 2014b, Fernández-Jiménez and Puertas, 2001, Fernández-Jiménez and Puertas, 2003b, Shi and Day, 1996). This was initially attributed to the reduced pH provided by this activator solution, compared with a sodium silicate or hydroxide (Fernández-Jiménez and Puertas, 2001, Shi and Day, 1995), as a limited dissolution rate of calcium aluminosilicate glasses is observed at moderate pH (<11) (Snellings, 2015). However, in recent years it has been proposed that the delayed setting is mainly an effect of the preferential reaction of the functional group present in the activator (CO_3^{2-}), with the calcium dissolving from the slag, to form calcite and mixed sodium-calcium carbonates prior to C-(A)-S-H formation (Bernal et al., 2014b). Bernal et al. (2014b) proposed that after the CO_3^{2-} ions in the liquid phase are consumed, as formation of carbonate salts takes place, the

alkalinity of the pore solution is likely to increase. This speeds up the dissolution process of the slag, so that reaction proceeds similarly to NaOH-activation of the slag. Understanding the mechanism of reaction of these binders has allowed identification of strategies for controlling and modifying the hydration kinetics of slags activated by sodium carbonate, and accelerating the strength development of these materials. One of the potential alternatives is to promote a reaction mechanism that consumes the CO_3^{2-} from the activator at the early stages.

Layered double hydroxides (LDHs) are minerals with positively charged brucite-like layered structures, which allow the incorporation/ion-exchange of anion species between the positive layers (Miyata, 1975). Thermally treated hydrotalcite, which is normally described as calcined layered double hydroxide (CLDH), is the product of dehydration, dehydroxylation and decarbonation processes of LDHs (Hibino et al., 1995). It has been widely used in the past decades as an adsorbent for water purification, as it has a high capacity for uptake of negative ions from the solution through ion-exchange (Lv et al., 2006b). CLDHs can also react with CO_3^{2-} ions to form hydrotalcite-like phases, corresponding to those that are commonly identified as secondary reaction phases in alkali-activated slag systems when the MgO content in the raw material is higher than 5 wt.% (Morimoto et al., 2012, Provis and Bernal, 2014). Therefore, CLDH could be a promising candidate to perform as a carbonate binding agent to expedite the reaction kinetics of sodium carbonate activated slags without introducing foreign components into the binder.

In this chapter, four commercial slags with different chemical compositions were used to produce Na_2CO_3-activated slag cements. The relationships between slag chemistry and sodium carbonate activation are discussed, covering both kinetics of reaction and phase assemblage evolution. CLDH was added as a carbonate binding agent in four different Na_2CO_3-activated slag systems, and its effects on the reaction rate, setting time and phase assemblage evolution were evaluated.

4.2. Materials and methods

Four different source of slag with different chemical compositions were used in this chapter. Sodium carbonate activated slag pastes with different doses of CLDH addition were prepared, as described in Chapter 3. To aid in understanding the effect of addition of CLDH to the activated system, the recrystallisation of pure CLDH in sodium carbonate solution was investigated, as well as two alkali-activated slag paste samples as reference samples prepared according to Table 4-2.

The recrystallisation of CLDH in sodium carbonate solution was investigated using the mix design shown in Table 4-1. The same sodium carbonate activator was used here, and the ratio of CLDH to activator solution was equivalent to that used in the 2 wt.% and 10 wt.% CLDH modified samples (but without the addition of any slag).

Table 4-1 Mix designs used for studying the recrystallisation of CLDH

Sample ID	**CLDH (g)**	**Activating Solution**	
		Na_2CO_3 (g)	**H_2O (g)**
2% CLDH	0.40	1.60	8.64
10% CLDH	2.00	1.60	8.64

Four parallel samples were prepared for each mixture in 15 mL centrifuge tubes. All the samples were kept in a roller mixer continuously for the first 3 days, and after this they were kept in the roller mixer for 8 hours per day (to avoid a fire hazard caused by overheating of the roller mixer during out-of-work hours). For each mix, the slurry was centrifuged and separated after 30 min, 1 h, 24 h and 7 days of reaction. The pH of the separated solution was measured using a pH electrode. The solid was dried in a drying oven at 40 °C for 24 hours

before XRD measurement, under the same instrument operating conditions as described in Chapter 3.

Two reference alkali-activated slag paste samples were prepared according to Table 4-2. Only slag M06 was used in this part of the study.

- For sample Ref-1, synthetic hydrotalcite (Sigma Aldrich) was used instead of CLDH, with the aim of evaluating potential seeding effects related to LDH addition.
- For sample Ref-2, a water to binder (anhydrous slag + anhydrous activator) ratio of 0.35 was used instead of 0.40, and no CLDH was added. The w/b ratio 0.35 was calculated by subtracting the amount of water consumed by CLDH from the total water content of the paste. This sample was designed with the aim of identifying any changes the in kinetics of reaction due to the water consumed during the re-hydration of the CLDH; this will be discussed in detail in section 4.4.2.

Table 4-2 Formulations of the additional pastes produced using slag M06.

No.	Slag (g)	Na_2CO_3 (g)	H_2O (g)	Chemical additive (g)	$\%Na_2CO_3$ (wt.%)	pH of activator	w/b*
Ref-1	10 (M06)	0.80	4.32	1.0 HT	8.0	11.70	0.40
Ref-2	10 (M06)	0.80	3.78	none	8.0	11.89	0.35

*w/b = water/binder mass ratio (where binder is defined as slag + mass of sodium carbonate)

4.3. Results

4.3.1. Kinetics of reaction

Figure 4-1 shows the heat flow from the four different slags studied, during activation with a sodium carbonate solution (Table 4-3), with addition of 0, 2 and 10 wt.% of CLDH. In all samples it is observed that the reaction takes place in two stages. The first occurs within the first 10 h of reaction (insets on each part of Figure 4-1), except for the case of the lowest-MgO slag (M01), where a low heat release was detected due to the low level of precipitation

of reaction products in the first hours of reaction. The first stage of the reaction is followed by a dormant or induction period, where a very low rate of heat release was detected. The duration of the pre-induction period is strongly dependent on the slag composition and the level of CLDH addition. In the second stage of heat release, the nucleation, growth and precipitation of a large amount of reaction products takes place, which is associated with a high heat release. This takes place between 25 h and 300 h after the start of the reaction, depending on the slag composition and the addition of CLDH. Samples prepared without CLDH addition show a very long delay in the appearance of this peak, consistent with the known slow setting of Na_2CO_3-activated slag binders, although the MgO content of the slag is seen to have a significant influence on the time at which this peak appears.

In the first stage of the reaction, a pre-induction band composed of two distinctive peaks was observed in all the samples, except for slag M01. The pre-induction peaks are associated with the formation of calcite and gaylussite, which have been reported as the initial reaction products forming in Na_2CO_3-activated slag binders (Bernal et al., 2014b, Fernández-Jiménez and Puertas, 2001). As slag dissolution progresses, even at low rates within the first hours of reaction, the formation of the reaction product phases such as calcium silicate hydrates (C-S-H) and secondary aluminate-containing reaction products has been observed (Bernal et al., 2014b, Fernández-Jiménez and Puertas, 2001, Fernández-Jiménez and Puertas, 2003b, Shi and Day, 1996), corresponding to the second peak identified within the pre-induction period (insets of each part of Figure 4-1).

For the slag M01 in the absence of CLDH, the initial precipitation of reaction products was observed after 25.7 h, and the peak was low and broad. The slowly evolving pre-induction period was followed by a prolonged dormant period that lasted for 90.1 h before the acceleration period started. The acceleration and deceleration period evolved slowly, with the slowest rate of acceleration among all of the samples studied. The addition of 2 wt.% and 10 wt.% CLDH shortened the dormant period to 32.0 h and 6.7 h (Table 4-3), respectively, and

the onset time of the acceleration period was thus shifted significantly earlier. The heat flow curve during the acceleration-deceleration period became less broad and more intense with the increasing addition of CLDH. The total heat release shown in Table 4-3 for M01 with 2 wt.% CLDH is significantly higher than M01 with 10 wt.% CLDH, this is likely due to missing the initial heat release during the external sample mixing process (Fernández-Jiménez and Puertas, 1997). However, this effect was minimized in the rest of the samples assessed in this part of the study where the increase in the total heat release was consistent with the expedited heat release flow.

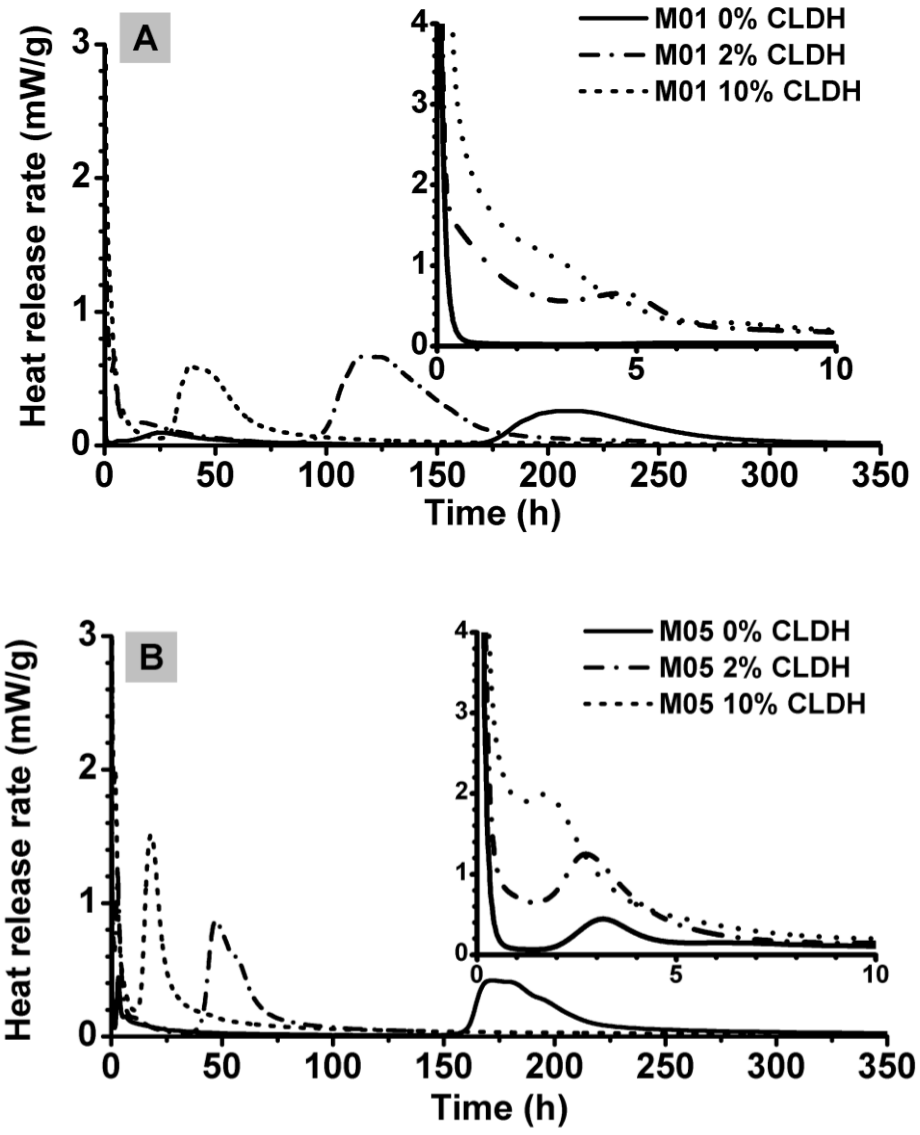

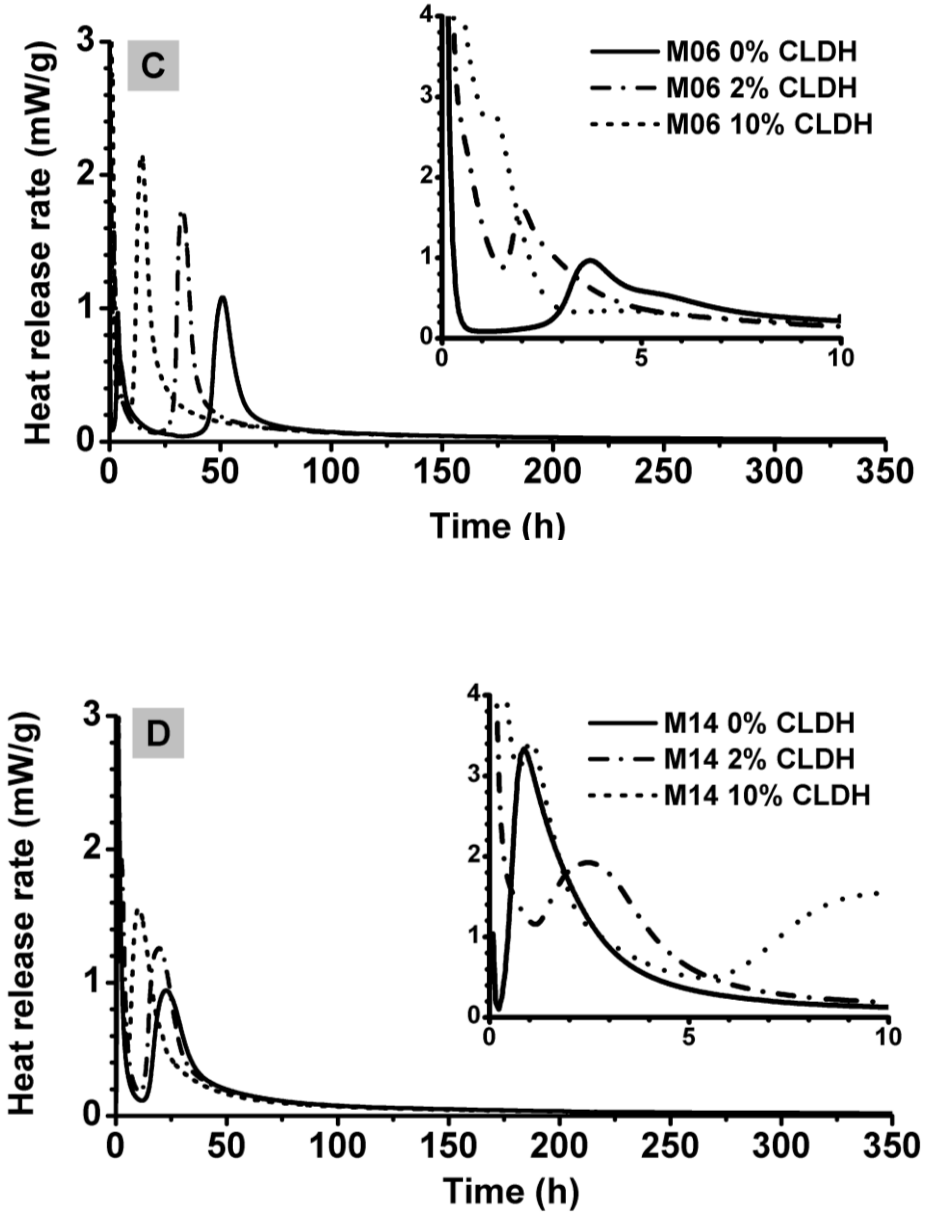

Figure 4-1 Isothermal calorimetry data for Na_2CO_3-activated slag cements, produced with slags (A) M01, (B) M05, (C) M06 and (D) M14, as a function of the percentage of CLDH addition. All curves are normalised by the total mass of the paste tested.

Table 4-3 Summary of the heat release curves shown in Figure 4-1

Slag	CLDH addition (wt. %)	Pre-induction period (h)		[+]Duration of induction period (h)	Acceleration-deceleration period		[++]Total heat release (J/g)
		Peak time (h)	[+]Duration (h)		[+]Onset time (h)	Peak time (h)	
M01	0	25.7	74.9	90.1	165.0	210	87.8
	2	4.6	56.3	32.0	88.3	120	172
	10	2.7	20.7	6.7	27.4	43.2	128
M05	0	3.2	62.2	79.6	151.4	170	98.2
	2	2.7	15.3	15.3	36.5	46.7	104
	10	1.7	2.1	2.1	11.4	17.6	142
M06	0	3.7	30.4	30.4	40.3	50.6	102
	2	2.0	14.7	14.7	24.3	33.1	119
	10	1.3	0.7	0.7	9.1	14.0	158
M14	0	0.87	2.48	2.48	13.0	22.3	135
	2	2.5	1.21	1.21	11.5	19.0	142
	10	1.1	0.42	0.42	5.56	10.8	189

[+] The duration of the induction period is determined using the first derivative of its heat flow rate. The start of the induction period (and correspondingly the end of the pre-induction period) is defined as when its first derivative increased from a negative value to greater than -5×10^{-5} mW/g·h. The end of the induction period is identified when its first derivative started to increase above 5×10^{-5} mW/g·h. The first derivative during the induction period is within the range $0\pm5\times10^{-5}$ mW/g·h.

[++] The total heat release here is the integrated reaction heat, from the start of the reaction to the long-term period where the heat flow is lower than 30 μW/g. The results were normalised by the mass of the paste.

The activated slag M05 paste without CLDH addition (Figure 4-1B) also presented a prolonged induction period; however, a secondary peak associated with precipitation of reaction products was identified in the pre-induction period after 3.2 h of reaction (Table 4-3). The acceleration period started after 151 h, and showed a much steeper acceleration than the slag M01, indicating that the growth of reaction products was much more rapid in the higher-MgO system once nucleation did take place. The deceleration period then evolved slowly, but showed two distinct humps that are likely to be indicating the precipitation of different types of reaction products at different times. With 2 wt.% CLDH addition, the induction period was shortened to 15.3 h, and the acceleration period started after 36.5 hours of activation, with the double-peak structure of the acceleration-deceleration period again notable. When the CLDH

addition was increased to 10 wt.%, all the stages of the reaction occurred within the first 24 hours after mixing. A negligible induction period was observed for this cement, and a single narrow peak with a rapid acceleration up to a maximum heat evolution at 18 h was identified. In the pre-induction period (insert Figure 4-1B), it is notable that the intensity of the secondary peak increased with the addition of higher contents of CLDH, and in the case of 10 wt.% of CLDH addition, the peak shifted towards shorter times of reaction.

For Na_2CO_3 activated M06 (Figure 4-1C) and M14 (Figure 4-1D) slags, the CLDH addition has a similar effect in modifying the kinetics of reaction of these cements, to the observations for M01 and M05 based pastes. The M06 and M14 activated slags without CLDH addition react significantly faster than samples prepared with slags M01 and M05 (Figure 4-1A, 1B), indicating that the slag chemistry has a significant effect on the kinetics of reaction of Na_2CO_3-activated cements. Each of the stages of the reaction processes becomes significantly more rapid with CLDH addition, and the peak heat evolution rates of both the pre-induction and the acceleration/deceleration peaks are also consistently increased. In contrast to the observations for Na_2CO_3-activated M01 and M05 slags, a much shorter dormant period is observed when using M06 and M14, with and without CLDH addition, and consequently the main peak is identified within the first 24 h of reaction for each of these slags. This suggests that the precipitation of the different reaction products forming when using high MgO content slags (>6 wt.%) is not significantly delayed when using a Na_2CO_3 solution as sole alkali activator, unlike the situation for lower-MgO slags.

4.3.2. XRD

Effects of slag chemistry and addition of CLDH on the phase assemblage of Na_2CO_3-activated cements

The X-ray diffraction patterns of the sodium activated slag cements after 28 days of reaction (Figure 4-2) show the formation of three types of crystalline phases in all the cements assessed: carbonates, LDHs, and tobermorite-like C-(A)-S-H gels, whose composition and features are strongly dependent on the slag chemistry and CLDH content.

Gaylussite ($Na_2Ca(CO_3)_2 \cdot 5H_2O$, PDF #00-021-0343) and calcite (PDF #01-086-0174) were the major carbonates identified in all samples, independent of the slag composition and the content of CLDH. The intensities of the gaylussite reflections are similar in all the 0 wt.% CLDH pastes after 28 days of curing. In samples modified by 2 wt.% CLDH, the intensities of the peaks assigned to gaylussite decrease compared to the 0 wt.% formulations, and this phase could barely be identified in the 10 wt.% CLDH modified samples. Additional metastable polymorphs of calcium carbonate including vaterite ($CaCO_3$, PDF #01-072-0506) and aragonite ($CaCO_3$, PDF #00-041-1475) were also observed in most slag pastes. The reflections assigned to calcite, vaterite and aragonite remained almost unchanged in the CLDH modified samples compared to the respective 0 wt.% samples. It is notable that higher intensity reflections of gaylussite are observed (Figure 4-2.D) in the specimens produced with the slag (M14) with higher MgO content and the higher CLDH addition. This might indicate the limited phase modification capacity of CLDH in MgO-rich slag cement.

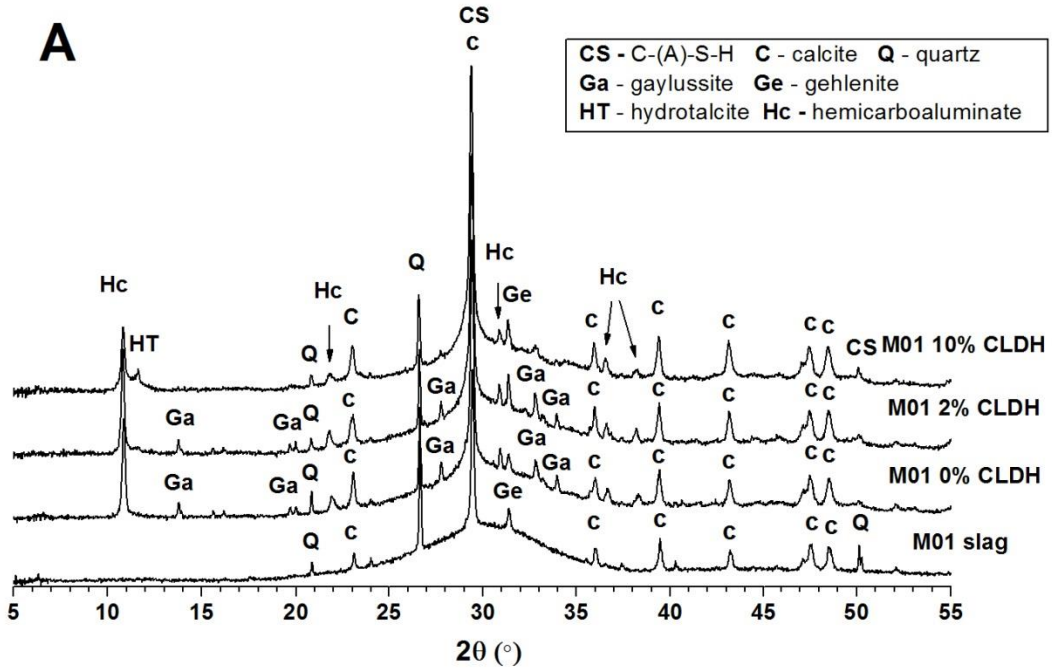
A
CS - C-(A)-S-H C - calcite Q - quartz
Ga - gaylussite Ge - gehlenite
HT - hydrotalcite Hc - hemicarboaluminate
M01 10% CLDH
M01 2% CLDH
M01 0% CLDH
M01 slag
2θ (°)

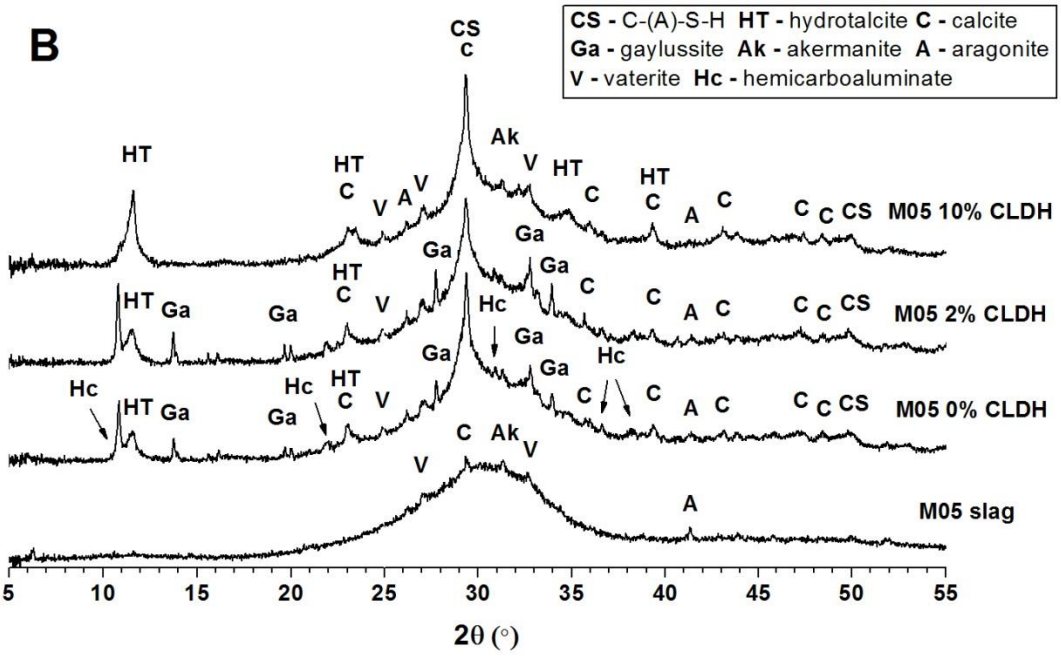
B
CS - C-(A)-S-H HT - hydrotalcite C - calcite
Ga - gaylussite Ak - akermanite A - aragonite
V - vaterite Hc - hemicarboaluminate
M05 10% CLDH
M05 2% CLDH
M05 0% CLDH
M05 slag
2θ (°)

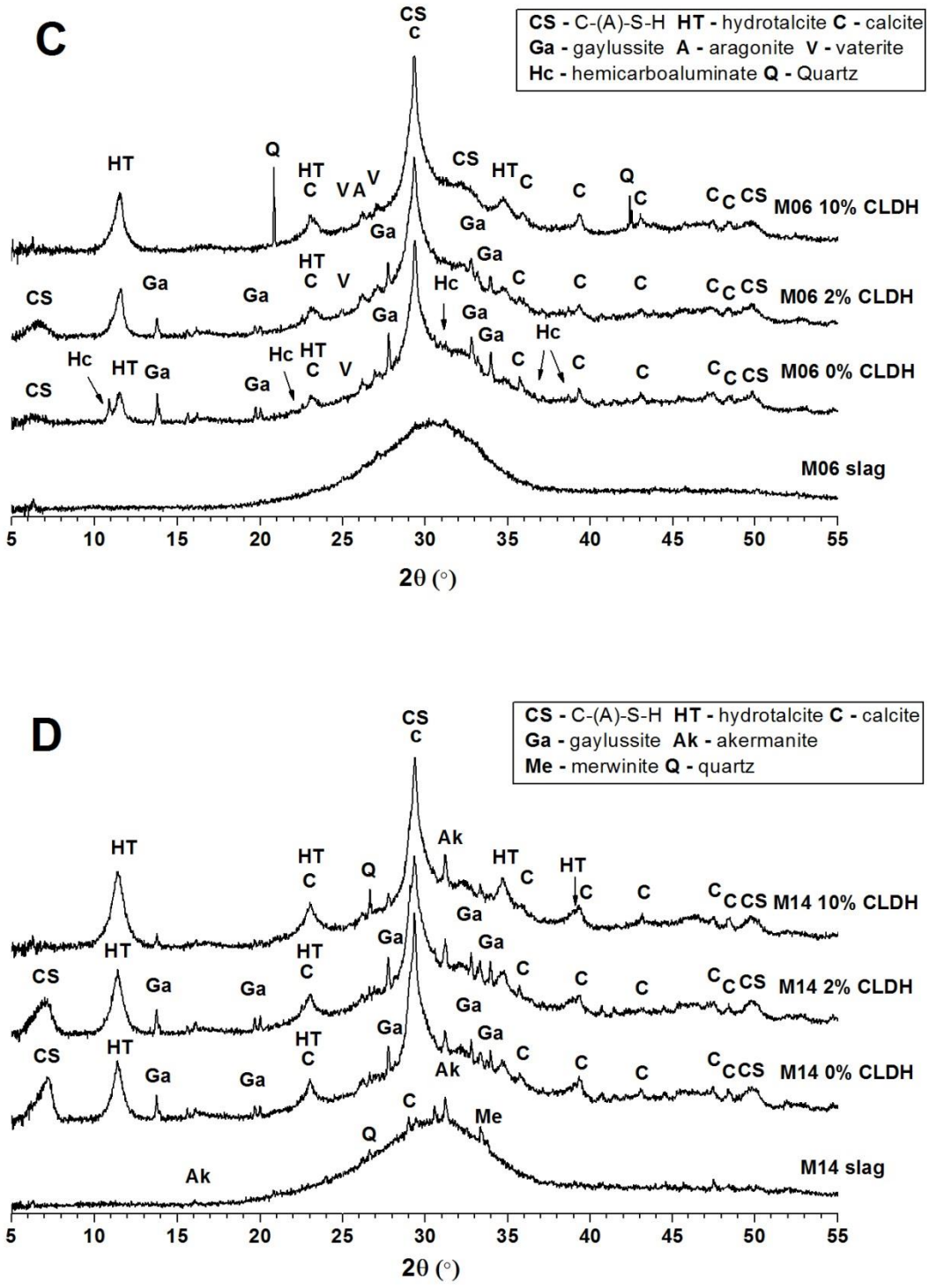

Figure 4-2 X-ray diffraction patterns of 28 day-cured sodium carbonate activated slag cements produced with slags: (A) M01, (B) M05, (C) M06, and (D) M14, with 0, 2 and 10 wt.% of CLDH added as marked. Data for each anhydrous slag are also shown in the plots.

Two types of LDH phases were identified in the Na_2CO_3 activated 0 wt.% samples: calcium hemicarboaluminate hydrate ($C_4A\underline{C}_{0.5}H_{12}$, PDF #00-036-0129), which is a member of the AFm (hydrocalumite-like) group and known in cement chemistry as 'hemicarbonate', and a hydrotalcite-like phase ($Mg_4Al_2(OH)_{12}CO_3{\cdot}3H_2O$, PDF #00-014-0525). The relative concentrations of these two types of LDH phase in each sample are directly related to the chemical composition of the slags, and the dose of CLDH added. A higher content of MgO in the slag precursor favoured the formation of Mg-Al type LDH phases to consume aluminium. However, with low MgO content but high Al_2O_3 content, there is not sufficient MgO to consume the excess aluminium, and therefore the hemicarbonate phase may form (Matschei et al., 2007a, Whittaker et al., 2014). Thus, in the paste with the lowest MgO content (Figure 4-2 (A), M01_0% CLDH), this was the only LDH phase identified. In the slags with moderate MgO content, M05 and M06, both types of LDH phases were present after 28 days of curing. When the anhydrous slag precursor contains a high MgO content, as in the case of M14, only the Mg-Al type of LDH (the hydrotalcite-like phase) was identified. The same trends are observed in the samples modified by 2 wt.% and 10 wt.% of CLDH, along with an increase in the content of the hydrotalcite-like phase in all the CLDH modified samples attributed to the recrystallisation of the CLDH (Mascolo and Mascolo, 2015, Morimoto et al., 2012, Rocha et al., 1999). However, the hydrotalcite-like phase derived from the recrystallisation of the CLDH cannot be distinguished by XRD from the additional hydrotalcite-like phase forming through activation of the slags.

It is worth noting that hemicarbonate has not been widely reported as a reaction product in sodium silicate-activated slag systems, but has been observed in Portland cement/slag blended systems when the Al_2O_3 content in the slag is high and calcite is present in the system, as such conditions favour the formation of AFm type phases, and the presence of carbonate stabilises the hemicarbonate member of this family (Damidot et al., 1994, Ipavec et al., 2011, Matschei et al., 2007a, Matschei et al., 2007b, Whittaker et al., 2014). A mixture of AFm and hydrotalcite-like phases has also been identified in NaOH-activated slag pastes cured for up to 15 months (Escalante-García et al., 2003, Wang and Scrivener, 1995). The

formation of mixed LDH phases in sodium carbonate-activated slag might have followed the same mechanism, as the reaction mechanism becomes comparable to NaOH-activation of the slag once the CO_3^{2-} is exhausted (Bernal et al., 2014b).

The C-(A)-S-H phases identified in all the samples are close to an aluminium substituted tobermorite-like phase ($Ca_5Si_5Al(OH)O_{17}\cdot 5H_2O$, PDF #00-019-0052; tobermorite-14Å, PDF #00-029-0331) (Myers et al., 2015a). The C-(A)-S-H phases formed in each of the slag systems cannot be distinguished solely via XRD, due to the poorly crystalline nature of this reaction product. However, the presence of a broad hump at around 6.4° 2θ in the sample M06_2% CLDH (Figure 4-2C), and the disappearance of the high intensity hump at 7.1° 2θ in the sample M14_10% CLDH (Figure 4-2D), suggest changes in either the composition or the structure of the C-(A)-S-H phase. This will be further assessed in the following sections via scanning electron microscopy and solid-state nuclear magnetic resonance spectroscopy.

Phase evolution over the time of curing

All of the main crystalline phases identified in the Na_2CO_3-activated slag cement, being gaylussite, LDH phases and C-(A)-S-H gel, present major diffraction peaks between 5° and 15° 2θ. For a clear and direct comparison across all the samples over the time of curing, XRD patterns in this angular range are presented in Figure 4-3 as a function of sample age.

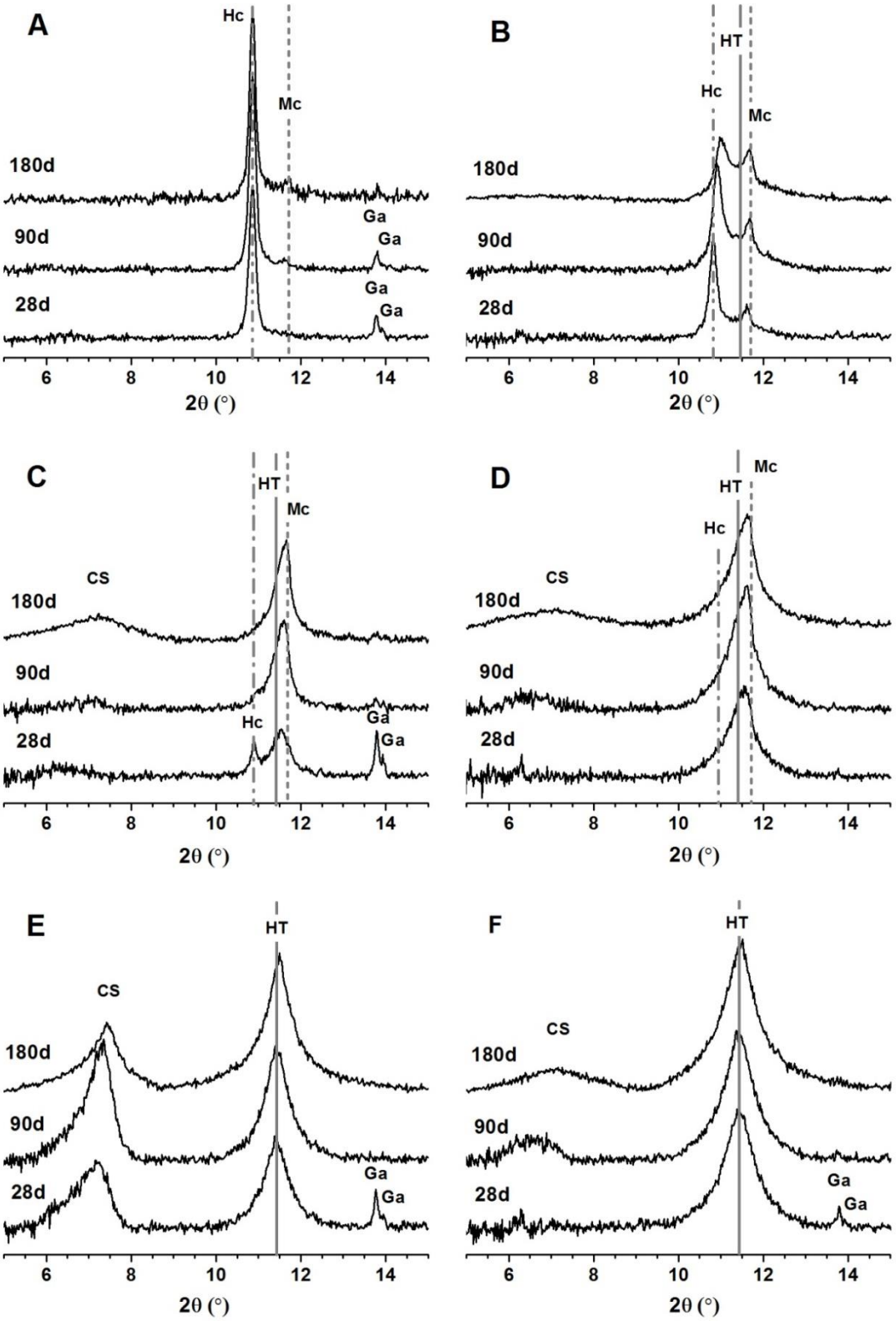

Figure 4-3 X-ray diffraction patterns of Na_2CO_3 activated slag M01 with (A) 0 wt.% and (B) 10 wt.% CLDH; slag M06 with (C) 0 wt.% and (D) 10 wt.% CLDH; and slag M14 with (E) 0 wt.% and (F) 10 wt.% CLDH, as a function of the time of curing. Phases marked are: HT – hydrotalcite-like, Hc – hemicarbonate, Mc – monocarbonate, Ga – gaylussite, CS – C-(A)-S-H.

It can be seen (Figure 4-3) that gaylussite disappeared from all samples over the time of curing, and it is present only in very small quantities in the M1, M05 and M06 samples containing CLDH. Gaylussite is a transient phase in sodium carbonate activated slag cement, and its consumption is associated with the formation of more stable carbonates. This will be discussed in detail in section 4.4.1. The hemicarbonate phase identified in the activated M01 slag with (Figure 4-3B) and without (Figure 4-3A) CLDH addition decreased over time, and the calcium monocarboaluminate ($C_4A\underline{c}H_{11}$, PDF#00-036-0377, 'monocarbonate') phase starts to form (Fischer and Kuzel, 1982, Lothenbach et al., 2008, Matschei et al., 2007b, Whittaker et al., 2014), predicted to be the stable AFm product in thermodynamic modelling of slag activation by Na_2CO_3 (Myers et al., 2015b). In Figure 4-3B, the basal reflection peak of hemicarbonate shifted towards higher angle, and became wider over time of curing, as a result of partial replacement of OH^- by CO_3^{2-} in hemicarbonate and the consequent formation of a poorly crystalline AFm-(OH^-,CO_3^{2-}) solid solution.

The basal reflection peak of monocarbonate is around 11.7° 2θ, which in some cases might overlap with that of the hydrotalcite-like phase, 11.2-11.6° 2θ (marked at 11.4° in Figure 4-3). However, in the M01-0% CLDH system (Figure 4-3A), the formation of monocarbonate is clearly identifiable, as no hydrotalcite-like phase is forming. In samples with moderate MgO content (Figure 4-3C, Figure 4-3E), monocarbonate could not be distinguished via distinct reflection peaks, but the broad peak centred at around 11.4° 2θ shows an asymmetric increase in intensity over time. This increasing asymmetry suggests the formation of a component peak at around 11.7° 2θ, most likely due to monocarbonate. Samples prepared using the high MgO slag M14 do not show reflections indicative of the formation of AFm phases, and thus the peak at around 11.4° 2θ for this formulation, whose intensity increases over the time of curing, is solely assigned to a hydrotalcite-like phase.

Similar trends are identified in the CLDH modified samples, where the high intensity peak of hydrotalcite overlaps with those assigned to hemicarbonate and monocarbonate,

obstructing their clear identification. Negligible structural changes are identified in the reaction products of the slag with intermediate content of MgO (Figure 4-3D) with the addition of CLDH. In the activated M14 samples with CLDH addition (Figure 4-3F), changes in the LDH phase were almost identical to those observed without CLDH addition (Figure 4-3E). However, the addition of CLDH seems to modify the structure of the C-A-S-H forming in these systems. This will be further evaluated in the following sections.

In sodium carbonate activated slag systems, hemicarbonate is formed at earlier age (i.e. during the first 28 days) when using slags with low to medium MgO content (M01, M05 and M06). The formation of hemicarbonate is reduced when a higher content of MgO is present, where a higher content of hydrotalcite-like phases is instead formed. In cements based on the high-MgO slag (M14), only the hydrotalcite-like phase was identified. In general, the addition of CLDH increases the formation of hydrotalcite-like phases, and seems also to accelerate the transformation from hemicarbonate to monocarbonate.

In the sodium carbonate activated slag system, the free carbonate ion content in the aqueous phase is reduced as the reaction evolves. Although the formation of monocarbonate from hemicarbonate under such circumstances seems unlikely as the conversion requires additional carbonate, the experimental results suggest that the previously carbonated hydrotalcite-like phase might be able to supply this carbonate. This is in line with recent thermodynamic modelling results for sodium carbonate activated slag, which revealed that monocarbonate is a thermodynamically stable phase in this system, together with a non-carbonated hydrotalcite-like phase (Myers et al., 2015b). The transformation between these two phases could also be associated with the availability of additional carbonate due to the reaction of precipitated $CaCO_3$, which drives the equilibrium towards the monocarbonate phase (Glasser et al., 1999, Lothenbach et al., 2008, Whittaker et al., 2014).

As seen in Figure 4-3, the positions of the basal reflection peaks of the hydrotalcite-like phase vary slightly in different samples with different ages. The basal reflection peak reflects the composition of the mixed metal oxide/hydroxide sheets, the type of interlayer species and the amount of chemically bound water (Duan and Evans, 2006, Gastuche et al., 1967). The shifts observed here could be caused either by formation of HT-(OH^-, CO_3^{2-}) solid solutions, or changes in the Mg/Al ratio, as more Al incorporation into a hydrotalcite-like phase leads to a decrease in the angle at which its basal reflection peak is observed (Gastuche et al., 1967).

4.3.3. SEM-EDX

Figure 4-4 shows backscattered electron (BSE) images of sodium carbonate activated slag pastes without and with 10 wt.% CLDH, after 180 days of curing. The light grey particles in the micrographs correspond to the unreacted slag particles remaining in the samples, while the grey regions between the remnant slag particles correspond to the main binding phase, consisting mainly of C-(A)-S-H gel and additional reaction product phases such as LDHs and carbonates, as identified by XRD (Figures 4-2 and 4-3). Regions darker in greyscale intensity than the general matrix, which were more numerous and clearly identifiable in moderate to high MgO activated slags (M06 (not shown) and M14) than in samples produced with slags with low MgO content (M01) samples, correspond to fully reacted slag grains and inner reaction product rims rich in Mg (with the hydrotalcite as a dominant phase) (Famy et al., 2002, San Nicolas et al., 2014). In Figure 4-4A, irregular dark grey areas are identified between the slag grains. These are most likely to be sodium-calcium carbonate phases (e.g. gaylussite), as identified from XRD (Figure 4-2). Similar features with a chemical composition comparable to that double salt have been observed in sodium carbonate/silicate activated slag cements (Bernal et al., 2015a), and the dark greyscale values are consistent with the low mean elemental number of hydrous carbonates.

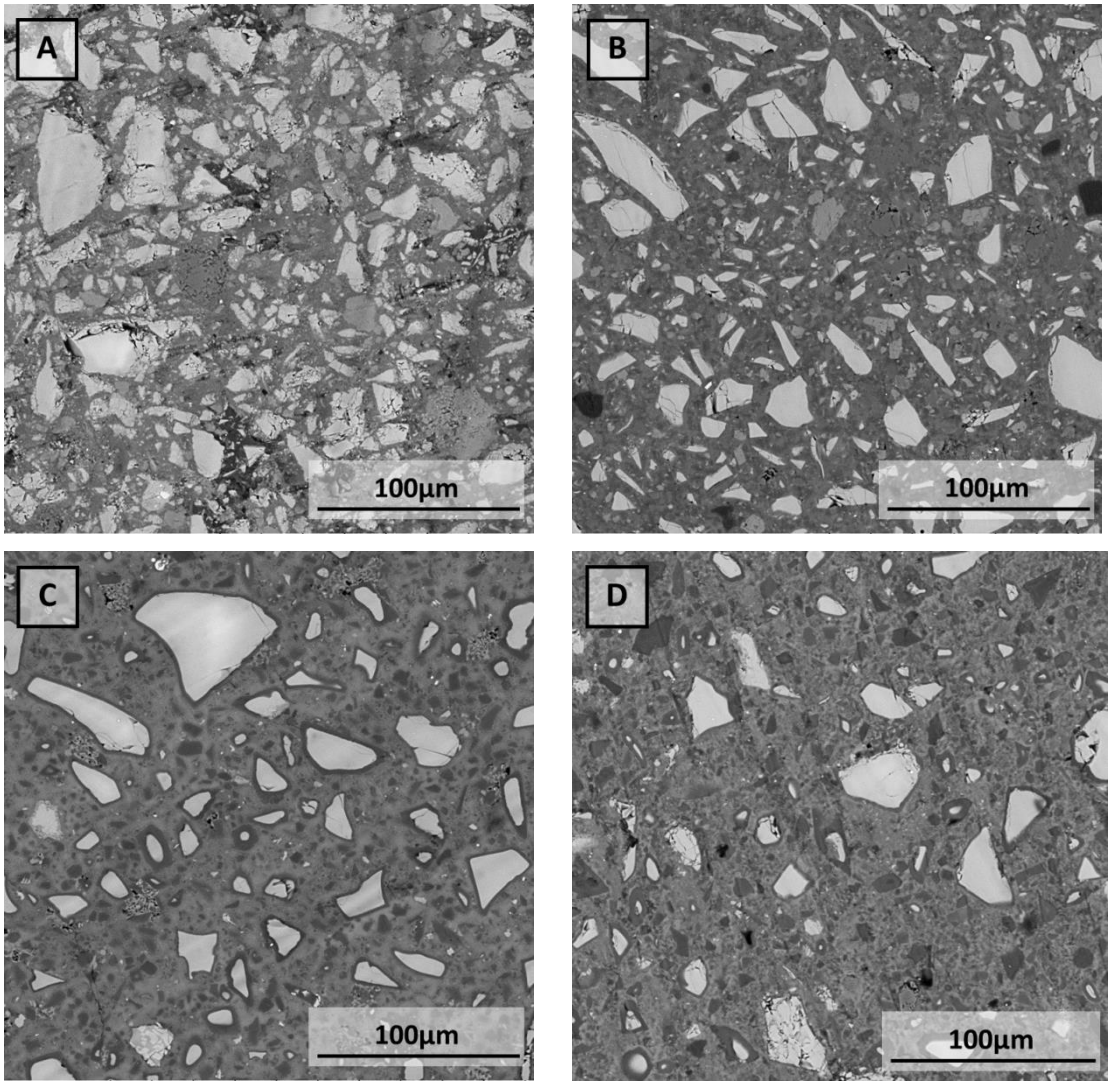

Figure 4-4 BSE images of pastes cured for 180 days: slag M01 with (A) 0 wt.% and (B) 10 wt.% CLDH; and slag M14 with (C) 0 wt.% and (D) 10 wt.% CLDH

Figure 4-5 shows atomic ratio correlation plots generated from EDX spot analyses of the samples prepared using different slags with 0 wt.% and 10 wt.% of CLDH addition. More than 60 data points were taken from each sample formulation following sampling methods as specified in Chapter 3 (section 3.3.4.). Locations near (<2 µm) unreacted slag grains and crystalline phase from raw materials, such as calcium and quartz in M01, were avoided for sampling (except for inner product from M14, where a minimum distance to unreacted slag grain of 2 µm was not achievable). The spots taken from outer reaction products are referred to as the general matrix in Table 4-4, excluding large recrystallised hydrotalcite gel clusters that were not well dispersed during the mixing of the paste. Inner product EDX spots were

only taken from slag M14, where clear inner rims were identified. The data presented here show the atomic ratios of the reaction product between the slag grains, which consists of C-(A)-S-H gel and intermixed LDHs. The dashed lines in Figure 4-5 showing the ratios Mg/Al=2 and Ca/Al=2 are given to clarify the existence of hydrotalcite-like phases and AFm phases (Matschei et al., 2007a). Data points with Al/Si ratios below 0.8 (shown) were chosen for investigation of the chemical composition of the hydrotalcite-like phase and C-(A)-S-H gel, to rule out any interference from well-crystallised AFm phases.

Without addition of CLDH, the MgO and Al_2O_3 content of the slag will control the chemistry of LDH phases formed as reaction products. With the highest Al_2O_3 content and very low MgO content, slag M01 formed a significant amount of AFm phases to consume excess Al. In slag M06, which has a slightly lower Al_2O_3 content but a much higher MgO content, the hydrotalcite-like phase was identified as the main LDH with traces of intermixed AFm phases, consistent with the XRD data presented above. This shows that in the presence of MgO, the excess Al present is more likely to form hydrotalcite-like phases than AFm phases, consistent with the fact that no AFm phase was identified in samples prepared using slag M14. However, the absence of AFm phases from samples based on slag M14 could also be related to the fact that it contains the lowest Al_2O_3 content and the highest MgO content. The additional CLDH contributed to the increased formation of hydrotalcite-like phase in samples based on all three slags. It also reduced the crystallinity of the AFm phases formed through reaction of slags M01 and M06, by forming disordered intermixed LDH phases. This corresponds to the XRD results shown in Figure 4-3.

The Al/Si ratio of the C-(A)-S-H gel in each alkali-activated slag sample was calculated using the method of Ben Haha et al. (2011), Table 4-4. These values demonstrate a close relationship between the Al_2O_3 content of the slag and the Al/Si ratio in C-(A)-S-H gel, where a higher bulk Al_2O_3 content results in a higher Al/Si ratio in the C-(A)-S-H gel (0.2 in slag M06 and 0.06 in slag M14, all with 0 wt.% CLDH addition). The Al/Si ratio of slag M01

calculated using the same method was higher than the maximum possible degree of Al substitution in C-(A)-S-H, due to the presence of intimately intermixed AFm and/or N-A-S-H phases (L'Hôpital et al., 2015, Myers et al., 2014). The Al_2O_3 content of the slag controls the degree to which aluminium is able to dissolve and be made available for through-solution reaction processes, and thus defines the Al/Si ratio in the C-(A)-S-H gel (L'Hôpital et al., 2015). This would also explain the observation that in 10 wt.% CLDH modified samples, the Al/Si ratio calculated by this method is slightly higher than that of the samples without CLDH samples. The recrystallisation of CLDH into hydrotalcite-like phases leads to an increase in pH (proven in detail in section 4.4.2), favouring the dissolution of aluminium and thus resulting in a higher Al/Si ratio in the C-(A)-S-H.

The Ca/Si ratio in the C-(A)-S-H gel did not change significantly with changes in slag chemistry, with all data points for all samples falling between ratios of 0.8 and 1.6. Those values are higher than the Ca/Si ratios identified in sodium hydroxide-activated or sodium silicate-activated slag cements where slags with similar chemical compositions were used (Ben Haha et al., 2011, 2012, Bernal et al., 2014c). This may be related to the lower alkalinity of the sodium carbonate activator, which brings a lower capacity to dissolve silicate species from the slag glass (Snellings, 2015). However, no systematic change in Ca/Si ratio was observed in the CLDH modified samples compared to the unmodified cements.

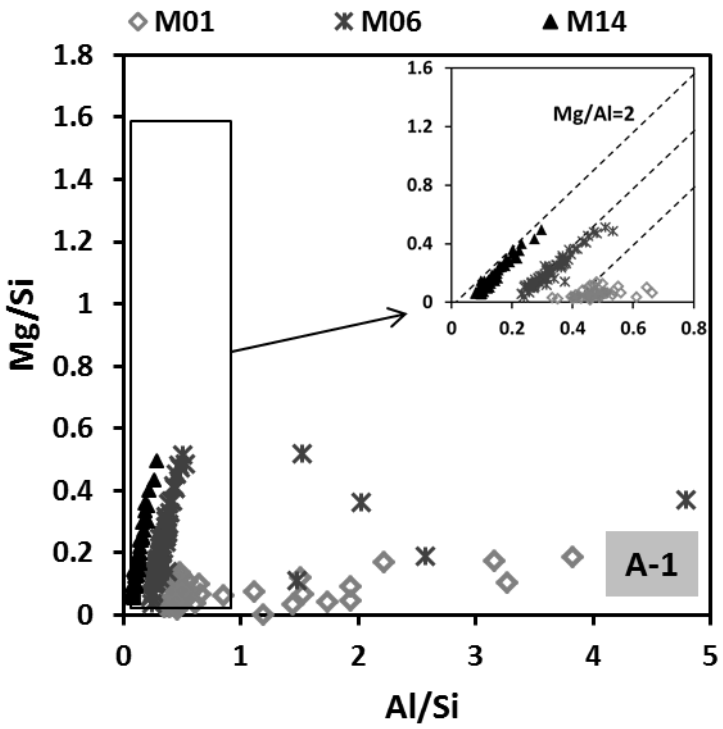
M01
M06
M14
Mg/Si
Al/Si
Mg/Al=2
A-1

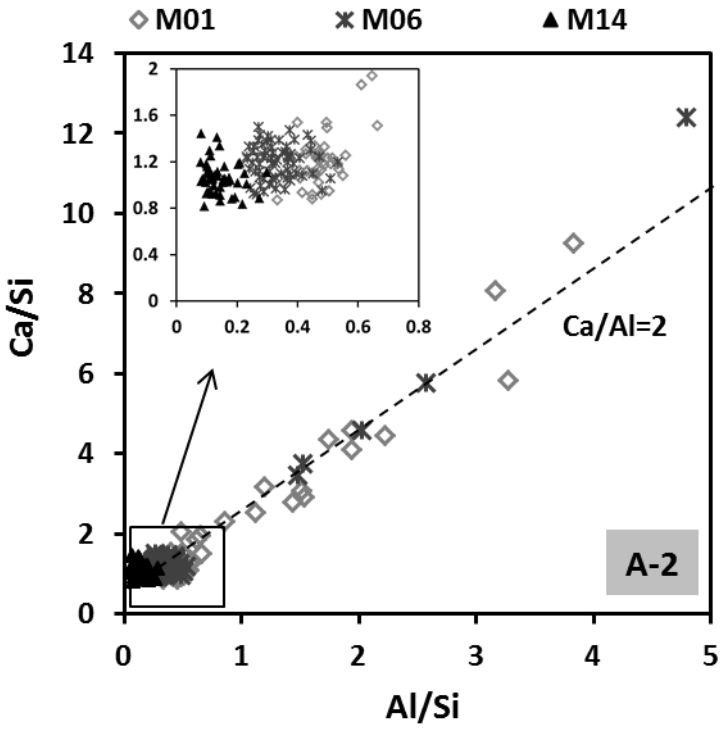
M01
M06
M14
Ca/Si
Al/Si
Ca/Al=2
A-2

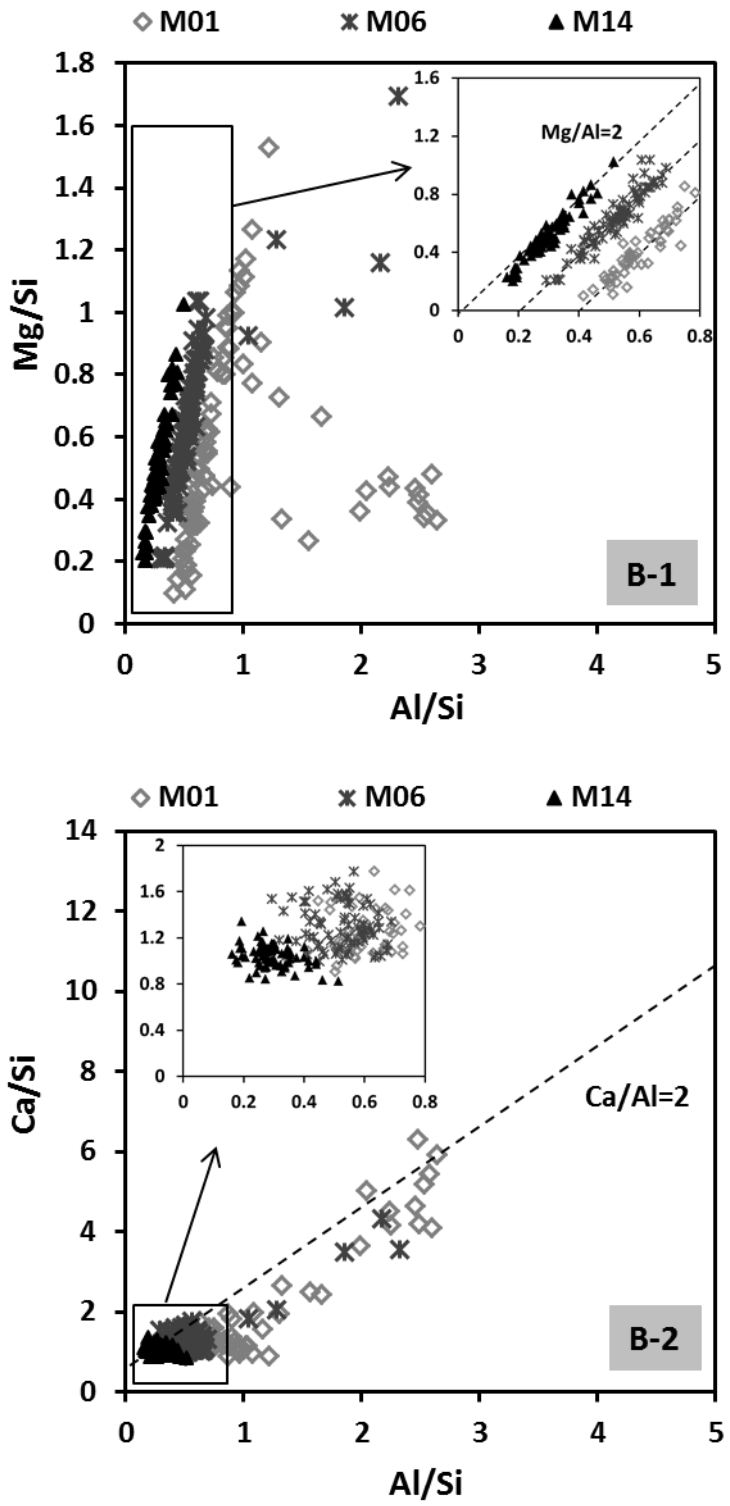

Figure 4-5 Atomic ratios calculated from EDX data for Na_2CO_3 activated samples with 0 wt.% (A-1 and A-2) and 10 wt.% (B-1 and B-2) of CLDH addition, all after 180 days of curing. (A-1) and (B-1) plotted as Mg/Si vs Al/Si and (A-2) and (B-2) plotted as Ca/Si vs Al/Si.

Table 4-4 Average atomic ratios (Ca/Si and Mg/Al) of Na_2CO_3-activated slag pastes cured for 180 days, using data points shown in the inset plots in Figure 4-5 (where Al/Si <0.8), obtained using EDX analyses of 60 spots per sample (uncertainty in each reported value ±0.02).

Slag		0 wt.% CDLH			10 wt.% CDLH		
		Ca/Si	Al/Si	[a]Mg/Al	Ca/Si	Al/Si	[a]Mg/Al
M01	General matrix	1.22	<0.33	[b] -	1.26	<0.33	1.91
M06		1.20	0.20	1.61	1.26	0.21	2.04
M14		1.05	0.06	2.09	1.04	0.06	2.16
M14	Inner rim	0.86	0.02	1.86	0.92	0.01	1.84

a. Mg/Al value is the slope of the line of best fit in a plot of Mg/Si vs Al/Si ratios.

b. The Mg/Al ratio of the sample M01_0wt.% could not be determined due to the low content of MgO in the anhydrous slag.

The chemical compositions of the inner and outer products of samples prepared using slag M14 were analysed separately using EDX (shown also in Table 4-4). The Ca/Si ratio of the inner product is distinctly lower than that of the outer product, suggesting that there might be other Ca containing phases forming in the outer product. This is also likely to be caused by existing of intermixed N-A-S-H gel in the inner product (Myers et al., 2015b, Provis and Bernal, 2014).

To obtain further insight into the chemistry and structure of the C-(A)-S-H gel in sodium carbonate activated slag cement, analysis by solid-state NMR is required, and is presented below.

4.3.4. ^{27}Al and ^{29}Si MAS NMR

The ^{29}Si MAS NMR spectra of the anhydrous slags shown in Figure 4-6 are in good agreement with the literature for a melilite-type glass (Kirkpatrick, 1988, Wang and Scrivener, 2003). For the sodium carbonate activated paste samples, three distinct bands at -79 ppm, -82

ppm and -85 ppm were identified in the main region of the ^{29}Si MAS NMR spectra, which are assigned to a Q^1 site (denoted Q^1(II) for consistency with the literature (Myers et al., 2014)), Q^2(1Al) and Q^2, respectively (Richardson et al., 1993, Schneider et al., 2001, Wang and Scrivener, 2003). The residual signal downfield of the -79 ppm band is assigned to Q^0 and Q^1(I) sites (Myers et al., 2014). The low intensity, but non-zero, component of the signal which lies upfield of -85 ppm is composed of two bands centred at -88 ppm and -92 ppm respectively, and assigned to highly crosslinked Si sites (Engelhardt and Michel, 1987). The bands in these two positions could be assigned to either Q^4(4Al) and Q^4(3Al) sites in N-A-S-H gel, and/or Q^3(1Al) and Q^3 sites in C-(A)-S-H gel, according to the findings reported by Myers *et al.* (2014) for sodium metasilicate activated slag cements.

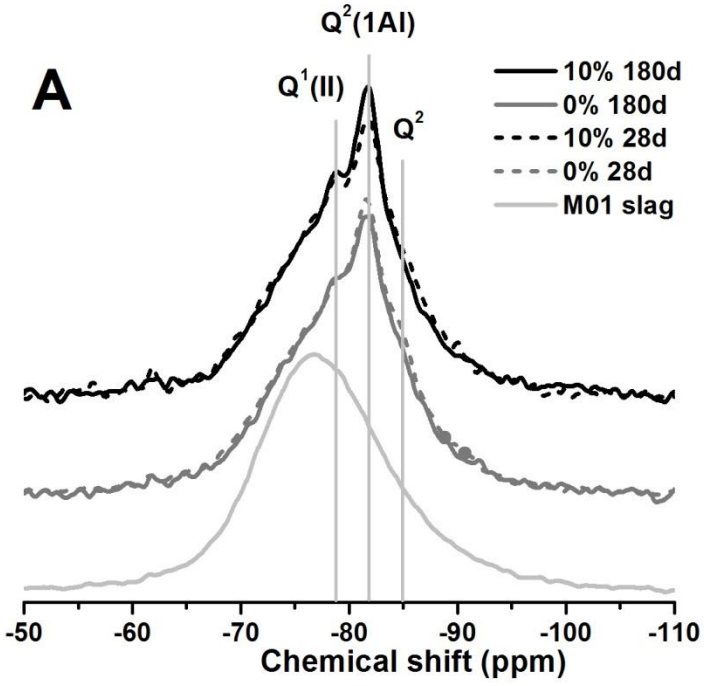

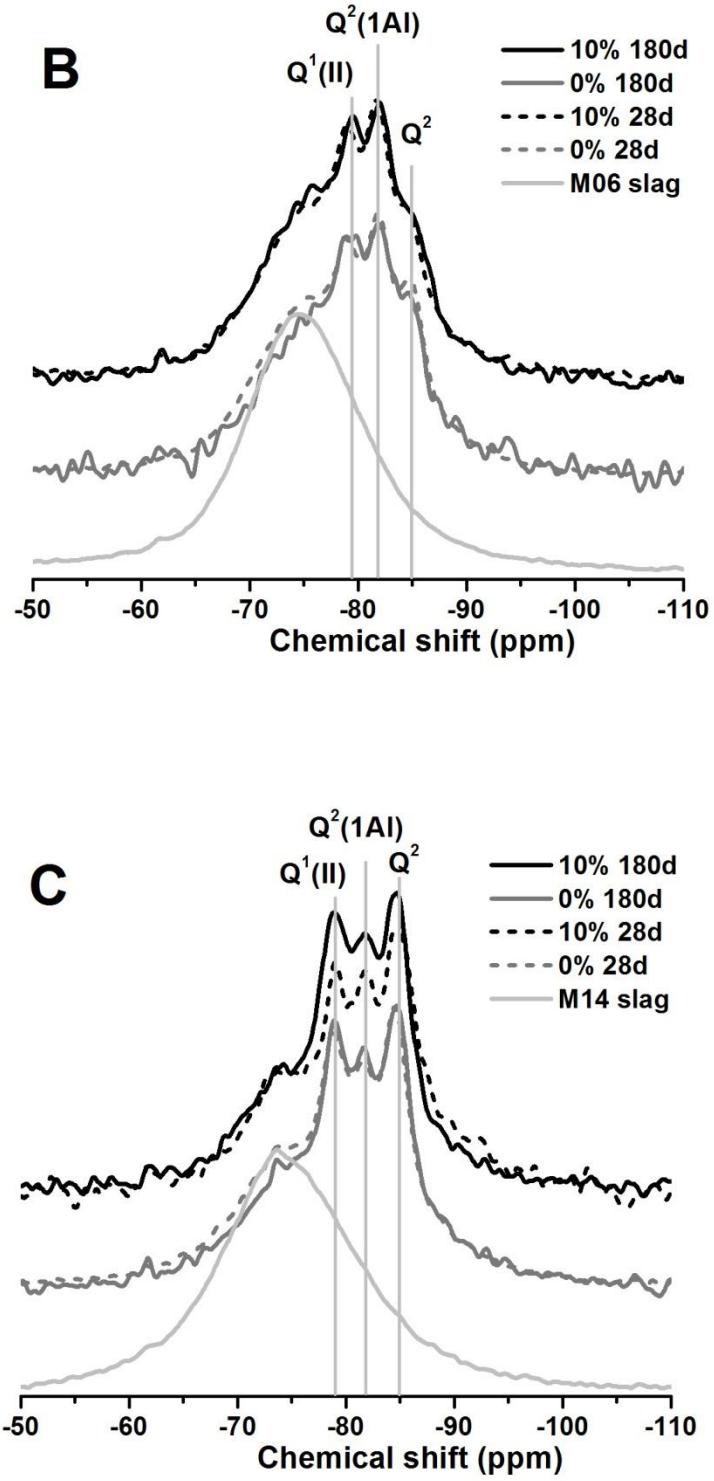

Figure 4-6 ^{29}Si MAS NMR spectra of slag pastes prepared using slags M01, M06 and M14, with 0 wt.% and 10 wt.% CLDH, cured for 28 and 180 days.

Table 4-5 shows the results of deconvolution of the ^{29}Si MAS NMR spectra using Gaussian curve fitting (carried out using Excel spread sheet, as exemplified in Figure 4-7), where the chemical shifts were fixed ($\pm$0.4 ppm) and by changing the peak height and width at half height of each fitted curve, to reach a minimised sum of squared residuals (using Solver add-in, Excel software). The unreacted slag, M01, M06, and M14, are first fitted with Gaussians centred at -72ppm, -85ppm, -77ppm and -64ppm to fit a melilite-type glass (Kirkpatrick, 1988, Wang and Scrivener, 2003). For consistency, the deconvolutions were conducted assuming that the anhydrous slag was dissolving congruently, as in sodium silicate or sodium hydroxide activation (Ben Haha et al., 2012, Bernal et al., 2014c, Myers et al., 2013). Therefore the signals contributed by the unreacted slag in the reacted paste sample were fitted by proportionally scaling down the peak heights fitting the anhydrous slag. This is generally correct when dissolving calcium aluminosilicate glasses in solutions at a pH above 12.5 (Snellings, 2015). The initial pH of the sodium carbonate activator used in this study was 11.7, which is expected to increase once the CO_3^{2-} in the pore solution is exhausted, either by formation of solid carbonate phases or removal by reaction with the CLDH additive. Therefore, incongruent dissolution of the slag might occur in the early stage of reaction, but it is not expected as the activation reaction progresses, as the chemistry becomes more comparable to that of NaOH-activation of slag as discussed above. Nonetheless, this must be considered as a potential source of error.

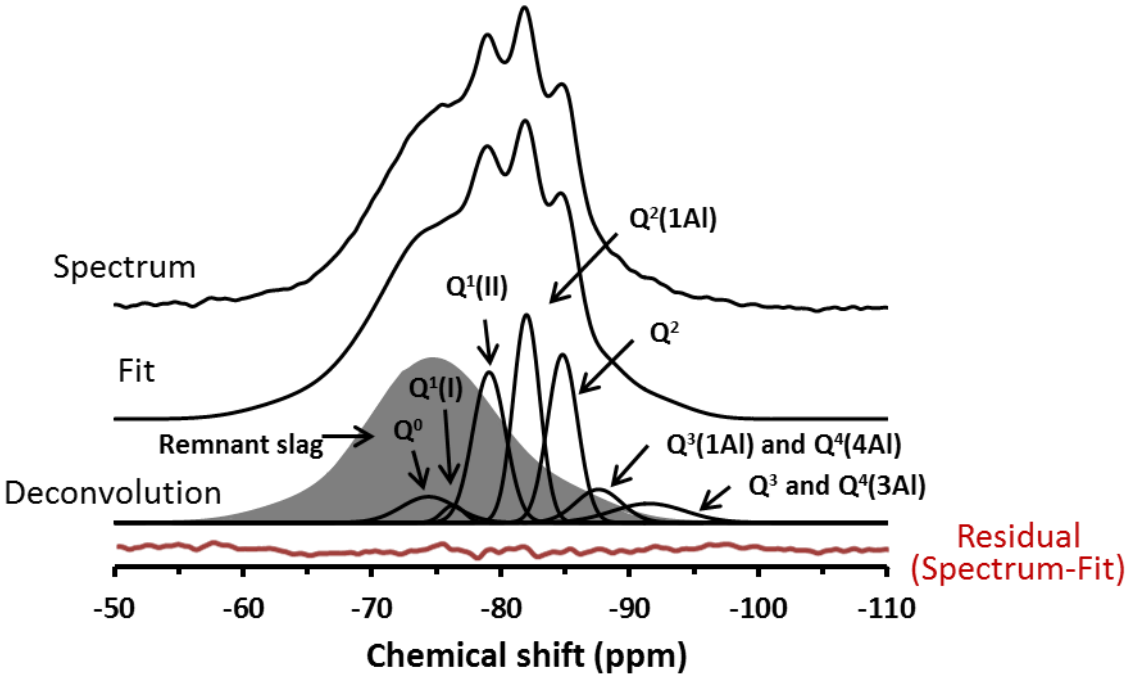

Figure 4-7 Deconvoluted ^{29}Si MAS NMR spectrum of slag M06_0% CLDH cured for 28 days. The dark grey band represents the contribution of the remnant slag, which is directly scaled from the spectrum collected for the unreacted slag using the assumption of congruent dissolution.

Table 4-5 Deconvolution results for ^{29}Si MAS NMR spectra of the sodium carbonate activated slag pastes. Estimated uncertainty in absolute site percentages is ± 2%.

			Reaction products						
	Samples	**Total unreacted slag (%)***	**Q^0 -74 ppm**	**Q^1(I) -76 ppm**	**Q^1(II) -79 ppm**	**Q^2(1Al) -82 ppm**	**Q^2 -85 ppm**	**Q^3(1Al) /Q^4(4Al) -88 ppm**	**Q^3/Q^4(3Al) -92 ppm**
M01	0% 28 d	64	0	2	7	12	10	2	2
	0% 180 d	64	0	3	5	14	9	3	2
	10% 28 d	64	0	3	5	14	7	4	3
	10% 180 d	62	0	3	6	16	7	3	3
M06	0% 28 d	54	3	1	11	13	12	3	3
	0% 180 d	50	3	2	15	13	11	4	3
	10% 28 d	49	5	1	14	14	10	3	3
	10% 180 d	48	6	2	14	12	12	3	3
M14	0% 28 d	41	4	2	14	12	17	8	4
	0% 180 d	37	3	3	14	13	18	9	4
	10% 28 d	32	5	3	12	14	16	12	6
	10% 180 d	30	6	1	20	15	17	7	3

*The actual total unreacted slag (%) might be higher than the calculated value shown here if the dissolution of the glassy slag is incongruent, but this cannot be accurately determined in the absence of a reliable method for the selective dissolution of reaction products in these alkali-activated binder systems.

From Figure 4-8, it is evident that a higher extent of slag reaction (as observed by the lower residual slag fraction and much higher C-A-S-H reaction product content) has been reached in mixes based on slags with higher MgO content and lower Al_2O_3 content. Both MgO content and Al_2O_3 content play important roles in defining the intrinsic reactivity of the slag glass, and this is also influenced by the formation of LDH phases which remove the dissolved Mg and Al from solution and provide a further driving force for glass dissolution. This is supported by the fact that the addition of 10 wt.% CLDH is seen to increase the total extent of slag reaction up to 180 days of curing, compared with samples with 0 wt.% CLDH based on the same slags. This shows that the influence of the CLDH is not simply a kinetic effect which accelerates the reaction at early age (as observed by calorimetry); the fact that the CLDH addition induces a higher extent of reaction even up to 180 days indicates that its seeding effect which enhances nucleation and growth of hydrotalcite-group phases is additionally important in defining binder chemistry in the long term.

However, comparing the line shapes of the ^{29}Si MAS NMR spectra of slag pastes prepared using different slags with and without CLDH addition, it is clear that the structure and composition of C-(A)-S-H gel is dominated by effects related to the slag chemistry over the effects of CLDH addition. The intensities of the Q^1(II) and Q^2 sites were higher in pastes prepared using the slag with the highest MgO content (M14), while the intensities of the Q^2(1Al) sites decreased. The increased intensity of Q^1(II) suggests an increase in the content of chain-end sites charge balanced by strongly positively charged cations such as Ca^{2+} (Myers et al., 2014), while the increased intensity of Q^2 sites suggests a higher mean chain length. The decrease in the intensities of Q^2(1Al) sites, associated with reduced Al uptake by the C-(A)-S-H gel, is due to the lower Al_2O_3 contents in slags M06 and M14 compared with slag M01, and also the formation of a higher content of LDH phases which consume Al, corresponding to the results of EDX analysis.

In Figure 4-8, three distinct Al environments are observable in each of the cement samples by ^{27}Al MAS NMR spectroscopy. The spectrum of the unreacted slag is observed as a broad hump centred at around 59 ppm representing the distribution of Al sites in the unreacted slag; a contribution from the remnant slag particles is also observed underlying the spectra of the reacted pastes. In the spectra of the pastes, the Al[VI] resonances at chemical shift values below 20 ppm are assigned to the Al sites in the two types of LDH structures (Mg-Al and AFm), and bands at around 60-80 ppm correspond to Al[IV] and are assigned to the tetrahedral Al environments in C-(A)-S-H gel (Engelhardt and Michel, 1987, Jones et al., 2003, Myers et al., 2014, Wang and Scrivener, 2003), and when Al[IV] substituted a Q^2 silica site, it is normally noted as q^2, and likewise Al[IV] in Q^3 silica site as q^3.

Significant reductions in the intensities of the broad slag peak centred around 59 ppm, along with an increase in the Al[IV] resonance at 64-80 ppm, take place from 28 to 180 days of curing, which is associated with an increased degree of reaction as the slag continues to be consumed and hydration products form. Unmodified slag pastes with different chemical compositions showed different line shapes between 64-80 ppm, which reflect different Al coordination environments in the C-(A)-S-H gel, the q^2 bridging sites within the higher chemical shift part of this region and the q^3 crosslinking sites at lower chemical shift. Compared with the unmodified samples, the further shift from 59 ppm towards higher chemical shift in 10 wt.% CLDH modified samples represent an increased degree of reaction, corresponding to the analysis presented above.

The peaks centred at 9 ppm in Figure 4-8 are attributed to overlapping contributions from the Ca-Al LDH type phases and the hydrotalcite-like phase (Jones et al., 2003, Rocha et al., 1999), and increased slightly in intensity from 28 to 180 days. Comparing binders produced with different slag sources, the relative intensity of Al[VI] sites compared to Al[IV] sites increased as the MgO content of the slag increased, consistent with the increased formation of LDH phases in the presence of more Mg. Since the slags tested here with higher MgO

content also had lower Al_2O_3 content, the total amount of Al incorporated into the C-(A)-S-H gel derived from high MgO content slag is much lower in low-MgO content slag pastes. This corresponds to the differences between the Al/Si ratios calculated in SEM-EDX analysis (Table 4-4), and the ^{29}Si MAS NMR analysis (Table 4-5).

Addition of 10 wt.% CLDH led to an increased intensity of the peak assigned to the hydrotalcite-like phase, as a consequence of the recrystallisation of the CLDH to form crystalline Mg-Al LDH. However, as the CLDH addition increased the total aluminium content in the paste, the ^{27}Al MAS NMR spectra do not display a clear trend in the total Al content in the C-(A)-S-H gel before and after CLDH modification.

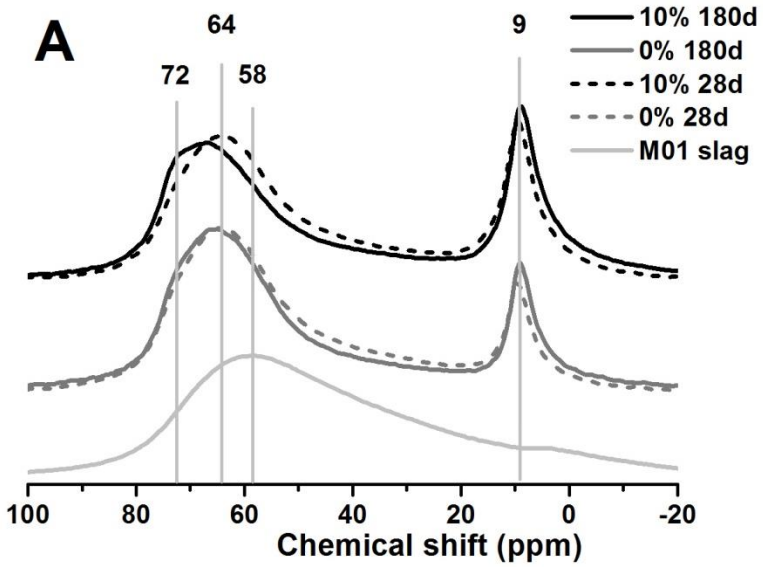

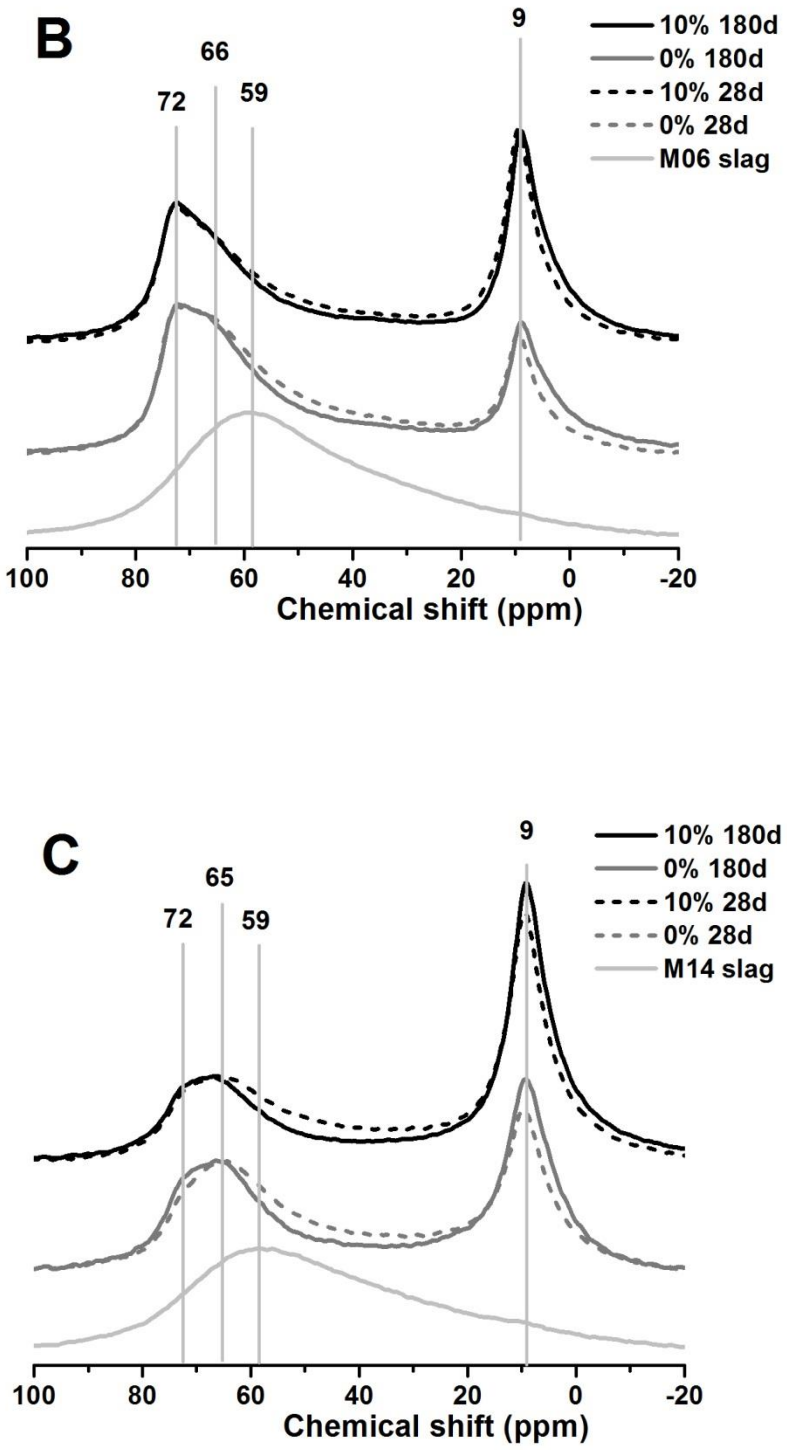

Figure 4-**8** ^{27}Al MAS NMR spectra of slag pastes prepared using (A) slag M01, (B) slag M06 and (C) slag M14, with 0 wt.% and 10 wt.% CLDH, cured for 28 and 180 days.

4.4. Discussion

4.4.1. The importance of slag chemistry in Na_2CO_3 activated cements

The hardening time of sodium carbonate activated slag pastes is strongly dependent on the slag chemistry. Significantly more rapid kinetics of reaction, and therefore faster setting, have been identified for slags with lower Al_2O_3 but much higher MgO contents, as a consequence of the formation of a high content of LDH phases), consistent with previous studies using sodium silicate as the activator (Ben Haha et al., 2011, 2012, Bernal et al., 2014c).

Figure 4-9 illustrates a conceptual model which is presented to describe the importance of the carbonate consumption process in sodium carbonate activation of slag. The black line represents the carbonate route in samples prepared without CLDH addition, while the grey line shows the influence of the CLDH.

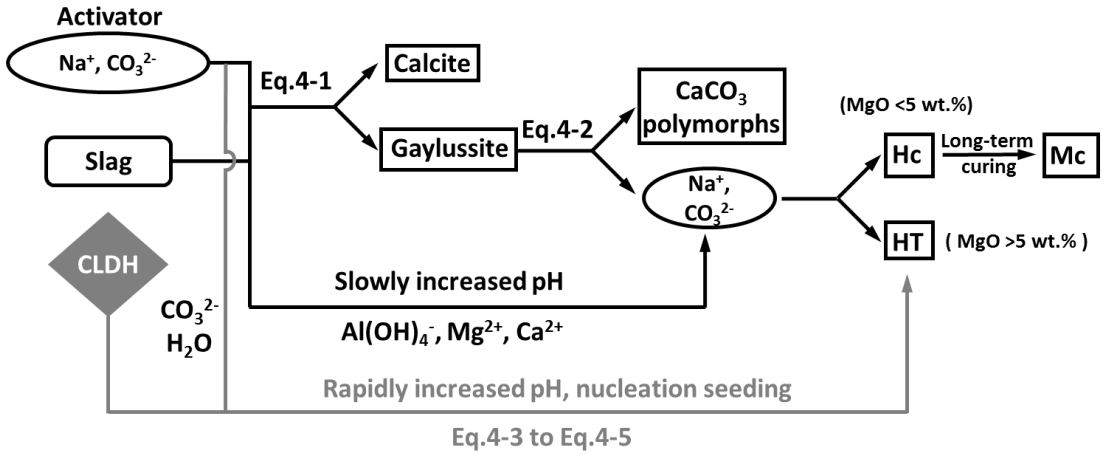

Figure 4-9 Simplified schematic diagram of the process of carbonate consumption through binding in mineral carbonates in the absence of CLDH (black), and the extra pathways introduced by CLDH addition, in an Na_2CO_3-activated slag cement.

Gaylussite is often formed at early age in the sodium carbonate activated paste prior to the formation of C-(A)-S-H (Bernal et al., 2014b, Fernández-Jiménez and Puertas, 2001). This is due to the fact that the breakage of O-Ca bonds and O-Mg bonds to release these species from the slag is able to take place at lower alkalinity than the breakage of O-Al and O-Si bonds (Shi and Day, 1995). Therefore, the aqueous phase reaches saturation with respect to gaylussite before other phases due to the high activator Na concentration, as shown in Figure 4-9. When the LDH phases and C-(A)-S-H gel start to precipitate, the gaylussite dissolves as a result of the decreased CO_3^{2-} ion concentration in the aqueous phase (Bernal et al., 2014b), with the carbonate reprecipitating rapidly as $CaCO_3$ polymorphs (e.g. the aragonite observed here) as shown in Eq.4-2 (Bischoff et al., 1991). This explains the formation of aragonite in most of the samples here.

$$5H_2O + 2Na^+ + Ca^{2+} + 2CO_3^{2-} \rightarrow Na_2Ca(CO_3)_2{\cdot}5H_2O \text{ (gaylussite)} \qquad \textbf{Eq.4-1}$$

$$Na_2Ca(CO_3)_2{\cdot}5H_2O \rightarrow CaCO_3 \text{ (aragonite)} + 2Na^+ + CO_3^{2-} + 5H_2O \qquad \textbf{Eq.4-2}$$

Both the hydrotalcite-like and AFm phases can be stable carbonate-bearing phases in cementitious binders (Bernal et al., 2014c, Matschei et al., 2007a). The dissolution of gaylussite would be accelerated if the dissolved CO_3^{2-} ions are taken by the LDH phases and removed from the pore solution. This explains the effect of the slag composition on the rate of reaction, where a higher degree of LDH phase formation accelerates the kinetics of reaction when using a sodium carbonate activator. Upon alkali activation of the slags, LDH phases form as a secondary reaction product, especially the hydrotalcite-like phase, and these phases can act as in-situ carbonate binding agents, promoting the carbonate removal process from the activator to solid phases and consequently accelerating the setting and hardening reaction sequence (Figure 4-9).

4.4.2. Recrystallisation of CLDH in sodium carbonate activator solution

Figure 4-10 shows the change of pH in the separated supernatant solution after reaction with CLDH. The pH in the supernatant increased dramatically after 1 hour of reaction, and increased slowly during the following 7 days. Sample "10% CLDH" results in a higher pH than "2% CLDH", which can be attributed to the higher content of CLDH. This proves that incorporation of CLDH in sodium carbonate activated slag could increase the pH of the activator significantly within the first hour after mixing.

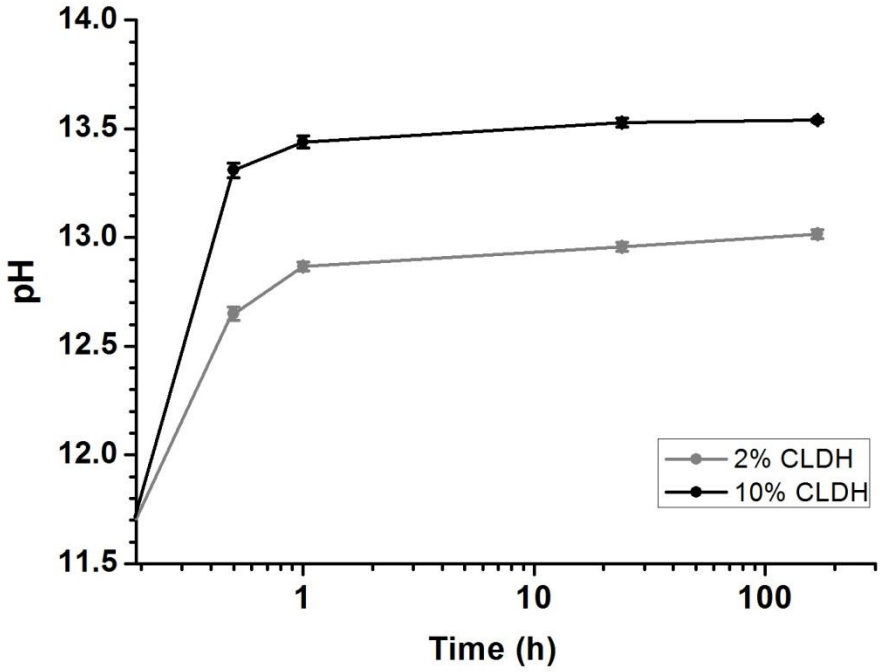

Figure 4-10 Change of pH in the separated supernatant solution as a function of time and dosage of CLDH added, results of triplicate samples.

Figure 4-11 shows the X-ray diffraction pattern of the synthetic hydrotalcite-type phase, consistent with the powder diffraction file ($Mg_4Al_2(OH)_{12}CO_3{\cdot}3H_2O$, PDF# 01-070-2151), and the pattern of the CLDH, where the crystalline reflections of the synthetic hydrotalcite are no longer observed. Instead, two broad humps centred at 43° and 63° 2θ are identified in the diffractogram of the CLDH. This demonstrates that the thermal treatment adopted in this study is effectively modifying the structure of the CLDH.

Upon hydration, a distinctive ordered crystal structure is observed in the hydrated CLDH sample after 30 min of mixing, resembling the diffraction pattern of the synthetic hydrotalcite. The intensities of the reflections observed in the hydrated samples increased at longer times of reaction, indicating the transformation of CLDH to a crystalline LDH phase. Along with a hydrotalcite-like phase, sodium carbonate (Na_2CO_3, PDF#01-077-2082) and its monohydrate (thermonatrite, $Na_2CO_3 \cdot H_2O$, PDF#00-008-0448) which precipitated from the residual solution (not removed by centrifugation) during the drying process, were also identified.

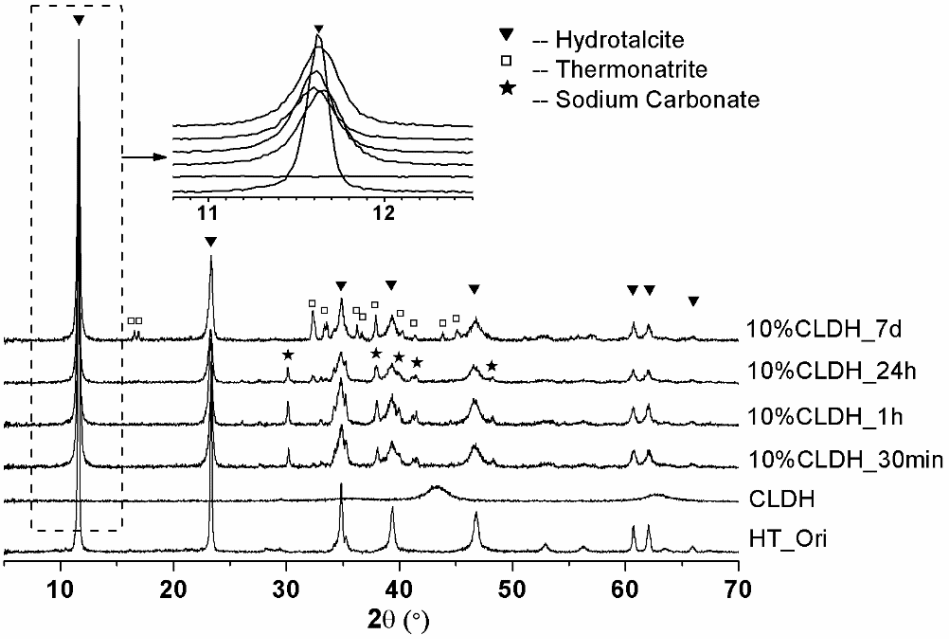

Figure 4-11 X-ray diffraction patterns of synthetic hydrotalcite (HT_Ori), anhydrous CLDH, and rehydrated CLDH, as a function of the mixing time of the CLDH with the Na_2CO_3 activating solution

4.4.3. Carbonate binding and reaction acceleration by CLDH

The kinetics of reaction of four different slags have all been expedited by the addition of CLDH (Figure 4-1), showing that the effectiveness of this addition is not dependent on the type of slag used. The added CLDH will react directly with the activator in aqueous solution, remove carbonate ions from the solution and form hydrotalcite-like phases. This is a shortcut for consumption of carbonate compared with the samples prepared without CLDH, and it also

favours the decomposition of gaylussite. However, CLDH does not only act as a carbonate binding agent, as the recrystallisation mechanism of CLDH in an aqueous environment will also modify the chemistry of the system, and this raises the need for further investigation to isolate the exact mechanisms taking place.

The recrystallisation processes of CLDH starts with its surface hydroxylation. As the surface oxygen ions of mixed metal oxides are undercoordinated with respect to metal ions, they are highly active in the presence of water and prone to be protonated to hydroxyl groups, as shown in Eq.4-3 (Tamura et al., 2001). When there is sufficient water to react, the mixed metal oxides behave as a Lewis base, forming a conjugate acid ($[Mg_{0.7}Al_{0.3}(OH)_2]^{0.3+}$) and a conjugate base ($OH^-$) as shown in Eq.4-4, and a material resembling the original brucite-like Mg-Al layered structure can recrystallise. As a result, the pH of the sodium carbonate solution is increased, as represented in Figure 4-10. The sites of conjugate bases are ion-exchangeable with other negatively charged ions (Tamura et al., 2001). When free CO_3^{2-} ions are available, they will be incorporated into the brucite-like layered structure, forming hydrotalcite as a stable ion-exchanged LDH phase, Eq.4-5 (Morimoto et al., 2012).

$$-O^{2-} + H_2O \rightarrow -OH^- + OH^- \qquad \text{Eq.4-3}$$

$$Mg_{0.7}Al_{0.3}O_{1.15} + 1.15H_2O \rightarrow [Mg_{0.7}Al_{0.3}(OH)_2]^{0.3+} + 0.3OH^- \qquad \text{Eq.4-4}$$

$$[Mg_{0.7}Al_{0.3}(OH)_2]^{0.3+} + 0.15\ CO_3^{2-} + nH_2O \rightarrow Mg_{0.7}Al_{0.3}(OH)_2(CO_3)_{0.15}\cdot nH_2O \qquad \text{Eq.4-5}$$

As shown in Eq.4-4 and Eq.4-5, the recrystallisation processes of the CLDH in sodium carbonate solution produced OH^- and consumed CO_3^{2-} during the initial stage of the reaction (within the first hour), leading to the increase in pH (Figure 4-10), which accelerates the reaction.

In addition to this chemical acceleration, the nucleation seeding effects of recrystallised hydrotalcite and the reduced w/b ratio due to the water consumption of CLDH also have the potential to alter the kinetics of reaction. The hydrotalcite-like phase produced by the recrystallisation of CLDH upon reaction with the activator solution (Figure 4-11) is very similar in nature to the Mg-Al LDH which forms as a reaction product in these alkali-activated slag systems, therefore the particle surface of the hydrotalcite-like phase could be amenable to precipitation and growth of slag reaction products, including both C-(A)-S-H gel and LDHs. It can be assumed that this would play a similar role in alkali-activated slag systems, acting as a nucleation seed. To investigate the influence of this seeding effect, the sample Ref-1 (Figure 4-12) was designed to reflect the seeding effects of the recrystallised hydrotalcite, by replacing CLDH with commercial hydrotalcite. The commercial hydrotalcite is already in its carbonated and hydrated form, and so would not further consume carbonate in the solution or undergo surface hydroxylation.

It is seen from Figure 4-12 that the onset time of the acceleration period of sample Ref-1 fell in between those of the plain paste and the 10 wt.% CLDH modified paste. The shift in the acceleration peak towards shorter times demonstrates the seeding effect of the incorporated commercial hydrotalcite, suggesting that the reformed hydrotalcite-like phase which is generated from CLDH upon reaction with the activating solution might also play a similar role in nucleation seeding during the alkali activation process.

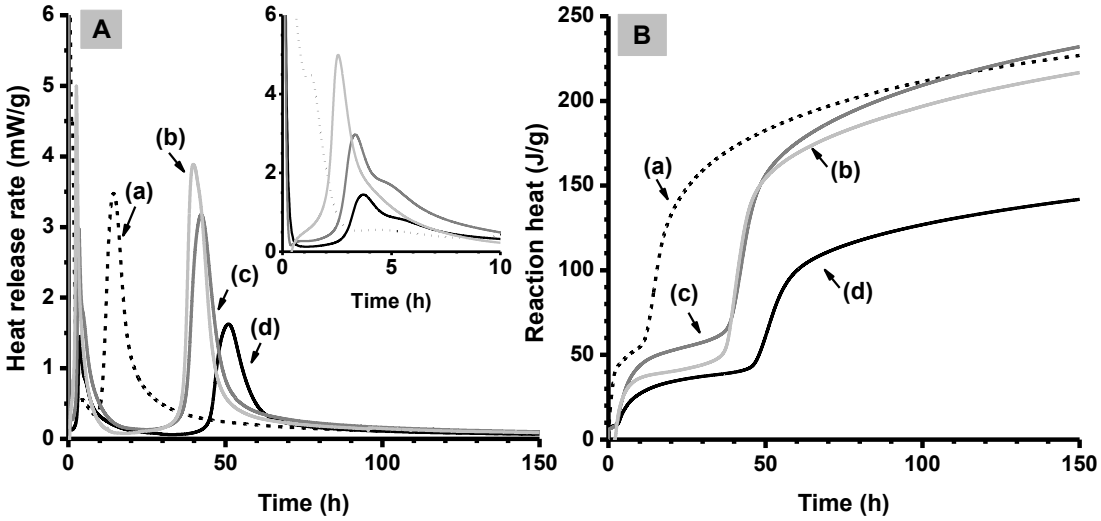

Figure 4-12 Isothermal calorimetry data for sodium carbonate activation of slag M06, with (a) a w/b ratio of 0.4, with 10 wt.% CLDH added; (b) a w/b ratio of 0.4 and 10 wt.% commercial hydrotalcite as additive (sample Ref-1); (c) a w/b ratio of 0.35 (sample Ref-2); (d) a w/b ratio of 0.4, without CLDH addition (all results normalised by the mass of slag)

However, these effects may also be convoluted by the effects of the change in w/b ratio induced by the uptake of water by the CLDH. Sample Ref-2 (Figure 4-12), which has a w/b ratio of 0.35 to correspond to the calculated potential water uptake by the CLDH (calculated according to Eq.4-4), thus aids in isolating any effect of reduced w/b ratio. In the alkali-activated slag system, there might be an optimum w/b ratio at which the hydration kinetics develop faster and the total hydration heat release is higher than at any other w/b ratio (Bernal et al., 2015b). For slag M06, w/b = 0.35 appeared to be more closely approaching the optimum w/b ratio than 0.4, which might explain the change of reaction kinetics. However, the workability of the pastes produced at this w/b ratio was more challenging than was the case at the higher w/b ratio used for the other pastes in this study, as the water consumption by the CLDH is gradual and so enables the pastes to be more fluid in the fresh state than is the case for a simple reduction in w/b ratio.

In summary, the incorporation of CLDH expedites the hardening process of sodium carbonate activated slags via several mechanisms, including:

- increasing the pH of the activator, as observed in Figure 4-10
- accelerated consumption of carbonate ions, and
- hydrotalcite nucleation seeding.

Controlling the reaction kinetics of sodium carbonate-activated slag paste to set within 24 hours is desirable for its adoption and implementation by the construction industry. Acceleration of the kinetics of reaction is promoted by expediting the removal of the carbonate supplied by the alkali activator, leaving the slag to react in a NaOH-rich environment (Bernal et al., 2015a). Incorporation of a carbonate binding agent that is more prone than Ca^{2+} to react with the CO_3^{2-} supplied by the sodium carbonate could thus be considered as a feasible approach to accelerate the kinetics of reaction.

4.5. Conclusions

Control of the kinetics of reaction of sodium carbonate-activated slag has been achieved in this study by adding CLDH as a carbonate binding agent, based on the understanding of the relationship between slag chemistry and the role of the functional group of the activator when producing activated slag cements. The relationships between the various Mg-Al (hydrotalcite-like) and Ca-Al (AFm) layered double hydroxides are essential in determining the overall characteristics of the binder system, as the uptake of Al by these phases restricts its availability for incorporation into C-A-S-H.

In a sodium carbonate-activated binder system, slags containing higher concentrations of MgO are seen to react much more rapidly, and to a greater extent within 180 days of curing. The MgO content of the slag controls the formation of a hydrotalcite-like phase with Mg/Al ~

2, and drives the removal of carbonate species from the pore solution. The process of removal of carbonate from the aqueous phase dominates the kinetics of reaction of sodium carbonate activated slag binders. A higher MgO content in the slag leads to faster dissolution and also results in formation of more hydrotalcite, which promotes the consumption of the carbonate species from solution, and accelerates the kinetics of reaction.

Incorporation of up to 10 wt.% CLDH in sodium carbonate activated slag pastes significantly accelerates the kinetics of reaction, enabling the slag pastes to set within 24 hours. The incorporated CLDH accelerates the consumption of carbonate, increasing the pH and driving the slag dissolution, and also reduces the effective water/binder ratio through uptake of water as it rehydrates. The hydrotalcite-like phase formed via recrystallisation was dispersed relatively homogeneously in the outer product region of the paste and acted as a nucleation seed, which benefited the precipitation of the gel product. CLDH addition has therefore been demonstrated to be an effective method by which the sodium carbonate activation of blast furnace slag can be used to produce a cementitious binder with an acceptably fast setting and hardening process for engineering purposes. This is particularly the case when the mix is prepared with a slag containing a high concentration of MgO.

However, although kinetically favouring the setting of the paste, whether the addition of CLDH would strengthen the mechanical and durability performance of sodium carbonate-activated slag cement is yet to be discovered. Before evaluating the durability performance of sodium carbonate-activated slag cement using current test methods, understanding of the ionic interactions between potentially corrosive ions (e.g. Cl^-, CO_3^{2-}) and binder phases in high alkaline pore solutions will be needed, which are investigated and discussed explicitly in the following Chapter.

Chapter 5.

CHEMICAL INTERACTION OF CHLORIDES WITH CEMENTITIOUS PHASES PRESENT IN ALKALI-ACTIVATED SLAG CEMENTS

Note: This chapter is primarily based on the paper "*Uptake of chloride and carbonate by Mg-Al and Ca-Al layered double hydroxides in simulated pore solutions of alkali-activated slag cements*", by X. Ke, S. A. Bernal, J. L. Provis, 100, 1-13.

5.1. Introduction

Alkali-activated slag (AAS) cements often exhibit low chloride permeability compared with Portland cement (Ismail et al., 2013, Ma et al., 2015, Shi, 1996). This has been partially attributed to the reduced capillarity identified in these materials (Bernal et al., 2011a, Shi, 2004), and the high concentration of free ions (including Na^+ and OH^-) present in the pore solution may also generate an osmotic gradient to counteract migration of Cl^-. The potentially high chloride binding capacity of the AAS cement binder postulated in some studies might also contribute to the higher resistance to chloride ingress (Ismail et al., 2013, Ma et al., 2015), and this is the core question to be examined in this Chapter. The retention of chlorides in the alkali-activation reaction products by chemical binding, when taking place, will delay the ionic transport of chlorides through the concrete, thus reducing the chloride migration rate (Yuan et al., 2009).

It can be expected that the chloride binding capacity of AAS cements is largely dependent on the chloride binding capacities of the individual phases forming in these systems. As

discussed in the preceding chapters, these phases include Mg-Al hydrotalcite-like layered double hydroxide (LDH) phases, Ca-Al AFm LDH phases such as strätlingite, and (Al,Na)-substituted calcium silicate hydrate (C-(N)-A-S-H) type gels, whose type and relative concentrations are governed by the chemistry of both the slag (Ben Haha et al., 2011, Bernal et al., 2014c) and the alkali-activator (Chapter 4). However, detailed assessment interlinking the phase assemblage of AAS cements and their potential chloride binding capacity has never been presented before. Understanding the ionic binding capacity of chlorides of each individual phase forming in cementitious matrices is crucial for determining the rate of chloride transport, as this underpins the correctly prediction of the long term performance of concretes based on these cements (Andrade et al., 2013, Arya et al., 1990, Yuan et al., 2009).

Chloride-bearing equivalents of each of the phases typically identified in AAS cements, i.e. both types of LDH phases and the C-(N)-A-S-H type gel, have been evaluated within the context of Portland blended systems, using external sources of chlorides (Beaudoin et al., 1990, Birnin-Yauri and Glasser, 1998, Kayali et al., 2012, 2013, Mesbah et al., 2011a, 2012, Yang et al., 2012). Previous studies (Châtelet et al., 1996, Morimoto et al., 2012) showed that chloride ions are mostly identified in the diffuse layer at the external surface of hydrotalcite-like phases, pairing with Na^+. The formation of a chloride-exchanged hydrotalcite-like phase with interlayer anion substitution has been claimed (Khan et al., 2016, Yoon et al., 2014b), however there is not yet sufficient information to fully describe its mineralogy. For AFm-phases, although the AFm(SO_4,Cl) (Mesbah et al., 2012), AFm(CO_3,Cl) (Mesbah et al., 2011a, 2012) and AFm(OH,Cl) (Birnin-Yauri and Glasser, 1998) solid solutions have been evaluated, the interaction of chloride ions with strätlingite has not yet been characterised in detail. The interactions between Cl^- ions and C-(A)-S-H type gel (usually evaluated under portlandite saturated conditions) are mainly through surface adsorption by ionic pairing effects (≡Si-O-Ca-Cl) (Elakneswaran et al., 2009). Adsorption of Cl^- onto the diffuse layer of a positively charged C-(A)-S-H gel surface is also a possible approach to binding chloride ions (Labbez et al., 2007).

The interactions controlled by surface adsorption (physical sorption) on the LDH phases studied here have been evaluated in the literature only to a limited degree. Chloride uptake can take place through surface adsorption in the diffuse electrical double layer (EDL) outside the positively charged LDH surface (Duan and Evans, 2006, Morimoto et al., 2012, Prasanna and Kamath, 2009). Also, given that the surfaces of LDHs are hydroxylated, the pH in the solution may affect the surface adsorption process by influencing the charge density of the surface (Morimoto et al., 2012, Shaw, 1992). Florea and Brouwers (2012) studied the physical sorption of NaCl onto Friedel's salt in Portland cement based systems, but found no significant effect. In AAS cements, the pore solution is of high alkalinity, approximately 1.0 mol/L NaOH (Myers et al., 2015b, Song and Jennings, 1999) and high ionic strength, thus greater surface adsorption on both types of LDH phase could be expected. Higher ionic strength could lead to higher surface adsorption (Trefalt et al., 2016), however the higher ionic strength in AAS pore solution is mostly contributed by a higher OH^- and Na^+ concentration (Myers et al., 2015b, Song and Jennings, 1999), and the OH^- might act as competitive anions with chlorides and reduce the chloride binding capacities.

Atmospheric carbonation of AAS cements leads to a reduction in alkalinity and an increase in the concentration of dissolved carbonates in the pore solution (Bernal et al., 2012, Fernández Bertos et al., 2004). Carbonate ions may also play important roles in determining chloride uptake by the solid phases present in in AAS cement; CO_3^{2-} can be consumed by LDH interlayers to form stable mineral phases (Morimoto et al., 2012). However, there has not been previous investigation of the stability of the chloride-bearing LDHs in presence of carbonate ions, in simulated pore solutions relevant to AAS cements.

In order to create a database which can be used in determining the chloride binding capacity of AAS paste as a whole, this study focuses on determination of the chloride binding capacities of a synthetic hydrotalcite-like phase, strätlingite, and three types of synthetic C-(N)-A-S-H gel (with Ca/Si ratios 1.0 and 1.4, the former at Al/Si ratios 0 and 0.1, and the

latter at Al/Si=0.1). This was carried out in chloride-rich simulated pore solutions with varying $[Cl^-]/[OH^-]$ ratios. LDH phases were also exposed to solutions with different $[CO_3^{2-}]/[OH^-]$ ratios. Changes in chemistry and mineralogy of the synthetic phases studied here were determined using X-ray fluorescence spectroscopy (XRF), X-ray diffraction (XRD), and thermogravimetry coupled with mass spectrometry (TG-MS). The respective contributions of surface adsorption and interlayer incorporation have also been determined.

5.2. Experimental method

5.2.1. Synthetic phases preparation

5.2.1.1. Mg-Al hydrotalcite-like phase

A calcined layered double hydroxide (CLDH) was produced from thermally treated synthetic hydrotalcite ($Mg_{0.7}Al_{0.3}(OH)_2(CO_3)_{0.15}\cdot 0.63H_2O$, Sigma-Aldrich), following the method described in Chapter 3, with an Mg/Al ratio of 2.0 to 2.3, and residual carbonate content lower than 0.1 wt.%. The CLDH is used for studying the ion-exchange capacity of hydrotalcite-like phases.

5.2.1.2. Strätlingite

Strätlingite ($Ca_2Al(AlSi)O_2(OH)_{10}\cdot 2.25H_2O$) was prepared according to the method described by Matschei et al. (Matschei et al., 2007b). Initially, stoichiometric quantities of CaO (obtained by calcining $CaCO_3$ (Sigma-Aldrich) at 1000°C for 12 hours), $Na_2SiO_3\cdot 9H_2O$ (Sigma-Aldrich, ≥98%), and $NaAlO_2$ (Sigma-Aldrich), were separately suspended in Milli-Q water, at 20 ± 3 °C. Then, the sodium aluminate slurry was added to the portlandite suspension formed by hydration of CaO. After shaking for 1 min, the sodium silicate solution was added into the mixture, which was sealed in HDPE bottles with Parafilm. The HDPE bottles were kept at 20 ± 3 °C and agitated daily for 6 weeks. Preparation of the synthetic

strätlingite was carried out in a nitrogen filled glove box to minimise any potential for carbonation.

5.2.1.3. (Sodium,Aluminium)-containing Calcium Silicate Hydrate (C-(N)-A-S-H) type gels

CaO was obtained from calcined calcium carbonate ($CaCO_3$, Sigma-Aldrich, ≥ 99.0%, powder) at 1000 °C for 12 hours. Fumed silica, AEROSIL® 200, with BET surface area of 200 ±25 m^2/g was used as the silica source. $CaO{\cdot}Al_2O_3$ (CA) was chosen as the aluminium source due to its high reactivity (Taylor, 1997). The CA used in this research was synthesised by heating homogenised $CaCO_3$ and Al_2O_3 (L'Hôpital et al., 2015) following the sintering schedule shown in Figure 5-1.

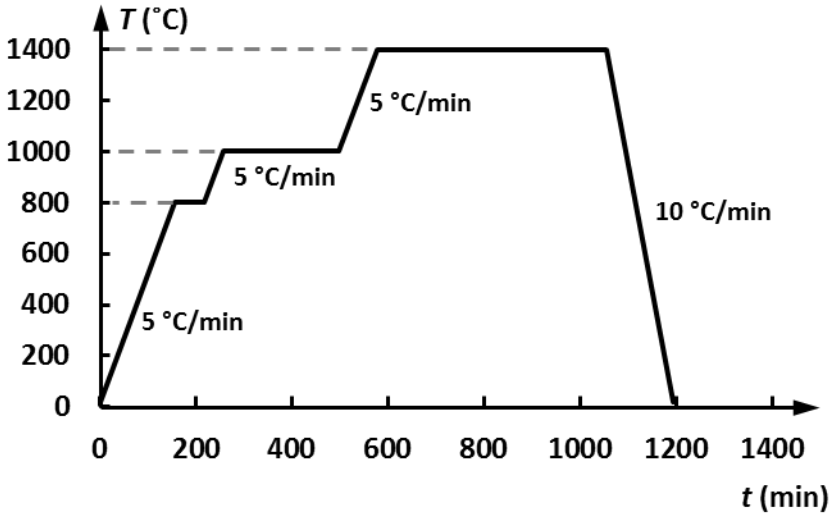

Figure 5-1 Sintering schedule applied for synthesis of $CaO{\cdot}Al_2O_3$ (CA).

The C-(N)-A-S-H samples were prepared according to the procedure described by L'Hôpital et al. (2015), mixing 2 g of CaO, CA and SiO_2 powder mixtures with 100 mL of 1.0 mol/L sodium hydroxide in 125 mL HDPE bottles. C-(A)-S-H samples with different Ca/Si and Al/Si ratios were produced according to the formulations shown in Table 5-1. The

synthesis processes of all samples were conducted in nitrogen filled glovebox to minimized possible CO_2 contamination. All the HDPE bottles were stored in an environmental chamber at 60 °C, regularly shaken (kept in rolling mixer for 1 hour at a time) twice a week for 10 weeks. Then the HDPE bottles were moved to an environmental chamber at 20°C for three days, until reaching room temperature prior to separation.

Table 5-1 Formulation of C-(N)-A-S-H gel-forming mixes for each batch prepared.

Sample ID	Molar ratio		Mass (g)			
	Ca/Si	Al/Si	CaO (40 g/mol)	$CaO\text{-}Al_2O_3$ (142 g/mol)	SiO_2 (60 g/mol)	0.5 M NaOH (1.02 g/mL)
CNASH-A	1.0	0	0.800	0.000	1.200	100.0
CNASH-B	1.0	0.1	0.723	0.135	1.142	100.0
CNASH-C	1.4	0.1	0.892	0.117	0.991	100.0

5.2.2. Chloride-rich simulated pore solution

Two groups of chloride rich simulated pore solutions were prepared: carbonate-free solutions and carbonated solutions (compositions shown in Table 5-2). Four carbonate-free solutions were produced, with a constant total Na^+ concentration and total ionic strength, but with varying $[Cl^-]/[OH^-]$ ratios. Two carbonated simulated pore solutions were designed: solution CH-3-1 has the same total Na^+ concentration as the carbonate-free solutions, but with hydroxides partially replaced by carbonate ions, resembling the natural carbonation process (Eq. 5-1) (Bernal et al., 2012). Solution CH-3-2 was designed for investigating the effect of hydroxide concentration on chloride binding in the presence of carbonate, therefore the chloride concentration and carbonate concentration were matched to CH-3-1, but with a much lower hydroxide concentration.

$$2OH^- + CO_2 \rightarrow H_2O + CO_3^{2-} \qquad \text{Eq. 5-1}$$

To study the interaction of chloride-rich simulated pore solution with the synthetic LDHs and C-(N)-A-S-H type gels, 40 g of pre-prepared solutions (Table 5-2) were weighed in 50 mL centrifuge tubes, and 0.4 g of solids (either CLDH, strätlingite, or C-(N)-A-S-H gel) were added to each tube, under a nitrogen atmosphere in a glove box. Each formulation was prepared in duplicate. All tubes were sealed with Parafilm to minimise water evaporation and sample carbonation, stored at 20 ± 3 °C, and were manually shaken for 3 min every day until the mixtures reached equilibrium. For C-(N)-A-S-H type gels, only carbonate-free solutions were used.

Table 5-2 Stoichiometric compositions of the simulated chloride-rich pore solutions studied

Carbonate-free solutions	**Concentration (mol/L)**				**$[Cl^-]/[OH^-]$**	**Total ionic strength, I (mol/L)**
	NaCl	**NaOH**	**Na_2CO_3**	**Total Na^+**		
CH-1	0.10	0.90	0	1.00	**0.1**	1.00
CH-2	0.25	0.75	0	1.00	**0.3**	1.00
CH-3	0.50	0.50	0	1.00	**1.0**	1.00
CH-4	0.75	0.25	0	1.00	**3.0**	1.00
Carbonated solutions	**NaCl**	**NaOH**	**Na_2CO_3**	**Total Na^+**	**$[Cl^-]/[OH^-]$**	**Total ionic strength, I (mol/L)**
CH3-1	0.50	0.30	0.10	1.00	**1.7**	1.10
CH3-2	0.50	0.10	0.10	0.80	**5.0**	0.90

5.2.3. Separation methods

After reaching equilibrium, which took 7 days for CLDH (Chapter 4), 3 weeks for strätlingite (Okoronkwo and Glasser, 2016b), and 4 months for C-(N)-A-S-H gel (at 60 °C, cooled at 20 °C for 3 days prior to separation) (L'Hôpital et al., 2015), the solids that had been mixed and reacted with the different Cl-rich pore solutions were separated from the chloride-rich solution using a centrifuge (Heraeus Biofuge Primo, at 4000 rpm for 6 min). Prior to analysis, the separated supernatant solutions were filtered through 0.45 μm PVDF filter membranes. The pH values of the supernatants were determined using a digital pH meter (Oakton Acorn Series). The chloride ion concentration was obtained using an ion

selective electrode (Cole-Parmer Epoxy solid-state chloride electrode, accuracy ± 2%) according to ASTM D512–12 (ASTM International, 2012b). The chloride binding capacity of CLDH was calculated using Eq. 5-2.

$$Q_e = (C_0 - C_e) \cdot V / m_{input} \quad \text{Eq. 5-2}$$

Q_e - Chloride binding capacity of solid, mg/g (by dry mass of initial solid).
C_e - Chloride concentration of the supernatant solution, mol/L.
C_0 - Initial chloride concentration, mol/L.
V - Volume of solution, mL.
m_{input} - Initial mass of solid, g.

After chloride immersion, two sets of solid LDH samples were conditioned. The first group of samples were dried in a vacuum desiccator at a controlled relative humidity at 30 ± 3% (reached using saturated $CaCl_2$ salt) for 4 days, immediately after the first filtration. These samples are referred to as "*first filtration samples*" throughout this chapter. The second group of LDH samples were washed with Milli-Q water, following the RILEM recommendations for analysis of water soluble chloride content in concrete (RILEM TC 178-TMC, 2002), centrifuged and separated again. The solids were then dried under the same conditions as described for the first filtration samples. These samples are referred to as "*second filtration samples*". For C-(N)-A-S-H type gels reacting with chloride-rich pore solutions, only one filtration was conducted.

5.3. Results and discussion

5.3.1. Aqueous equilibrium

5.3.1.1. Mg-Al hydrotalcite-like phase

The initial and equilibrium chloride and hydroxide concentration values of two groups of the Cl-rich solution prior and after addition of CLDH solids were measured. The chloride binding capacity (Q_e) of the CLDH in each environment tested was calculated according to

Eq. 5-2, and results are reported in Figure 5-2A. The $[Cl^-]/[OH^-]$ ratios at equilibrium in the measured solutions are reported as a function of their initial $[Cl^-]/[OH^-]$ ratios (Figure 5-2B). These values represent the total amount of free chloride removed from the bulk solution per unit of CLDH solid, via both ion-exchange and surface adsorption in the solid CLDH, under various aqueous conditions. The rehydration of the CLDH increased the alkalinity of the supernatant at equilibrium, even in these already highly alkaline solutions.

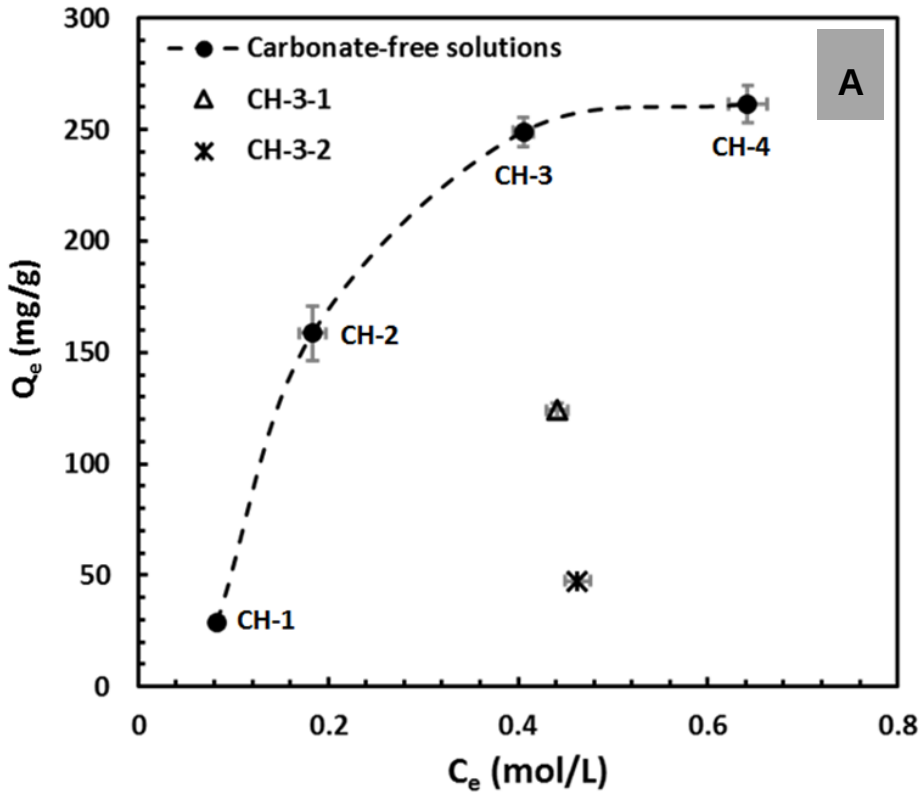

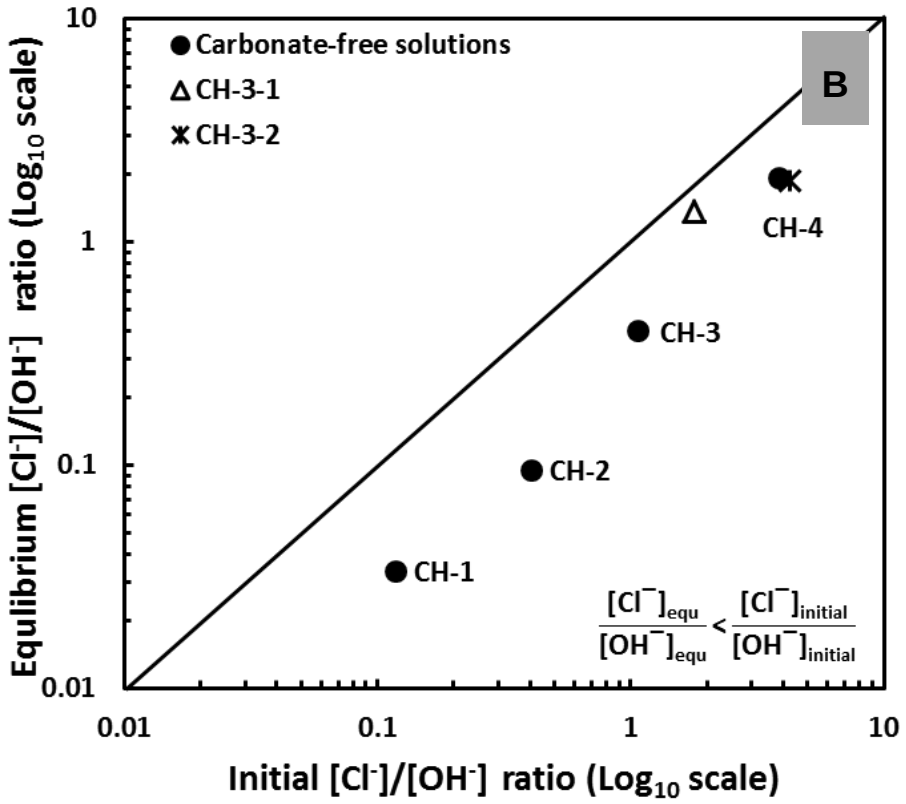

Figure 5-2 (A) Chloride binding capacities of the Mg-Al LDH (calculated with respect to the mass of the CLDH used) in various chloride-rich simulated pore solutions. The error bars correspond to one standard deviation among three replicates; (B) Correlation of the $[Cl^-]/[OH^-]$ ratios at equilibrium as a function of their initial values in each solution

For the carbonate-free systems, where the equilibrium chloride concentrations ranged from 0 to 0.8 mol/L, the Q_e value increased significantly at increased $[Cl^-]/[OH^-]$ ratios, reaching a plateau above 0.5 mol/L initial chloride concentration (equivalent to $[Cl^-]/[OH^-]=1$) at around 250 mg Cl/g CLDH. Carbonated solutions CH-3-1 and CH-3-2 contained the same initial chloride concentration as solution CH-3; however, the equilibrium chloride concentrations in these two solutions are much lower than that of solution CH-3. This indicates a reduction in chloride binding capacities in the solid phase when carbonate is present. Between the two carbonated samples, the chloride binding capacity in solution CH-3-2 is lower than that of solution CH-3-1.

The reaction between CLDH and chloride rich solutions through exchange of interlayer species could be conceptualised as a two-step process: (i) hydrolysis of the dehydrated CLDH to form a hydroxylated structure similar to meixnerite (Eq. 5-3) (Tamura et al., 1999), followed by (ii) ion-exchange between interlayer OH^- ions and anions in the liquid phase (Eq. 5-4) (Miyata, 1983). Therefore, the availability of different types and concentrations of ions in the aqueous solution has an important effect on the solid phase at equilibrium. In reality these processes will not necessarily be consecutive, as it is possible for some chloride to act directly in the re-formation of the LDH structure from the anhydrous material, but conceptualisation in this way does assist in assigning the potential contributions of different binding mechanisms. A higher initial $[Cl^-]/[OH^-]$ ratio and the absence of carbonate favour the uptake of chloride ions over hydroxide ions via the law of mass action, leading to determination of a higher Q_e value at higher chloride content. The plateau at high aqueous chloride concentration represents saturation of the available sites in the LDH material (interlayer and external surface) with chloride ions.

$$Mg_{1-x}Al_xO_{(1+x/2)} + (1+x/2)\ H_2O \rightarrow [Mg_{1-x}Al_x(OH)_2]^{x+} + x\ OH^- \quad \text{Eq. 5-3}$$

$$[Mg_{1-x}Al_x(OH)_2]^{x+} + (a-2)\ OH^- + b\ Cl^- + c\ CO_3^{2-} + nH_2O \rightarrow Mg_{1-x}Al_x(OH)_a(Cl)_b(CO_3)_c{\cdot}n\ H_2O \quad \text{Eq. 5-4}$$

Where in Eq. 5-4, (a-2)+b+2c=x

In carbonated solutions, since the positively charged metal oxide sheets have stronger affinity for multivalent ions than monovalent ions (Miyata, 1983, Morimoto et al., 2012), the carbonate ion is more competitive than both chloride and hydroxide ions as interlayer species. The incorporation of carbonate in hydrotalcite-like phase reduces the available chloride binding sites, resulting in lower Q_e values even at the same initial chloride concentration and higher initial $[Cl^-]/[OH^-]$ ratio. This suggests that the greatly reduced chloride binding capacity observed in solution CH-3-2 could be caused by the incorporation of carbonate ions into the interlayers due to a reduced hydroxide concentration.

The chloride uptake capacity of the Mg-Al LDH via surface adsorption is clearly important, as a mass balance calculation shows that the mass of chloride taken up by the LDH structure exceeds the quantity which could realistically be accommodated in interlayer sites. However, quantification of the partitioning of chlorides between the interlayer and the surface requires determination of the chemical composition of the solid phase after chloride binding, which will be discussed in detail in the following sections.

5.3.1.2. Strätlingite

Figure 5-3 shows the chloride uptake of strätlingite immersed in solutions with different chloride concentrations, and the $[Cl^-]/[OH^-]$ ratio in equilibrium solution in comparison with initial $[Cl^-]/[OH^-]$ ratios. The chloride uptake capacities of strätlingite under different aqueous conditions were also calculated using Eq. 5-2.

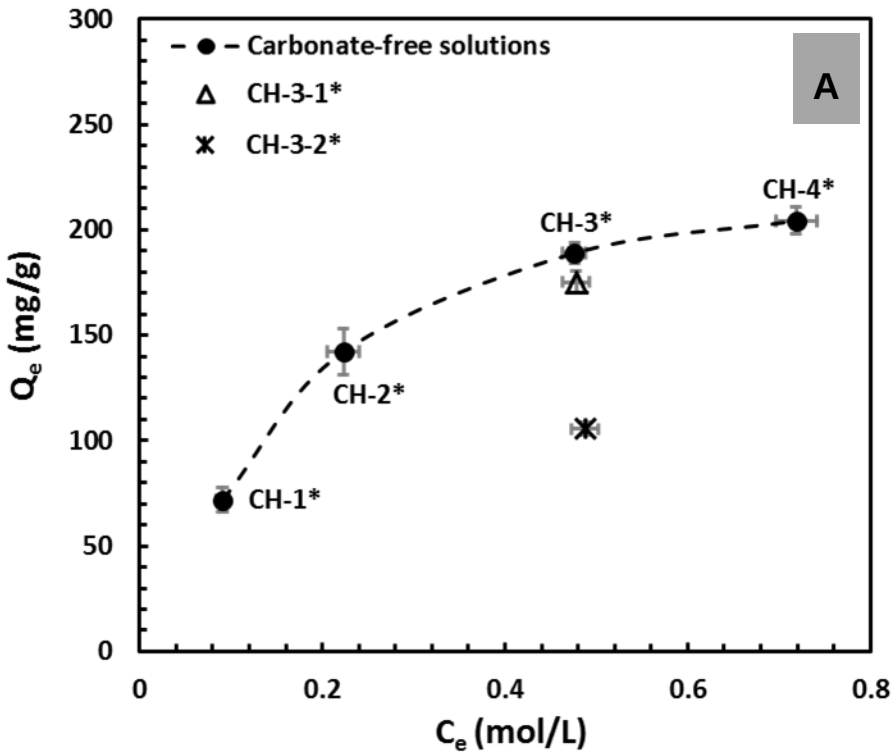

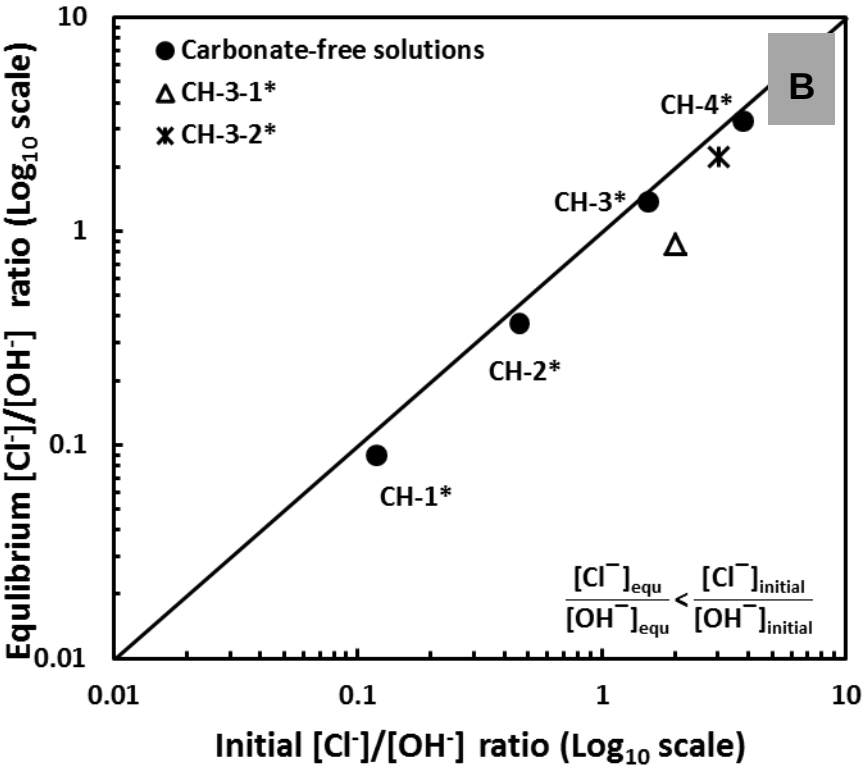

Figure 5-3 (A) Chloride binding capacity of strätlingite in various chloride rich simulated pore solutions. Q_e calculated using Eq. 5-2. The error bars indicate one standard deviation among three replicates. (B) Correlation of the $[Cl^-]/[OH^-]$ ratios measured at equilibrium as a function of their initial values

Similar to the trends identified for the Mg-Al LDH, for carbonate-free solutions the total chloride uptake capacity of the AFm phase rises as the $[Cl^-]/[OH^-]$ ratio increases. The chloride binding capacity of strätlingite is higher than that of Mg-Al LDH at lower initial $[Cl^-]/[OH^-]$ ratio (<0.3), but lower at higher initial $[Cl^-]/[OH^-]$ ratios (>0.3). The maximum chloride binding capacity achieved was about 204 mg/g, at an initial $[Cl^-]/[OH^-]$ ratio of 3.

The differences in chloride binding isotherm for strätlingite, compared with that of Mg-Al LDH, suggest that the interaction between chloride ions and strätlingite might involve different binding mechanisms, most likely a lattice substitution (Balonis et al., 2010, Mesbah et al., 2011a). The decrease in chloride uptake by strätlingite induced by increased $[CO_3^{2-}$

]/[OH^-] ratio is similar to that identified for the hydrotalcite-like phase, although less significant changes were observed in the chloride uptake from solutions CH-3-1* and CH-3-2* compared with the sample CH-3* in strätlingite compared to that identified for Mg-Al LDH. It is possible that the decreased chloride binding capacity of strätlingite in carbonated solutions is due to the formation of carbonate-rich AFm phases, such as hemicarbonate or monocarbonate (Mesbah et al., 2011a). This will be examined in detail in the following sections.

5.3.1.3. C-(N)-A-S-H type gels

The total chloride uptake in chloride-rich pore solutions with different [Cl^-]/[OH^-] ratios was measured and calculated using a similar method to that described for synthetic LDHs (e.g. hydrotalcite and strätlingite), and the results are shown in Figure 5-4. The chloride binding capacities of C-(N)-A-S-H with different Al/Si ratios increase when exposed to solutions with higher [Cl^-]/[OH^-] ratios. However, the increase in Q_e values for each type of C-(N)-A-S-H assessed were not significant when the initial [Cl^-]/[OH^-] ratios were lower than 1.0. Instead, the chemistry of the synthetic C-(N)-A-S-H type gel appears to be the main factor governing the overall chloride uptake. The C-(N)-A-S-H type gel 'C' with a Ca/Si ratio around 1.4, and Al/Si=0.1, showed the lowest chloride uptake at lower [Cl^-]/[OH^-] ratios (<1.0), but the highest chloride uptake when immersed in a [Cl^-]/[OH^-] ratio around 3.0. C-(N)-A-S-H type gel 'B', with a bulk Ca/Si ratio of 1.0 and the same Al substitution (Al/Si=0.1) as C-(N)-A-S-H gel 'C', showed the highest chloride uptake at a low [Cl^-]/[OH^-] ratio, but lowest at highest [Cl^-]/[OH^-] ratios.

The uptake of chloride ions by C-(A)-S-H type gels mostly takes place in the diffuse layers surrounding the gel surface, and no significant chemical binding has been observed between chloride ions and C-(A)-S-H phases (Beaudoin et al., 1990, Plusquellec and Nonat, 2016, Yoon et al., 2014a). The C-(N)-A-S-H type gels present a positively charged surface in calcium-rich alkaline solutions (Labbez et al., 2007), and a more positively charged surface

will most likely result in a higher uptake of counter-ions, including both OH^- and Cl^-. A higher bulk Ca/Si ratio increases the positive charge density at the C-(N)-A-S-H type gel surface (Labbez et al., 2007, Yoon et al., 2014a), while increased Al-substitution (higher Al/Si ratio) decreases the overall surface charge density (Schneider et al., 2001, Sun et al., 2006). The presence of excess Na^+ might also balance the charge of substituted Al in the C-(N)-A-S-H gel (Hong and Glasser, 2002, Myers et al., 2014). However, only when chloride ions are the dominant anions (i.e. the initial $[Cl^-]/[OH^-]$ ratio>1), less OH^- is competing with Cl^-, therefore the overall chloride uptake by C-(N)-A-S-H gels is positively correlated with its positive surface charge density.

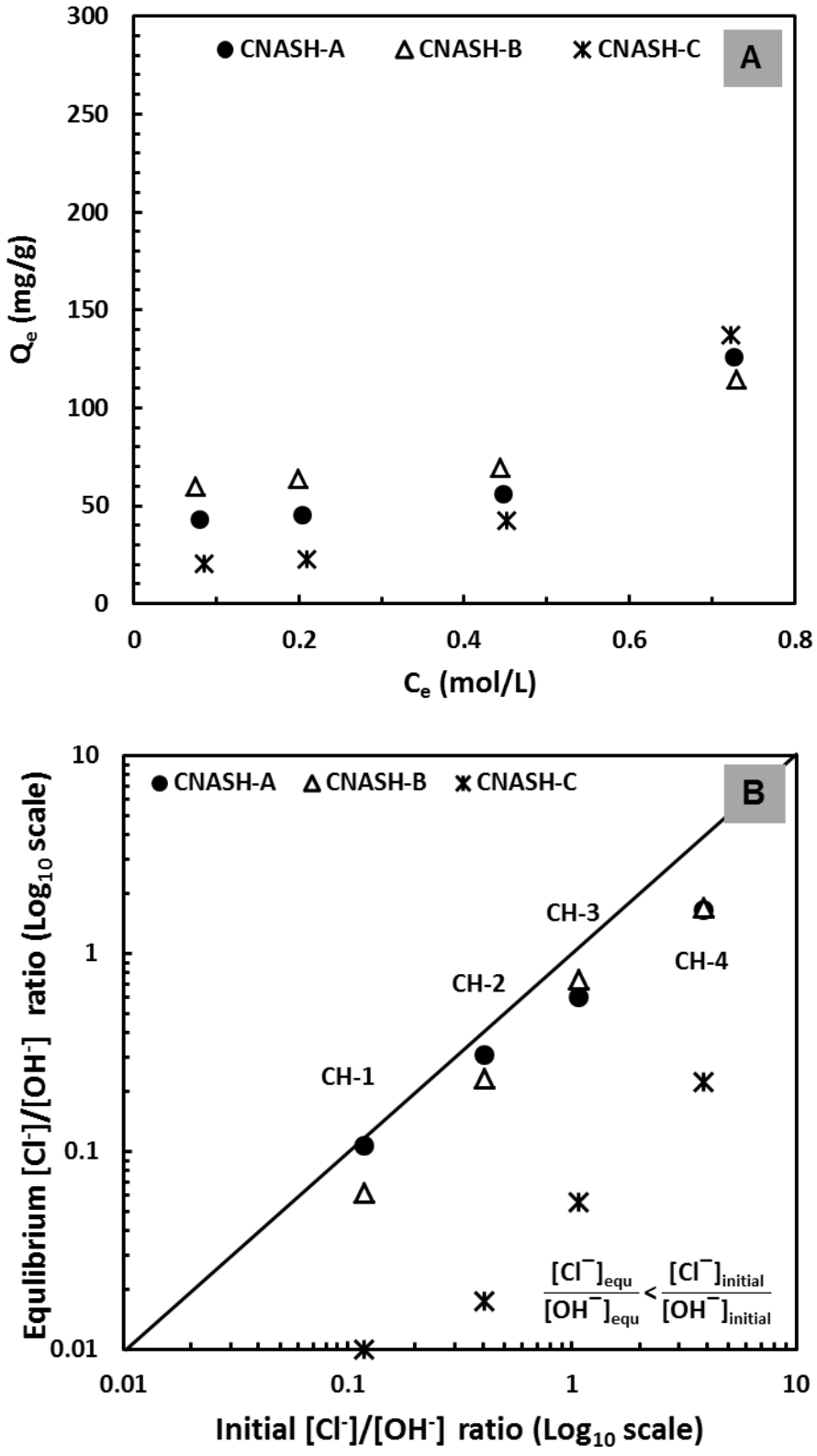

Figure 5-4 (A) Chloride binding capacity of three types of synthetic C-(N)-A-S-H type gels in various chloride rich simulated pore solutions. Q_e calculated using Eq. 5-2. The error in the measurement is lower than 1.0%. (B) Correlation of the $[Cl^-]/[OH^-]$ ratios measured at equilibrium as a function of their initial values

5.3.2. Mineralogy of solid phases

5.3.2.1. Mg-Al hydrotalcite-like phase

Chemical analysis of the solid Mg-Al LDH products

The elemental analysis of the solid material obtained after the first and second filtrations is reported in Table 5-3. In solid samples after the second filtration, the detected percentages of sodium and chloride were much lower than the values obtained after the first filtration, by as much as a factor of 10 for chloride in particular.

Table 5-3 XRF results for solids after first and second filtration. Carbon is not detectable by the instrument used here. Data presented as elemental mass percentage

Elements	**1st filtration**				**2nd filtration**					
	CH-1	**CH-2**	**CH-3**	**CH-4**	**CH-1**	**CH-2**	**CH-3**	**CH-4**	**CH-3-1**	**CH-3-2**
Na	17.8	17.6	12.9	40.1	9.0	6.7	2.2	1.0	1.0	0.5
Cl	9.1	11.2	9.5	53.5	0.2	0.5	0.7	1.2	0.4	0.3
Mg	14.8	16.9	18.4	3.7	20.9	21.2	22.1	19.1	20.8	20.6
Al	8.2	8.8	9.1	2.6	11.5	10.9	11.8	9.5	11.0	10.5
O	50.1	45.4	50.1	*n.d.	58.4	60.7	63.2	69.1	66.8	68.2
Atomic ratio										
Mg/Al	2.0	2.1	2.3	null	2.0	2.2	2.1	2.3	2.1	2.2

*n.d. represents “not detected”

Mg/Al ratios of the recrystallised LDH ranged from 2.0 to 2.3 (Table 5-3), similar to that of the original CLDH, except for the Mg/Al ratio detected from sample CH-4 after the first filtration, which is lower than the lowest acceptable Mg/Al ratio in the hydrotalcite-like phase family (Gastuche et al., 1967), and so is reported as a null measurement. A very high percentage of intermixed NaCl crystals (as is evidently the case here from the Na and Cl contents) would make the calculation of Mg/Al ratio in hydrotalcite-like phase less reliable.

In the diffuse layer, both Cl^- and OH^- can act as counter-ions. When the initial $[Cl^-]/[OH^-]$ is lower than 1, OH^- is the dominant anion in the solution, resulting in a significant amount of OH^- retention in diffuse layers as well. Since OH^- cannot be detected by XRF, the amount of Na detected would be much higher than the amount of Cl. This explains why all samples, except CH-4, presented a Na content significantly higher than that of the stoichiometric composition of NaCl.

X-ray diffraction analysis of the recrystallised Mg-Al LDH

Figure 5-5 shows the XRD patterns of recrystallised LDH after the first (Figure 5-2A) and second (Figure 5-2B) filtration. A hydrotalcite-like phase, and crystallised NaCl (Powder Diffraction File (PDF) # 01-078-0751), were identified after the first filtration. The intensities of NaCl reflections in Figure 5-5A increased with increasing chloride concentration in the bulk solution. However, NaCl crystals are not identified in any of the samples after the second filtration, and only the hydrotalcite-like phase was observed in solids after the second filtration (Figure 5-5B).

The basal peak position of the hydrotalcite-like phase after the first filtration was centred at 11.6°, although the intensities and widths of this peak vary for the hydrotalcite-like phases which recrystallised in solutions with different chloride concentrations. This is most likely associated with changes in the amount of bound chlorides interrupting the regularity of the layered structure (Figure 5-5A). In carbonate-free solutions, the basal peak of the hydrotalcite-like phase was broader and less intense after chloride exposure compared to the material obtained by recrystallising the same CLDH in water (marked CLDH-H2O in Figure 5-5B). This was more notable in solutions with high chloride concentrations. Changes in the basal peak shape but not its position indicate that the average interlayer spacing in chloride-exchanged hydrotalcite-like phases remain largely unchanged on average, but variation between different unit cells becomes more marked with a higher chloride loading.

In the carbonate-containing samples CH-3-1, the basal reflection peak of the CLDH is even more diffuse than that of the samples with the highest chloride loadings in carbonate-free systems. This suggests that the incorporation of carbonate ions in the interlayer might induce a greater degree of local disorder in the hydrotalcite-like phase compared with chloride ions. After the second filtration, Figure 5-5B, the basal peak reflections shifted slightly towards lower angle, while the peak shape stayed relatively unchanged. The shift in the basal peak reflection is attributed to either changes in the Mg/Al ratios (Table 5-3), or different combinations of interlayer species (Miyata, 1975, 1983). However, since the Mg/Al ratios in those samples were around 2.0 to 2.3, and the lattice parameters are rather insensitive to Mg/Al ratio in this range (Richardson, 2013a, b), it is expected that this is at most a secondary effect. Thus, the variation of interlayer species mainly defines the changes in crystal structures.

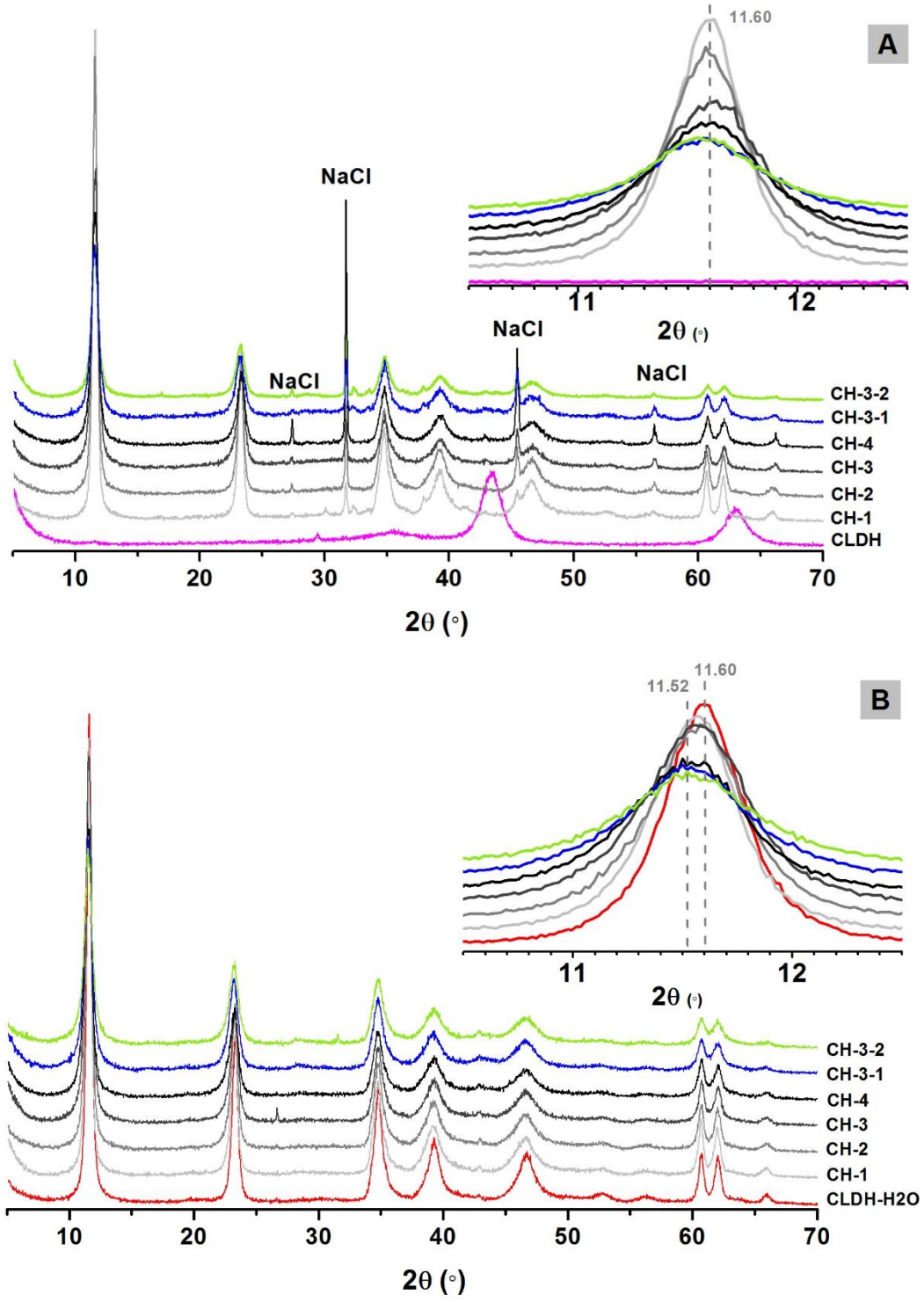

Figure 5-5 XRD patterns of recrystallised LDH in chloride-rich simulated pore solutions, (A) after the first filtration, with the pattern of the original CLDH; (B) after the second filtration, with the pattern of the CLDH recrystallised in distilled water (CLDH-H2O)

The solid phase obtained after the first filtration contains chloride chemically or electrostatically bound in the interlayer, as well as chloride adsorbed to the diffuse electrical double layer (EDL) through surface adsorption. For ions retained in the diffuse layer, the total ion uptake is proportional to the capacity of the EDL (C_{EDL}, Eq. 5-5), and closely related to the total ionic strength (I, Eq. 5-7) in the solution (via Debye length λ_D,, Eq. 5-6) (Butt et al., 2003, Trefalt et al., 2016).

$$C_{EDL} = \frac{\varepsilon\varepsilon_0}{\lambda_D} \qquad \text{Eq. 5-5}$$

$$\lambda_D = \sqrt{\frac{\varepsilon\varepsilon_0 kT}{2N_A e^2 I}} \qquad \text{Eq. 5-6}$$

$$I = \frac{1}{2}\sum_i C_i Z_i^2 \qquad \text{Eq. 5-7}$$

ε - dielectric constant (relative permittivity), C/V·m
ε_0 - permittivity of free space, C/V·m
k - Boltzmann's constant, J/K
T - temperature, K
N_A - Avogadro's number, mol^{-1}
e - elementary charge, C
C_i - concentration of the i^{th} ion, mol/L
Z_i - valence of the i^{th} ion

It was previously identified (Châtelet et al., 1996, Morimoto et al., 2012) that chloride ions tend to become sorbed in the diffuse layer at the external surface of hydrotalcite-like phases, pairing with Na^+. A higher chloride concentration coupled with a lower hydroxide concentration will increase the thickness of the diffuse layer (i.e. the Debye length) on the outer surface of the hydrotalcite-like phase, increasing the capacity of the electrical double layer (Eq. 5-5), and promoting the uptake of both sodium and chloride ions from the bulk solution (Trefalt et al., 2016). For the samples obtained after the first filtration, the Na^+-Cl^- ion pairs in the diffuse layers crystallise to form NaCl upon drying (Figure 5-5A). After the second filtration, the diffuse layer was diluted by the milli-Q water (ionic strength approaching 10^{-7} mol/L), so that the amount of chloride bound in the diffuse layer should become negligible. The remaining chloride identified in the solid phase by XRF (Table 5-3), should thus be considered to be interlayer species bound to the metal hydroxide layers.

In contrast to chloride ions, carbonate ions are linked to the metal hydroxyl layer of hydrotalcite-group minerals via H-bonding (Cavani et al., 1991, Constantino and Pinnavaia, 1995). Binding of carbonate ions neutralises the interlayer acid hydroxyl groups, lowers the charge density of the surface (and so reduces the thickness of the diffuse layer), and thus limits the chloride uptake (Morimoto et al., 2012, Trefalt et al., 2016). Hydroxide also bonds to the interlayer through H-bonding, and so there is direct competition between these ions; the relative bound concentrations will thus depend on the hydroxide concentration of the aqueous solution. A higher degree of carbonate ion-exchange in the interlayers leads to further reduction in surface charge density (Morimoto et al., 2012), and a reduced chloride uptake in the diffuse layer as a result. This is demonstrated by the low intensities of the reflections of NaCl crystals identified in Figure 5-5A, for the carbonate-containing sample CH-3-1and CH-3-2.

Thermogravimetric analysis of the solid CLDHs

Figure 5-6 shows the TG-MS data for the solid phase after second filtration. The weight loss between room temperature and 228°C is assigned to loss of chemically bound water (interlayer water molecules), and weight loss between 228 to 550°C is due to both dehydroxylation of metal hydroxyl layers, and decarbonation of carbonate ions bonded to the metal hydroxyl layers present in a hydrotalcite-like structure (Hibino et al., 1995, Zhang et al., 2016).

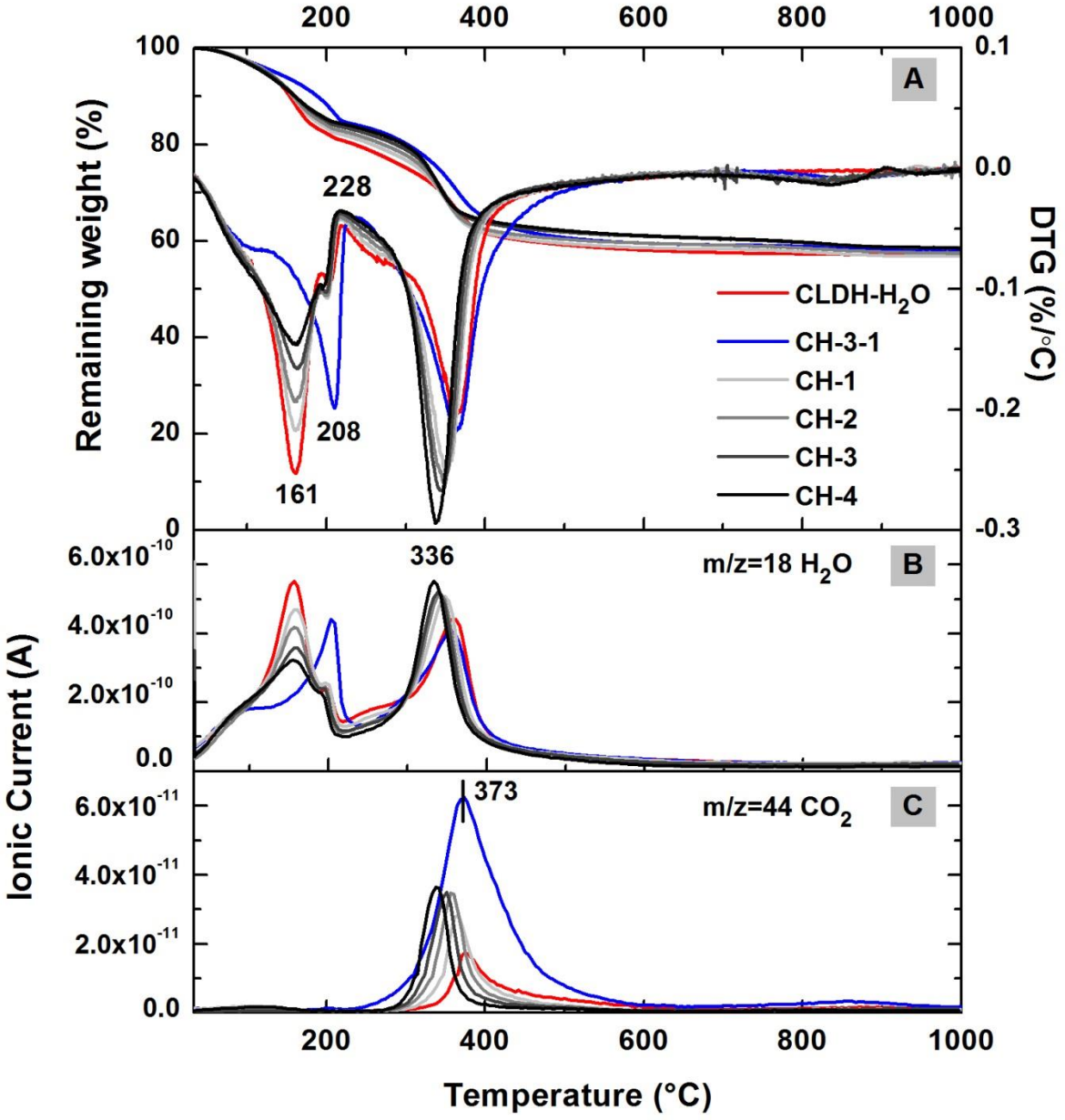

Figure 5-6 Thermogravimetry curves (A); and mass spectra of (B) H_2O (*m*/*z*=18), and (C) CO_2 (*m*/*z*=44), of recrystallised MgAl LDH immersed in various chloride rich simulated pore solutions, after the second filtration. Reference data for the thermally treated hydrotalcite (CLDH) immersed in milli-Q water (CLDH-H2O) are also reported

The loss of chemically bound water from recrystallised Mg-Al LDH is a multi-step process. In carbonate-free systems, two water loss peaks appear: an intense and sharp peak at centred at 161 °C, the sharpness of which decreases with increased chloride concentrations in the solution, followed by a small peak centred at 208 °C, the intensity of which stays relatively unchanged across the samples immersed in solutions with different chloride concentrations. In samples immersed in the carbonate-containing solution CH-3-1, only a small shoulder at around 161 °C is observed, along with a high intensity peak at 208 °C.

The interlayer water molecules are also bound to the LDH structure through H-bonding, although with a binding energy lower than those of carbonate and hydroxide ions. In the carbonate- and chloride-free sample (Figure 5-6; CLDH-H_2O), the only interlayer species are hydroxide and water, as well as traces of carbonates. The H-bonding environment surrounding the interlayer water molecules in this sample (CLDH-H_2O) is more ordered (Zhang et al., 2016); therefore, a sharp and strong water loss peak was identified at 161 °C. It is likely that an increased chloride concentration in the LDH interlayer induces an increase in the average H-bonding energy for water molecules, as the chloride ions add attraction to water molecules through H-bonding (Wang et al., 2003). With a higher content of interlayer carbonate, as in CH-3-1, the H-bonding network would be more complex, thus a higher temperature is required for the interlayer water to be removed (Zhang et al., 2016), as shown in Figure 5-5A. This is consistent with the XRD results (Figure 5-5), where broader basal reflections were identified in samples with more complex interlayer species.

In Figure 5-6C, a single CO_2 release peak was identified in all samples between 373 to 400 °C. In samples where carbonate ions were not added to the solution, the CO_2 release peak indicates some CO_2 contamination, probably caused during the sample separation or drying process. However, the amounts of carbonate which became incorporated in these samples without added carbonate samples were comparable across all samples.

Figure 5-7 shows the mass spectra of all the chlorine-containing gases released during the thermal analysis process. The identification of loss of chlorine during thermogravimetric analysis is complicated by its low content in the solid phase, as well as the presence of different Cl isotopes (Lv et al., 2006b). However, Figure 5-6 indicates that the weight loss contributed by release of chlorine from the solid phase takes place above 600 °C.

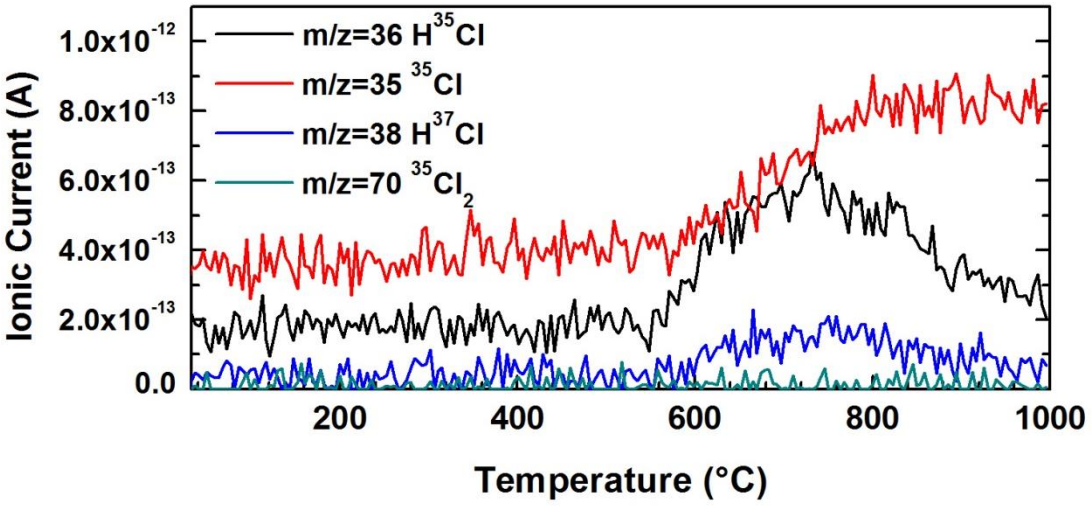

Figure 5-7 Mass spectra of all Cl-containing gases released during thermogravimetric analysis of sample CH-3 after the second filtration

Table 5-4 summarises the chemical formulae of the hydrotalcite-group solids obtained after the second filtration from each solution studied, showing the compositions of interlayer species (OH^-, Cl^-, and CO_3^{2-}), calculated based on the XRF results and TG-MS data. The determination of chemical formulae was carried out assuming that the loss of chemical bounded water took place only between room temperature and 228 °C, the loss of hydroxyl groups and interlayer carbonates between 228 °C and 550°C, and the loss of chlorine-containing gases above 600 °C.

Table 5-4 Chemical compositions of recrystallised Mg-Al LDH after the second filtration, after equilibration under different conditions

	General formulation: $Mg_xAl_y(OH)_a(Cl)_b(CO_3)_c \cdot nH_2O$ x+y=1	**$Q^*_{e\text{-}Cl}$ mg/g (CLDH)**	**$Q_e - Q^*_{e\text{-}Cl}$ mg/g (CLDH)**
CH-1	$Mg_{0.672}Al_{0.328}(OH)_{2.272}(Cl)_{0.004}(CO_3)_{0.026} \cdot 0.985H_2O$	3.3	25.4
CH-2	$Mg_{0.687}Al_{0.313}(OH)_{2.262}(Cl)_{0.011}(CO_3)_{0.020} \cdot 0.929H_2O$	9.0	149.6
CH-3	$Mg_{0.679}Al_{0.321}(OH)_{2.265}(Cl)_{0.014}(CO_3)_{0.021} \cdot 0.888H_2O$	11.4	237.6
CH-4	$Mg_{0.693}Al_{0.307}(OH)_{2.233}(Cl)_{0.031}(CO_3)_{0.022} \cdot 0.855H_2O$	25.3	236.2
CH-3-1	$Mg_{0.679}Al_{0.321}(OH)_{2.100}(Cl)_{0.010}(CO_3)_{0.105} \cdot 0.819H_2O$	8.2	115.9
CH-3-2	$Mg_{0.688}Al_{0.312}(OH)_{2.071}(Cl)_{0.007}(CO_3)_{0.117} \cdot 0.826H_2O$	5.7	41.7

* Q_e*-Cl values were calculated using the chemical formulas based on the mass of CLDH.

The reduction in interlayer hydroxyl groups with increased interlayer chloride and carbonate ions is consistent with the discussion in section 5.3.1.1 regarding the ion-exchange mechanism. In sample CH-4, where a maximum chloride uptake (from the bulk solution) of 262 mg/g was calculated, the interlayer chloride occupies only 10% of the available anion sites. Reduced interlayer chloride contents were identified in samples that were immersed in carbonated solutions (CH-3-1 and CH-3-2). The carbonate contamination in all non-carbonate added samples is almost constant, about 12% of the maximum carbonate uptake by the LDH. In samples with 0.1 mol/L carbonate ions added to the bulk solution, the interlayer carbonate ions reached about 73% of the maximum carbonate capacities.

The $Q^*_{e\text{-}Cl}$ values shown in Table 5-4 correspond to the weight percentage of interlayer chloride in the hydrotalcite-like phase, which are 5-10% of the Q_e values reported in Figure 5-2A. The amount of chloride taken up by the rehydrated CLDH via surface adsorption, corresponding to the final column in Table 5-4, is calculated by subtracting $Q^*_{e\text{-}Cl}$ calculated from the solid phase from Q_e calculated from the aqueous solutions. Chloride uptake by Mg-Al LDH phase via surface adsorption is influenced by the chemical binding capacity of the diffuse electrical double layer in each sample.

5.3.2.2. Strätlingite

X-ray diffraction analysis of the strätlingite

Figure 5-8 shows the XRD patterns of strätlingite after being immersed in chloride-rich solutions. Distinctive peaks assigned to crystallised NaCl were identified in the solid phase after the first filtration, where the Na^+ and Cl^- ions are still retained in the diffuse layer. Similar to the case identified for the hydrotalcite-like phase (Figure 5-5), the intensities of the NaCl reflections in Figure 5-8 decrease with a reduced initial $[Cl^-]/[OH^-]$ ratio. Minor traces of NaCl are identified in sample CH-1* (Figure 5-8A). As discussed above, the reduced $[Cl^-]/[OH^-]$ ratio (lower chloride concentration but higher NaOH content) results in a lower surface charge density and probably a thinner diffuse layer (Trefalt et al., 2016), reducing the amount of chloride retained in the diffuse layer upon filtration.

A chloride-bearing AFm phase (AFm-Cl), with a crystal structure resembling the Cl-substituted hydrocalumite-type phase Friedel's salt ($Ca_2Al(OH)_6Cl{\cdot}2H_2O$, PDF# 01-078-1219), was identified in samples immersed in the non-carbonated chloride rich solutions. Only part of the strätlingite converted to Friedel's salt though ion-exchange, as residual strätlingite reflections were identified along with the chloride-bearing AFm phase, and the correspondence between the XRD data here and the reference PDF pattern for a pure Friedel's salt is not exact. This indicates some degree of ionic substitution or disorder in this phase. Although the positively charged layers in strätlingite, $CaAl_2(OH)_6^+$, are the same as in all the other AFm phases (Okoronkwo and Glasser, 2016b, Rinaldi et al., 1990), the amount of ion-exchangeable hydroxyl sites bound to the mixed metal sheets in strätlingite is much more limited (Okoronkwo and Glasser, 2016b). Also, for full replacement of the complex interlayer aluminosilicate ion species, $[AlSi(O_8H_8){\cdot}0.25H_2O]^-$, a higher chloride concentration or ionic strength might be required.

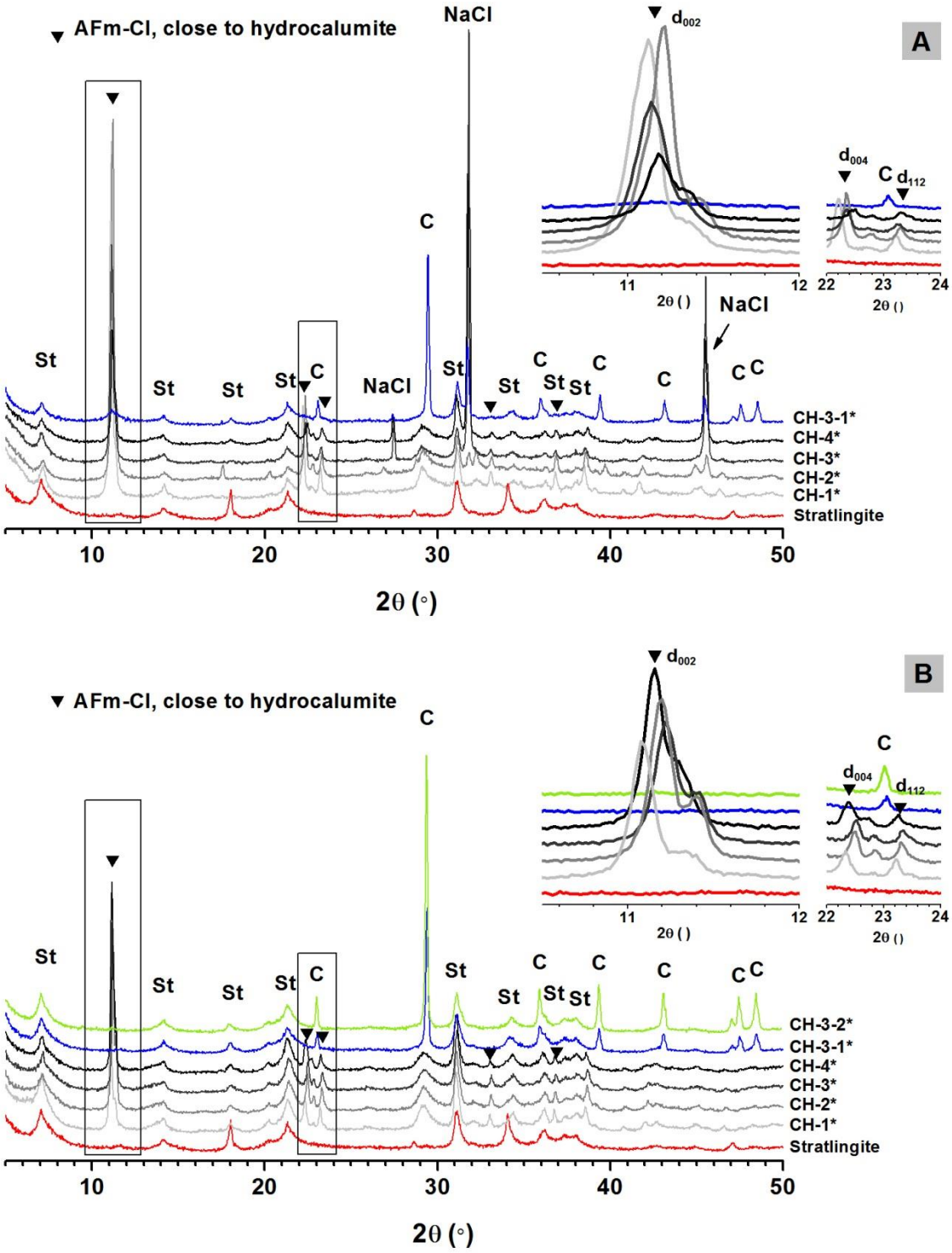

Figure 5-**8** XRD pattern of strätlingite after interaction with chloride rich simulated pore solutions, (A) after first filtration; (B) after second filtration. Insets in each case show expansions of the regions highlighted with rectangles

In the strätlingite immersed in the carbonate-free solutions, the chloride-bearing AFm phase formed has a $d_{(002)}$ spacing ranging from 7.88 Å to 7.98 Å (inset in Figure 5-8). The shift of the basal peak position in hydrocalumite-like AFm phases is correlated to the composition of the interlayer anions, as well as interlayer water (Balonis et al., 2010). However, the intensities of hydrocalumite basal peaks are not linearly related to the Cl content in the interlayers.

In samples immersed in carbonated solutions, calcite ($CaCO_3$, PDF# 00-005-0586) was identified as a reaction product. Chloride-bearing AFm phases were not observed in these specimens. This is probably associated with the decomposition of the hydrocalumite-like phase upon carbonation, as proposed by Anstice et al. (Anstice et al., 2005). However, the existence of a disordered ('X-ray amorphous') AFm(CO_3, Cl) solid solution is also plausible (Mesbah et al., 2011a). When keeping the chloride concentration and carbonate concentrations constant, but decreasing the OH^- concentration from 0.3 mol/L to 0.1 mol/L (i.e. moving from system CH3-1* to CH3-2*), the amount of calcite increased significantly, indicating that more extraction of the calcium from strätlingite to form calcite in the presence of dissolved carbonate will occur at lower OH^- concentrations, consistent with the data reported by Okoronkwo and Glasser (2016b).

Thermogravimetric analysis of the solid strätlingite

Figure 5-9 shows the TG-MS data obtained for solid AFm samples after the second filtration, in comparison with the synthetic strätlingite. For the synthetic strätlingite, the chemically bound interlayer water was lost at around 145 °C, and the structural hydroxyl groups were decomposed before 250 °C (Kwan et al., 1995, Okoronkwo and Glasser, 2016a). There are two small CO_2 release peaks observed in the CO_2 mass spectra (Figure 5-9C), centred at 400 °C and 800 °C, respectively. This is consistent with the decarbonation of minor interlayer carbonate ions in strätlingite, and/or decomposition of sodium carbonate (Kaufhold

et al., 2013). The formation of these carbonate-containing phases is attributed to CO_2 contamination during the sample preparation process. It has been reported (Okoronkwo and Glasser, 2016b) that strätlingite accommodates a small amount of carbonate ions as interlayer species without significant changes in its crystal structure. Combining the MS data for CO_2 (Figure 5-9C) with the TG data (Figure 5-9A), a total CO_2 contamination in the input strätlingite of less than 1.0 wt.% was calculated.

The mixture of strätlingite and hydrocalumite-like phases in the solid samples after the second filtration makes the interpretation of the thermogravimetric results challenging. No significant changes in samples immersed in chloride-rich solutions are observable from the TG-MS results, apart from minor shifts in the dehydroxylation peaks at around 202 °C and weight loss peaks at around 830 °C. For samples prepared in carbonate-free solutions, less intense dehydroxylation peaks were observed for samples with lower chloride content. In contrast to the trends identified for Mg-Al LDH (Figure 5-6), there is not a clear trend of changes in the dehydration/dehydroxylation peak intensity and/or width in chloride bearing strätlingite. This is possibly due to its more complex interlayer structure. The weight loss at around 830 °C seems to relate to the release of chlorine-containing gases, as the intensity of the weight loss peak rises with increased chloride content in the solids.

Quantification of the amount of chloride bounded to the strätlingite via lattice substitution is complicated, considering the intimate intermixture of strätlingite with the newly-formed Friedel's salt-like phase, after immersion in chloride-rich simulated pore solutions. However, in aiming to enable estimation of chloride binding capacity for known phase assemblages in alkali-activated binders, this study has provided very valuable information regarding estimation of chloride uptake by strätlingite, as shown in Figure 5-3. The amount of chloride taken up through surface adsorption would be more sensitive to changes in the aqueous environment, while the formation of the chloride-AFm solid solution is relatively more stable as the chloride bearing phase.

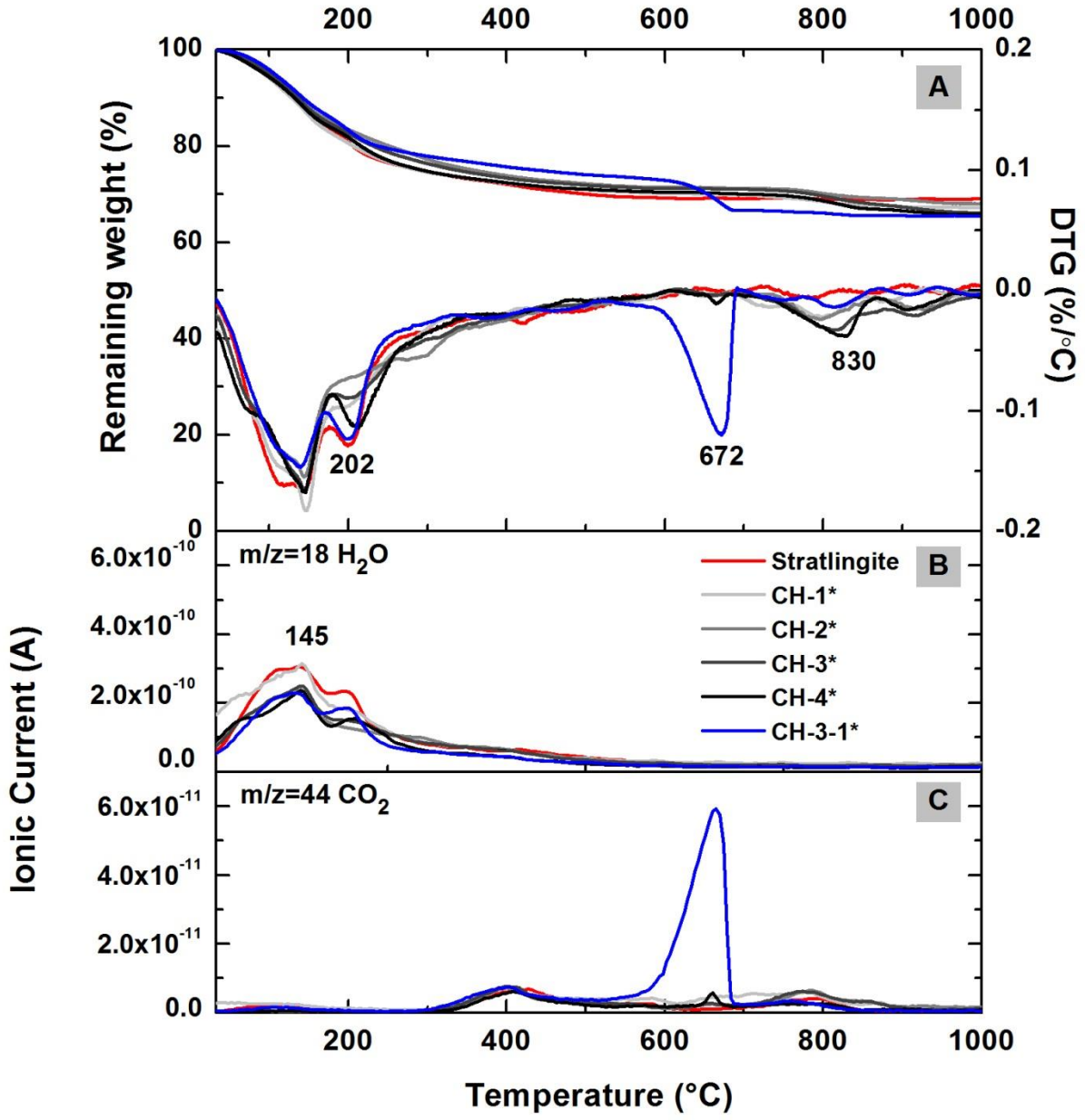

Figure 5-9 Thermogravimetry curves (A) and mass spectra of (B) H_2O (m/z=18), and (C) CO_2 (*m/z*=44), for strätlingite immersed in various chloride rich simulated pore solution, after the second filtration. Reference results for the synthesised strätlingite are also reported.

5.3.2.3. C-(N)-A-S-H

X-ray diffraction analysis of the C-(N)-A-S-H gels

Figure 5-10 shows the XRD patterns of C-(N)-A-S-H type gels with varying compositions after immersion in chloride-rich solutions. Similar to the results for LDH phases as described above, crystallised NaCl was identified in the solid phase after the first filtration, as a result of the retention of Na^+ and Cl^- ions in the diffuse layer. Reduced intensities of the NaCl reflections were seen in samples exposed to solutions at lower initial $[Cl^-]/[OH^-]$ ratio. As discussed above, the reduced $[Cl^-]/[OH^-]$ ratio (lower chloride concentration but higher NaOH content) results in a lower surface charge density and probably a thinner diffuse layer (Trefalt et al., 2016), reducing the amount of chloride retained in the diffuse layer upon filtration.

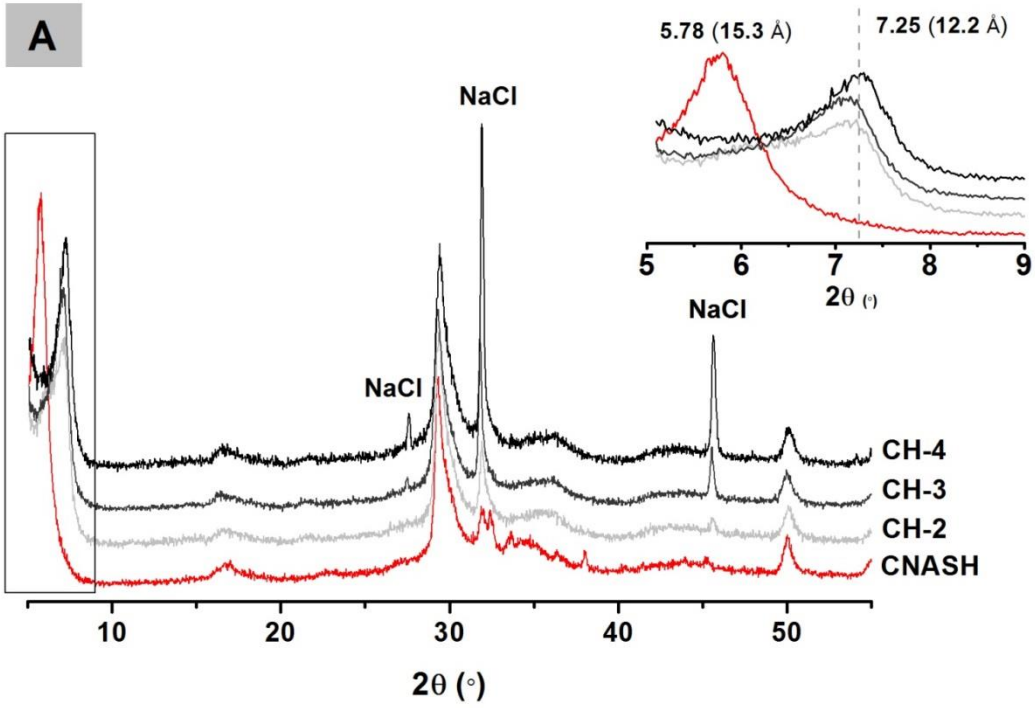

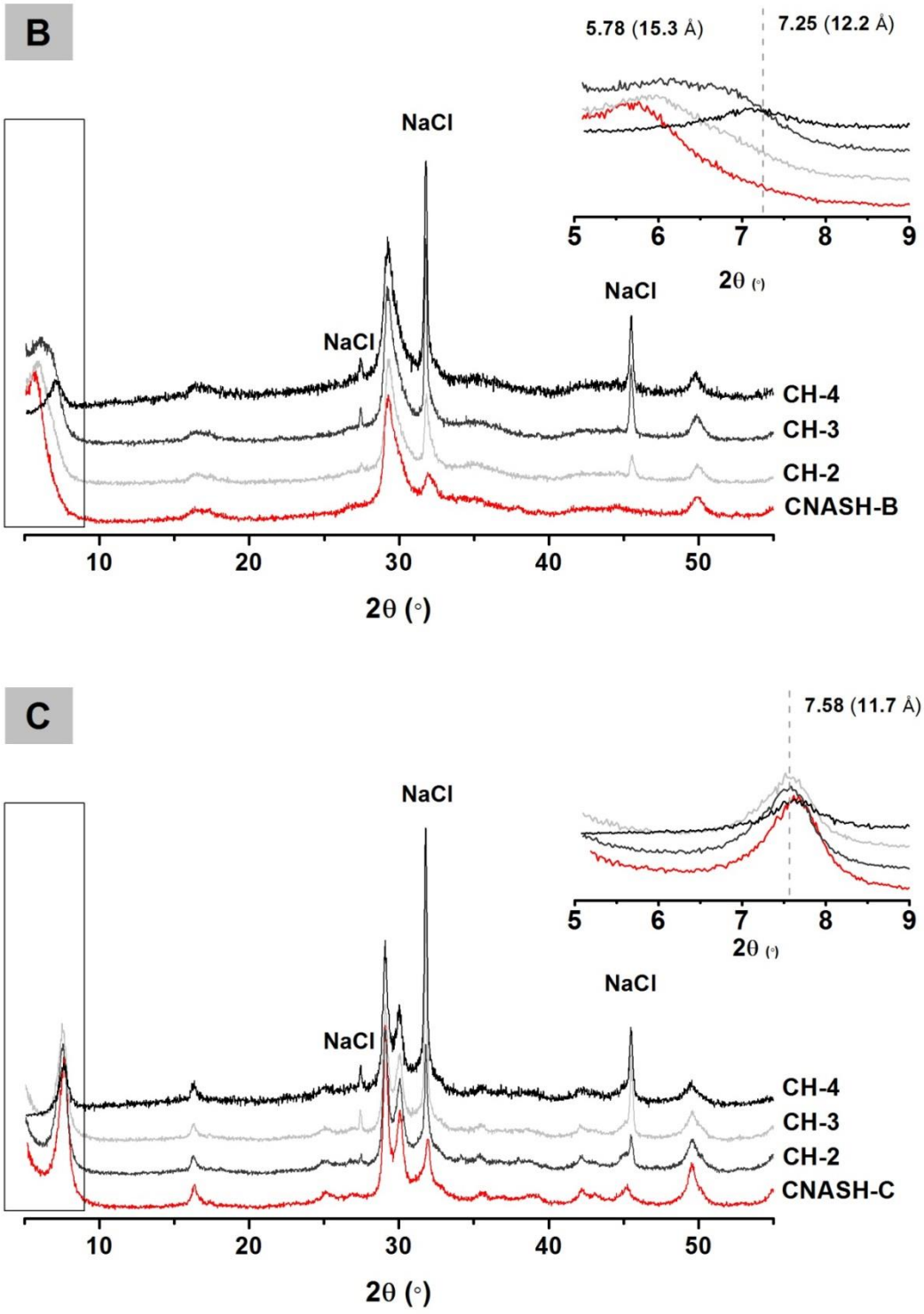

Figure 5-10 XRD patterns of C-(N)-A-S-H type gels after interaction with chloride-rich simulated pore solutions, (A) Ca/Si=1, Al/Si=0, (B) Ca/Si=1, Al/Si=0.1, (C) Ca/Si =1.4, Al/Si=0.1. In each case, the inset shows the basal peak observed at low angle, with the peak positions marked in terms of degrees 2θ, as well as a conversion to Å to present *d*-spacing values via Bragg's law.

It is worthwhile to note that the d_{002} peak of C-(N)-A-S-H type gels 'A' and 'B' shifted to higher diffraction angles (shorter *d*-spacings) after interacting with sodium chloride, while the d_{002} peak in C-(N)-A-S-H type gel 'C' stayed unchanged even after binding of chloride. The d_{002} peak at higher diffraction angel correlates to lower basal spacing. The results shown here are contrary to the outcomes of studies using pH-neutral NaCl solution as chloride source (Yoon et al., 2014a). The presence of excess Na^+ and the high alkalinity in the aqueous phase might be responsible for the differences, however further analysis is needed before coming to a definitive conclusion.

5.4. Implications of chloride interactions with cementitious phases in alkali-activated slag cements

Figure 5-11 illustrates the different factors which contribute to controlling the rate of the transport of chloride permeability of in alkali-activated slag materials. In the first instance, the phase assemblage of these materials and the chloride binding capacity of each of the individual phases forming will play a key role in the mitigation of chloride penetration.

The pH value of the pore solution in alkali-activated slag cement is expected to change during exposure to a near-neutral external chloride source, such as sea water or de-icing salt solutions, due to alkali leaching from the pore network. The $[Cl^-]/[OH^-]$ ratios will also be influenced by this characteristic, and this may in fact give both buffering and additional binding capacity for chloride, as the hydroxide bound in the LDH phases formed during the hydration of the binder can be released and replaced by incoming chloride.

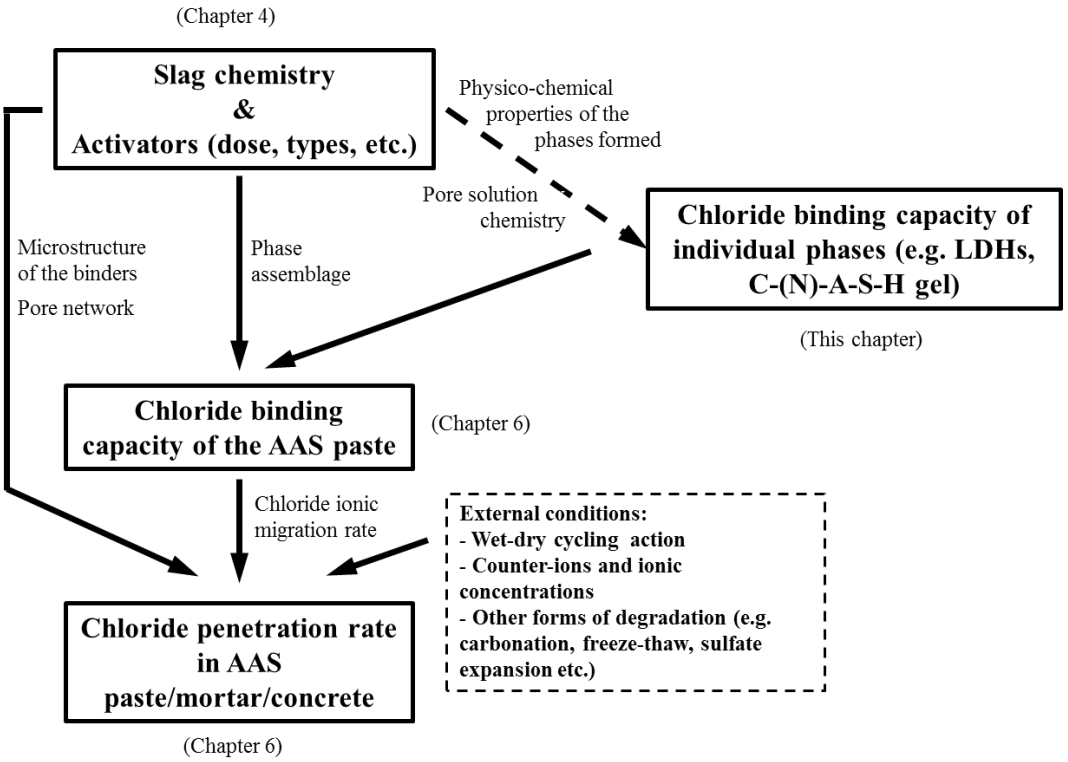

Figure 5-11 Illustration of some of the factors which control chloride transport in AAS

The results presented in this Chapter show that the binding capacities of LDHs and C-(N)-A-S-H type gels change as a function of the $[Cl^-]/[OH^-]$ ratios, implying that the chloride binding capacities of these phases will differ at different depths of chloride penetration into a hardened monolithic specimen. The $[Cl^-]/[OH^-]$ ratio in the pore solution is likely to increase over time, resulting in high chloride uptake, until the LDHs and the C-(N)-A-S-H type gels reach their maximum chloride uptake capacity. This process is expected to significantly retard the ingress of chloride, and is a key factor underlying the observed slow movement of chloride through alkali-activated concretes compared to Portland cement concretes of comparable total pore volume (Ismail et al., 2013, Ma et al., 2015, Shi, 1996). From Figure 5-2A and Figure 5-3A, it can be estimated that the maximum chloride uptake capacities of the hydrotalcite-like phase and strätlingite are about 250 mg/g and 200 mg/g, respectively, even at $[Cl^-]/[OH^-]$ ratios higher than 3. The maximum chloride uptake of C-(N)-A-S-H gel varies with its chemical composition, and could potentially reach much higher values (compared

with the maximum uptake shown in Figure 5-4) when the $[Cl^-]/[OH^-]$ ratio in the solution is higher.

Hydrotalcite-group minerals are well known as effective chloride binding phases, contributing to the low chloride penetration rate of cementitious materials containing slag as a main binder material (Baroghel-Bouny et al., 2012, Kayali et al., 2012). This study has illustrated that, in chloride-rich simulated alkali-activated slag pore solutions, most of the chlorides are taken up by hydrotalcite-like phases through surface adsorption in the diffuse layer rather than through direct ion-exchange. However, since the mobility of chloride in the diffuse layer is much slower than that in the bulk solution, a high contribution from surface adsorption may effectively slow down the ingress of free chloride in the cement matrix (Friedmann et al., 2008, He et al., 2016). Similarly, the binding of chloride in the AFm phases which can form within alkali-activated slag binders also offers significant scope for restriction of chloride movement.

5.5. Conclusions

This chapter reports for the first time the chloride binding capacities, under high alkalinity conditions, of the hydrotalcite-like (Mg-Al), strätlingite (AFm) layered double hydroxides, and C-(N)-A-S-H type gels, which are identified as reaction products in many Portland blended cements and alkali-activated slag cements. It has been demonstrated that this hydrotalcite-like phase and strätlingite can effectively take up chloride from highly alkaline solutions with different initial $[Cl^-]/[OH^-]$ ratios. For a hydrotalcite-like phase, surface adsorption is the main binding mechanism, responsible for around 90% of the total chloride uptake, with around 10% contribution from ion exchange. For strätlingite, surface adsorption of chlorides is less dominant, and lattice substitution of chloride also takes place. The overall chloride binding capacities of C-(N)-A-S-H gels are much lower than that of LDHs.

The presence of carbonates in the pore solution, along with a decrease in the alkalinity of the system, significantly decreases the chloride uptake by both LDH minerals assessed. Carbonate in hydrotalcite-like phases will occupy the chloride-exchangeable interlayer hydroxyl sites and reduce surface adsorption, while in strätlingite it can participate in ion exchange, but also (when the aqueous environment is poor in aluminium) leads to partial decomposition of the AFm phase, inducing the precipitation of calcite instead.

The modification in the chloride binding capacities of hydrotalcite-like phase, strätlingite, and C-(N)-A-S-H type gels with different chemical composition as a function of $[Cl^-]/[OH^-]$ ratio, should be taken into consideration when building up a detailed model for prediction of chloride penetration profiles, as different chloride binding capacities will need to be applied when considering the changes in the pore fluid composition depending on depth from the surface of the sample. In the following chapter, the chloride binding capacities of AAS pastes with different phase assemblages are tested and analysed according to the results discussed above, which then provides valuable perspective for understanding the chloride transport in the sodium carbonate-activated slag mortars.

Chapter 6.

CHLORIDE BINDING AND MOBILITY IN SODIUM CARBONATE-ACTIVATED SLAG PASTES AND MORTARS

6.1. Introduction

The interactions of chloride with cementitious materials are governed by physico-chemical phenomena associated with its transport property into the hardened solid cement or concrete through its pore network, and its ability to chemically bind to the hydrated phases present in the matrix. There are two main aspects to be taken into account when studying the chloride binding capacities of alkali-activated slag cement: the chemistry of the aqueous environment studied (e.g. pH, ionic concentration), and the phase assemblage of the cementitious matrix (Dhir et al., 1996, Florea and Brouwers, 2014, Yuan et al., 2009). The aqueous environment under which the chloride binding capacity is determined has to be comparable to that of the pore solution chemistry present in hardened samples, so that the results are sufficiently representative. Nonetheless, chloride binding capacities of cementitious materials are normally measured in neutral chloride solutions (Dhir et al., 1996, Thomas et al., 2012). This, in theory, might lead to overestimation of the chloride binding capacity, as a very high initial $[Cl^-]/[OH^-]$ ratio will favour the binding of chlorides in the solid phases, either through ion-exchange or surface adsorption (Trefalt et al., 2016). The use of chloride and alkalis-rich simulated pore solution mitigates this preferential effect.

The phase assemblages of AAS binders are mainly controlled by the chemistry of the slags and activators used (Provis and Bernal, 2014, Winnefeld et al., 2015). Slags activated using

either sodium carbonate or sodium silicate could potentially have different chloride binding capacities, due to the differences in phase assemblage between these two AAS binders (Bernal et al., 2014b). Chapters 4 and 5 discussed the role of CLDH in controlling the kinetics of reaction, and the chloride binding capacities of different layered double hydroxide (LDH) type phases typically identified in alkali-activated slag paste. Although LDHs can chemically bind chlorides, their potential role in the mechanical and durability performance of alkali-activated slag cement is yet to be investigated and understood.

The properties of AAS binders, including mechanical and durability aspects of AAS binders are strongly dependent on the chemical and physical properties of slag, the type and dose of activators, as well as the water to binder ratio (Fernández-Jiménez et al., 1999, Shi, 1996, Wang et al., 1994). Among these factors, the type of activator used seems to be the most important factor when using slags with the same chemical composition (Fernández-Jiménez et al., 1999, Shi, 1996). When a given slag is activated with a similar alkali dose and cured under the same conditions, but different activators, the properties change. Samples activated with sodium silicate normally develop the highest compressive strength compared with using sodium hydroxide or sodium carbonate activators (Fernández-Jiménez et al., 1999, Shi, 1996). This is mostly attributed to the development of a dense and homogeneous microstructure in sodium silicate activated slag cements/mortars (Brough and Atkinson, 2002, Fernández-Jiménez et al., 1999).

As discussed in the preceding chapters, the durability performance of AAS binders is closely correlated to the microstructural features of the binder, as well as the chemical reactions taking place between the reaction products present in the binder and the different chemical species present in the service environment (Collins and Sanjayan, 2000, Cui and Cahyadi, 2001, Halamickova et al., 1995, Schlegel et al., 2015, Shi, 1996). The overall porosity and pore size distribution, as well as the interconnectivity of pores, are important factors controlling the transport property of potentially damaging chemical species (e.g.

chloride, sulphate or CO_2) within cementitious materials (Cui and Cahyadi, 2001, Halamickova et al., 1995).

The chloride transport in a cementitious binder is often evaluated by measuring its diffusion and/or migration coefficients. The NordTest method NT BUILD 492 measures the chloride migration coefficient in hardened concrete specimens using a non-steady-state experiment, showing the resistance of the tested material to chloride penetration (NordTest Method, 1999, Tang and Sørensen, 2001). It has also been proven to be a rapid and precise method to determine the chloride diffusion coefficient in cementitious materials (Tang and Sørensen, 2001).

In this chapter, chemical binding capacities of AAS binders were determined using two chloride-rich solution systems: a neutral NaCl salt solution, and simulated chloride-rich pore solutions. Sodium carbonate-activated slag pastes with 0 wt.% and 5 wt.% CLDH addition were studied. A sodium metasilicate-activated slag paste was also produced and tested under the same condition, as a reference sample for comparison of the performance of the sodium carbonate activated slag cements. Chloride binding isotherms of all samples in these two solution systems were calculated. The changes in phase assemblage after exposure to chloride-rich simulated pore solutions have been characterised using XRD and SEM-EDX.

Mortar specimens with equivalent compositions to the Na_2CO_3 and Na_2SiO_3-activated slag pastes as previously described were prepared, and tested according to NT Build 492 as a function of curing time and mix design. Compressive strengths of mortars at different curing durations, and pore size distributions of selected samples according to MIP, were also determined; and together with the chloride binding isotherms determined using paste samples, which indicate the amount of chloride ions retained in the paste section, the migration coefficients measured from accelerated test methods were assessed.

6.2. Experimental method

6.2.1. Alkali-activated slag pastes

The paste samples studied in this Chapter were prepared according to the procedures described in Chapter 3, section 3.2.2. After 28 days of curing, slag pastes produced with sodium carbonate activators without CLDH (i.e. P-NC-0) and with CLDH addition (i.e. P-NC-1), or sodium metasilicate activator without CLDH addition (i.e. P-NS-0), were crushed with a hammer in sealed plastic bags, and sieved using sieves of 0.25 mm and 0.6 mm aperture size, to obtain particulate samples with particle sizes ranging from 0.25 mm to 0.6mm.

Immediately after crushing, the sieved paste powders were added to chloride-rich solutions to prepare suspensions with a solid/liquid mass ratio of 1/7 (2 g solid/14 g liquid) in 15 mL centrifuge tubes. Two groups of chloride-rich solutions were prepared using Milli-Q water, according to Table 6-1 and Table 6-2. The centrifuge tubes containing suspension samples were sealed with Parafilm, and stored at 23±2 °C for 2 months to allow them to reach reaction equilibrium. To achieve homogeneous reaction in all particles, the centrifuge tubes were rotated in a roller mixer for 1 hour once per week.

Table 6-1 Chemical compositions and pH values of the neutral chloride-rich solutions studied in this chapter

	pH	$[OH^-]$ (mol/L)	$[Cl^-]$ (mol/L)	$[Cl^-]/[OH^-]$
N-1	6.80	1.0×10^{-7}	0.001	1.2×10^{4}
N-2	6.80	1.0×10^{-7}	0.516	5.2×10^{6}
N-3	6.80	1.0×10^{-7}	1.085	1.1×10^{7}
N-4	6.80	1.0×10^{-7}	2.797	2.8×10^{7}

Table 6-2 Chemical compositions and pH values of the chloride-rich simulated pore solutions studied in this chapter

	pH	$[OH^-]$ (mol/L)	$[Cl^-]$ (mol/L)	$[Cl^-]/[OH^-]$
CH-1	13.98	0.953	0.099	0.1
CH-2	13.87	0.740	0.242	0.3
CH-3	13.70	0.500	0.497	1.0
CH-4	13.42	0.262	0.759	2.9

After two months, all the samples were separated using a centrifuge (Heraeus Biofuge Primo, at 4000 rpm for 6 min). The supernatants were collected for calculation of chloride binding capacity. The chloride concentrations and pH of the supernatant were measured using chloride ion-selective electrode (Cole-Parmer Epoxy solid-state chloride electrode, accuracy ± 2%) and pH meter (Oakton Acorn Series).

The remaining solids separated from chloride-rich simulated pore solutions were washed using Milli-Q water according to the recommendations of RILEM TC 178-TMC (2002), and then dried in a desiccator with relative humidity controlled (30±3%) by saturated $CaCl_2$ salt prior to further analysis, the same procedure as described in Chapter 5 for samples after the 2nd filtration. The dried solids were separated into two parts, one part was embedded in epoxy resin and polished for SEM-EDX analysis; the other part was powdered and analysed via XRD and TG-MS. All the solid samples exposed to chloride-rich simulated pore solutions were analysed through XRD, and only samples exposed to the solution CH-3 were analysed by TG-MS and SEM-EDX, as a representative condition for comparison between the three binders studied.

6.2.2. Alkali-activated slag mortars

The monoliths studied in this chapter were prepared according to the procedure described in Chapter 3, section 3.2.3, and their mix designs are presented in Table 3-5 of that Chapter.

Three types of mortars were prepared, namely sodium carbonate-activated mortars without CLDH (i.e. M-NC-0) and with CLDH addition (i.e. M-NC-1), and sodium metasilicate-activated mortars without CLDH addition (i.e. M-NS-0). All samples were cured in tightly sealed plastic bags for up to 180 days.

Mercury intrusion porosity (MIP) was measured according to the test methods recommended by Ma (2014). Samples were sectioned from cubic specimens using a slow saw, with dimensions of no less than 5 mm each side. About 3 g of mortar samples were used in each measurement to get representative results. The sectioned mortar samples were immersed in isopropanol for 24 hours, followed by vacuum drying for 3 days for complete removal of pore water. The MIP tests were then conducted using a Micromeritics Autopore 9600 Mercury Porosimeter, with an intrusion angle of 130° and an extrusion angle of 104° for each measurement.

Compressive strength was determined using an automatic compressive strength testing machine Controls Automax5, with a loading speed of 0.25 MPa/s. Mortar cubes with dimensions of 50×50×50 mm were used for testing compressive strength. Triplicate samples were measured per formulation per curing age.

Non-steady state chloride migration coefficients of mortars were determined following the NordTest method, NT BUILD 492 (NordTest Method, 1999). Mortar cylinder discs (Ø100 × 50 mm) were used, and duplicate samples were prepared per formulation per curing age. Prior to the accelerated chloride migration test, each of the cylinder discs was immersed in 1.0 M NaOH solutions under vacuum to obtain pore water-saturated samples; the immersion fluid was selected with a comparable composition to those predicted for the cements assessed by thermodynamic modelling (Myers et al., 2015b). At the end of the test, the disc sample was split, and immediately sprayed with 0.1 M silver nitrate ($AgNO_3$) to obtain the chloride

ingress profile (He et al., 2012). After spraying with $AgNO_3$ agent, the samples were left in a cupboard (to avoid direct light exposure) for 15 minutes to allow a full reaction between $AgNO_3$ agent and free chloride, as suggested in the NordTest method, NT BUILD 492 (NordTest Method, 1999). Directly after 15 minutes, the chloride ingress profile was marked down using a marker pen.

The non-steady-state migration was coefficient calculated from (NordTest Method, 1999), the symbols used in Eq. 6-1 to Eq. 6-3 are in SI base units:

$$D_{nssm} = \frac{RT}{zFE} \cdot \frac{x_d - \alpha\sqrt{x_d}}{t_s} \quad \text{Eq. 6-1}$$

$$E = \frac{U - 2}{L} \quad \text{Eq. 6-2}$$

$$\alpha = 2\sqrt{\frac{RT}{zFE}} \cdot erf^{-1}\left(1 - \frac{2C_d}{C_0}\right) \quad \text{Eq. 6-3}$$

D_{nssm}: non-steady-state migration coefficient, m^2/s;

z: absolute value of ion valence; for chloride, $z = 1$

F: Faraday constant, $F = 9.648 \times 10^4$ J/(V·mol);

U: absolute value of the applied voltage, V;

R: gas constant, $R = 8.314$ J/(K·mol);

T: average value of the initial and final temperatures in the anolyte solution, K;

L: thickness of the specimen, m;

x_d: value of the penetration depths, m;

t_s: test duration, seconds;

erf^{-1}: inverse of error function;

C_d: chloride concentration at which the colour changes, $C_d \approx 0.16$ N for alkali-activated mortars (Yuan et al., 2008);

C_0: chloride concentration in the catholyte solution, $C_0 \approx 2$ N.

The highest and lowest chloride penetration depths were recorded for each sample tested, measured using a calliper from the marked down chloride profile as described previously, representing the worst and best case scenarios respectively. Figure 6-1 shows an example of

the data recorded using the colorimetry methods. Since $\text{erf}^{-1}(1 - \frac{2\times0.16}{2}) = 0.84$, Eq. 6-1 can be simplified, and the highest and lowest possible chloride migration coefficients were calculated as Eq. 6-4 and Eq. 6-5, where symbols have been converted to units that could be directly measured during the experiments .

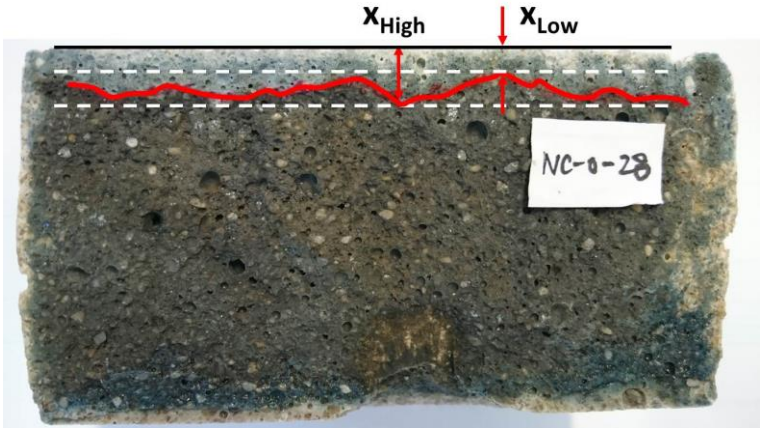

Figure 6-1 Illustration mortar sprayed with silver nitrate showing the highest and lowest chloride penetration depths for a sodium carbonate activated slag mortar with 28d of curing

$$D_L = \frac{0.0239(273+T)L}{(U-2)t}\left(x_{Low} - 0.0186\sqrt{\frac{(273+T)Lx_{Low}}{U-2}}\right) \quad \text{Eq. 6-4}$$

$$D_H = \frac{0.0239(273+T)L}{(U-2)t}\left(x_{High} - 0.0186\sqrt{\frac{(273+T)Lx_{High}}{U-2}}\right) \quad \text{Eq. 6-5}$$

D_L: lowest possible non-steady-state migration coefficient, $\times10^{-12}$ m^2/s;

D_H: highest possible non-steady-state migration coefficient, $\times10^{-12}$ m^2/s;

U: absolute value of the applied voltage, V;

T: average value of the initial and final temperatures in the anolyte solution, °C;

L: thickness of the specimen, mm

x_{Low}: lowest value of the penetration depths, mm;

$x_{High:}$ highest value of the penetration depths, mm

t: test duration, hours

6.3. Results and discussion

6.3.1. Chloride binding capacity of alkali-activated slag pastes

For the specimens assessed, the pH and chloride concentration in the supernatant at equilibrium were measured, and so the hydroxyl concentration and $[Cl^-]/[OH^-]$ ratios in the supernatant were calculated. The chloride binding capacity (Q_e) of the slag pastes under various aqueous environments was calculated using Eq. 5-2 (Chapter 5). The results for neutral NaCl systems and simulated pore solutions are shown in Table 6-3 and Table 6-4. The corresponding binding isotherms are presented in Figure 6-2.

Table 6-3 pH, $C_e(OH^-)$, $C_e(Cl^-)$, and $[Cl^-]/[OH^-]$ in supernatant solutions at equilibrium, and Q_e calculated using Eq. 5-2(Chapter 5), when using neutral NaCl solutions

P-NC-0-28d

	pH	$[OH^-]$ (mol/L)	$[Cl^-]$ (mol/L)	$[Cl^-]/[OH^-]$	Q_e (mg/g)
N-1	12.52	0.0331	0	0	0
N-2	12.25	0.0178	0.454	25.5	15.5
N-3	12.06	0.0115	0.984	85.7	24.8
N-4	11.84	0.0069	2.593	375	50.3

P-NC-1-28d

	pH	$[OH^-]$ (mol/L)	$[Cl^-]$ (mol/L)	$[Cl^-]/[OH^-]$	Q_e (mg/g)
N-1	12.72	0.0525	0	0	0
N-2	12.42	0.0263	0.453	17.2	15.6
N-3	12.24	0.0174	0.971	55.9	28.2
N-4	11.95	0.0089	2.572	289	55.7

P-NS-0-28d

	pH	$[OH^-]$ (mol/L)	$[Cl^-]$ (mol/L)	$[Cl^-]/[OH^-]$	Q_e (mg/g)
N-1	12.69	0.0490	0	0	0
N-2	12.36	0.0229	0.467	20.4	12.4
N-3	12.20	0.0158	0.993	62.7	22.6
N-4	11.96	0.0091	2.671	293	40.2

Table 6-4 pH, $C_e(OH^-)$, $C_e(Cl^-)$, and $[Cl^-]/[OH^-]$ in supernatant solutions at equilibrium, and Q_e calculated using Eq. 5-2 (Chapter 5), when using simulated chloride-rich pore solutions

P-NC-0-28d

	pH	$[OH^-]$ (mol/L)	$[Cl^-]$ (mol/L)	$[Cl^-]/[OH^-]$	Q_e (mg/g)
CH-1	14.20	1.581	0.095	0.060	1.1
CH-2	14.14	1.377	0.226	0.164	4.1
CH-3	13.99	0.975	0.468	0.480	7.3
CH-4	13.75	0.561	0.693	1.235	16.6

P-NC-1-28d

	pH	$[OH^-]$ (mol/L)	$[Cl^-]$ (mol/L)	$[Cl^-]/[OH^-]$	Q_e (mg/g)
CH-1	14.25	1.774	0.097	0.055	0.6
CH-2	14.03	1.069	0.206	0.192	9.0
CH-3	14.00	0.998	0.417	0.418	19.7
CH-4	13.83	0.674	0.607	0.901	37.6

P-NS-0-28d

	pH	$[OH^-]$ (mol/L)	$[Cl^-]$ (mol/L)	$[Cl^-]/[OH^-]$	Q_e (mg/g)
CH-1	14.30	1.990	0.090	0.045	2.2
CH-2	14.13	1.346	0.221	0.164	5.3
CH-3	14.06	1.145	0.433	0.378	15.9
CH-4	13.72	0.5246	0.654	1.249	26.2

Figure 6-2A shows the chloride binding capacity of the pastes studied in neutral solutions up to 3.0 mol/L NaCl. A higher initial chloride concentration increased the total bound chloride. The sodium carbonate activated samples (P-NC-0) consistently showed higher chloride binding capacity compared with sodium silicate activated samples (P-NS-0) under the same exposure conditions. The addition of 5 wt.% CLDH in sodium carbonate activated slag pastes improves the chloride binding capacity of these cements. This is more notable as the chloride concentration increases, especially above 0.5 mol/L NaCl. At the highest concentration studied (3.0 mol/L NaCl), the chloride binding capacity of the CLDH modified sodium carbonate slag pastes is up to 11% higher than that determined for the same sample without CLDH addition (P-NC-0).

Figure 6-2B shows the chloride binding capacities of the slag pastes studied in the simulated chloride-rich pore solutions, as a function of the $[Cl^-]/[OH^-]$ ratio in the solution. Conversely to the observations when using neutral NaCl solutions (Figure 6-2A), the chloride binding capacity of sodium carbonate activated slag paste is much lower than that of sodium silicate activated slag paste. It seems that a highly alkaline aqueous environment (higher than pH 13) does not favour the binding of chlorides in the sodium carbonate activated slag paste, most likely due to the competition between hydroxyl ions and chlorides for potential binding sites. However, the alkaline environment seems to favour chloride binding in CLDH modified sodium carbonate-activated paste. Similar to the results shown in Figure 6-2A, the chloride binding capacity of sample P-NC-1 is higher than both sample P-NC-0 and P-NS-0. The differences in chloride binding capacity between samples P-NC-0 to P-NC-1 are much higher than those shown in Figure 6-2A.

For the three activated slag pastes studied here, the $[Cl^-]/[OH^-]$ ratios remaining in the alkaline solutions after chloride binding decrease (Table 6-4), as a combined effect of the reduction in Cl^- concentration and the increase in the pH. The differences in the $[Cl^-]/[OH^-]$ ratio between the supernatant solutions of the three alkali-activated slag pastes are small, even though different chloride binding capacities were observed.

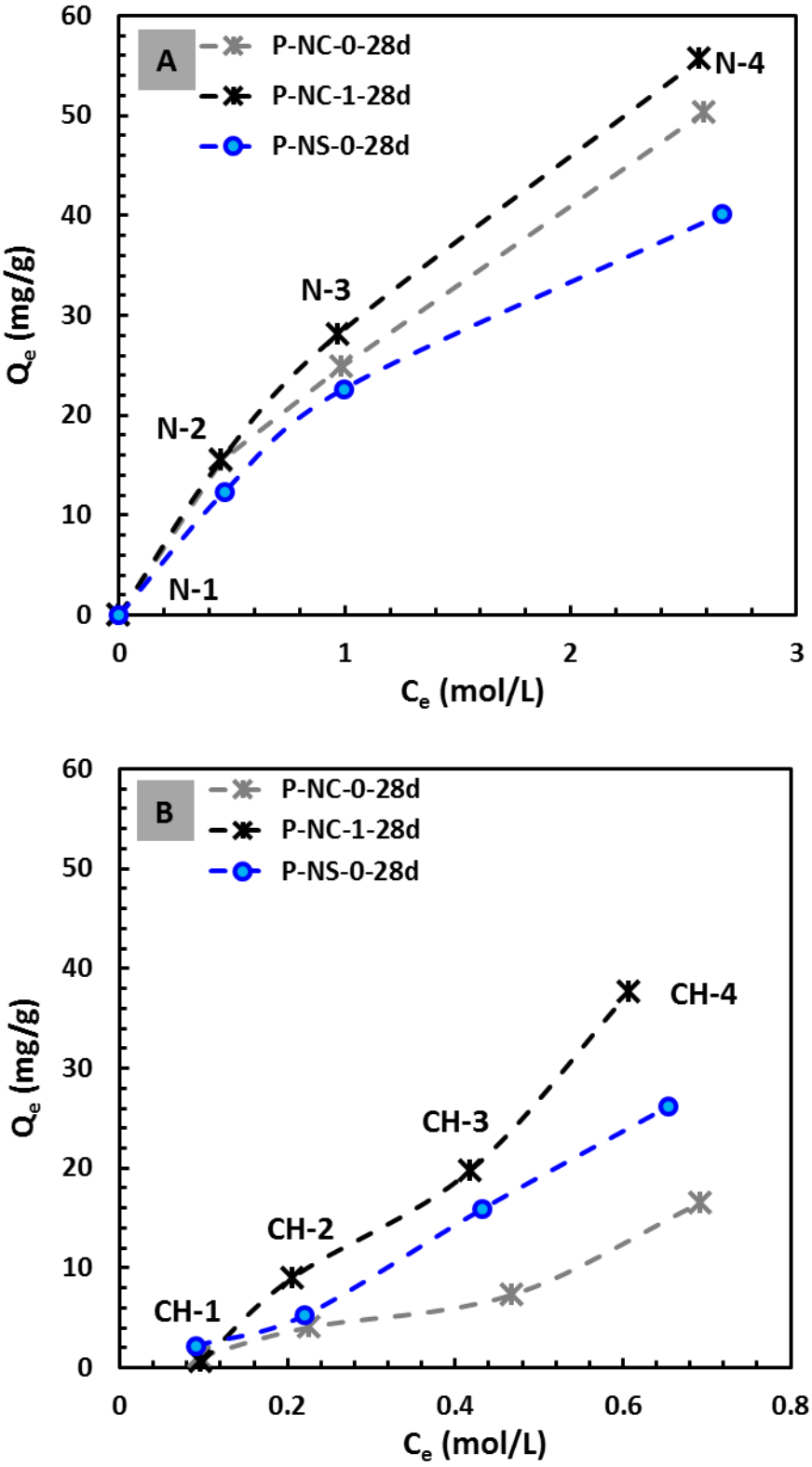

Figure 6-2 Chloride binding capacities of 28-day cured alkali-activated slag pastes determined in (A) neutral NaCl solutions or (B) in chloride-rich simulated pore solutions.

As discussed in Chapter 4, the incorporation of CLDH in sodium carbonate-activated slag cements increases the content of hydrotalcite-like phase in the binder. Although the content of AFm phases would decrease, the overall content of LDHs (hydrotalcite-like phase + AFm phases) in the AAS binder will still be higher compared with AAS paste without CLDH modification (Chapter 4). Also, a higher degree of reaction has been observed in CLDH modified sodium carbonate-activated slag paste, suggesting that there will be a higher portion of reaction products available for binding chlorides (Chapter 4). Both hydrotalcite-like phases and (hemi-)carbonate AFm are effective chloride binding phases, as discussed in Chapter 5 and in (Mesbah et al., 2011a). The main reaction product C-(N)-A-S-H gel, can also bind chlorides, but with a much lower binding capacity compared with LDHs. The increased chloride binding capacity in CLDH modified AAS pastes is most likely attributed to the higher overall LDH contents.

Figure 6-3 shows the comparison between experimental and theoretical prediction of chloride binding isotherms as a function of initial chloride concentrations, using sample P-NS-0 as an example. The theoretical predictions were calculated using binding isotherms of individual reaction products presented in Chapter 5, and the phase assemblage in sample P-NS-0 was quantified using the thermodynamic modelling given in (Myers et al., 2015b). The theoretical chloride binding capacity shown here is about 3 to 6 times higher than that measured experimentally. The lower crystallinity of individual reaction phases presented in AAS paste, in comparison with the synthetic phases studied in Chapter 5, could be responsible for the lower experimental value shown in Figure 6-3. However, for better understanding of the changes in the mineralogy of AAS binders after exposed to external chlorides, it is essential to study the solid samples after exposure to chloride-rich simulated pore solutions.

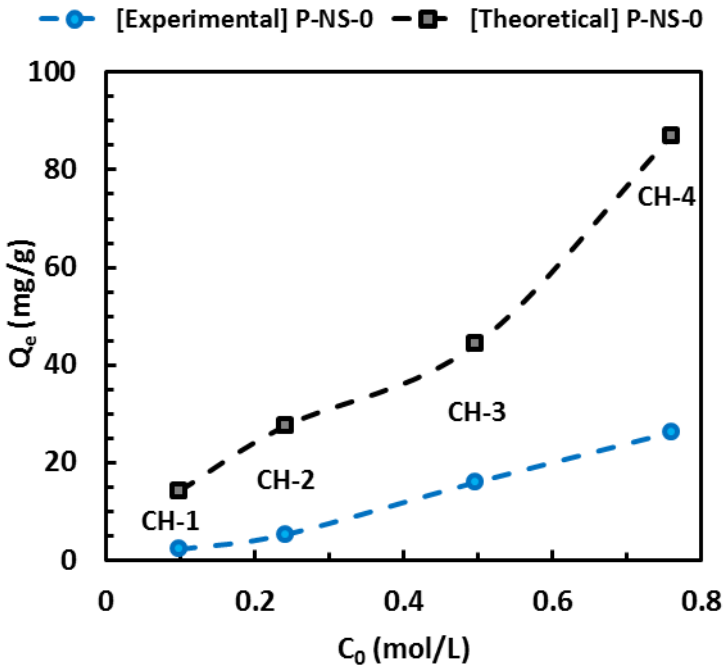

Figure 6-3 Comparison of chloride binding isotherms of sample P-NS-0, between experimental data and theoretical prediction using binding isotherms presented in Chapter 5. The phase assemblage in sample P-NS-0 was quantified using thermodynamic modelling given in (Myers et al., 2015b), according to the chemical composition shown in Table 3-1 (Chapter 3). The phase densities used for calculation were: pore solution 1.04 g/cm^3, C-(N)-A-S-H gel 2.6 g/cm^3, hydrotalcite-like phase 2.02 g/cm^3, strätlingite 1.79 g/cm^3, anhydrous slag 2.8 g/cm^3 (Matschei et al., 2007b, Myers et al., 2015b, Richardson, 2013a).

6.3.2. Mineralogy of alkali-activated slag pastes after exposure to chloride-rich simulated pore solutions

6.3.2.1. X-ray diffraction (XRD)

Figure 6-4 shows the XRD patterns in selected angle ranges to highlight the changes in LDH phases with chloride uptake. In both sodium carbonate-activated samples, with or without CLDH addition, the intensity of the main reflection peak assigned to monocarbonate decreases as the chloride binding increases. Two polymorphs of Friedel's salt are observed in these specimens, ^{R}AFm-(CO_3^{2-},Cl^-) which is close to the rhombohedral hydrocalumite

($Ca_2Al(OH)_6Cl•2H_2O$, PDF# 00-035-0105), and ^{M}AFm-(CO_3^{2-},Cl^-) which is close to the monoclinic hydrocalumite ($Ca_2Al(OH)_6Cl•2H_2O$, PDF# 00-019-0202), but has a lower basal peak position (Mesbah et al., 2011c). The hydrocalumite-type phases formed in sodium carbonate activated samples were transformed from monocarboaluminate to Friedel's salt type phases, most likely by replacement of some of the interlayer CO_3^{2-} ions with Cl^- ions, as has been proposed by Mesbah et al. (Mesbah et al., 2011a, 2011c). The transformation between these two polymorphs of Friedel's salt is described in the literature to be mainly temperature controlled, and between ^{R}AFm-(CO_3^{2-}, Cl^-) and ^{M}AFm-(CO_3^{2-}, Cl^-), the formation of the rhombohedral structure is preferred at higher temperature (above 35° C) (Andersen et al., 2002, Mesbah et al., 2011a, Renaudin et al., 1999). The differences in interlayer species might affect the transition temperature, however there has not been any evidence directly correlating the transition between the two polymorphs with changes in interlayer chloride content.

The main reflection peak of a CO_2-containing hydrotalcite-like phase with basal spacing 7.67 Å is shown in Figure 6-4, as a guideline for identifying hydrotalcite-like phases. In sodium carbonate activated slag pastes (P-NC-0) the interlayer species in the hydrotalcite-like phase can be a mixture of Cl^-, OH^- and CO_3^{2-}, considering the chemical composition of the aqueous phase at equilibrium before separation. The intensities of reflections assigned to AFm-(CO_3, Cl) are much higher in samples without CLDH (Figure 6-4B) compared to those in CLDH-added specimens (Figure 6-4A). This most likely relates to the fact that less AFm phase was formed in sodium carbonate-activated slag pastes with added CLDH (P-NC-1), as observed in Chapter 4, reducing the amount of monocarbonate available to chemically bind chlorides. This emphasises the role of CLDH in increasing the chloride binding capacity of alkali-activated slag cements, as its inclusion modifies the phase assemblage of these cements, impacting how chloride binding occurs in these systems.

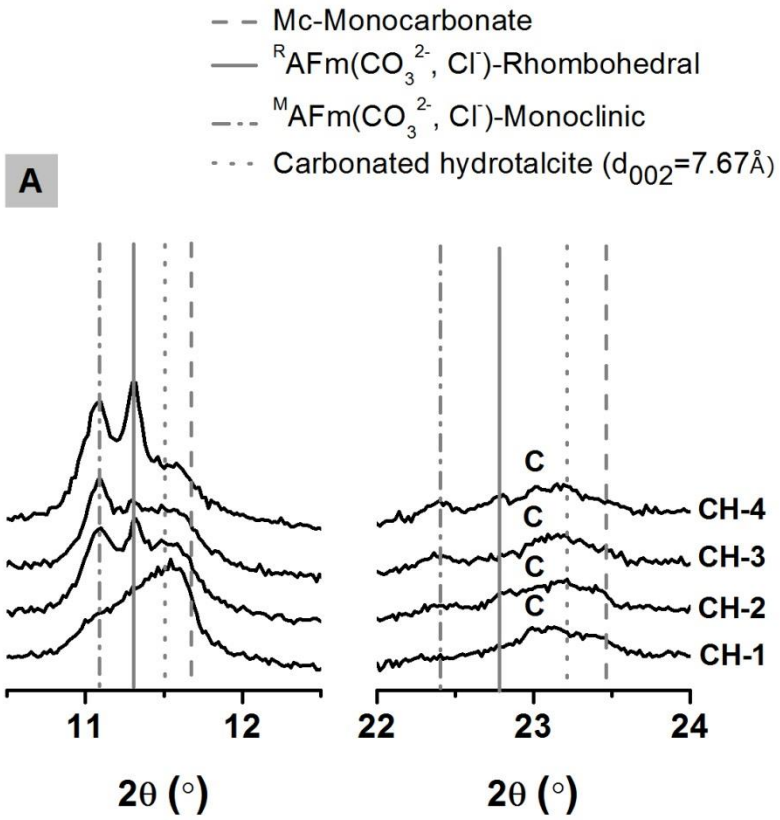
Mc-Monocarbonate
RAFm(CO3 2-, Cl-)-Rhombohedral
MAFm(CO3 2-, Cl-)-Monoclinic
Carbonated hydrotalcite (d002=7.67Å)
A
C
C
C
C
CH-4
CH-3
CH-2
CH-1
11
12
22
23
24
2θ (°)
2θ (°)

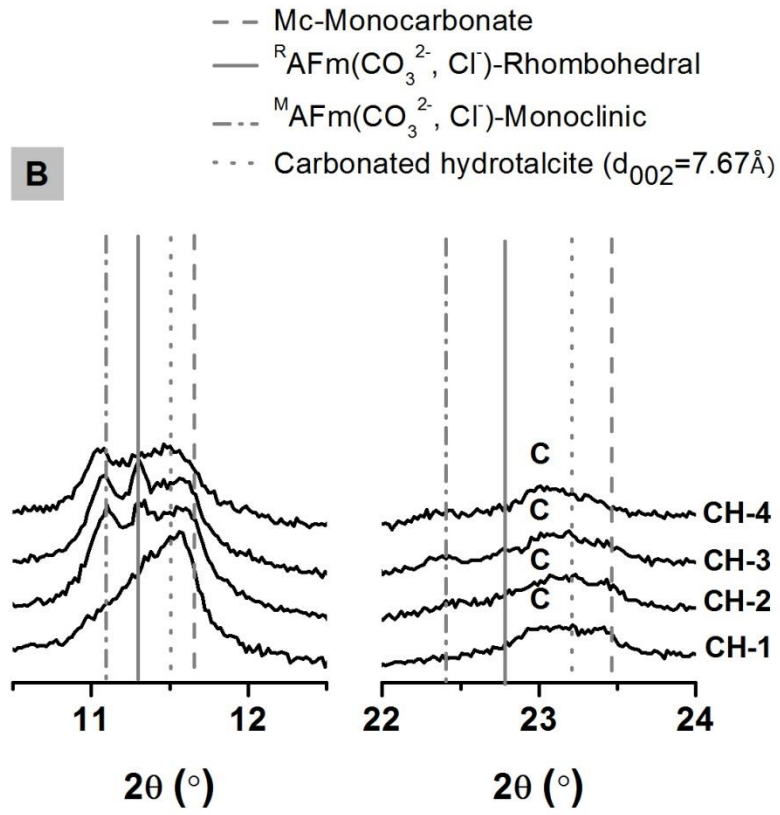
Mc-Monocarbonate
RAFm(CO3 2-, Cl-)-Rhombohedral
MAFm(CO3 2-, Cl-)-Monoclinic
Carbonated hydrotalcite (d002=7.67Å)
B
C
C
C
C
CH-4
CH-3
CH-2
CH-1
11
12
22
23
24
2θ (°)
2θ (°)

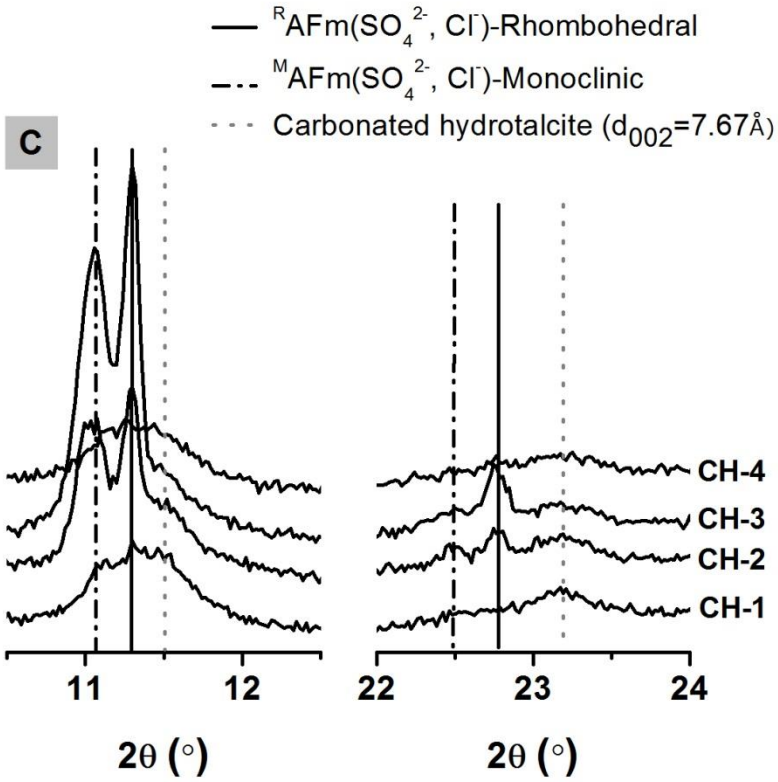

Figure 6-4 XRD patterns of 28-day cured sodium carbonate activated slag pastes (A) without CLDH (P-NC-0), and (B) with CLDH (P-NC-1) addition; and (C) sodium metasilicate activated slag paste without CLDH (P-NS-0), at chloride binding equilibrium in different simulated pore solutions. C-Calcite (PDF# 00-005-0586)

In sodium silicate activated samples (P-NS-0), the poorly crystalline AFm phase (strätlingite-like) transformed into a Friedel's salt-like phase after exposure to a chloride-rich solution. Two polymorphs of chloro-carboaluminate phases were again identified after chloride binding in this specimen. The intensities of basal peaks assigned to both phases increase as the external $[Cl^-]/[OH^-]$ ratio rises. This is associated with an increased formation of chloride bearing AFm type phases, although in specimens exposed to solutions with the higher $[Cl^-]/[OH^-]$ ratio (CH-4), peaks corresponding to chloride bearing AFm phases were not clearly identified. As discussed in Chapter 5, any Friedel's salt-like phases formed through the uptake of chlorides by strätlingite will decompose even in alkaline solution (pH around 13.6) in the presence of carbonate ions. It is possible that according to such a

mechanism, a Friedel's salt-like phase was originally formed in this paste, but decomposed during sample processing, since sample P-NS-0 in solution CH-4 has the lowest pH at equilibrium (Table 6-4).

6.3.2.2. Thermogravimetric analysis–mass spectrometry (TG–MS)

As shown in Figure 6-5A, the main mass loss peaks centred at around 70 °C (below 200 °C) are observed in all three samples. These peaks are associated with the loss of loosely bound water and some of the chemically bonded water in reaction products, mostly likely related to the loss of water of the C-(N)-A-S-H type gel (Ben Haha et al., 2011, Bernal et al., 2013, L'Hôpital et al., 2015). The small shoulder observed at around 138 °C in sample P-NC-1 is attributed to the dehydration of a hydrotalcite-like phase (Chapter 5). The mass loss at around 315 °C is assigned to the decomposition of structural hydroxyl ions and interlayer carbonate ions during present in the hydrotalcite-like phase (Hibino et al., 1995, Zhang et al., 2016), correlating with the high intensity peaks identified in the mass spectra of water and carbon dioxide shown in Figure 6-5B and Figure 6-5C, respectively. The positions of these two mass loss peaks for the chloride-bearing hydrotalcite-like phase present in AAS paste are observed at a slightly lower temperature compared with the results from a pure hydrotalcite-like phase, as shown in Chapter 5. More intense mass loss peaks were observed in sample P-NC-1 compared with the other paste samples, due to a higher hydrotalcite-like phase content in this paste, as a result of incorporation of CLDH (Chapter 4).

The small hump at around 450 °C and the sharp mass loss peak at 600 °C are related to the decarbonation of monocarbonate and calcite (Mesbah et al., 2011c, Wieczorek-ciurowa et al., 1980), which have been observed in sodium carbonate-activated samples only (Chapter 4). The relative mass losses due to these two phases suggest that sample P-NC-0 contains a slightly higher amount of monocarbonate phase and a relatively similar amount of calcite,

consistent with the results reported in Chapter 4. The mass loss peak at around 800 °C observed in all three samples is likely associated with loss of chloride-bearing gases, similar to that observed in chloride-bearing LDH phases (Chapter 5).

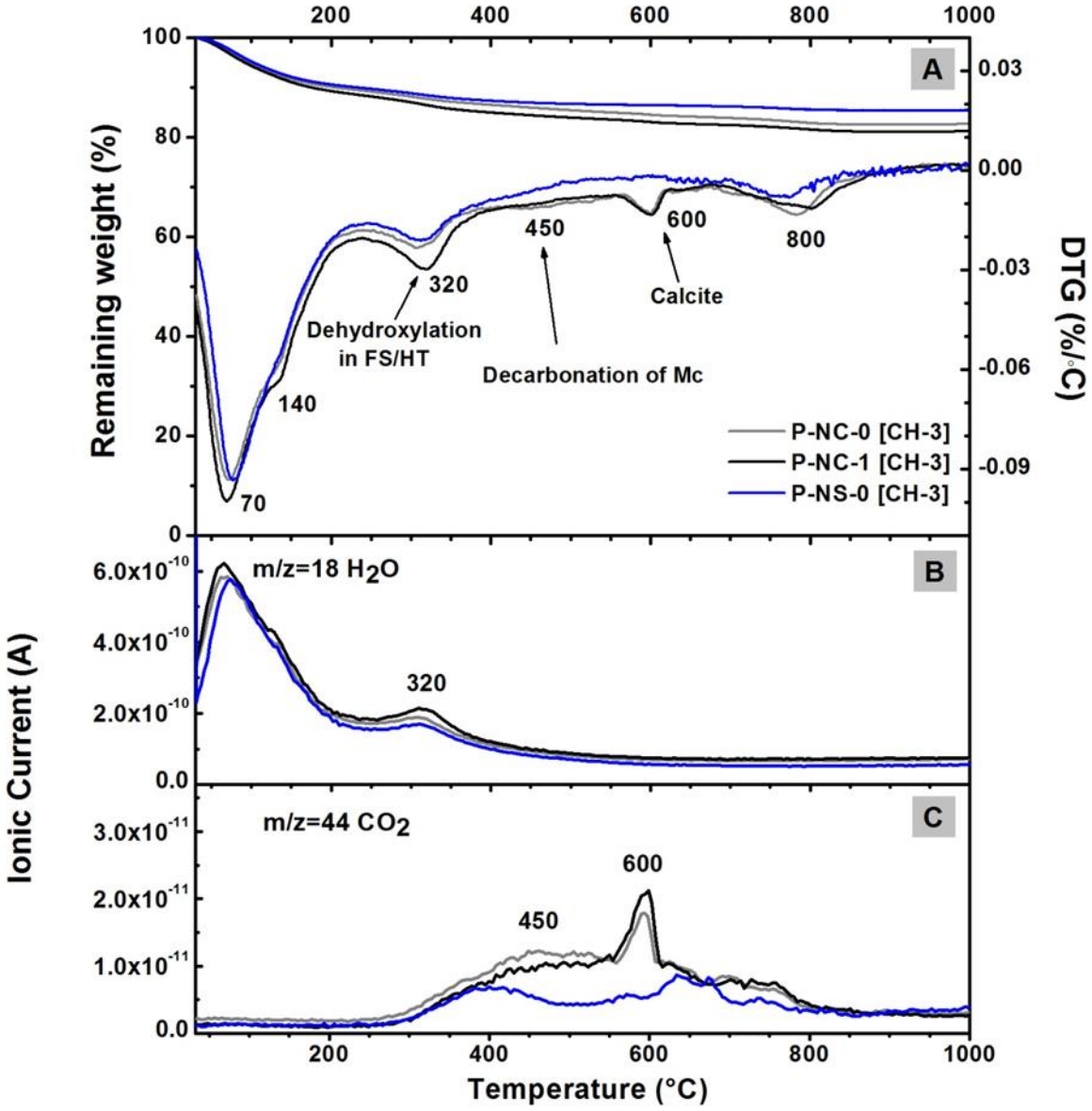

Figure 6-5 Thermogravimetric analysis results of three paste samples after exposure to solution CH-3: (A) TG and DTG; mass spectra of escaped gases (B) H_2O (m/z = 18) and (C) CO_2 (m/z = 44).

6.3.2.3. Scanning electron microscopy (SEM-EDX)

Figure 6-6 shows the atomic ratios calculated from EDX data for alkali-activated slag pastes embedded in epoxy resin, after exposure to the chloride-rich solution CH-3. More than 60 data points were randomly (however a minimum distance to unreacted slag grain of 2 μm was kept) taken from each sample, following the method specified in section 3.3.4. (Chapter 3). The dashed lines in Figure 6-6A and Figure 6-6B showing the ratios Ca/Al=2 and Mg/Al=2 are included to visualise the composition regions where AFm and/or hydrotalcite-like phases have been reported (Matschei et al., 2007a). The dashed lines of different Cl/Al ratios in Figure 6-6C were given as a guideline for evaluating the Cl content of the reaction products. The maximum Cl/Al ratio possible in an AFm phase is around 1.0, Friedel's salt (Birnin-Yauri and Glasser, 1998), while the highest Cl/Al ratio in a hydrotalcite-like phase measured in simulated pore solutions was around 0.1, as calculated in Chapter 5. The results discussed in this section do not directly link to the binding isotherms shown in section 6.3.1., simply because the SEM sample processing procedures have excluded the adsorbed chlorides at the sample surface. However, the results discussed in this section would contribute to understanding of the distribution of chlorides among different reaction phases.

The EDX plots for chloride-bearing sodium carbonate-activated samples, shown in Figure 6-6A and Figure 6-6B, are generally similar to those of sodium carbonate activated samples without exposure to chlorides (as discussed in Chapter 4). The data points in Figure 6-6A with Al/Si ratios higher than 0.8 and Ca/Si ratios around Ca/Al=2 suggest the formation of crystallised AFm phases in both of the sodium carbonate activated slag pastes, with and without inclusion of CLDH (P-NC-0 and P-NC-1). Between these two samples, the Mg/Si atomic ratio in sample P-NC-1 is higher than that in P-NC-0 (Figure 6-6B), consistent with the addition of CLDH in this paste. These results also indicate the existence of intermixed hydrotalcite-like phase with crystallised AFm phases in sample P-NC-1 (Chapter 4). However, the Cl/Al ratios in data points collected from regions mainly consisting of hydrotalcite-like and AFm (Al/Si>0.8) phases seem to be similar between sample P-NC-0-

28d and P-NC-1 (Figure 6-6C). It seems that the bulk Cl/Al ratios in the Friedel's salt-like AFm-(CO_3^{2-},Cl^-) phase and chloride-bearing hydrotalcite-like phase are similar, at around Cl/Al=0.3.

The crystallised AFm type phase was not observed in sample P-NS-0 after exposure to solution CH-3, even though a Friedel's salt-like phase was identified though XRD (Figure 6-4). This could possibly be explained by the fact that the AFm phase in sodium silicate-activated slag paste is intimately intermixed with C-(N)-A-S-H gel (Bernal et al., 2013, Wang and Scrivener, 1995), and therefore it is not distinguishable by SEM-EDX.

The inset plots in Figure 6-6 show data points with Al/Si ratios between 0.1 and 0.8, representing data collected from locations where the C-(N)-A-S-H type gel is the dominant phase, most likely from the outer product with intermixed hydrotalcite-like phase and AFm phase as well (Bernal et al., 2014c, Famy et al., 2002, San Nicolas et al., 2014). From the inset plot in Figure 6-6A, the Ca/Si ratios in sodium carbonate-activated samples with and without CLDH addition are similar to each other, and slightly higher than in sodium silicate activated slag paste, in accordance with the observations in Chapter 4. Negligible differences between these three samples were observed from the inset plot in Figure 6-6B. Comparing with sample P-NC-0, the overall Al/Si ratio is lower in sample P-NS-0 and higher in sample P-NC-1, due to an additional supply of Si from the activator (sodium silicate) and Al from the smart addition CLDH respectively. In the Figure 6-6C inset plot, the Cl/Al ratio is higher in sample P-NS-0, mostly attributed to the intermixed Friedel's salt-like phase, as observed from XRD patterns (Figure 6-4C). It seems that sample P-NC-0 has a higher Cl/Al ratio than P-NC-1, however, this could be attributed to a higher Al content in P-NC-1 (due to addition of CLDH) rather than higher Cl content in P-NC-0. According to the results discussed in Chapter 5, the differences in Ca/Si ratio and Al/Si ratios of C-(N)-A-S-H type gels would lead to different chloride binding capacities. However, because of the intermixing with the LDH phases, it would be difficult to distinguish the contribution of C-(N)-A-S-H type phases in chloride binding from the EDX plots.

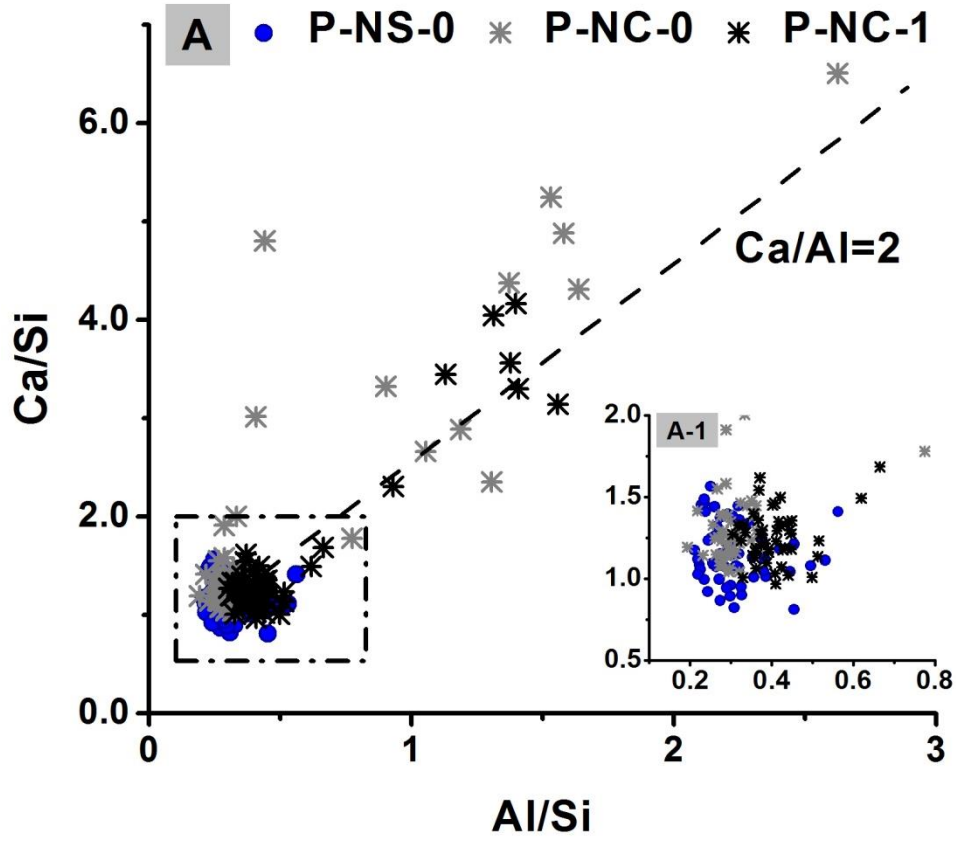
A
P-NS-0
P-NC-0
P-NC-1
Ca/Al=2
A-1
Ca/Si
Al/Si
0.0
2.0
4.0
6.0
0
1
2
3
0.5
1.0
1.5
0.2
0.4
0.6
0.8

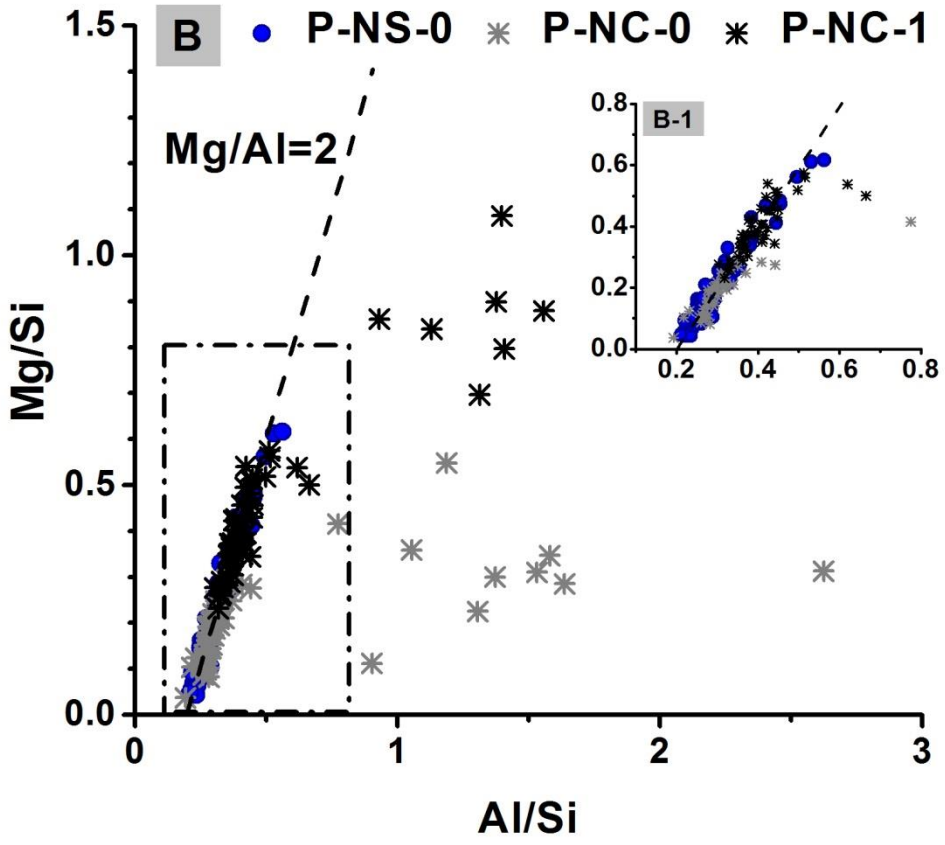
B
P-NS-0
P-NC-0
P-NC-1
Mg/Al=2
B-1
Mg/Si
Al/Si
0.0
0.5
1.0
1.5
0
1
2
3
0.2
0.4
0.6
0.8

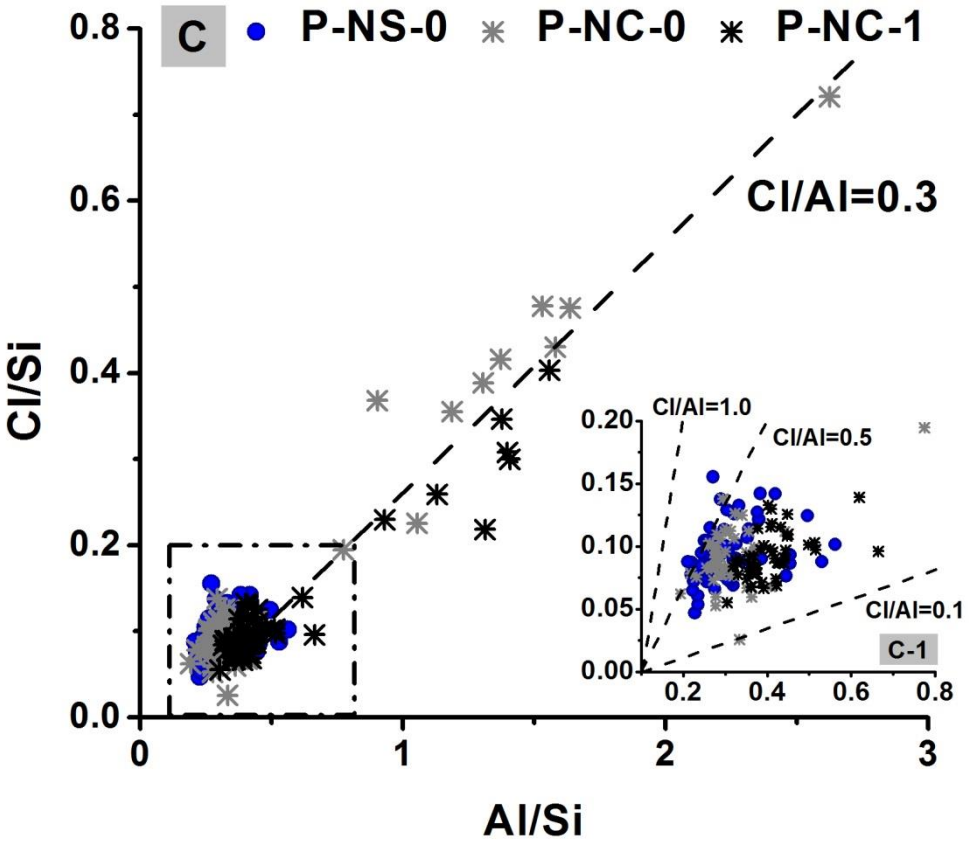

Figure 6-6 Atomic ratios calculated from EDX data for 28-day cured alkali-activated slag pastes after exposure to solution CH-3 (A) and (A-1) plotted as Ca/Si vs Al/Si, (B) and (B-1) plotted as Mg/Si vs Al/Si, (C) and (C-1) plotted as Cl/Si vs Al/Si.

6.3.3. Factors controlling mobility of chlorides in alkali-activated slag mortars

6.3.3.1. Pore structure (MIP)

For cementitious materials, mercury porosimetry can effectively measure pores that are directly connected to the sample surface, or through large pores (Cook and Hover, 1999). Small pores with narrow openings, like the ink-bottle effect, and enclosed/isolated pores are not detectable by this technique (Moro and Böhni, 2002). In mortar sample, the overlapped transition zones between the aggregate and paste contain higher porosity and/or larger connected pores, also referred as percolating porosity (Winslow et al., 1994). However in

both paste and mortar samples, the overall intrudable porosity measured using MIP could reflect the pore entry size, directly related to the water permeability and thus, ionic transport properties in cementitious materials (Aït-Mokhtar et al., 2002, Gallé, 2001, Halamickova et al., 1995).

Figure 6-7 shows the pore structures of mortar samples after 180 days of curing as measured by MIP. Sample M-NC-0-180d has the highest overall intrudable porosity, while sample M-NS-0-180d has the lowest overall intrudable porosity. The CLDH modified sample, M-NC-1-180d, showed much lower overall intrudable porosity than the unmodified sample M-NC-0-180d, and only slightly higher than that of the sodium silicate-activated mortar sample. Table 6-5 shows the fraction of pores smaller than 10 nm, where the mobility of free ions is restrained and has little effect on ionic transporting properties (Cui and Cahyadi, 2001), within the total intrudable porosities. Based on the results reported in Figure 6-7A and Table 6-5, it is observed that the lower overall intrudable porosity of the CLDH modified sample (M-NC-1-180d) than the unmodified sample (M-NC-0-180d) is mainly due to the existence of less pores smaller than 10 nm. The absolute value of the fraction of pores larger than 10 nm in these two samples is almost the same. Compared with sodium silicate-activated mortars, sodium carbonate-activated mortars exhibit a higher overall intrudable porosity as well as a higher percentage of pores smaller than 10 nm, while CLDH modified sodium carbonate-activated mortar has a lower percentage of pores smaller than 10 nm despite its slightly higher overall intrudable porosity.

The critical pore diameters derived from MIP measurement represents the maximum continuous pore diameters (Katz and Thompson, 1986), and a larger critical pore diameter often relates to higher water diffusivity and ion mobility in cementitious materials (Cui and Cahyadi, 2001, Halamickova et al., 1995, Ye et al., 2006). As shown in Table 6-5, sample M-NC-0-180d has the highest critical pore diameter among the three samples tested, while sample M-NS-0-180d shown the lowest critical pore diameters. Smaller critical pore

diameters are often observed in mortar samples compromising a lower fraction of aggregates, higher content of fine fillers (e.g. silica fume), or samples with lower degree of reaction in the paste section (Halamickova et al., 1995, Winslow et al., 1994). In this study, the sand fractions were kept constant in all samples. The lowest critical pore diameter observed in sodium silicate activated mortar likely relates to both the nature of the activator and a higher degree of reaction (comparing with near neutral salt activation at the same age of curing).

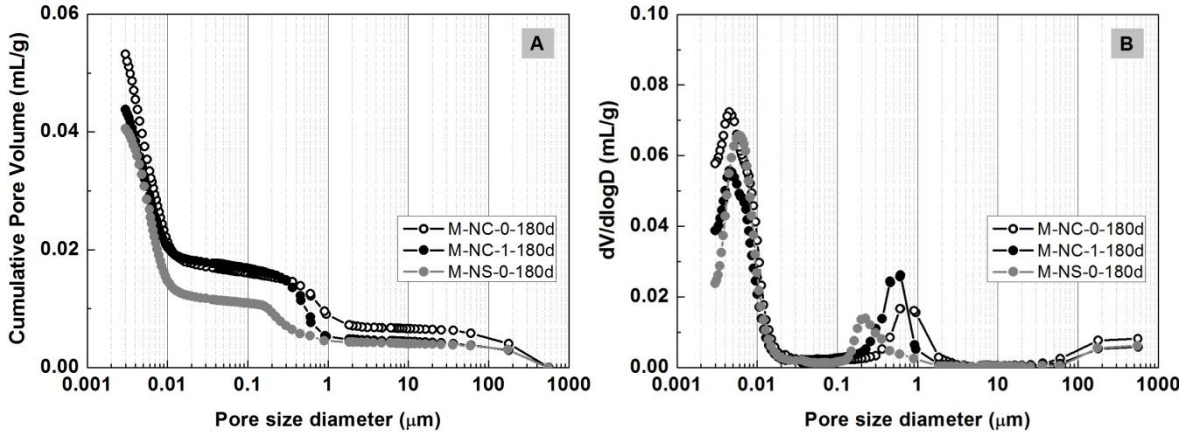

Figure 6-7 (A) cumulative pore volume and (B) differential pore volume distributions of mortar samples NC-0, NC-1, and NS-0 at 180 days of curing.

Table 6-5 Summary of intrudable porosities, critical pore diameters and apparent bulk densities of mortar samples.

	Intrudable porosity (%)				
	Total	**(<0.01 μm)**	**(>0.01 μm)**	**Critical pore diameter (μm)**	**+Bulk density (g/mL)**
M-NC-0-180d	11.94	6.98	4.96	0.763	2.2
M-NC-1-180d	9.93	5.18	4.75	0.532	2.3
M-NS-0-180d	9.37	5.95	3.42	0.209	2.3

[+] Measured at 2.27 kPa

Previous studies proved that CLDH incorporated in sodium carbonate-activated slag paste consumes free water and increases the degree of reaction of slag, as CLDH particles act as

nucleation seeding points (Chapter 4). Between sample M-NC-0-180d and M-NC-1-180d, the addition of CLDH extends the degree of reaction in sodium carbonate-activated slag cement and at the same time performs partially as a filler (Chapter 4), both of which explain the lower critical pore diameter observed in sample M-NC-180d. The denser microstructure in the paste section (between the unreacted slag grains) in CLDH modified sodium carbonate-activated slag paste contributes to lower overall porosity of mortars produced with these additions as well.

6.3.3.2. Compressive strength

Figure 6-8 shows that at the different curing ages tested here, between the three alkali-activated systems studied, the compressive strength was higher in M-NS-0 than M-NC-1, which was in turn stronger than M-NC-0. The addition of 5 wt.% of CLDH to sodium carbonate-activated slag mortar promoted a significantly increased compressive strength, compared with that obtained for sodium carbonate-activated slag mortars without CLDH, by at least 12%.

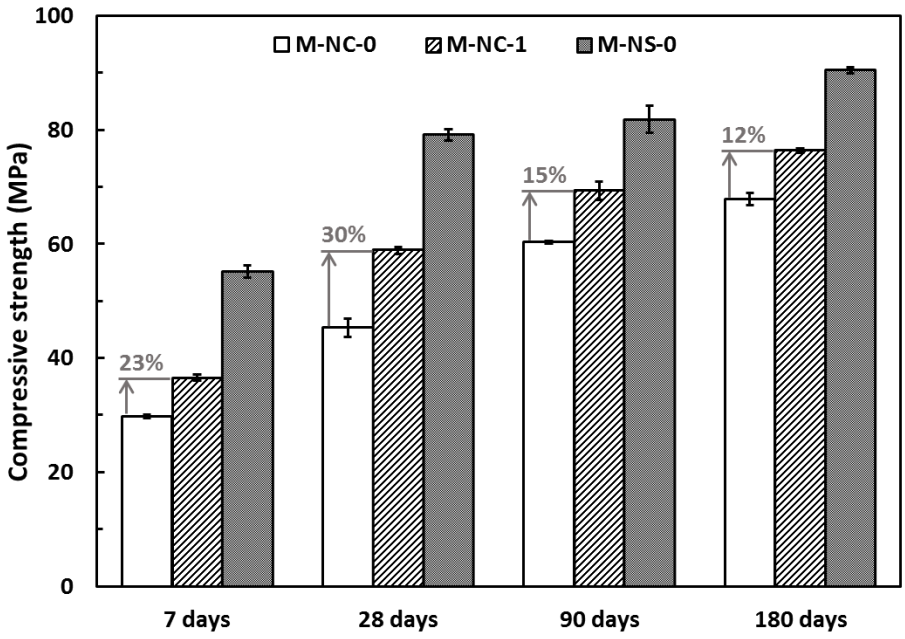

Figure 6-8 Compressive strength of M-NC-0, M-NC-1, and M-NS-0 mortar cubes at 7, 28, 90, and 180 days of curing. The results displayed are average values and standard deviation of three replicates. The 28 day compressive strength of M-NC-1 and M-NS-0 are comparable with high strength CEM I cement, whose minimal 28 day compressive strength is about 52.5 MPa (British standard, BS EN 197-1-2011).

The lower strength development of sodium carbonate activated slag cement in comparison with sodium metasilicate-activated slag cement (under similar activation conditions) has been reported in the literature (Duran Atiş et al., 2009, Fernández-Jiménez et al., 1999, Shi, 1996, Wang et al., 1994), and is associated with the differences in phase assemblage and permeability developed in activated slag systems when using different activators. A higher overall intrudable porosity of the binders would likely lead to lower compressive strength (Shi, 1996). The 180 days intrudable porosity of the three types of mortar studied (shown in Figure 6-7) correlates well with the 180 day compressive strength (shown in Figure 6-8), suggesting that differences in the porosity might be one of the main factors that controls the strength differences in these mortars.

Also, it is worthwhile to note that, when CLDH was blended with sulphoaluminate cement, changes in sample strength were insignificant (Duan et al., 2013); when blended into Portland cement, decreases in sample strength were observed (Yang et al., 2015, Yoon et al., 2014b). In those cementitious systems the hydrotalcite-like phase is not an intrinsic reaction product; therefore the recrystallised CLDH in those systems performs most likely just as a filler. The promotion of higher compressive strength in CLDH modified samples here emphasised the unique benefit of CLDH for tailoring sodium carbonate-activated slag cement.

6.3.3.3. Non-steady state chloride migration coefficient (NT BUILD 492)

The NordTest accelerated migration test results for the three mortar mixes assessed are reported in Table 6-6, Table 6-7, and Table 6-8. The lowest and highest possible chloride

migration coefficients of these samples have been calculated according to Eq. 6-4 and Eq. 6-5, based on the maximum and minimum points of chloride ingress into the samples tested.

Table 6-6 NordTest BUILD 492 results for sodium carbonate activated slag mortars as a function of the curing age

	Temperature (°C)		Voltage (V)	x_{Low} (mm)	x_{High} (mm)	Duration (h)
	Initial	End				
M-NC-0-28	19	21	40	2.1	4.7	24
	19	16*	60	4.3	7.0	24
	19	17*	40	3.5	6.1	27
M-NC-0-90	18	24	60	2.0	4.4	24
	19	22	60	2.9	4.8	24
M-NC-0-180	21	23	40	1.7	3.3	24
	21	22	40	2.6	4.9	39

*Decrease in temperature at the end of the experiment was due to decrease in ambient temperature during the overnight experiment.

Table 6-7 NordTest BUILD 492 results for sodium carbonate activated slag mortars, with 5% CLDH addition, as a function of the curing age

	Temperature (°C)		Voltage (V)	x_{Low} (mm)	x_{High} (mm)	Duration (h)
	Initial	End				
M-NC-1-28	20	15*	60	1.8	4.2	23
	19	22	60	1.9	5.3	24
M-NC-1-90	19	22	50	1.9	2.7	24
	19	22	50	1.1	2.9	24
M-NC-1-180	24	29	50	1.9	3.1	27
	24	28	50	1.9	3.1	26

*Decrease in temperature at the end of the experiment was due to decrease in ambient temperature during the overnight experiment.

Table 6-8 NordTest BUILD 492 results for sodium silicate activated slag mortars, as a function of the curing age

	Temperature (°C)		Voltage (V)	x_{Low} (mm)	x_{High} (mm)	Duration (h)
	Initial	End				
NS-0-28	18	19	50	2.2	4.1	29
	19	20	50	1.6	2.6	17.5
NS-0-90	16	19	60	2.0	4.2	28
	18	21	60	4.0	7.0	46
NS-0-180	21	23	60	1.9	3.4	24
	19	21	50	1.5	3.3	26

For sodium carbonate-activated samples, shown in Figure 6-9A and Figure 6-9B, from 28 days to 90 days of curing, both the highest possible chloride migration coefficients and the differences between the average highest and the lowest possible migration coefficients decrease significantly. From 90 days till 180 days of curing, changes in the average highest and the lowest possible migration coefficients in these two samples (M-NC-0 and M-NC-1) are almost negligible. Between sample M-NC-0 and M-NC-1, CLDH modified samples cover a lower range of possible chloride migration coefficient values at all ages of curing. For sodium silicate activated samples, the differences between the average highest and the lowest possible migration coefficients stayed relatively unchanged, while the highest possible chloride migration coefficients decreases slightly up to 180 days of curing

The differences between the average highest and the lowest possible migration coefficients represent the range of values that the chloride migration coefficient could possibly fall into, and a smaller difference indicates a narrower range of variability. The results in Figure 6-9 suggest sodium carbonate-activated mortars without CLDH (M-NC-0) have significantly higher chloride migration coefficients compared with sodium silicate activated slag, even at extended curing times. While the CLDH modified sodium carbonate-activated slag mortar (M-NC-1) has higher D_{nssm} values than M-NS-0 up to 90 days of curing, the possible D_{nssm} ranges correspond more closely at 180 days of curing.

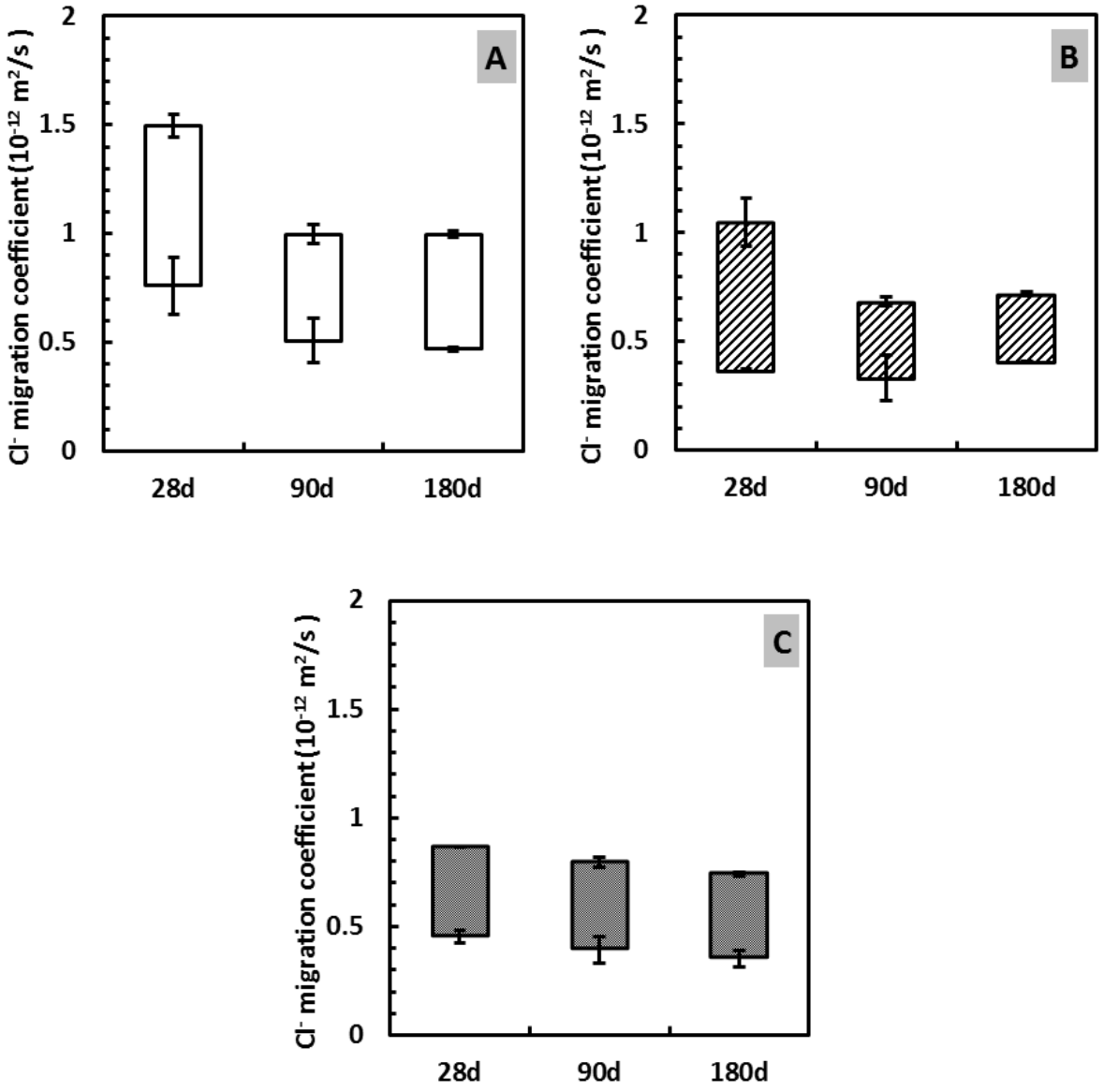

Figure 6-9 Chloride migration coefficient (according to NT BUILD 492) of (A) M-NC-0, (B) M-NC-1, and (C) M-NS-0 mortar at 28, 90, and 180 days of curing. The results displayed are average values and standard deviation calculated from the highest (upper limit) and lowest (lower limit) chloride ingression depth of duplicate tests.

The non-steady state migration coefficients D_{nssm} are determined in part by the material microstructure, where a decrease in the critical pore size, as well as in total intrudable porosity (as determined by MIP), could result in lower mobility of chlorides through the

samples (Ravikumar and Neithalath, 2013, Yang et al., 2015). The mobility of ionic species in pores smaller than 10 nm is much slower than that in mesopores/macropores, and often considered insignificant for influencing the permeability of gas molecules and ionic species through the samples (Cui and Cahyadi, 2001, Halamickova et al., 1995). A higher percentage of pores larger than 10 nm could result in higher chloride transport parameters (Neithalath and Jain, 2010). However, considering the short duration of this accelerated chloride test, the chemical interactions between chlorides and the gel binders would mostly take place locally in pores larger than 10 nm, as it takes much longer time for ionic species to mobilise into the pores smaller than 10 nm (Friedmann et al., 2008, He et al., 2016).

Combining the chloride binding capacity (Figure 6-2B) and MIP results (Table 6-5) shown in previous sections, it seems that the higher chloride migration coefficient of sample M-NC-0 compared with M-NS-0 even at 180 days of curing is most likely caused by a combination effect of higher permeable porosity and lower chloride binding capacity. As for CLDH modified sodium carbonate-activated mortar M-NC-1-180d, even though it has lower permeable porosity than M-NS-0-180d, its stronger capacity to bind free chloride (compared with M-NS-0-180d), might be the reason that similar chloride coefficients have been observed for both samples at 180 days of curing. Between these two factors, chloride binding capacity and the permeable porosity of the binders, it seems that the latter might be the dominant factor that controls the chloride migration coefficient under the currently tested methods. However, the NordTest method NT 492 was carried out under non-steady state and with a short test duration (up to 48 hours), while the chloride binding capacities were measured after 2 months of reaction, at equilibrium. The effect of chloride binding in such an accelerated test method could be underestimated or undermined.

6.4. Conclusions

Using neutral chloride-rich solutions for measuring the chloride binding capacity of alkali-activated slag cement, results in overestimated values. Using chloride-rich simulated pore solutions is a more suitable approach, as it takes into consideration the effects of competition between Cl^- and OH^-.

Sodium carbonate-activated slag paste has a lower chloride binding capacity than with sodium silicate-activated slag paste. The incorporation of 5 wt.% CLDH in the sodium carbonate-activated slag leads to an increased chloride binding capacity by up to 120%, resulting in higher binding capacities than those of sodium silicate-activated slag pastes under the same testing conditions.

Sodium carbonate activated samples have higher total intrudable porosity (MIP), lower compressive strength, and higher chloride migration coefficient, compared with sodium silicate slag materials at equivalent times of curing. However, with the incorporation of 5 wt.% CLDH into sodium carbonate-activated slag mortar, the overall intrudable porosity of the sample has been effectively reduced, promoting a more refined pore structure. The effect of CLDH on densifying the microstructure, as well as increasing the chloride binding capacity of sodium carbonate-activated slag cement, results in higher compressive strength and lower chloride migration coefficient, the values of which are almost comparable[5] to those of sodium silicate-activated slag mortars produced under similar activation conditions.

[5] As explained previously, compressive strength performance of M-NC-1 and M-NS-0 are comparable with high strength CEM I cement, therefore their compressive strengths are comparable as they could both be classified as high strength cement.

Chapter 7.

CONCLUSIONS AND FUTURE WORK

7.1. Conclusions

The results discussed in the preceding chapters have shown that the near-neutral salt sodium carbonate can be used effectively to prepare alkali-activated slag (AAS) cements with desirable performance, if slags with specific chemical compositions (e.g. MgO content >5 wt.%) are used. However, when a small amount of calcined layered double hydroxide (CLDH) is incorporated into sodium carbonate activated slag cement as a chemical addition, the performance of these cements can be tailored considering the chemistry of the slag utilised, and properties in the fresh and hardened states that are targeted. Therefore, AAS cement products with improved sustainability can be produced using sodium carbonate as the sole alkali activator, without having to compromise mechanical performance and long-term stability.

7.1.1. The influence of slag chemistry on its reactivity with sodium carbonate

There is a strong correlation between slag chemistry, especially its MgO content, and the kinetics of reaction and phase assemblage of sodium carbonate-activated binder system.

In general, two types of LDHs are formed in sodium carbonate-activated slag binders. Slags with higher MgO and lower Al_2O_3 contents yield higher contents of hydrotalcite-like phases as secondary reaction products, and a lower content of carbonated Ca-Al AFm-type

phases, due to the limited availability of Al. The relationships between the Mg-Al (hydrotalcite-like) and Ca-Al (AFm) layered double hydroxides are also essential in determining the overall characteristics of the binder system, as the uptake of Al by these phases restricts its availability for incorporation into C-(N)-A-S-H type gel.

When preparing sodium carbonate-activated slag binders, slags containing higher contents of MgO and less Al_2O_3 react much more rapidly, compared with those with lower MgO content but higher Al_2O_3 content. The process of removal of carbonate, supplied by the activator, from the aqueous phase dominates the kinetics of reaction of sodium carbonate activated slag binders. A higher MgO content in the slag leads to its faster dissolution and also results in formation of more hydrotalcite type phases, which promotes the consumption of the carbonate species from solution, and accelerates the kinetics of reaction. A higher extent of slag reaction, as observed by the lower residual slag fraction and much higher C-(N)-A-S-H reaction product content, has been reached in mixes prepared using slags with higher MgO content and lower Al_2O_3 content.

7.1.2. Interaction of chlorides with cementitious phases at high alkalinity

The use of neutral chloride-rich solutions in measuring the chloride binding capacity of alkali-activated slag cement, as is commonly done in the literature, leads to overestimation of binding. The use of high alkalinity chloride-rich simulated pore solutions is a more suitable approach, as it takes into consideration the effects of competition between Cl^- and OH^-.

Under highly alkaline solutions with different initial $[Cl^-]/[OH^-]$ ratios, both surface adsorption and ion exchange (evidenced by changes in basal spacings) of chlorides were

observed in the three main reaction products in AAS cement: the hydrotalcite-like (Mg-Al) and strätlingite (AFm) layered double hydroxides, and C-(N)-A-S-H type gels.

Hydrotalcite-like phases and strätlingite are effective chloride binding phases, while the C-(N)-A-S-H type gels, regardless of the variations in chemical compositions assessed in this study, have much lower overall chloride binding capacities than that of LDHs. Surface adsorption is the main binding mechanism between chloride and hydrotalcite-like phases, responsible for approximately 90% of the total chloride uptake. As for strätlingite, surface adsorption of chloride is less dominant, and lattice substitution of chloride also takes place.

The presence of carbonates in the pore solution, along with a decrease in the alkalinity of the system, significantly decreases the chloride uptake by both LDH minerals assessed, however through different underlying mechanisms. In hydrotalcite-like phases, the carbonate ions occupy the chloride-exchangeable interlayer hydroxyl sites and reduce surface adsorption, while in strätlingite although it can also participate in ion exchange, exposure to chloride mostly (when the aqueous environment is poor in aluminium) leads to partial decomposition of the AFm phase, inducing the precipitation of calcite instead.

7.1.3. CLDH as a smart addition in sodium carbonate-activated slag cement

7.1.3.1. Controlling the kinetics of reaction

It has been demonstrated that the incorporation of CLDH effectively expedites the hardening process of sodium carbonate activated slags to achieve an acceptably fast setting and hardening process for engineering purposes. The added CLDH promotes the kinetics of reaction in sodium carbonate-activated slag mixes via several mechanisms, including:

- **Increasing the pH of the activator.** The recrystallisation process of CLDH involves protonation of surface oxygens in mixed metal oxides to form hydroxyl groups, which increases the pH in activator solutions and therefore drives the slag dissolution. The reduction of the effective water/binder ratio through uptake of water during the protonation process also contributes to speed up the reaction.
- **Accelerating consumption of carbonate ions.** The incorporated CLDH accelerates the consumption of carbonate by direct formation of a stable carbonated hydrotalcite-like phase, instead of calcium-containing carbonate minerals like gaylussite, calcite and carbonated AFm phases. The consumption of calcium in the initial stages of reaction delays the precipitation of the strength-giving C-(N)-A-S-H type gel.
- **Hydrotalcite nucleation seeding.** The hydrotalcite-like phase formed via recrystallisation is dispersed relatively homogeneously in the outer product region of the paste and acts as a nucleation seed, which benefits the precipitation of the gel products.

7.1.3.2. Modification of phase assemblage and refinement of microstructure

The addition of CLDH increases the formation of hydrotalcite-like phases in sodium carbonate-activated slag cement, while reducing the crystallinity of the carbonate AFm phases formed.

The addition of up to 10 wt.% CLDH increases the total extent of slag reaction for at least 180 days of curing, compared with samples without addition of CLDH. The seeding effect of recrystallised CLDH enhances the nucleation and growth of hydrotalcite-group phases, which is important in defining the binder phase assemblage in the long term.

Compared with sodium carbonate-activated slag paste without CLDH addition, the incorporation of 5 wt.% CLDH in the sodium carbonate-activated slag leads to a significant increase in chloride binding capacity, by up to 120%. The higher chloride binding capacity in CLDH modified samples is attributed to additional formation of hydrotalcite-like phases.

The addition of 5 wt.% CLDH into sodium carbonate-activated slag mortars effectively reduced the overall intrudable porosity (MIP) at equivalent times of curing, comparing with slag mortars prepared and tested under the same conditions but without CLDH modification. This indicates the formation of a more refined pore structure and more densified microstructure in the CLDH modified mortar samples.

7.1.3.3. Strength and durability of sodium carbonate-activated slag mortars

Higher compressive strengths and lower chloride migration coefficients were achieved by sodium carbonate-activated slag mortar with the addition of 5 wt.% CLDH, the values of which are almost comparable to sodium silicate-activated slag mortars produced under similar activation conditions. The effects of CLDH on densifying the microstructure, as well as increasing the chloride binding capacity of sodium carbonate-activated slag cement, contribute to the improved compressive strength and durability performance of these materials.

7.2. Directions for future work

The work presented in this study has provided a feasible solution for producing alkali-activated slag cement with potentially reduced environmental impact compared to that of sodium hydroxide/silicate activated slag systems, as near-neutral salts can be mined or

obtained from other industrial processes. Discussions regarding the interactions between free chlorides and synthetic phases resembling those forming in AAS cement, assessed in high alkalinity simulated pore solutions, have also underpinned a new conceptual mechanistic description of the factors controlling durability of these materials in service.

For optimising the production of alkali-activated slag cement as a green and sustainable alternative to PC, and for developing deeper and more thorough understanding of the durability performance of alkali-activated slag cement in service, there are still a number of open questions that need to be investigated:

- The use of other near neutral salts such as sodium sulfate as alternative activators might also have the merits of low environmental impact. Based on the knowledge obtained from this study, it would be important to emphasise the importance of chemical compositions of precursors when investigating different activators.

- Changes in lattice parameters (basal spacing) in C-(N)-A-S-H type gels after binding of chloride have been observed, however more evidence is required to elucidate if the changes in basal spacing were caused by replacement of hydroxyl sites by chlorides. It will be valuable to investigate the arrangements of the interlayer species in chloride-bearing C-(N)-A-S-H type gel using other advanced test methods in addition to those utilised in this study.

- With the data for chloride binding capacities of individual reaction products in contact with highly alkaline simulated pore solutions presented in this study, a model could be developed to predict the chloride binding capacity of AAS paste considering the phase assemblage developed for these materials as a function of the slag composition, activator types and degree of reaction.

- Similar to the results described for chloride binding, CLDH can effectively bind

carbonate ions as well. It will be interesting to assess if the inclusion of CLDHs will improve the materials' resistance to carbonation.

- As discussed previously, the high concentration of free ions (including Na^+ and OH^-) present in the pore solution may also generate an osmotic gradient to counteract migration of Cl^-. This factor might particularly be influential when applying test methods involving external electrical fields for determining the chloride migration coefficient. It would be beneficial to measure the chloride diffusion coefficients of sample with comparable formulation, tested under non-accelerated conditions, or through bulk diffusion tests such as NordTest Build 443.

In summary, this study pioneered the use of CLDH as a smart addition for tailoring sodium carbonate activated slag cements. However, there are still lines of work to be followed, and questions to be answered, before achieving massive production of sodium carbonate-activated slag concrete with guaranteed in-service performance. The results concluded from this research have indeed unveiled a bright future, and hopefully inspired increased interest, for studying the utilisation of near-neutral salts as alternative activators.

References

Aït-Mokhtar, A., Amiri, O., Dumargue, P. & Sammartino, S. 2002. A new model to calculate water permeability of cement-based materials from MIP results. *Advances in Cement Research,* 14**,** 43-49.

Allada, R. K., Pless, J. D., Nenoff, T. M. & Navrotsky, A. 2005. Thermochemistry of hydrotalcite-like phases intercalated with CO_3^{2-},NO_3^-,Cl^-,I^-, and ReO_4^-. *Chemistry of Materials,* 17**,** 2455-2459.

Alonso, S. & Palomo, A. 2001. Calorimetric study of alkaline activation of calcium hydroxide–metakaolin solid mixtures. *Cement and Concrete Research,* 31**,** 25-30.

Andersen, M. D., Jakobsen, H. J. & Skibsted, J. 2002. Characterization of the a-b phase transition in Friedels salt ($Ca_2Al(OH)_6Cl,2H_2O$) by variable-temperature ^{27}Al MAS NMR spectroscopy. *Journal of Physical Chemistry A,* 106**,** 6676-6682.

Andersen, M. D., Jakobsen, H. J. & Skibsted, J. 2006. A new aluminium-hydrate species in hydrated Portland cements characterized by ^{27}Al and ^{29}Si MAS NMR spectroscopy. *Cement and Concrete Research,* 36, 3-17.

Andersson, K., Allard, B., Bengtsson, M. & Magnusson, B. 1989. Chemical composition of cement pore solutions. *Cement and Concrete Research,* 19**,** 327-332.

Andrade, C., Castellote, M., Alonso, C. & González, C. 2000. Non-steady-state chloride diffusion coefficients obtained from migration and natural diffusion tests. Part I: Comparison between several methods of calculation. *Materials and Structures,* 33**,** 21-28.

Andrade, C., Prieto, M., Tanner, P., Tavares, F. & D'andrea, R. 2013. Testing and modelling chloride penetration into concrete. *Construction and Building Materials,* 39**,** 9-18.

Angst, U., Elsener, B., Larsen, C. K. & Vennesland, 2009. Critical chloride content in reinforced concrete — A review. *Cement and Concrete Research,* 39**,** 1122-1138.

Ann, K. Y. & Song, H.-W. 2007. Chloride threshold level for corrosion of steel in concrete. *Corrosion Science,* 49**,** 4113-4133.

Anstice, D. J., Page, C. L. & Page, M. M. 2005. The pore solution phase of carbonated cement pastes. *Cement and Concrete Research,* 35**,** 377-383.

Arya, C., Buenfeld, N. R. & Newman, J. B. 1990. Factors influencing chloride-binding in concrete. *Cement and Concrete research,* 20**,** 291-300.

Astm International 2012a. ASTM C1202-12. *Standard test method for electrical indication of concrete's ability to resist chloride ion penetration.* West Conshohocken.

ASTM International 2012b. ASTM D512-12. *Standard test methods for chloride ion in water*. ASTM International.

ASTM International 2016. ASTM C1556-11a. *Standard test method for determining the apparent chloride diffusion coefficient of cementitious mixtures by bulk diffusion.* West Conshohocken.

Bai, Y., Collier, N., Milestone, N. & Yang, C. 2011. The potential for using slags activated with near neutral salts as immobilisation matrices for nuclear wastes containing reactive metals. *Journal of Nuclear Materials,* 413**,** 183-192.

Balonis, M., Lothenbach, B., Le Saout, G. & Glasser, F. P. 2010. Impact of chloride on the mineralogy of hydrated Portland cement systems. *Cement and Concrete Research,* 40**,** 1009-1022.

Barneyback, J. R. S. & Diamond, S. 1981. Expression and analysis of pore fluids from hardened cement pastes and mortars. *Cement and Concrete Research,* 11**,** 279-285.

Baroghel-Bouny, V., Wang, X., Thiery, M., Saillio, M. & Barberon, F. 2012. Prediction of chloride binding isotherms of cementitious materials by analytical model or numerical inverse analysis. *Cement and Concrete Research,* 42**,** 1207-1224.

Beaudoin, J. J., Ramachandran, V. S. & Feldman, R. F. 1990. Interaction of chloride and C-S-H. *Cement and Concrete Research,* 20**,** 875-883.

Ben Haha, M., Lothenbach, B., Le Saout, G. & Winnefeld, F. 2011. Influence of slag chemistry on the hydration of alkali-activated blast-furnace slag — part I: effect of MgO. *Cement and Concrete Research,* 41**,** 955-963.

Ben Haha, M., Lothenbach, B., Le Saout, G. & Winnefeld, F. 2012. Influence of slag chemistry on the hydration of alkali-activated blast-furnace slag — part II: effect of Al_2O_3. *Cement and Concrete Research,* 42**,** 74-83.

Bernal, S. A., Mejía de Gutierrez, R., Pedraza, A. L., Provis, J. L., Rodríguez, E. D. & Delvasto, S. 2011a. Effect of binder content on the performance of alkali-activated slag concretes. *Cement and Concrete Research,* 41**,** 1-8.

Bernal, S. A., Provis, J. L., Brice, D. G., Kilcullen, A., Duxson, P. & Van Deventer, J. S. J. 2012. Accelerated carbonation testing of alkali-activated binders significantly underestimates service life: The role of pore solution chemistry. *Cement and Concrete Research,* 42**,** 1317-1326.

Bernal, S. A., Provis, J. L., Fernández-Jiménez, A., Krivenko, P. V., Kavalerova, E., Palacios, M. & Shi, C. 2014a. Binder chemistry–high-calcium alkali-activated materials. *Alkali-activated materials:State of the Art Report,RILEM TC 224-AAM.* Springer/RILEM, Dordrecht, pp. 59-91.

Bernal, S. A., Provis, J. L., Myers, R. J., San Nicolas, R. & Van Deventer, J. S. J. 2014b. Role of carbonates in the chemical evolution of sodium carbonate-activated slag binders. *Materials and Structures,* 48**,** 517-529.

Bernal, S. A., Provis, J. L., Rose, V. & Mejía De Gutierrez, R. 2011b. Evolution of binder structure in sodium silicate-activated slag-metakaolin blends. *Cement and Concrete Composites,* 33**,** 46-54.

Bernal, S. A., Provis, J. L., Walkley, B., San Nicolas, R., Gehman, J. D., Brice, D. G., Kilcullen, A. R., Duxson, P. & Van Deventer, J. S. J. 2013. Gel nanostructure in alkali-activated binders based on slag and fly ash, and effects of accelerated carbonation. *Cement and Concrete Research,* 53**,** 127-144.

Bernal, S. A., San Nicolas, R., Myers, R. J., Mejía De Gutiérrez, R., Puertas, F., Van Deventer, J. S. J. & Provis, J. L. 2014c. MgO content of slag controls phase evolution and structural changes induced by accelerated carbonation in alkali-activated binders. *Cement and Concrete Research,* 57**,** 33-43.

Bernal, S. A., San Nicolas, R., Van Deventer, J. S. J. & Provis, J. L. 2015a. Alkali-activated slag cements produced with a blended sodium carbonate/silicate activator. *Advances in Cement Research,* 28**,** 262-273.

Bernal, S. A., San Nicolas, R., Van Deventer, J. S. J. & Provis, J. L. 2015b. Water content modifies the structural development of sodium metasilicate-activated slag binders. *ALCONPAT Journal,* 5**,** 29-40.

Birnin-Yauri, U. A. & Glasser, F. P. 1998. Friedel's salt, $Ca_2Al(OH)_6(Cl,OH)\cdot 2H_2O$: its solid solutions and their role in chloride binding. *Cement and Concrete Research,* 28**,** 1713-1723.

Bischoff, J. L., Herbst, D. B. & Rosenbauer, R. J. 1991. Gaylussite formation at Mono Lake, California. *Geochimica et Cosmochimica Acta,* 55**,** 1743-1747.

Boclair, J. W. & Braterman, P. S. 1999. Layered double hydroxide stability. 1. relative stabilities of layered double hydroxides and their simple counterparts. *Chemistry of Materials,* 11**,** 298-302.

Brindley, G. W. & Kikkawa, S. 1979. A crystal-chemical study of Mg, Al and Ni, Al hydroxy-perchlorates and hydroxy-carbonates. *American Mineralogist,* 64**,** 836-843.

Brindley, G. W. & Kikkawa, S. 1980. Thermal behavior of hydrotalcite and of anion-exchange forms of hydrotalcite. *Clays and Clay Minerals,* 28**,** 87-91.

British Standards Institute 2002. BS EN 1008:2002. *Mixing water for concrete — Specification for sampling, testing and assessing the suitability of water, including water recovered from processes in the concrete industry, as mixing water for concrete.*

British Standards Institute 2013. BS EN 206:2013+A1:2016. *Concrete. Specification, performance, production and conformity.*

Brough, A. R. & Atkinson, A. 2002. Sodium silicate-based, alkali-activated slag mortars: Part I. Strength, hydration and microstructure. *Cement and Concrete Research,* 32**,** 865-879.

Buchwald, A., Vanooteghem, M., Gruyaert, E., Hilbig, H. & De Belie, N. 2015. Purdocement: application of alkali-activated slag cement in Belgium in the 1950s. *Materials and Structures,* 48**,** 501-511.

Burciaga-Díaz, O. & Escalante-García, J. I. 2013. Structure, mechanisms of reaction, and strength of an alkali-activated blast-furnace slag. *Journal of the American Ceramic Society,* 96**,** 3939-3948.

Butt, H. J., Graf, K. & Kappl, M. 2003. *Physics and Chemistry of Interfaces,* Wiley.

Catti, M., Ferraris, G., Hull, S. & Pavese, A. 1995. Static compression and H disorder in brucite, $Mg(OH)_2$, to 11 GPa: a powder neutron diffraction study. *Physics and Chemistry of Minerals,* 22**,** 200-206.

Cavani, F., Trifirò, F. & Vaccari, A. 1991. Hydrotalcite-type anionic clays: Preparation, properties and applications. *Catalysis Today,* 11**,** 173-301.

Châtelet, L., Bottero, J. Y., Yvon, J. & Bouchelaghem, A. 1996. Competition between monovalent and divalent anions for calcined and uncalcined hydrotalcite: anion exchange and adsorption sites. *Colloids and Surfaces A: Physicochemical and Engineering Aspects,* 111**,** 167-175.

Chen, J. J., Thomas, J. J., Taylor, H. F. W. & Jennings, H. M. 2004. Solubility and structure of calcium silicate hydrate. *Cement and Concrete Research,* 34**,** 1499-1519.

Collins, F. & Sanjayan, J. G. 2000. Effect of pore size distribution on drying shrinkage of alkali-activated slag concrete. *Cement and Concrete Research,* 30**,** 1401-1406.

Constantino, V. R. L. & Pinnavaia, T. J. 1995. Basic properties of $Mg_{1-x}^{2+}Al_x^{3+}$ layered double hydroxides intercalated by carbonate, hydroxide, chloride, and sulfate anions. *Inorganic Chemistry,* 34**,** 883-892.

Cook, R. A. & Hover, K. C. 1999. Mercury porosimetry of hardened cement pastes. *Cement and Concrete Research,* 29**,** 933-943.

Cui, L. & Cahyadi, J. H. 2001. Permeability and pore structure of OPC paste. *Cement and Concrete Research,* 31**,** 277-282.

Damidot, D., Stronach, S., Kindness, A., Atkins, M. & Glasser, F. P. 1994. Thermodynamic investigation of the $CaO\text{-}Al_2O_3\text{-}CaCO_3\text{-}H_2O$ closed system at 25°C and the influence of Na_2O. *Cement and Concrete Research,* 24**,** 563-572.

Delagrave, A., Marchand, J., Ollivier, J.-P., Julien, S. & Hazrati, K. 1997. Chloride binding capacity of various hydrated cement paste systems. *Advanced Cement Based Materials,* 6**,** 28-35.

Demoulian, E., Gourdin, P., Hawthorn, F. & Vernet, C. Influence of slags chemical composition and texture on their hydraulicity. Proceedings of 7th International Congress on the Chemistry of Cement, Paris, 1980.

Dhir, R. K., El-Mohr, M. A. K. & Dyer, T. D. 1996. Chloride binding in GGBS concrete. *Cement and Concrete Research,* 26**,** 1767-1773.

Duan, P., Chen, W., Ma, J. & Shui, Z. 2013. Influence of layered double hydroxides on microstructure and carbonation resistance of sulphoaluminate cement concrete. *Construction and Building Materials,* 48**,** 601-609.

Duan, X. & Evans, D. G. 2006. *Layered Double Hydroxides*, Springer Berlin Heidelberg.

Duran Atiş, C., Bilim, C., Çelik, & Karahan, O. 2009. Influence of activator on the strength and drying shrinkage of alkali-activated slag mortar. *Construction and Building Materials,* 23**,** 548-555.

Ehrenberg, A. Granulated blast furnace slag-from laboratory into practice. The 14th International Congress on the Chemistry of Cement, 2015 Beijing. CD-ROM Proceedings.

Elakneswaran, Y., Nawa, T. & Kurumisawa, K. 2009. Electrokinetic potential of hydrated cement in relation to adsorption of chlorides. *Cement and Concrete Research,* 39**,** 340-344.

Elfmarkova, V., Spiesz, P. & Brouwers, H. J. H. 2015. Determination of the chloride diffusion coefficient in blended cement mortars. Cement and Concrete Research, 78, Part B, 190-199.

Engelhardt, G. & Michel, D. 1987. *High Resolution SolidState NMR of Silicates and Zeolites*, Chichester, John Wiley & Sons.

Escalante-García, J. I., Fuentes, A. F., Gorokhovsky, A., Fraire-Luna, P. E. & Mendoza-Suarez, G. 2003. Hydration products and reactivity of blast-furnace slag activated by various alkalis. *Journal of the American Ceramic Society,* 86**,** 2148-2153.

Famy, C., Scrivener, K. L. & Crumbie, A. K. 2002. What causes differences of C-S-H gel grey levels in backscattered electron images? *Cement and Concrete Research,* 32**,** 1465-1471.

Faucon, P., Delagrave, A., Richet, C., Marchand, J. M. & Zanni, H. 1999. Aluminum incorporation in calcium silicate hydrates (C−S−H) depending on their Ca/Si ratio. *The Journal of Physical Chemistry B,* 103**,** 7796-7802.

Fawer, M., Concannon, M. & Rieber, W. 1999. Life cycle inventories for the production of sodium silicates. The International Journal of Life Cycle Assessment, 4, 207.

Feldman, R. F. & Sereda, P. J. 1970. A new model for hydrated portland cement and its practical implications. *Engineering Journal of Canada,* 53**,** 53-59.

Fernández-Jiménez, A., Palomo, J. G. & Puertas, F. 1999. Alkali-activated slag mortars: Mechanical strength behaviour. *Cement and Concrete Research,* 29**,** 1313-1321.

Fernández-Jiménez, A. & Puertas, F. 2001. Setting of alkali-activated slag cement. Influence of activator nature. *Advances in Cement Research,* 13**,** 115-121.

Fernández-Jiménez, A. & Puertas, F. 2003a. Effect of activator mix on the hydration and strength behaviour of alkali-activated slag cements. *Advances in Cement Research,* 15**,** 129-136.

Fernández-Jiménez, A. & Puertas, F. 2003b. Effect of activator mix on the hydration and strength behaviour of alkali-activated slag cements. *Advances in Cement Research,* 15**,** 129-136.

Fernández-Jiménez, A., Puertas, F., Sobrados, I. & Sanz, J. 2003. Structure of calcium silicate hydrates formed in alkaline-activated slag: influence of the type of alkaline activator. *Journal of the American Ceramic Society,* 86**,** 1389-1394.

Fernández Bertos, M., Simons, S. J. R., Hills, C. D. & Carey, P. J. 2004. A review of accelerated carbonation technology in the treatment of cement-based materials and sequestration of CO_2. *Journal of Hazardous Materials,* 112**,** 193-205.

Fischer, R. & Kuzel, H. J. 1982. Reinvestigation of the system $C_4A.nH_2O$-$C_4A.CO_2.nH_2O$. *Cement and Concrete Research,* 12**,** 517-526.

Florea, M. V. A. & Brouwers, H. J. H. 2012. Chloride binding related to hydration products: part I: ordinary Portland cement. *Cement and Concrete Research,* 42**,** 282-290.

Florea, M. V. A. & Brouwers, H. J. H. 2014. Modelling of chloride binding related to hydration products in slag-blended cements. *Construction and Building Materials,* 64**,** 421-430.

François, M., Renaudin, G. & Evrard, O. 1998. A cementitious compound with composition $3CaO.Al_2O_3.CaCO_3.11H_2O$. *Acta Crystallographica Section C,* 54**,** 1214-1217.

Friedmann, H., Amiri, O. & Aït-Mokhtar, A. 2008. Physical modeling of the electrical double layer effects on multispecies ions transport in cement-based materials. *Cement and Concrete Research,* 38**,** 1394-1400.

Gallé, C. 2001. Effect of drying on cement-based materials pore structure as identified by mercury intrusion porosimetry: A comparative study between oven-, vacuum-, and freeze-drying. *Cement and Concrete Research,* 31**,** 1467-1477.

Gastuche, M. C., Brown, G. & Mortland, M. M. 1967. Mixed magnesium-aluminium hydroxides i. preparation and characterization of compounds formed in dialysed systems. *Clay Minerals,* 7**,** 177-192.

Glasser, F. P., Kindness, A. & Stronach, S. A. 1999. Stability and solubility relationships in AFm phases: Part I. Chloride, sulfate and hydroxide. *Cement and Concrete Research,* 29**,** 861-866.

Glasser, F. P., Marchand, J. & Samson, E. 2008. Durability of concrete — Degradation phenomena involving detrimental chemical reactions. *Cement and Concrete Research,* 38**,** 226-246.

Glukhovsky, V. D., Krivenko, P. V., Rostovskaya, G. S., Timkovich, V. J. & Pankratov, V. L. 1983. Binder. United States Patent.

Goñi, S. & Andrade, C. 1990. Synthetic concrete pore solution chemistry and rebar corrosion rate in the presence of chlorides. *Cement and Concrete Research,* 20**,** 525-539.

Goñi, S., Frias, M., Vigil De La Villa, R. & García, R. 2013. Sodium chloride effect on durability of ternary blended cement. Microstructural characterization and strength. *Composites Part B: Engineering,* 54**,** 163-168.

Goto, S. & Roy, D. M. 1981. Diffusion of ions through hardened cement pastes. *Cement and Concrete Research,* 11**,** 751-757.

Gruskovnjak, A., Lothenbach, B., Holzer, L., Figi, R. & Winnefeld, F. 2006. Hydration of alkali-activated slag: comparison with ordinary Portland cement. *Advances in Cement Research,* 18**,** 119-128.

Habert, G., D'espinose De Lacaillerie, J. B. & Roussel, N. 2011. An environmental evaluation of geopolymer based concrete production: reviewing current research trends. *Journal of Cleaner Production,* 19**,** 1229-1238.

Habert, G. & Ouellet-Plamondon, C. 2016. Recent update on the environmental impact of geopolymers. *RILEM Technical Letters,* 1**,** 7.

Halamickova, P., Detwiler, R. J., Bentz, D. P. & Garboczi, E. J. 1995. Water permeability and chloride ion diffusion in Portland cement mortars: Relationship to sand content and critical pore diameter. *Cement and Concrete Research,* 25**,** 790-802.

He, F., Shi, C., Hu, X., Wang, R., Shi, Z., Li, Q., Li, P. & An, X. 2016. Calculation of chloride ion concentration in expressed pore solution of cement-based materials exposed to a chloride salt solution. *Cement and Concrete Research,* 89**,** 168-176.

He, F., Shi, C., Yuan, Q., Chen, C. & Zheng, K. 2012. $AgNO_3$-based colorimetric methods for measurement of chloride penetration in concrete. *Construction and Building Materials,* 26**,** 1-8.

Hibino, T., Yamashita, Y., Kosuge, K. & Tsunashima, A. 1995. Decarbonation behavior of Mg-Al-CO_3 hydrotalcite-like compounds during heat treatment. *Clays and Clay Minerals,* 43**,** 427-432.

Hong, S.-Y. & Glasser, F. P. 1999. Alkali binding in cement pastes: Part I. The C-S-H phase. *Cement and Concrete Research,* 29**,** 1893-1903.

Hong, S.-Y. & Glasser, F. P. 2002. Alkali sorption by C-S-H and C-A-S-H gels: Part II. Role of alumina. *Cement and Concrete Research,* 32**,** 1101-1111.

Ipavec, A., Gabrovšek, R., Vuk, T., Kaučič, V., Maček, J. & Meden, A. 2011. Carboaluminate phases formation during the hydration of calcite-containing portland cement. *Journal of the American Ceramic Society,* 94**,** 1238-1242.

Ismail, I., Bernal, S. A., Provis, J. L., San Nicolas, R., Brice, D. G., Kilcullen, A. R., Hamdan, S. & Van Deventer, J. S. J. 2013. Influence of fly ash on the water and chloride permeability of alkali-activated slag mortars and concretes. *Construction and Building Materials,* 48**,** 1187-1201.

Ismail, I., Bernal, S. A., Provis, J. L., San Nicolas, R., Hamdan, S. & Van Deventer, J. S. J. 2014. Modification of phase evolution in alkali-activated blast furnace slag by the incorporation of fly ash. *Cement and Concrete Composites,* 45**,** 125-135.

Jennings, H. M. 2008. Refinements to colloid model of C-S-H in cement: CM-II. *Cement and Concrete Research,* 38**,** 275-289.

Jin, F. & Al-Tabbaa, A. 2015. Strength and drying shrinkage of slag paste activated by sodium carbonate and reactive MgO. *Construction and Building Materials,* 81**,** 58-65.

Jones, M. R., Macphee, D. E., Chudek, J. A., Hunter, G., Lannegrand, R., Talero, R. & Scrimgeour, S. N. 2003. Studies using ^{27}Al MAS NMR of AFm and AFt phases and the formation of Friedel's salt. *Cement and Concrete Research,* 33**,** 177-182.

Kalinichev, A. G. & Kirkpatrick, R. J. 2002. Molecular dynamics modeling of chloride binding to the surfaces of calcium hydroxide, hydrated calcium aluminate, and calcium silicate phases. *Chemistry of Materials,* 14**,** 3539-3549.

Kameda, T., Yoshioka, T., Hoshi, T., Uchida, M. & Okuwaki, A. 2005. The removal of chloride from solutions with various cations using magnesium–aluminum oxide. *Separation and Purification Technology,* 42**,** 25-29.

Kameda, T., Yoshioka, T., Mitsuhashi, T., Uchida, M. & Okuwaki, A. 2003. The simultaneous removal of calcium and chloride ions from calcium chloride solution using magnesium–aluminum oxide. *Water Research,* 37**,** 4045-4050.

Kashani, A., Provis, J. L., Qiao, G. G. & Van Deventer, J. S. J. 2014. The interrelationship between surface chemistry and rheology in alkali activated slag paste. *Construction and Building Materials,* 65**,** 583-591.

Katz, A. J. & Thompson, A. H. 1986. Quantitative prediction of permeability in porous rock. *Physical Review B,* 34**,** 8179-8181.

Kaufhold, S., Emmerich, K., Dohrmann, R., Steudel, A. & Ufer, K. 2013. Comparison of methods for distinguishing sodium carbonate activated from natural sodium bentonites. *Applied Clay Science,* 86**,** 23-37.

Kayali, O., Khan, M. S. H. & Sharfuddin Ahmed, M. 2012. The role of hydrotalcite in chloride binding and corrosion protection in concretes with ground granulated blast furnace slag. *Cement and Concrete Composites,* 34**,** 936-945.

Khan, M. S. H., Kayali, O. & Troitzsch, U. 2016. Chloride binding capacity of hydrotalcite and the competition with carbonates in ground granulated blast furnace slag concrete. *Materials and Structures,* 49**,** 4609-4619.

Kirkpatrick, R. J. 1988. MAS NMR-spectroscopy of minerals and glasses. *Reviews in Mineralogy,* 18**,** 341-403.

Kirkpatrick, R. J., Ping, Y. & Kalinichev, A. 2001. Chloride binding to cement phases: Exchange isotherm, ^{35}Cl NMR and molecular dynamics modeling studies. *Materials Science of Concrete,* Special volume: Calcium Hydroxide in Concrete**,** 77-92.

Kostick, D. S. 2012. 2011Minerals Yearbook. Soda ash. U.S. Department of the Interior, U.S. Geological Survey.

Kovtun, M., Kearsley, E. P. & Shekhovtsova, J. 2015. Chemical acceleration of a neutral granulated blast-furnace slag activated by sodium carbonate. *Cement and Concrete Research,* 72**,** 1-9.

Krizan, D. & Zivanovic, B. 2002. Effects of dosage and modulus of water glass on early hydration of alkali–slag cements. *Cement and Concrete Research,* 32**,** 1181-1188.

Kuzel, H. J. & Pöllmann, H. 1991. Hydration of C_3A in the presence of $Ca(OH)_2$, $CaSO_4 \cdot 2H_2O$ and $CaCO_3$. *Cement and Concrete Research,* 21**,** 885-895.

Kwan, S., Larosa, J. & Grutzeck, M. W. 1995. ^{29}Si and ^{27}Al MAS NMR study of strätlingite. *Journal of the American Ceramic Society,* 78**,** 1921-1926.

L'hôpital, E., Lothenbach, B., Le Saout, G., Kulik, D. & Scrivener, K. 2015. Incorporation of aluminium in calcium-silicate-hydrates. *Cement and Concrete Research,* 75**,** 91-103.

Labbez, C., Nonat, A., Pochard, I. & Jönsson, B. 2007. Experimental and theoretical evidence of overcharging of calcium silicate hydrate. *Journal of Colloid and Interface Science,* 309**,** 303-307.

León, M., Díaz, E. & Ordóñez, S. 2011. Ethanol catalytic condensation over Mg–Al mixed oxides derived from hydrotalcites. *Catalysis Today,* 164**,** 436-442.

Lloyd, R. R., Provis, J. L. & Van Deventer, J. S. J. 2010. Pore solution composition and alkali diffusion in inorganic polymer cement. *Cement and Concrete Research,* 40**,** 1386-1392.

Loewenstein, W. 1954. The distribution of aluminum in the tetrahedra of silicates and aluminates *American Mineralogist,* 39**,** 92-96.

Lothenbach, B. & Gruskovnjak, A. 2007. Hydration of alkali-activated slag: thermodynamic modelling. *Advances in Cement Research,* 19**,** 81-92.

Lothenbach, B., Le Saout, G., Gallucci, E. & Scrivener, K. 2008. Influence of limestone on the hydration of Portland cements. *Cement and Concrete Research,* 38**,** 848-860.

Lothenbach, B., Scrivener, K. & Hooton, R. D. 2011. Supplementary cementitious materials. *Cement and Concrete Research,* 41**,** 1244-1256.

Lv, L., He, J., Wei, M. & Duan, X. 2006a. Kinetic studies on fluoride removal by calcined layered double hydroxides. *Industrial & Engineering Chemistry Research,* 45**,** 8623-8628.

Lv, L., He, J., Wei, M., Evans, D. G. & Duan, X. 2006b. Uptake of chloride ion from aqueous solution by calcined layered double hydroxides: equilibrium and kinetic studies. *Water Research,* 40**,** 735-743.

Ma, H. 2014. Mercury intrusion porosimetry in concrete technology: tips in measurement, pore structure parameter acquisition and application. *Journal of Porous Materials,* 21**,** 207-215.

Ma, Q., Nanukuttan, S. V., Basheer, P. a. M., Bai, Y. & Yang, C. 2015. Chloride transport and the resulting corrosion of steel bars in alkali activated slag concretes. *Materials and Structures,* 49**,** 3663-3667.

Marchi, A. J. & Apesteguía, C. R. 1998. Impregnation-induced memory effect of thermally activated layered double hydroxides. *Applied Clay Science,* 13**,** 35-48.

Martín-Pérez, B., Zibara, H., Hooton, R. D. & Thomas, M. D. A. 2000. A study of the effect of chloride binding on service life predictions. *Cement and Concrete Research,* 30**,** 1215-1223.

Mascolo, G. & Mascolo, M. C. 2015. On the synthesis of layered double hydroxides (LDHs) by reconstruction method based on the "memory effect". *Microporous and Mesoporous Materials,* 214**,** 246-248.

Matschei, T., Lothenbach, B. & Glasser, F. P. 2007a. The AFm phase in Portland cement. *Cement and Concrete Research,* 37**,** 118-130.

Matschei, T., Lothenbach, B. & Glasser, F. P. 2007b. Thermodynamic properties of Portland cement hydrates in the system $CaO–Al_2O_3–SiO_2–CaSO_4–CaCO_3–H_2O$. *Cement and Concrete Research,* 37**,** 1379-1410.

Mcgrath, P. F. & Hooton, R. D. 1999. Re-evaluation of the AASHTO T259 90-day salt ponding test. *Cement and Concrete Research,* 29**,** 1239-1248.

Mehta, P. K. & Monteiro, P. J. M. 2006. *Concrete: Microstructure, Properties and Materials,* McGrawHill.

Mesbah, A., Cau-Dit-Coumes, C., Frizon, F., Leroux, F., Ravaux, J. & Renaudin, G. 2011a. A new investigation of the $Cl^–$-$CO_3^{2–}$ substitution in AFm phases. *Journal of the American Ceramic Society,* 94**,** 1901-1910.

Mesbah, A., Cau-Dit-Coumes, C., Renaudin, G., Frizon, F. & Leroux, F. 2012. Uptake of chloride and carbonate ions by calcium monosulfoaluminate hydrate. *Cement and Concrete Research,* 42**,** 1157-1165.

Mesbah, A., François, M., Cau-Dit-Coumes, C., Frizon, F., Filinchuk, Y., Leroux, F., Ravaux, J. & Renaudin, G. 2011b. Crystal structure of Kuzel's salt $3CaO·Al_2O_3·1/2CaSO_4·1/2CaCl_2·11H_2O$ determined by synchrotron powder diffraction. *Cement and Concrete Research,* 41**,** 504-509.

Mesbah, A., Rapin, J.-P., François, M., Cau-Dit-Coumes, C., Frizon, F., Leroux, F. & Renaudin, G. 2011c. Crystal structures and phase transition of cementitious bi-anionic AFm-($Cl^–$, $CO_3^{2–}$) compounds. *Journal of the American Ceramic Society,* 94**,** 261-268.

Mills, S. J., Christy, A. G., Genin, J.-M. R., Kameda, T. & Colombo, F. 2012. Nomenclature of the hydrotalcite supergroup: natural layered double hydroxides. *Mineralogical Magazine,* 76**,** 1289-1336.

Miyata, S. 1975. The syntheses of hydrotalcite-like compounds and their structures and physico-chemical properties I: The systems Mg^{2+}-Al^{3+}-NO_3^-, Mg^{2+}-Al^{3+}-Cl^-, Mg^{2+}-Al^{3+}-ClO_4^-, Ni^{2+}-Al^{3+}-Cl^- and Zn^{2+}-Al^{3+}-Cl^-. *Clays and Clay Minerals,* 23**,** 369-375.

Miyata, S. 1983. Anion-exchange properties of hydrotalcite-like compounds. *Clays and Clay Minerals,* 31**,** 305-311.

Morimoto, K., Anraku, S., Hoshino, J., Yoneda, T. & Sato, T. 2012. Surface complexation reactions of inorganic anions on hydrotalcite-like compounds. *Journal of Colloid and Interface Science,* 384**,** 99-104.

Moro, F. & Böhni, H. 2002. Ink-bottle effect in mercury intrusion porosimetry of cement-based materials. *Journal of Colloid and Interface Science,* 246**,** 135-149.

Mourad, M. C. D., Mokhtar, M., Tucker, M. G., Barney, E. R., Smith, R. I., Alyoubi, A. O., Basahel, S. N., Shaffer, M. S. P. & Skipper, N. T. 2011. Activation and local structural stability during the thermal decomposition of Mg/Al-hydrotalcite by total neutron scattering. *Journal of Materials Chemistry,* 21**,** 15479-15485.

Muller, A. C. A., Scrivener, K. L., Gajewicz, A. M. & Mcdonald, P. J. 2013. Densification of C–S–H measured by ^{1}H NMR relaxometry. *Journal of Physical Chemistry C,* 117**,** 403-412.

Myers, R. J., Bernal, S. A., Gehman, J. D., Van Deventer, J. S. J. & Provis, J. L. 2014. The role of Al in cross-linking of alkali-activated slag cements. *Journal of the American Ceramic Society,* 98**,** 996-1004.

Myers, R. J., Bernal, S. A., San Nicolas, R. & Provis, J. L. 2013. Generalized structural description of calcium-sodium aluminosilicate hydrate gels: the cross-linked substituted tobermorite model. *Langmuir,* 29**,** 5294-306.

Myers, R. J., L'Hôpital, E., Provis, J. L. & Lothenbach, B. 2015a. Effect of temperature and aluminium on calcium (alumino)silicate hydrate chemistry under equilibrium conditions. *Cement and Concrete Research,* 68**,** 83-93.

Myers, R. J., Lothenbach, B., Bernal, S. A. & Provis, J. L. 2015b. Thermodynamic modelling of alkali-activated slag cements. *Applied Geochemistry,* 61**,** 233-247.

Neithalath, N. & Jain, J. 2010. Relating rapid chloride transport parameters of concretes to microstructural features extracted from electrical impedance. *Cement and Concrete Research,* 40**,** 1041-1051.

Nordtest Method 1995. NT BUILD 443. *Concrete, Hardened: Accelerated Chloride Penetration.*

Nordtest Method 1999. NT BUILD 492. *Concrete, Mortar and Cement-Based Repair Materials: Chloride Migration Coefficient from Non-Steady-State Migration Experiments.*

Office of Air and Radiation 2009. Technical support document for the soda ash manufacturing sector: proposed rule for mandatory reporting of greenhouse gases. In: AGENCY, U. S. E. P. (ed.). U.S.

Okoronkwo, M. U. & Glasser, F. P. 2016a. Stability of strätlingite in the CASH system. *Materials and Structures,* 49**,** 4305-4318.

Okoronkwo, M. U. & Glasser, F. P. 2016b. Strätlingite: compatibility with sulfate and carbonate cement phases. *Materials and Structures,* 49**,** 3569-3577.

Osborn, E., Roeder, P. & Ulmer, G. 1969. Part I–phase equilibria at solidus temperatures in the quaternary system CaO-MgO-Al_2O_3-SiO_2 and their bearing on optimum composition of blast furnace slag and on slag properties. *Bull. Earth Miner. Sci. Exp. Stat. Penn. State Univ,* 85**,** 1-22.

Page, C. L., Short, N. R. & El Tarras, A. 1981. Diffusion of chloride ions in hardened cement pastes. *Cement and Concrete Research,* 11**,** 395-406.

Page, C. L. & Vennesland, 1983. Pore solution composition and chloride binding capacity of silica-fume cement pastes. *Matériaux et Construction,* 16**,** 19-25.

Plusquellec, G. & Nonat, A. 2016. Interactions between calcium silicate hydrate (C-S-H) and calcium chloride, bromide and nitrate. *Cement and Concrete Research,* 90**,** 89-96.

Prasanna, S. V. & Kamath, P. V. 2009. Anion-exchange reactions of layered double hydroxides: interplay between coulombic and H-bonding interactions. *Industrial & Engineering Chemistry Research,* 48**,** 6315-6320.

Provis, J. L. 2014a. Geopolymers and other alkali activated materials: why, how, and what? *Materials and Structures,* 47**,** 11-25.

Provis, J. L. 2014b. Green concrete or red herring? – future of alkali-activated materials. *Advances in Applied Ceramics,* 113**,** 472-477.

Provis, J. L. & Bernal, S. A. 2014. Geopolymers and related alkali-activated materials. *Annual Review of Materials Research,* 44**,** 299-327.

Provis, J. L., Brice, D. G., Buchwald, A., Duxson, P., Kavalerova, E., Krivenko, P. V., Shi, C., Van Deventer, J. S. J. & Wiercx, J. a. L. M. 2014. Demonstration projects and applications in building and civil infrastructure. *In:* PROVIS, J. L. & VAN DEVENTER, J. S. J. (eds.) *Alkali Activated Materials: State-of-the-Art Report, RILEM TC 224-AAM.* Dordrecht: RILEM/Springer.

Puertas, F., Fernández-Jiménez, A. & Blanco-Varela, M. T. 2004. Pore solution in alkali-activated slag cement pastes. Relation to the composition and structure of calcium silicate hydrate. *Cement and Concrete Research,* 34**,** 139-148.

Puertas, F., Palacios, M., Manzano, H., Dolado, J. S., Rico, A. & Rodríguez, J. 2011. A model for the C-A-S-H gel formed in alkali-activated slag cements. *Journal of the European Ceramic Society,* 31**,** 2043-2056.

Puertas, F., Palacios, M. & Vázquez, T. 2006. Carbonation process of alkali-activated slag mortars. *Journal of Materials Science,* 41**,** 3071-3082.

Ramachandran, V. S. 1971. Possible states of chloride in the hydration of tricalcium silicate in the presence of calcium chloride. *Matériaux et Construction,* 4**,** 3-12.

Ravikumar, D. & Neithalath, N. 2013. Electrically induced chloride ion transport in alkali activated slag concretes and the influence of microstructure. *Cement and Concrete Research,* 47**,** 31-42.

Renaudin, G., Kubel, F., Rivera, J. P. & Francois, M. 1999. Structural phase transition and high temperature phase structure of Friedels salt, $3CaO \cdot Al_2O_3 \cdot CaCl_2 \cdot 10H_2O$. *Cement and Concrete Research,* 29**,** 1937-1942.

Richardson, I. 2013a. Clarification of possible ordered distributions of trivalent cations in layered double hydroxides and an explanation for the observed variation in the lower solid-solution limit. *Acta Crystallographica Section B: Structural Science,* 69**,** 629-633.

Richardson, I. 2013b. The importance of proper crystal-chemical and geometrical reasoning demonstrated using layered single and double hydroxides. *Acta Crystallographica Section B,* 69**,** 150-162.

Richardson, I. G., Brough, A. R., Brydson, R., Groves, G. W. & Dobson, C. M. 1993. Location of aluminum in substituted calcium silicate hydrate (C-S-H) gels as determined by ^{29}Si and ^{27}Al NMR and EELS. *Journal of the American Ceramic Society,* 76**,** 2285-2288.

Richardson, I. G., Brough, A. R., Groves, G. W. & Dobson, C. M. 1994. The characterization of hardened alkali-activated blast-furnace slag pastes and the nature of the calcium silicate hydrate (C-S-H) phase. *Cement and Concrete Research,* 24**,** 813-829.

RILEM TC 178-Tmc 2002. Recommendations of RILEM TC 178-TMC: 'Testing and modelling chloride penetration in concrete analysis of water soluble chloride content in concrete. *Materials and Structures,* 35**,** 586-588.

Rinaldi, R., Sacerdoti, M. & Passaglia, E. 1990. Strätlingite: crystal structure, chemistry, and a reexamination of its polytpye vertumnite. *European Journal of Mineralogy,* 2**,** 841-850.

Rocha, J., Del Arco, M., Rives, V. & Ulibarri, M. A. 1999. Reconstruction of layered double hydroxides from calcined precursors: a powder XRD and ^{27}Al MAS NMR study. *Journal of Materials Chemistry,* 9**,** 2499-2503.

Saillio, M., Baroghel-Bouny, V. & Barberon, F. 2014. Chloride binding in sound and carbonated cementitious materials with various types of binder. *Construction and Building Materials,* 68**,** 82-91.

Sakulich, A. R., Anderson, E., Schauer, C. & Barsoum, M. W. 2009. Mechanical and microstructural characterization of an alkali-activated slag/limestone fine aggregate concrete. *Construction and Building Materials,* 23**,** 2951-2957.

Sakulich, A. R., Anderson, E., Schauer, C. L. & Barsoum, M. W. 2010. Influence of Si:Al ratio on the microstructural and mechanical properties of a fine-limestone aggregate alkali-activated slag concrete. *Materials and Structures,* 43**,** 1025-1035.

Samson, E., Marchand, J. & Snyder, K. A. 2003. Calculation of ionic diffusion coefficients on the basis of migration test results. *Materials and Structures,* 36**,** 156-165.

San Nicolas, R., Bernal, S. A., Mejía de Gutiérrez, R., Van Deventer, J. S. J. & Provis, J. L. 2014. Distinctive microstructural features of aged sodium silicate-activated slag concretes. *Cement and Concrete Research,* 65**,** 41-51.

Sato, T., Fujita, H., Endo, T., Shimada, M. & Tsunashima, A. 1988. Synthesis of hydrotalcite-like compounds and their physico-chemical properties. *Reactivity of Solids,* 5**,** 219-228.

Schlegel, M. C., Stroh, J., Malaga, K., Meng, B., Panne, U. & Emmerling, F. 2015. Pathway of a damaging mechanism – Analyzing chloride attack by synchrotron based X-ray diffraction. *Solid State Sciences,* 44**,** 45-54.

Schneider, J., Cincotto, M. A. & Panepucci, H. 2001. ^{29}Si and ^{27}Al high-resolution NMR characterization of calcium silicate hydrate phases in activated blast-furnace slag pastes. *Cement and Concrete Research,* 31**,** 993-1001.

Scott , P. W., Critchley, S. R. & Fwilkinson, C. F. 1986. The chemistry and mineralogy of some granulated and pelletized blastfurnace slags *Mineralogical Magazine,* 50**,** 141-147.

Sharma, B. K. 1991. Industrial Chemistry, GOEL Publishing House.

Shaw, D. J. 1992. *Introduction to Colloid and Surface Chemistry,* London, Butterworth-Heinemann.

Shi, C. 1996. Strength, pore structure and permeability of alkali-activated slag mortars. *Cement and Concrete Research,* 26**,** 1789-1799.

Shi, C. & Day, R. L. 1995. A calorimetric study of early hydration of alkali-slag cements. *Cement and Concrete Research,* 25**,** 1333-1346.

Shi, C. & Day, R. L. 1996. Some factors affecting early hydration of alkali-slag cements. *Cement and Concrete Research,* 26**,** 439-447.

Shi, C., Roy, D. & Krivenko, P. 2006. *Alkali-Activated Cements and Concretes,* Taylor & Francis.

Shi, C. J. 2004. Effect of mixing proportions of concrete on its electrical conductivity and the rapid chloride permeability test (ASTM C1202 or ASSHTO T277) results. *Cement and Concrete Research,* 34**,** 537-545.

Sideris, P. J., Nielsen, U. G., Gan, Z. & Grey, C. P. 2008. Mg/Al ordering in layered double hydroxides revealed by multinuclear NMR spectroscopy. *Science,* 321**,** 113-117.

Snellings, R. 2015. Surface chemistry of calcium aluminosilicate glasses. *Journal of the American Ceramic Society,* 98**,** 303-314.

Song, H.-W., Lee, C.-H. & Ann, K. Y. 2008a. Factors influencing chloride transport in concrete structures exposed to marine environments. *Cement and Concrete Composites,* 30**,** 113-121.

Song, H. W., Lee, C. H., Jung, M. S. & Ann, K. Y. 2008b. Development of chloride binding capacity in cement pastes and influence of the pH of hydration products. *Canadian Journal of Civil Engineering,* 35**,** 1427-1434.

Song, S. & Jennings, H. M. 1999. Pore solution chemistry of alkali-activated ground granulated blast-furnace slag. *Cement and Concrete Research,* 29**,** 159-170.

Song, S., Sohn, D., Jennings, H. M. & Mason, T. O. 2000. Hydration of alkali-activated ground granulated blast furnace slag. *Journal of Materials Science,* 35**,** 249-257.

Stebbins, J. F. & Du, L.-S. 2002. Chloride ion sites in silicate and aluminosilicate glasses: A preliminary study by ^{35}Cl solid-state NMR. *American Mineralogist,* 87**,** 359-363.

Sun, G. K., Young, J. F. & Kirkpatrick, R. J. 2006. The role of Al in C–S–H: NMR, XRD, and compositional results for precipitated samples. *Cement and Concrete Research,* 36**,** 18-29.

Tamura, H., Mita, K., Tanaka, A. & Ito, M. 2001. Mechanism of hydroxylation of metal oxide surfaces. *Journal of Colloid and Interface Science,* 243**,** 202-207.

Tamura, H., Tanaka, A., Mita, K.-Y. & Furuichi, R. 1999. Surface hydroxyl site densities on metal oxides as a measure for the ion-exchange capacity. *Journal of Colloid and Interface Science,* 209**,** 225-231.

Tang, L. 1996. Electrically accelerated methods for determining chloride diffusivity in concrete—current development. *Magazine of Concrete Research,* 48**,** 173-179.

Tang, L. & Nilsson, L.-O. 1992. Rapid determination of the chloride diffusivity in concrete by applying an electric field. *ACI Materials Journal,* 89**,** 49-53.

Tang, L. & Nilsson, L.-O. 1993. Chloride binding capacity and binding isotherms of OPC pastes and mortars. Cement and Concrete Research, 23, 247-253.

Tang, L. & Sørensen, H. E. 2001. Precision of the Nordic test methods for measuring the chloride diffusion/migration coefficients of concrete. *Materials and Structures,* 34**,** 479-485.

Taylor, H. F. W. 1997. *Cement Chemistry,* Thomas Telford.

Theiss, F., López, A., Frost, R. L. & Scholz, R. 2015. Spectroscopic characterisation of the LDH mineral quintinite $Mg_4Al_2(OH)_{12}CO_3 \cdot 3H_2O$. *Spectrochimica Acta Part A: Molecular and Biomolecular Spectroscopy,* 150**,** 758-764.

Theiss, F. L., Couperthwaite, S. J., Ayoko, G. A. & Frost, R. L. 2014. A review of the removal of anions and oxyanions of the halogen elements from aqueous solution by layered double hydroxides. *Journal of Colloid and Interface Science,* 417**,** 356-368.

Thomas, M. D. A., Hooton, R. D., Scott, A. & Zibara, H. 2012. The effect of supplementary cementitious materials on chloride binding in hardened cement paste. *Cement and Concrete Research,* 42**,** 1-7.

Thunqvist, E.-L. 2004. Regional increase of mean chloride concentration in water due to the application of deicing salt. *Science of The Total Environment,* 325**,** 29-37.

Tichit, D., Naciri Bennani, M., Figueras, F., Tessier, R. & Kervennal, J. 1998. Aldol condensation of acetone over layered double hydroxides of the meixnerite type. *Applied Clay Science,* 13**,** 401-415.

Tong, L. & Gjørv, O. E. 2001. Chloride diffusivity based on migration testing. *Cement and Concrete Research,* 31**,** 973-982.

Tongamp, W., Zhang, Q. & Saito, F. 2007. Preparation of meixnerite (Mg–Al–OH) type layered double hydroxide by a mechanochemical route. *Journal of Materials Science,* 42**,** 9210-9215.

Trefalt, G., Behrens, S. H. & Borkovec, M. 2016. Charge regulation in the electrical double layer: ion adsorption and surface interactions. *Langmuir,* 32**,** 380-400.

Tritthart, J. 1989. Chloride binding in cement II. The influence of the hydroxide concentration in the pore solution of hardened cement paste on chloride binding. *Cement and Concrete Research,* 19**,** 683-691.

Tuutti, K. 1982. *Corrosion of steel in concrete,* CBI Forskning 82:4, KTH, Kungliga Tekniska Högskolan i Stockholm.

Van Deventer, J. S. J., Provis, J. L., Duxson, P. & Brice, D. G. 2010. Chemical research and climate change as drivers in the commercial adoption of alkali activated materials. *Waste and Biomass Valorization,* 1**,** 145-155.

Vollpracht, A., Lothenbach, B., Snellings, R. & Haufe, J. 2016. The pore solution of blended cements: a review. *Materials and Structures,* 49**,** 3341-3367.

Wan, D., Liu, Y., Xiao, S., Chen, J. & Zhang, J. 2015. Uptake fluoride from water by caclined Mg-Al-CO_3 hydrotalcite: Mg/Al ratio effect on its structure, electrical affinity and adsorptive property. *Colloids and Surfaces A: Physicochemical and Engineering Aspects,* 469**,** 307-314.

Wang, J., Kalinichev, A. G., Amonette, J. E. & Kirkpatrick, R. J. 2003. Interlayer structure and dynamics of Cl-bearing hydrotalcite: far infrared spectroscopy and molecular dynamics modeling. *American Mineralogist,* 88**,** 398-409.

Wang, S.-D. & Scrivener, K. L. 1995. Hydration products of alkali activated slag cement. *Cement and Concrete Research,* 25**,** 561-571.

Wang, S.-D. & Scrivener, K. L. 2003. ^{29}Si and ^{27}Al NMR study of alkali-activated slag. *Cement and Concrete Research,* 33**,** 769-774.

Wang, S.-D., Scrivener, K. L. & Pratt, P. L. 1994. Factors affecting the strength of alkali-activated slag. *Cement and Concrete Research,* 24**,** 1033-1043.

Whiting, J. 1895. *Manufacture of cement*. United States patent application.

Whittaker, M., Zajac, M., Ben Haha, M., Bullerjahn, F. & Black, L. 2014. The role of the alumina content of slag, plus the presence of additional sulfate on the hydration and microstructure of Portland cement-slag blends. *Cement and Concrete Research,* 66**,** 91-101.

Wieczorek-Ciurowa, K., Paulik, J. & Paulik, F. 1980. Influence of foreign materials upon the thermal decomposition of dolomite, calcite and magnesite part I. Influence of sodium chloride. *Thermochimica Acta,* 38**,** 157-164.

Winnefeld, F., Ben Haha, M., Le Saout, G., Costoya, M., Ko, S.-C. & Lothenbach, B. 2015. Influence of slag composition on the hydration of alkali-activated slags. *Journal of Sustainable Cement-Based Materials,* 4**,** 85-100.

Winslow, D. N., Cohen, M. D., Bentz, D. P., Snyder, K. A. & Garboczi, E. J. 1994. Percolation and pore structure in mortars and concrete. *Cement and Concrete Research,* 24**,** 25-37.

Wong, H. S. & Buenfeld, N. R. 2006. Monte Carlo simulation of electron-solid interactions in cement-based materials. Cement and Concrete Research, 36, 1076-1082.

Wu, X., Jiang, W. & Roy, D. M. 1990. Early activation and properties of slag cement. *Cement and Concrete Research,* 20**,** 961-974.

Xu, H., Provis, J. L., Van Deventer, J. S. J. & Krivenko, P. V. 2008. Characterization of aged slag concretes. *ACI Materials Journal,* 105, 131-139.

Yang, Z., Fischer, H., Cerezo, J., Mol, J. M. C. & Polder, R. 2013a. Aminobenzoate modified MgAl hydrotalcites as a novel smart additive of reinforced concrete for anticorrosion applications. *Construction and Building Materials,* 47**,** 1436-1443.

Yang, Z., Fischer, H. & Polder, R. 2012. Possibilities for improving corrosion protection of reinforced concrete by modified hydrotalcites – a literature review. *In:* ANDRADE, C. & GULIKERS, J. (eds.) *Advances in Modeling Concrete Service Life.* Springer Netherlands.

Yang, Z., Fischer, H. & Polder, R. 2013b. Modified hydrotalcites as a new emerging class of smart additive of reinforced concrete for anticorrosion applications: A literature review. *Materials and Corrosion,* 64**,** 1066-1074.

Yang, Z., Fischer, H. & Polder, R. 2014. Synthesis and characterization of modified hydrotalcites and their ion exchange characteristics in chloride-rich simulated concrete pore solution. *Cement and Concrete Composites,* 47**,** 87-93.

Yang, Z., Fischer, H. & Polder, R. 2015. Laboratory investigation of the influence of two types of modified hydrotalcites on chloride ingress into cement mortar. *Cement and Concrete Composites,* 58**,** 105-113.

Ye, G., Lura, P. & Van Breugel, K. 2006. Modelling of water permeability in cementitious materials. *Materials and Structures,* 39**,** 877-885.

Yoon, S., Ha, J., Chae, S., Kilcoyne, A. L. D. & Monteiro, P. J. M. 2014a. X-ray spectromicroscopic study of interactions between NaCl and calcium silicate hydrates. *Magazine of Concrete Research,* 66**,** 141-149.

Yoon, S., Moon, J., Bae, S., Duan, X., Giannelis, E. P. & Monteiro, P. M. 2014b. Chloride adsorption by calcined layered double hydroxides in hardened Portland cement paste. *Materials Chemistry and Physics,* 145**,** 376-386.

Yu, S. W. & Page, C. L. 1991. Diffusion in cementitious materials: 1. Comparative study of chloride and oxygen diffusion in hydrated cement pastes. *Cement and Concrete Research,* 21**,** 581-588.

Yuan, Q., Shi, C., De Schutter, G., Audenaert, K. & Deng, D. 2009. Chloride binding of cement-based materials subjected to external chloride environment – A review. *Construction and Building Materials,* 23**,** 1-13.

Yuan, Q., Shi, C., He, F., De Schutter, G., Audenaert, K. & Zheng, K. 2008. Effect of hydroxyl ions on chloride penetration depth measurement using the colorimetric method. *Cement and Concrete Research,* 38**,** 1177-1180.

Zhang, S.-T., Dou, Y., Zhou, J., Pu, M., Yan, H., Wei, M., Evans, D. G. & Duan, X. 2016. DFT-based simulation and experimental validation on the topotactic transformation of MgAl-layered double hydroxides. *ChemPhysChem,* 17**,** 2754-2766.

Zhang, T. & Gjørv, O. E. 1996. Diffusion behavior of chloride ions in concrete. *Cement and Concrete Research,* 26**,** 907-917.

Zhu, Q., Jiang, L., Chen, Y., Xu, J. & Mo, L. 2012. Effect of chloride salt type on chloride binding behavior of concrete. *Construction and Building Materials,* 37**,** 512-517.

Publications from the thesis

Journal publication

Ke, X.; Bernal, S.A.; Hussein, O.H., Provis, J.L., Chloride binding and diffusivity in sodium carbonate-activated slag pastes and mortars. Manuscript in preparation.

Ke, X.; Bernal, S.A.; Provis, J.L., Uptake of Chloride and Carbonate by Mg-Al and Ca-Al Layered Double Hydroxides in Simulated Pore Solutions of Alkali-Activated slag cement. Cem. Concr. Res., 100, 1-13.

Ke, X.; Bernal, S.A.; Provis, J.L., (2016) Controlling the Kinetics of Reaction of Sodium Carbonate-activated Slag Cements Using Calcined Layered Double Hydroxides. Cem. Concr. Res., 81, 24-37. .

Conference publications

Ke, X.; Bernal, S. A.; Provis, J. L.,(2017), Assessing the Chloride Binding Capacity of Synthetic Cementitious Phases in Alkali-Activated Slag Simulated Pore Solutions. 1st International Conference on Construction Materials for Sustainable Future. Apr 19-21, Zadar, Croatia (under review).

Bernal, S. A.; **Ke, X.**; Hussein, O. H.; Provis, J. L., (2016), Effect of Testing Conditions on the Loss on Ignition Results of Anhydrous Granulated Blast Furnace Slags Determined via Thermogravimetry. International RILEM Conference on Materials, Systems and Structures in Civil Engineering Conference segment on Concrete with Supplementary Cementitious Materials. Aug 22-24, Technical University of Denmark, Lyngby, Denmark.

Ke, X.; Bernal, S. A.; Provis, J. L.,(2015), Can We Make Sodium Carbonate-activated Slags React Faster? The 14th International Congress on the Chemistry of Cement (ICCC). Oct 13-16, Beijing, China, CD-ROM proceedings.

Bernal, S. A.; **Ke, X.;** Provis, J. L.,(2015), Activation of Slags using Near-Neutral Salts: The Importance of Slag Chemistry. The 14th International Congress on the Chemistry of Cement (ICCC). Oct 13-16, Beijing, China, CD-ROM proceedings.

Ke, X.; Bernal, S. A.; Provis, J. L.,(2015),The Role of LDHs in the Chloride Intrusion in Alkali-activated Slag Cement, Proceedings of the 35th Cement and Concrete Science Conference, Aug 25-28, University of Aberdeen, UK. (poster and extended abstract)

Ke, X.; Bernal, S. A.; Provis, J. L.,(2014), Chloride Binding Behaviour of Hydrotalcite in Simulated Chloride-Rich Pore solution, Proceedings of the 34th Cement and Concrete Science Conference, Sep 14-17, University of Sheffield, UK.

Other conference presentations

Ke, X.; Bernal, S. A.; Brice, D; van Deventer, J.S.J.; Provis, J. L.,(2017) Correlating Structural Evolution of Long-Duration Ambient and Rapid Hydrothermal Curing of Metakaolin based Geopolymers. 92nd DKG Annual Conference & Symposium on High-Performance Ceramics, Mar 19-22, TU Berlin, Germany (oral presentation).

Ke, X.; Bernal, S. A.; Provis, J. L., (2016), Tailoring Sodium Carbonate-Activated Slag Cements with a Smart Chemical Addition. ACI Fall Meeting- Revolutionary Concrete, Oct 23-27, Philadelphia, US (oral presentation).

Ke, X.; Bernal, S. A.; Hussein, O. H.; Provis, J. L.,(2015) Advances in the Thermal Analysis of Supplementary Cementitious Materials. TAC 2015, 50th Anniversary Conference of the Royal Society Chemistry Thermal Methods Group. 30th March to 1st April, Churchill College, Cambridge.

Ke, X.; Bernal, S. A.; Provis, J. L.,(2015), Controlling the Hydration Kinetics and Phase Evolution of Alkali-Activated Slag Paste by Seeding with Layered Double Hydroxides, International Conference on Applied Mineralogy & Advanced Materials, Jun 7-12, Castellaneta Marina – Taranto, Italy (oral presentation).

Additional publications during the period of doctoral studies

Criado M., **Ke X**., Provis J.L., Bernal S.A. Part 2 – Chapter 8: Alternative inorganic binders based on alkali-activated metallurgical slags, in Sustainable & Non-Conventional Construction Materials Using Inorganic Bonded Fiber Composites, Eds. H. Savastano Jr., J. Fiorelli, S. F. dos Santos, Woodhead Elsevier, Cambridge UK, 2017. In press.

Bernal, S.A.; Juenger, M.C.G.; **Ke, X.;** Matthes, W; Lothenbach, B.; De Belie, N.; Provis, J.L., (2017) Characterization of Supplementary Cementitious Materials by Thermal Analysis. Mater. Struct., 50:26.

Ke, X.; Bernal, S. A.; Ye, N.; Provis, J. L. Yang, J., (2015), One-Part Geopolymers Based on Thermally Treated Red Mud/NaOH Blends. J. Am. Ceram. Soc., 98, (1), 5-11.